SATCOM Antenna Siting Study on P-3C Aircraft

D.A. Bensman and R.J. Marhefka

The Ohio State University
ElectroScience Laboratory
Department of Electrical Engineering
Columbus, Ohio 43212

Final Report 721711-4, Volume I
Grant No. NAG 2-542
September 1991

Naval Air Test Center
Patuxent River, MD 20670
and
NASA — Ames Research Center
Moffett Field, CA 94035

A. Approved for public release; Distribution is unlimited

NOTICES

When Government drawings, specifications, or other data are used for any purpose other than in connection with a definitely related Government procurement operation, the United States Government thereby incurs no responsibility nor any obligation whatsoever, and the fact that the Government may have formulated, furnished, or in any way supplied the said drawings, specifications, or other data, is not to be regarded by implication or otherwise as in any manner licensing the holder or any other person or corporation, or conveying any rights or permission to manufacture, use, or sell any patented invention that may in any way be related thereto.

50272-101

REPORT DOCUMENTATION PAGE	1. REPORT NO.	2.	3. Recipient's Accession No.
4. Title and Subtitle SATCOM Antenna Siting Study on P-3C Aircraft			5. Report Date September 1991
7. Author(s) D.A. Bensman and R.J. Marhefka			6. 8. Performing Org. Rept. No. 721711-4, Volume I
9. Performing Organization Name and Address The Ohio State University ElectroScience Laboratory 1320 Kinnear Road Columbus, OH 43212			10. Project/Task/Work Unit No. 11. Contract(C) or Grant(G) No. (C) (G) NAG 2-542
12. Sponsoring Organization Name and Address University Affairs Branch NASA — Ames Research Center Moffett Field, CA 94035			13. Report Type/Period Covered Final Report 14.

15. Supplementary Notes

16. Abstract (Limit: 200 words)

The purpose of this effort is to use the NEC-BSC to study the performance of a SATCOM antenna on a P-3C aircraft. After plate - cylinder fields are added to Version 3.1 of the NEC-BSC, it is shown that the NEC-BSC can be used to accurately predict the performance of a SATCOM antenna system on a P-3C aircraft. The study illustrates that the NEC-BSC gives good results when compared with scale model measurements provided by Boeing and Lockheed.

17. Document Analysis a. Descriptors

AIRCRAFT
DIFFRACTION
UTD
ANALYSIS
MODELLING

b. Identifiers/Open-Ended Terms

c. COSATI Field/Group

18. Availability Statement	19. Security Class (This Report)	21. No. of Pages
A. Approved for public release; Distribution is unlimited.	Unclassified	192
	20. Security Class (This Page) Unclassified	22. Price

(See ANSI-Z39.18) *See Instructions on Reverse* OPTIONAL FORM 272 (4-77)
Department of Commerce

[redacted]

Contents

List of Figures

Chapter 1

Introduction

1.1 Objective

The purpose of this effort is to study the performance of SATCOM antennas on aircraft. The potential locations of the antenna system to achieve a desired pattern and polarization coverage is being assessed on a P-3C aircraft. The aircraft is being modeled using a computer code based on the Uniform Geometrical Theory of Diffraction (UTD), which is the NEC-BSC Version 3.1 [1].

In this study a circular polarized antenna composed of crossed dipoles is being considered. In particular, the antenna to be modeled represents a Dorne & Margolin DM 1501341 (Batwing) airborne UHF satellite communications antenna. The objective is to try to find a location for the antenna on the P-3C that will provide a minimum coverage of 330° azimuth, from zenith to 10° above the horizon of the aircraft. It is desired for the system to provide performance to maintain the satellite link in areas of high signal fading due to multipath effects. This study extends the work presented in References [2,3].

1.2 Overview

The rest of this report is organized as follows. The remainder of this chapter discusses some of the relevant background of the modeling effort pertaining to UTD and the NEC-BSC. The NEC-BSC model used to describe the UHF SATCOM antenna in this study is validated in Chapter 2. In Chapter 3, different NEC-BSC models of the P-3C aircraft are investigated. It is demonstrated from the patterns calculated using these models that additional fields which contain the interactions between plates and cylinders are needed in Version 3.1 of the NEC-BSC. In Chapter 4, these additional fields are defined and incorporated in the NEC-BSC. Using the improved code, the most accurate model for the P-3C aircraft is then determined in Chapter 5 and is validated by comparing the NEC-BSC calculated radiation patterns with scale model measurements taken independently by Boeing and Lockheed. Finally, a summary and some general conclusions are presented in Chapter 6.

1.3 UTD Background

The use of computer codes based on UTD to analyze antenna system performance has a long history at The Ohio State University ElectroScience Laboratory. This has included the modeling of aircraft, ships and many other structures [4]. The accuracy of the modeling is dependent on many factors. They may be grouped into three broad categories, that is, theoretical completeness, modeling capabilities, and numerical considerations.

The issue of theoretical completeness in the context of UTD is associated with UTD being an asymptotic theory. The scattered field is assumed to come from local scattering centers or combination of centers. It is not necessary that all terms be considered, only the ones that are largest for the application under study. For

most antenna pattern prediction work, this has been determined to be no more than second order interaction terms. The diffraction coefficients for these terms also must be known at least approximately. In addition, the size of the objects should be around a wavelength in extent or larger. Good engineering results, however, are often obtainable with distances as small as a quarter wavelength.

The issue of modeling capabilities of the code are associated with how accurately the individual building blocks of the code match the actual object being modeled. The building blocks of the NEC-BSC are discussed in Section 1.4. Experience has shown that the model only needs to match the real scattering object near the antenna and in the general proximity of the pattern cut desired. The details necessary to be included for a given application can be determined by a modeling sensitivity study. At first a simple version of the model is used and then additional features are added to it. If the patterns change significantly, then more details are added until little change is detected. The modeling sensitivity study for this particular antenna siting study is investigated in Chapter 5.

The issue of numerical considerations are present in all computer codes. It is dependent on the computer as well as the algorithms used. Numerical difficulties do not generally affect the entire pattern of a UTD code. It usually manifests itself near shadow boundaries or at start up locations for approximate ray tracing algorithms.

All of the above situations need to be kept in mind when a new class of applications is being considered. It is best to start from known situations and slowly build up to the ultimate solution. Scale model measurements or alternative calculations are often available for a couple of cases. This allows bounds to be placed on the accuracy of the patterns for the rest of the unknown situations. If there are discrepancies, they are limited to small regions of the patterns of interest. The

following sections of this report attempt to address the application under question based on these considerations.

1.4 NEC-BSC Modeling Capabilities

The analysis is based on uniform asymptotic techniques formulated in the Uniform Geometrical Theory of Diffraction (UTD) [5,6,7], sometimes referred to as the modern Geometrical Theory of Diffraction (GTD). The UTD approach is ideal for a general high frequency study of antennas in a complex environment. Only the most basic structural features of an otherwise very complicated structure need to be modeled. This is because ray optical techniques are used to determine components of the field incident on and diffracted by the various structures. Components of the diffracted fields are found using the UTD solutions for individual rays. They are summed with the geometrical optics terms in the far zone of the scattering centers, but, they can be in the near zone of the entire structure. The rays from a given scatterer interact with other structures causing various higher-order terms. One can trace out the various possible combinations of rays that interact between scatterers and determine and include only the dominant terms. Thus, one need only be concerned with the important scattering components and neglect all other higher-order terms. This method normally leads to accurate and efficient computer codes that can be systematically written and tested. Complex problems can be built up from simpler problems in manageable pieces.

The limitations associated with the computer code result mainly from the basic nature of the analysis. The solution is derived using the UTD which is a high frequency approach. For the scattering from plate structures, this means that each plate should have edges at least a wavelength long. If a dielectric slab is used, the source must be at least a wavelength from the surface. Also, the incident field

should not strike the slab too close to grazing. In addition, each antenna element should be at least a wavelength from all edges. For curved surfaces, the antenna can not be mounted directly on the curved part of the structure. The active element should be approximately a wavelength off the curved surface. In many cases, the wavelength limit can be reduced to a quarter wavelength for engineering purposes.

Note that the NEC-BSC is meant to complement other design techniques such as scale model measurements. It is a fast and cost effective means of anticipating problems at the early design stages of a system and to optimize design parameters such as antenna placement. In addition, it can be used at the measurement stage of development to confirm the experimental results. Also, near zone measurements can be projected into far zone patterns when it is very difficult to obtain the necessary range to be in the far zone of a whole structure.

A summary of the basic capabilities of the code are listed here:

- User oriented command word based input structure.
- Pattern calculations.
  - Near zone source fixed or moving.
  - Far zone observer.
  - Near zone observer.
- Single or multiple frequencies.
- Antenna to antenna spacial coupling calculations.
  - Near zone receiver fixed or moving.
- Efficient representation of antennas.
  - Infinitesimal Green's function representation.

  - Six built-in antenna types.
  - Linear interpolation of table look up data.
  - Method of Moments code or Reflector Code interface.
- Multiple sided flat plates.
  - Separate or joined.
  - Infinite ground plane.
  - Limited dielectric plate capability.
- Multiple elliptic cylinders.
- UTD single and multiple interactions included.
  - Second order plate terms not including double diffraction.
  - First order cylinder terms only.
  - First order plate - cylinder interaction terms.

1.5 Polarization Definition

In this report, the majority of the patterns are plotted for right hand circular polarization and left hand circular polarization [8]. The right hand circular polarized and left hand circular polarized fields are also referred to as co-polarized and cross-polarized fields, respectively, throughout the remainder of the report. The procedure used to define right hand circular polarization and left hand circular polarization is shown below. The direction vectors for the right hand and left hand circular polarized fields denoted by $\hat{R}$ and $\hat{L}$, respectively, are

$$\hat{R} = \frac{1}{\sqrt{2}}(\hat{\theta} - j\hat{\phi}) \tag{1.1}$$

$$\hat{L} = \frac{1}{\sqrt{2}}(\hat{\theta} + j\hat{\phi}). \tag{1.2}$$

The total $\vec{E}$ field at any point in the pattern is defined by

$$\vec{E}^{Tot} = \hat{R}E_R + \hat{L}E_L \tag{1.3}$$

where E_R is the right hand circular polarized field component and E_L is the left hand circular polarized field component. The magnitude for the right hand and left hand circular polarized field components are

$$E_R = \frac{1}{\sqrt{2}}(E_\theta + jE_\phi) \tag{1.4}$$

$$E_L = \frac{1}{\sqrt{2}}(E_\theta - jE_\phi) \tag{1.5}$$

where E_θ and E_ϕ are the field components in the $\hat{\theta}$ and $\hat{\phi}$ directions, respectively. These definitions for the right hand and left hand circular polarized fields given by equations (1.4) and (1.5), respectively, are used throughout the remainder of this report.

1.6 Normalization Procedures

The NEC-BSC is not an antenna code per se. It does not know the complete current distribution of the antenna that it is modeling. It just knows the pattern factor based on the type chosen and the amplitude and phase of each of the elements representing the antenna. Therefore, it does not know the power radiated or the input impedance of the antenna unless it is provided the information.

If the information of the antenna is obtained by a method of moments code, than the power budget along with the appropriate currents provided will be sufficient to normalize the code to a directive gain quantity. If the antenna is described by built-in factors with user supplied currents, then the user must also supply an

estimate of the power budget. This is accomplished by integrating the volumetric pattern of the fields radiated by the antenna as supplied by the code. The best results are provided by calculating the volumetric pattern of the antenna at its location on the model of the aircraft being used. This can be quite costly, however, since only a portion of the pattern may be of interest even though a complete volumetric pattern is being calculated for each location. It has been determined, however, that sufficiently accurate results are obtainable by determining the power radiated by integrating the volumetric pattern provided by the code for the antenna in free space or over an infinite ground plane which ever is more appropriate. It is obvious that the current distribution will not change for the NEC-BSC antenna model. Hence, if one assumes that power is conserved when the model is changed, the same number can be used for all the different antenna positions and aircraft models. This concept is confirmed here by the good overall results for the directive gain obtained by comparing with measured results.

Chapter 2

Antenna Model Validation

2.1 Introduction

The first step in this antenna siting study has been to analyze the present candidate UHF SATCOM antenna system and validate the antenna model which has been used in the NEC-BSC. In order to validate the antenna model, NEC-BSC calculated antenna patterns have been compared to both measured antenna patterns and antenna patterns calculated using other numerical methods. All the results found throughout this report have been referenced to an isotropic circular polarized radiator. In order to reference these results to an isotropic circular polarized radiator, the average power level of the antenna model placed over an infinite ground plane is first calculated. This average power level is then subtracted in dB from the absolute levels calculated for the various patterns to give the isotropic levels shown in the patterns throughout this report.

Section 2.2 defines the NEC-BSC model which is used to represent the UHF SATCOM antenna. Section 2.3 compares the NEC-BSC calculated antenna patterns with measured patterns provided by the manufacturer and Section 2.5 compares the calculated patterns with measured patterns provided by Naval Air Test Center. In these sections, the results are plotted in absolute gain. Section 2.4

compares NEC-BSC calculated antenna patterns with antenna patterns calculated using a moment method analysis. In Section 2.6, an exact eigenvalue solution is used to validate the accuracy of the NEC-BSC to model a crossed dipole antenna positioned near the surface of a cylinder. In these two sections, the results are plotted in relative gain. These results are plotted in relative gain because of the requirements in the plotting routines for the moment method and the exact eigenvalue solutions. In all cases, the results confirm that the antenna model used in the NEC-BSC is an accurate representation of the actual UHF SATCOM antenna.

2.2 Antenna Model

The Dorne & Margolin DM 1501341 (Batwing) airborne UHF satellite communication antenna is shown in Figure 1. This antenna is designed to provide high performance satellite communications for satellite elevation intercept angles of +35° above the horizon through the aircraft zenith. The important physical aspects as pertains to modeling this antenna are that the antenna consists of two orthogonal dipoles and that each of these dipoles has an element length of 16.5 inches and is located 7.6 inches above and parallel to the structure to which the antenna is mounted as shown in the figure.

To model this antenna, a simple crossed dipole antenna has been used in the NEC-BSC. This simple crossed dipole antenna consists of two orthogonal dipoles which are fed 90° out of phase with each other. Each of these orthogonal dipoles has an element length of 16.5 inches and is located 7.6 inches above and parallel to the structure to which the antenna is mounted corresponding with the actual dimensions of the Dorne & Margolin antenna.

OUTLINE DIMENSIONS
Inches (Centimeters)

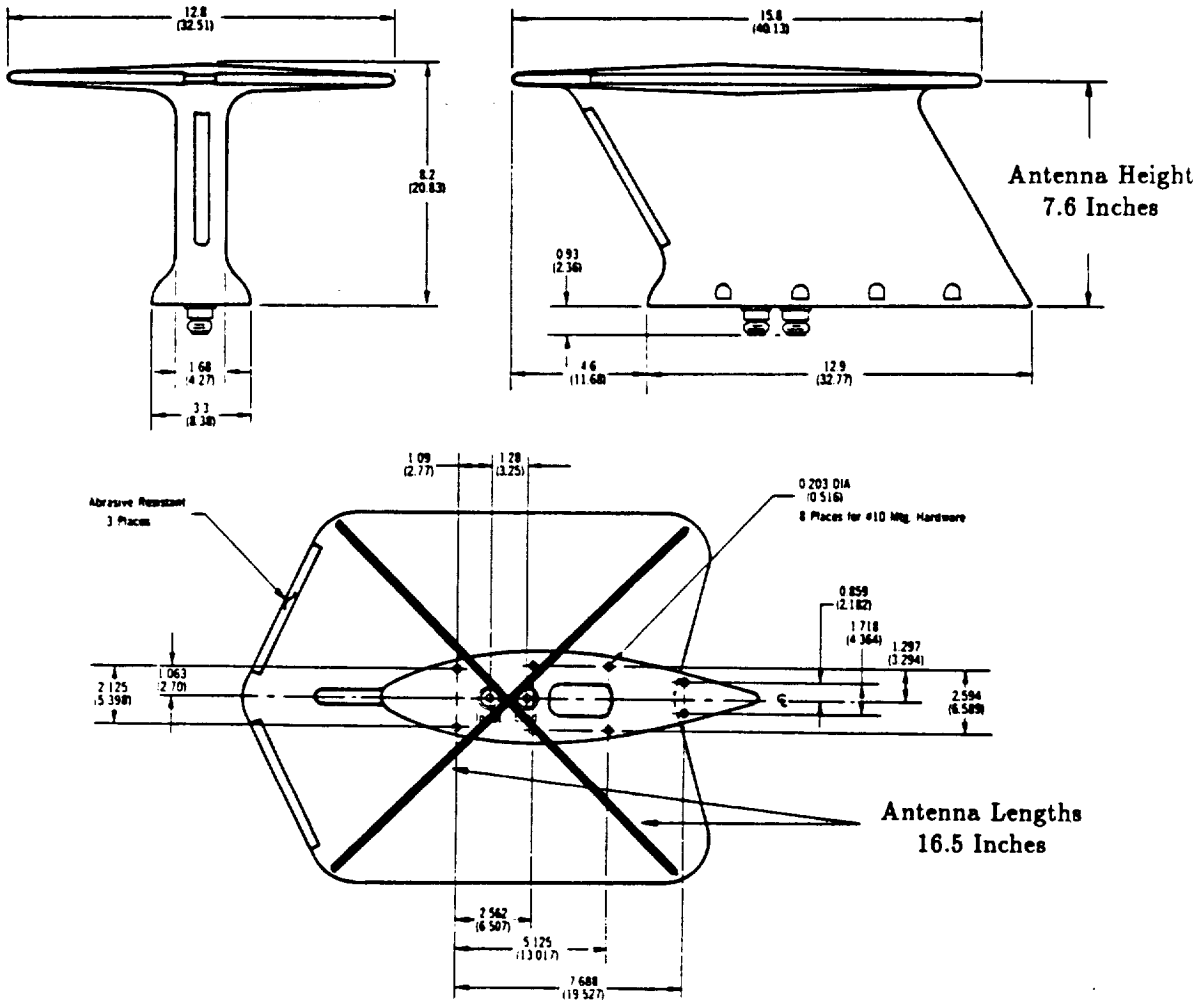

Figure 1: Batwing airborne UHF satellite communication antenna of Dorne & Margolin.

2.3 Dorne & Margolin Results

Dorne & Margolin has provided antenna system information for its DM 1501341 (Batwing) airborne UHF satellite communication antenna. The calculated results at 244 MHz and 318 MHz can be compared with the measured results supplied by the manufacturer in Figures 2 and 3, respectively, for the antenna on a 8 foot diameter ground plane in the principal elevation plane of the antenna. The principal elevation plane is defined as the plane which is perpendicular to the plane containing the dipoles and rotated 45° from the plane containing one of the dipoles. The results compare very well and show that this antenna model is an accurate representation of the actual Dorne & Margolin antenna in the principal elevation plane.

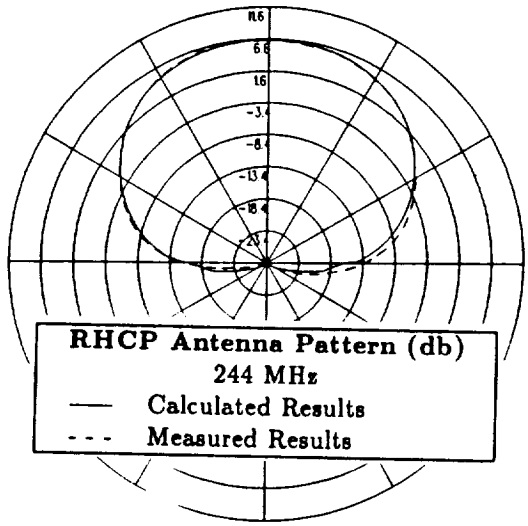

Figure 2: Right hand circular polarized antenna pattern in principal elevation plane at 244 MHz for Batwing antenna on a 8' diameter ground plane.

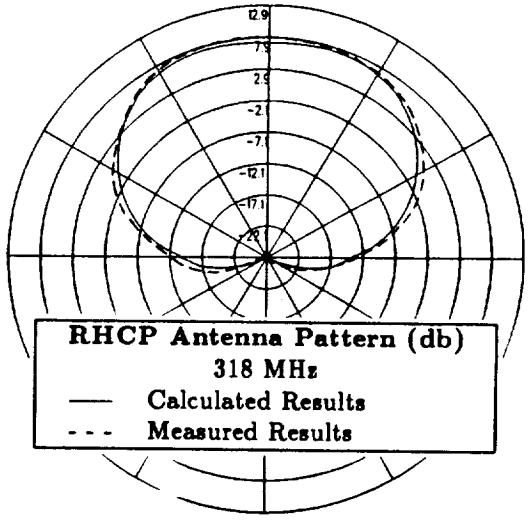

Figure 3: Right hand circular polarized antenna pattern in principal elevation plane at 318 MHz for Batwing antenna on a 8' diameter ground plane.

2.4 Method of Moments Results

Because the manufacturer has only provided information in the principal elevation plane, a moment method approach using the Electromagnetic Surface Patch Code Version IV [9] must be used in order to test the NEC-BSC's representation of the antenna in the elevation plane containing one of the dipoles. Since the antenna is circular polarized, the antenna pattern is identical for the elevation planes through both of the dipoles. Therefore, the free space pattern in the elevation plane containing one of the dipoles at 300 MHz using the NEC-BSC shown in Figure 4 can be compared with the method of moments result shown in Figure 5. Note that the results are plotted in relative gain.

Then antenna patterns are taken for the antenna placed on an infinite ground plane using both the NEC-BSC and the ESP IV code to ensure that the presence of the ground plane does not effect the validity of the antenna model. The ESP IV code does not contain an infinite ground plane option, therefore, the ground plane must be simulated using image theory. The pattern in the elevation plane containing one of the dipoles in the presence of an infinite ground plane at 300 MHz using the NEC-BSC is shown in Figure 6 and can be compared with the method of moments result shown in Figure 7. Again the results are plotted in relative gain. Above the ground plane the results compare very well. The field present below the ground plane in the method of moments pattern is caused by the imaging technique used to simulate the infinite ground plane in the ESP IV code and is not physically real. The good agreement between the NEC-BSC calculated results and the ESP IV calculated results both in free space and in the presence of an infinite ground plane suggests that the antenna model is also an accurate representation of the actual Dorne & Margolin antenna in the elevation plane containing one of the dipoles.

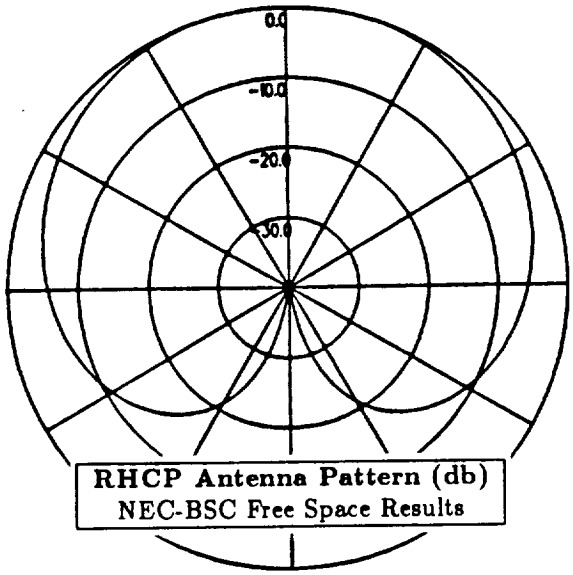

Figure 4: Calculated right hand circular polarized antenna pattern in the elevation plane containing one of the dipoles at 300 MHz for antenna model in free space using the NEC-BSC.

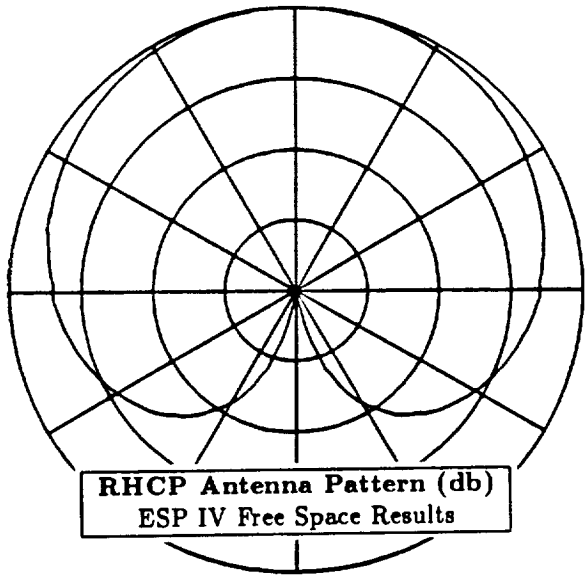

Figure 5: Calculated right hand circular polarized antenna pattern in the elevation plane containing one of the dipoles at 300 MHz for antenna model in free space using the ESP IV code.

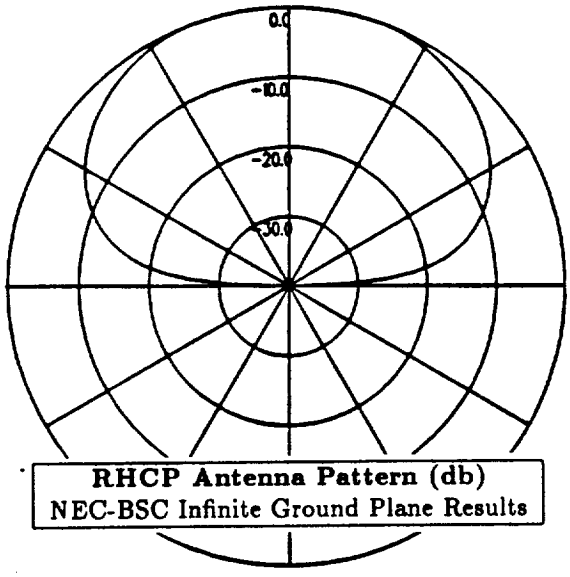

Figure 6: Calculated right hand circular polarized antenna pattern in the elevation plane containing one of the dipoles at 300 MHz for antenna model on an infinite ground plane using the NEC-BSC.

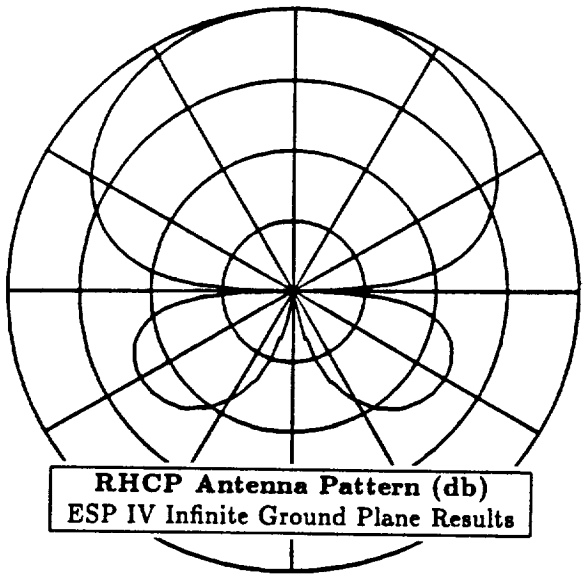

Figure 7: Calculated right hand circular polarized antenna pattern in the elevation plane containing one of the dipoles at 300 MHz for antenna model on an infinite ground plane using the ESP IV code.

2.5 Naval Air Test Center Results

The Naval Air Test Center has also provided measured antenna radiation patterns for the full-sized DM 1501341 Batwing antenna on a 6 foot diameter ground plane. These antenna patterns for the E_θ or vertical polarization and the E_ϕ or horizontal polarization have been taken at 300 MHz for various elevation planes. The calculated results for the E_θ and E_ϕ polarizations in the principal elevation plane can be compared to the measured results in Figures 8 and 9, respectively. The calculated results for the E_θ and E_ϕ polarizations in the elevation plane containing one of the dipoles can be compared to the measured results in Figures 10 and 11, respectively. Again there is good agreement between the calculated results and the measured results for both the E_θ and E_ϕ polarizations in each of the elevation planes studied.

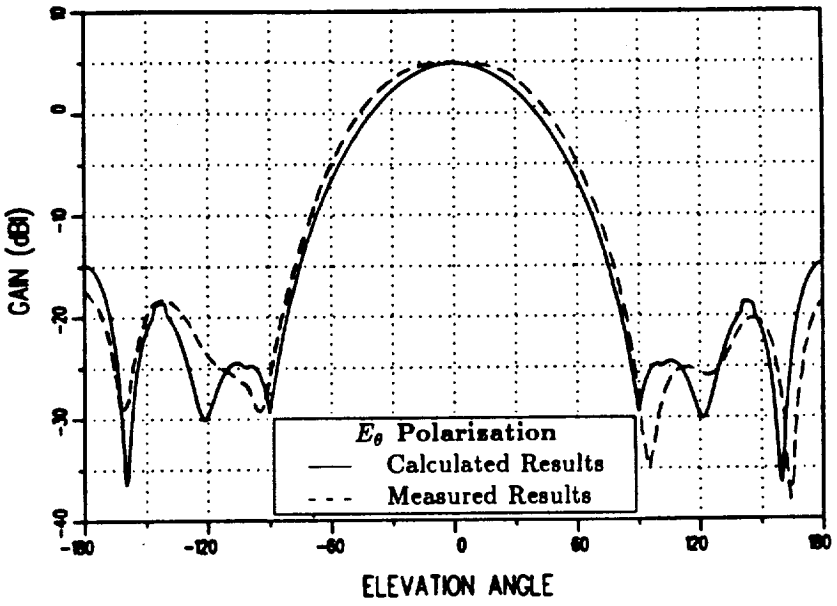

Figure 8: E_θ polarized antenna pattern in principal elevation plane at 300 MHz for Batwing antenna on a 6' diameter ground plane.

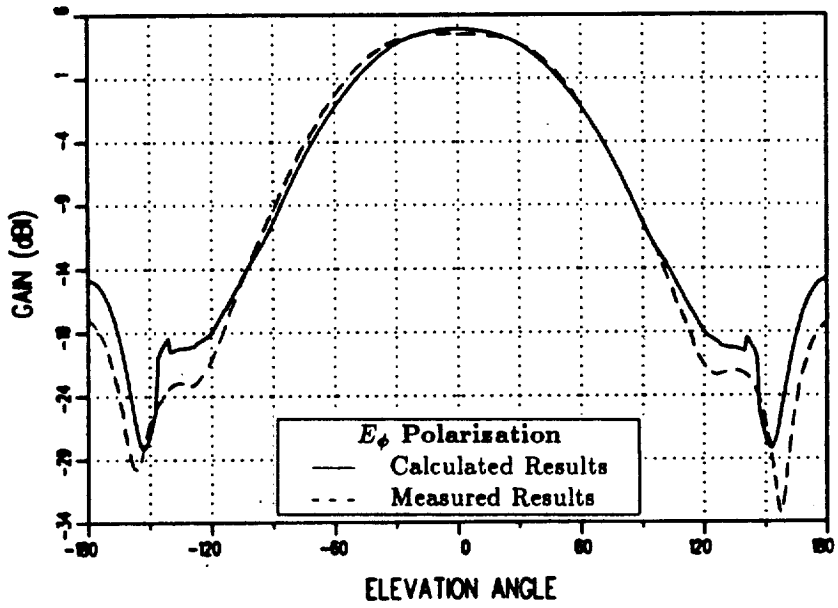

Figure 9: E_ϕ polarized antenna pattern in principal elevation plane at 300 MHz for Batwing antenna on a 6' diameter ground plane.

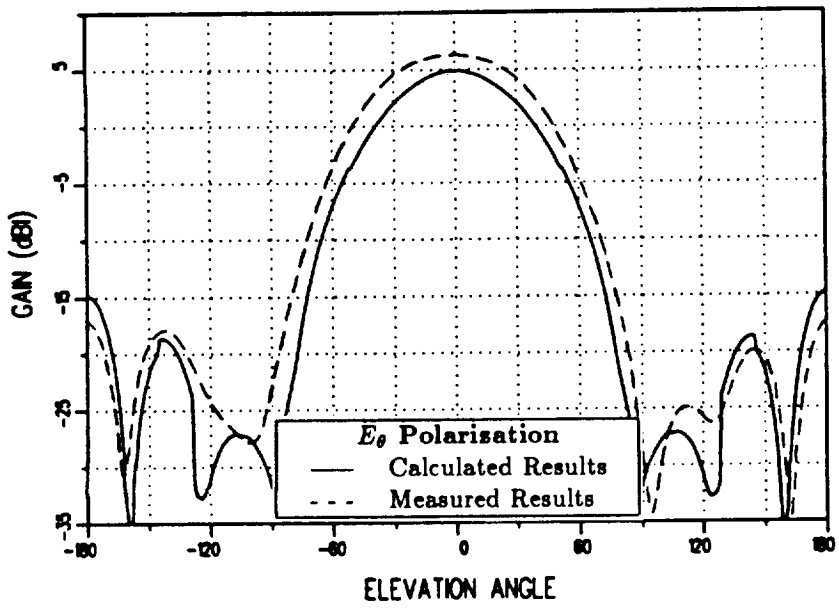

Figure 10: E_θ polarized antenna pattern in elevation plane containing one of the dipoles at 300 MHz for Batwing antenna on a 6' diameter ground plane.

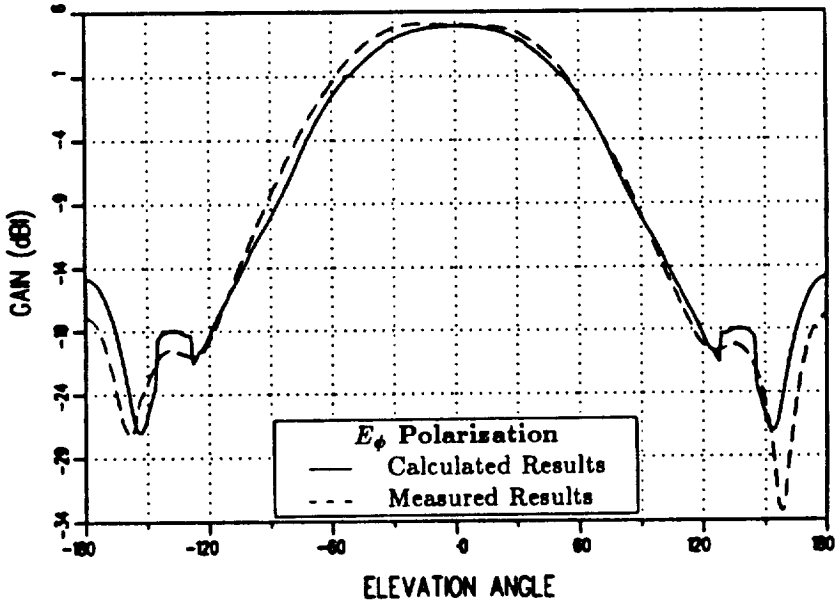

Figure 11: E_ϕ polarized antenna pattern in elevation plane containing one of the dipoles at 300 MHz for Batwing antenna on a 6' diameter ground plane.

2.6 Exact Eigenvalue Solution Results

In the majority of the cases investigated, the crossed dipole antenna is positioned near the surface of a cylinder which is used to represent the aircraft fuselage. In order to ensure that the NEC-BSC correctly calculates the fields for this situation, the NEC-BSC calculated radiation patterns for an infinitesimal crossed dipole positioned near the surface of an infinite cylinder can be compared to the radiation patterns determined from the exact eigenvalue solution [10]. For this problem, the dipoles had to be oriented axially and circumferentially to the cylinder due to the eigenfunction solution. In the actual situation, the dipoles are rotated 45°. The NEC-BSC calculated results for the right hand and left hand polarizations in the plane of the crossed dipole antenna shown in Figure 12 can be compared to the results determined from the exact eigenvalue solution shown in Figure 13. Also, the NEC-BSC calculated results for the right hand and left hand polarizations in a conic plane taken 45° from the axis of the infinite cylinder is shown in Figure 14. It can be compared to the results determined from the exact eigenvalue solution shown in Figure 15. Note that the results in this section are also plotted in relative gain. Again there is good agreement between the calculated results using NEC-BSC and the calculated results using the exact eigenvalue solution for both the right hand and left hand polarizations in each of the patterns studied.

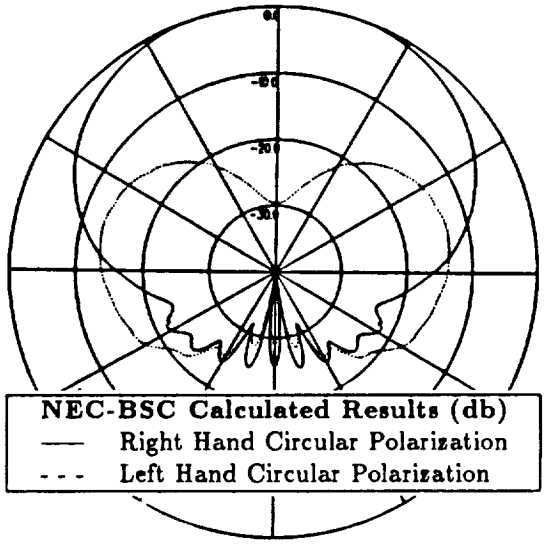

Figure 12: Calculated right hand and left hand circular polarized antenna patterns in the plane of infinitesimal crossed dipole antenna positioned near an infinite cylinder using NEC-BSC.

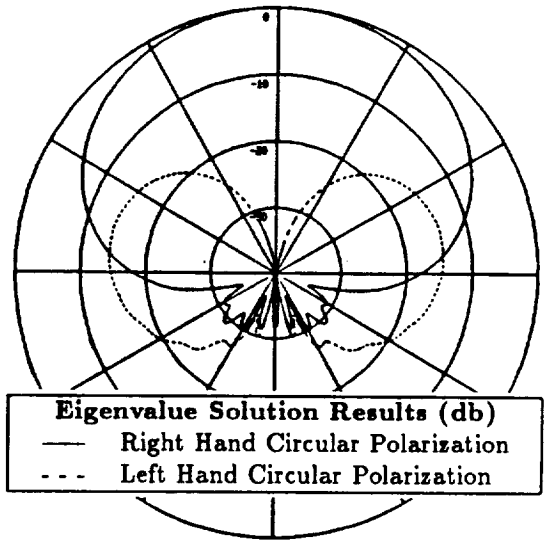

Figure 13: Calculated right hand and left hand circular polarized antenna patterns in the plane of infinitesimal crossed dipole antenna positioned near an infinite cylinder using exact eigenvalue solution.

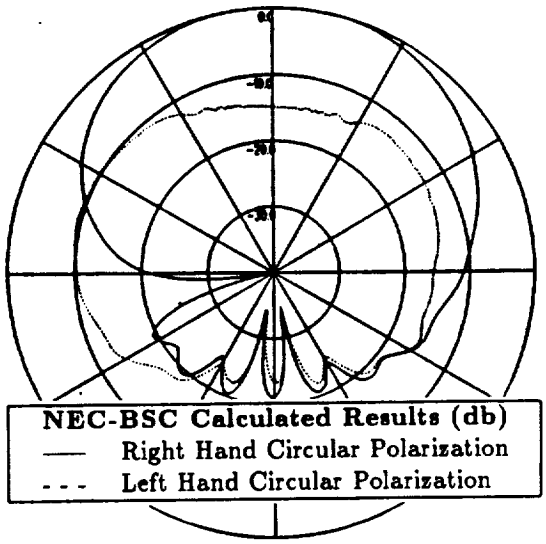

Figure 14: Calculated right hand and left hand circular polarized antenna patterns in a conic plane taken 45° from the axis of the cylinder for an infinitesimal crossed dipole antenna positioned near an infinite cylinder using NEC-BSC.

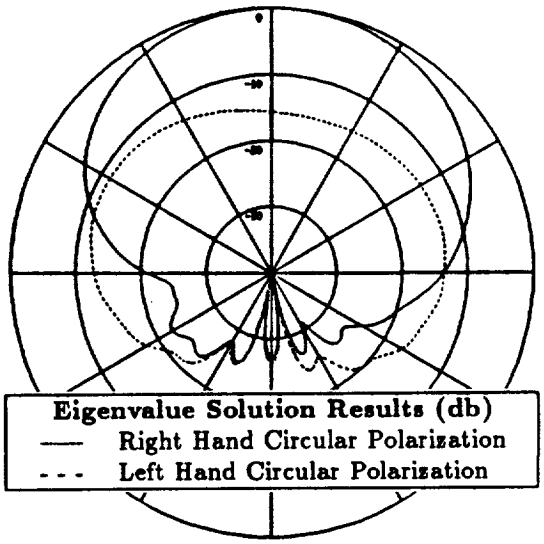

Figure 15: Calculated right hand and left hand circular polarized antenna patterns in a conic plane taken 45° from the axis of the cylinder for an infinitesimal crossed dipole antenna positioned near an infinite cylinder using exact eigenvalue solution.

Chapter 3

Investigation of Aircraft Model

3.1 Introduction

In this chapter, three different aircraft models are investigated using the NEC-BSC. All of the aircraft models investigated use flat plates to represent the wings, the horizontal stabilizers and the vertical stabilizers. The difference between the three aircraft models involves the way the aircraft fuselage is represented. The first case uses a cylinder to represent the fuselage, the second case uses a composite ellipsoid, and the third case uses a cone frustum. All of these scattering structures which are used to represent the different P-3C aircraft models have perfectly conducting surfaces.

The validity of these aircraft models can be determined by comparing the NEC-BSC calculated patterns to measurements conducted by Boeing on a 1/17 scale model of the P-3C aircraft [11]. The NEC-BSC calculations are compared to the measured patterns in order to determine which aircraft model gives the best representation of the actual P-3C aircraft. In this chapter and throughout the remainder of the report, the radiation patterns for the calculated and measured results are plotted in absolute gain in dB relative to an isotropic circular polarized radiator.

Section 3.2 defines the pattern coordinate system which is used throughout the report. In Section 3.3, calculated patterns in the roll plane, the azimuth plane and the elevation plane for each of the three aircraft models are compared to the measured results provided by Boeing. Section 3.4 investigates which fields contribute to the radiation patterns and determines which fields might need to be added to the NEC-BSC to improve the agreement between the calculated and measured patterns. Section 3.5 defines a method in which these additional fields can be temporarily simulated and compares the improved calculated patterns which contain these additional terms to the original calculated patterns and to the measured results. Section 3.6 summarizes the work done in this chapter and draws a conclusion on the most accurate NEC-BSC model representation of the P-3C aircraft.

3.2 Pattern Coordinate System Definition

The remainder of the report contains radiation patterns in the roll plane, the azimuth plane, the elevation plane and the conical cuts from 10° to 30° above the horizon for various antenna locations on the P-3C aircraft. In order to interpret these results, one must first know what the pattern coordinate systems are relative to the aircraft. The spherical coordinate system relative to the aircraft which is used in this report is given in Figure 16. The pattern coordinate system for each of the various radiation patterns relative to the aircraft is illustrated in Figure 17. These pattern coordinate systems are used throughout the remainder of the report.

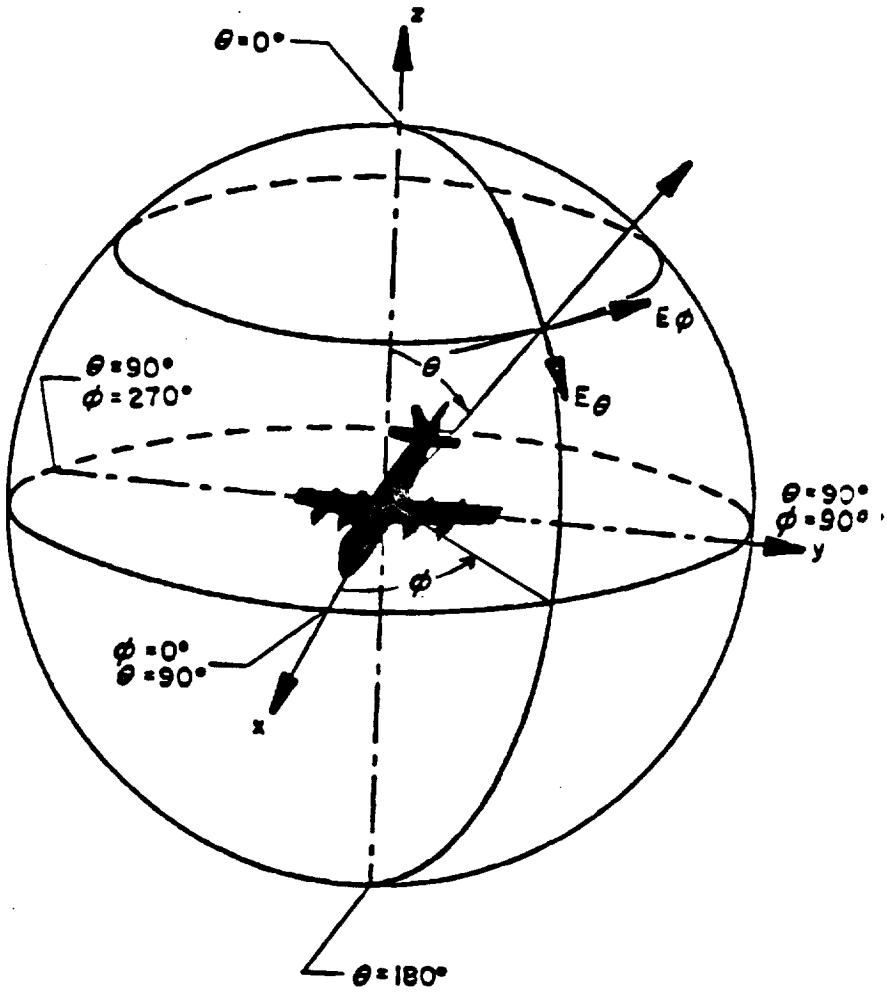

Figure 16: Spherical coordinate system relative to the aircraft which is used in the remainder of the report.

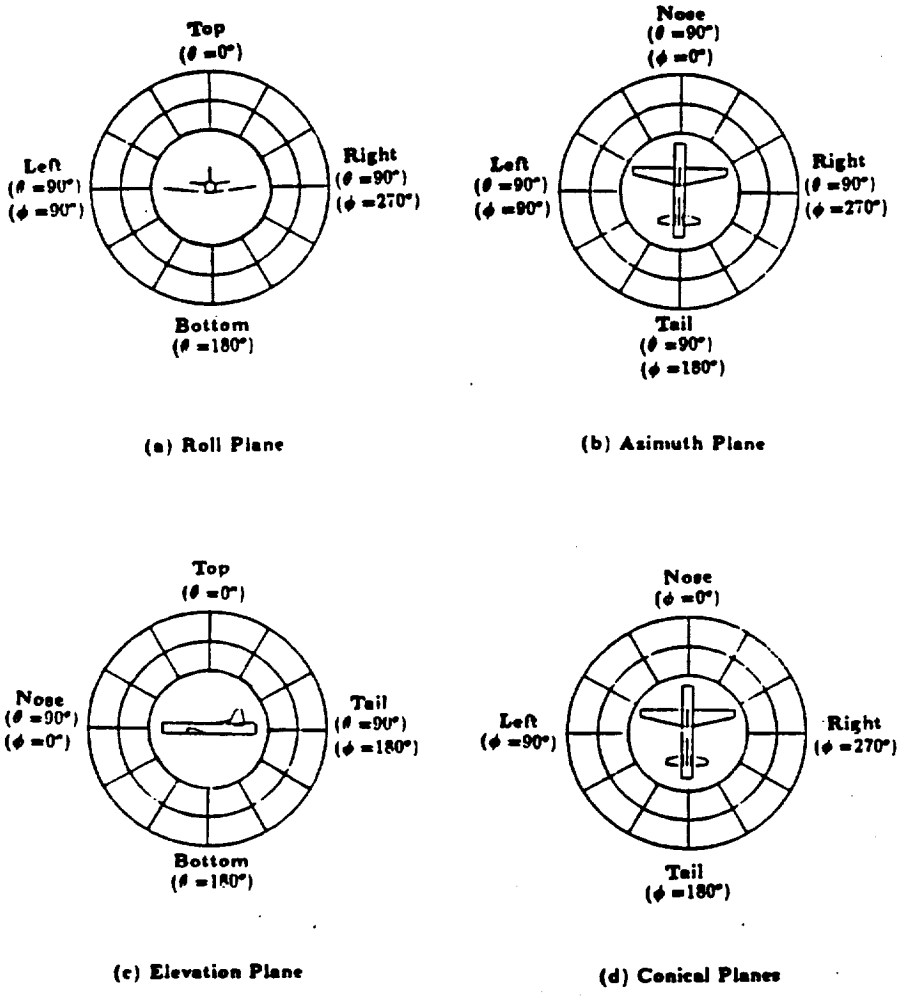

Figure 17: Pattern coordinate systems relative to the aircraft for (a) roll plane, (b) azimuth plane, (c) elevation plane, and (d) conical planes.

3.3 Comparison of NEC-BSC Calculated Results with Boeing Measured Results

The results computed in this section are compared to the measured results provided by Boeing [11]. The antenna location is defined in the Boeing report as Station 910 LBL 55.7, which means that the antenna is located on the port side of the fuselage between the wing and the horizontal stabilizer 55.7° down from the top center-line. The calculated results at 300 MHz for the right hand circular polarized or co-polarized fields are compared to the measurements for the roll plane, the elevation plane and the azimuth plane for each of the aircraft models investigated.

Since the co-polarized results are of primary importance in this report, the left hand circular polarized or cross-polarized results are not included here. However, the cross-polarized results calculated using Version 3.1 of the NEC-BSC for the cylindrical aircraft model are included in Section 5.2. The cross-polarized levels for the composite ellipsoid and cone frustum aircraft models are similar to the levels for the cylindrical aircraft model, therefore, the cross-polarized results for these aircraft models are not included in this study.

3.3.1 Aircraft Model with Cylindrical Fuselage

An illustration of the actual P-3C aircraft [12] is given in Figure 18. The NEC-BSC aircraft model investigated here uses a simple cylinder to represent the fuselage of the P-3C aircraft. This computer model is illustrated in Figure 19, which also shows the location of the antenna on the aircraft fuselage. The calculated results at 300 MHz for right hand circular polarization are compared to the measurements for the roll plane in Figure 20, for the elevation plane in Figure 21 and for the azimuth plane in Figure 22. The results obtained in this section are calculated

using Version 3.1 of the NEC-BSC, which includes the individual UTD terms detailed in Section 3.4.

The calculated and measured roll plane results shown in Figure 20 agree to within 1–2 dB throughout the majority of the pattern. Comparing the elevation plane results in Figure 21 shows that in the region directly above the aircraft (i.e., over 30° above the horizon) and towards the nose of the aircraft, the radiation patterns agree to within 1–3 dB. However as the pattern approaches the horizon near the tail, the calculated pattern reaches levels which are as much as 10–12 dB higher than the measured results. Comparing the calculated and measured azimuth plane results in Figure 22 shows that the agreement is within 1–2 dB in the region 45° from the nose of the aircraft to 30° off of the tail of the aircraft. However, as the pattern approaches both the nose and the tail of the aircraft, the calculated levels increase to as much as 10–12 dB higher than the measured levels.

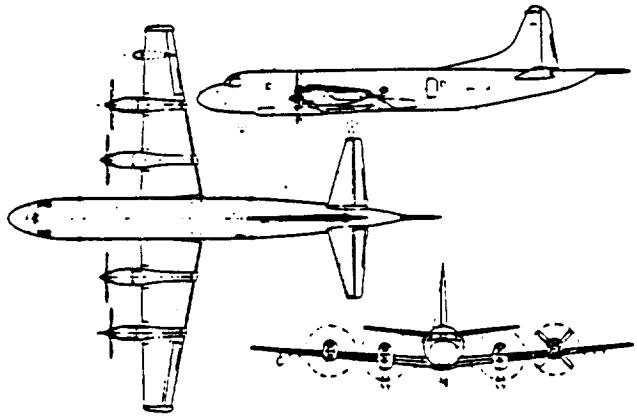

Figure 18: Illustration of the actual P-3C aircraft.

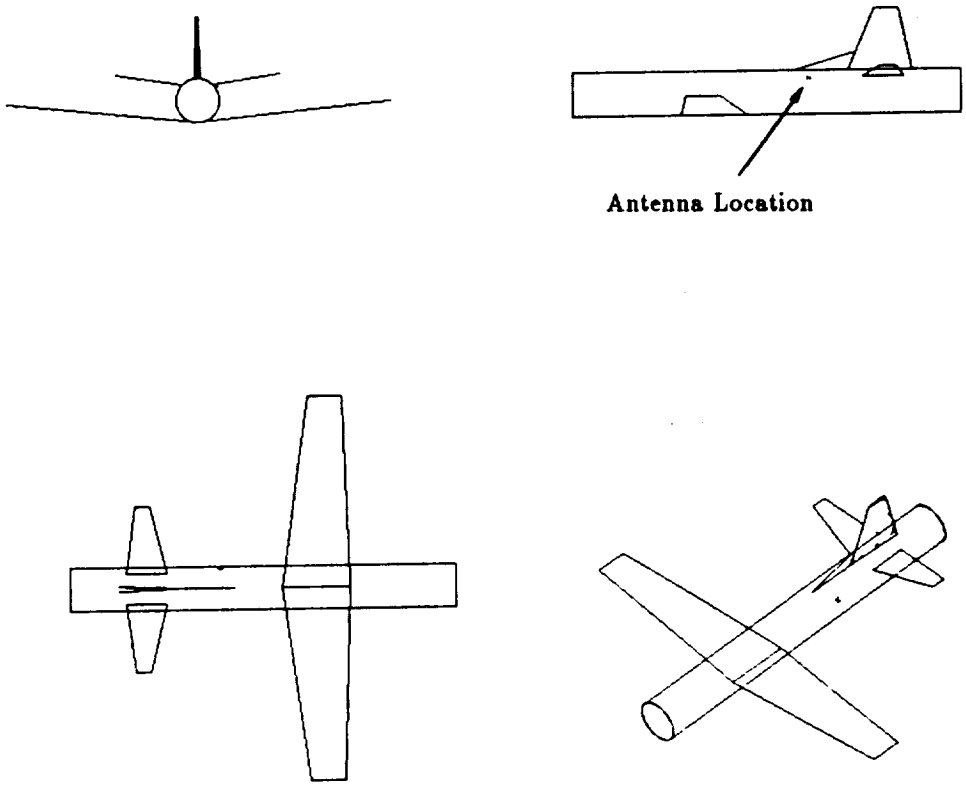

Figure 19: Geometry of the cylindrical model of the P-3C aircraft used in the NEC-BSC showing the location of the antenna.

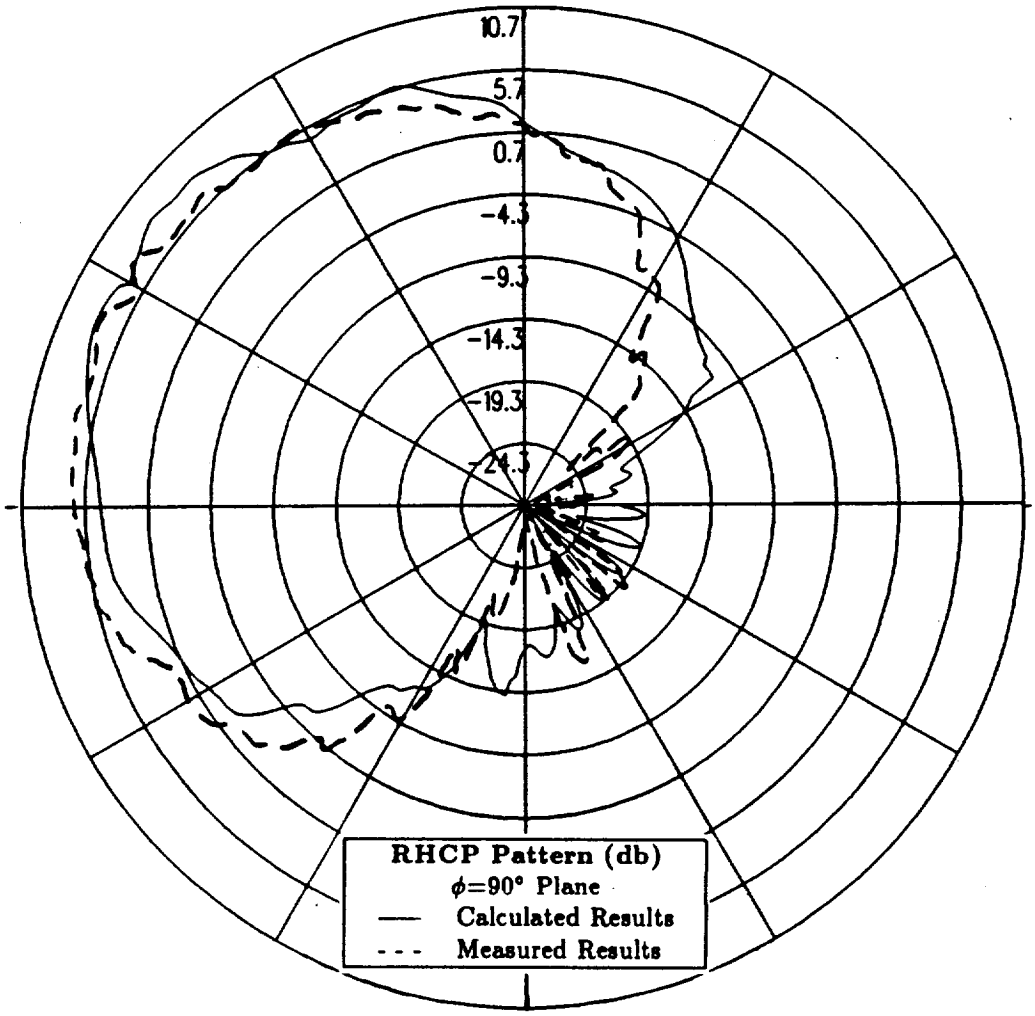

Figure 20: Roll plane pattern for batwing antenna on a P-3C for right hand circular polarization at 300 MHz. (Cylindrical Aircraft Model)

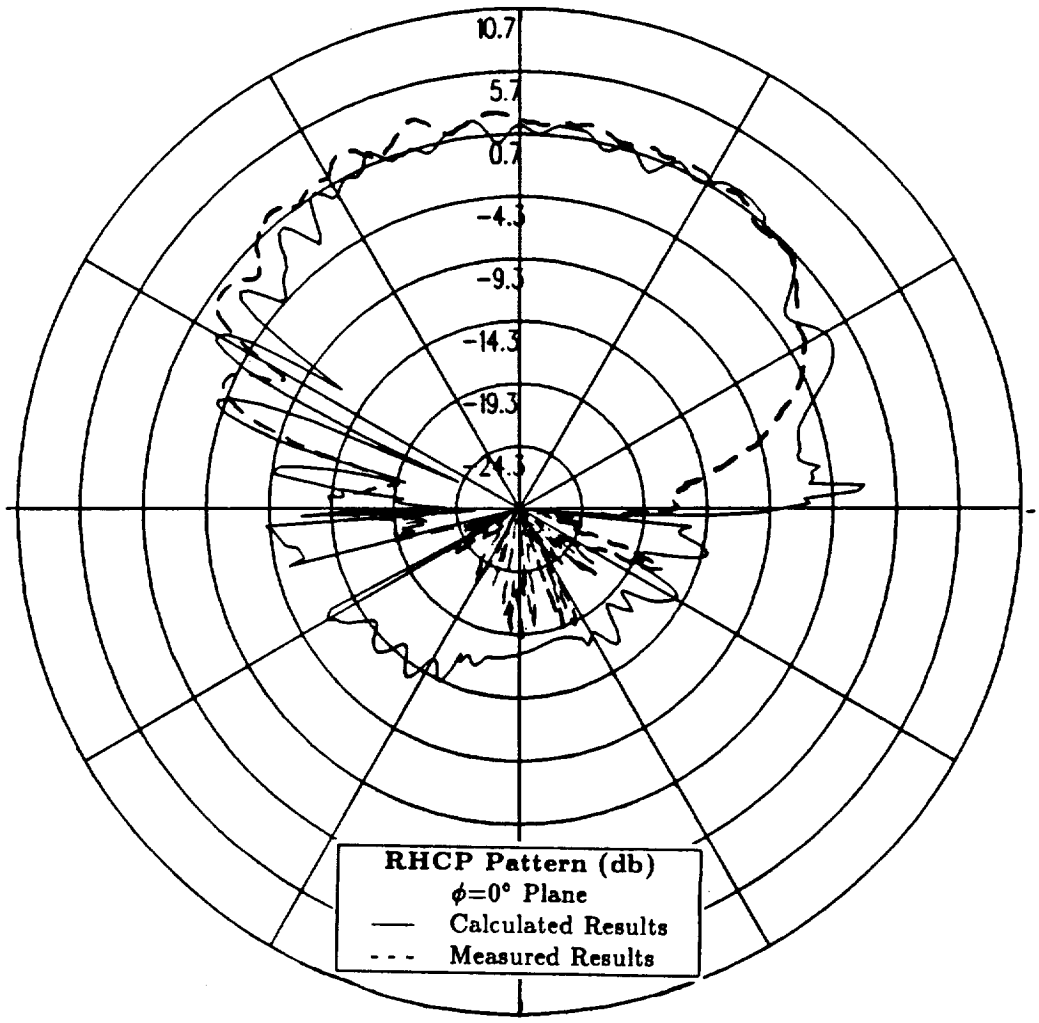

Figure 21: Elevation plane pattern for batwing antenna on a P-3C for right hand circular polarization at 300 MHz. (Cylindrical Aircraft Model)

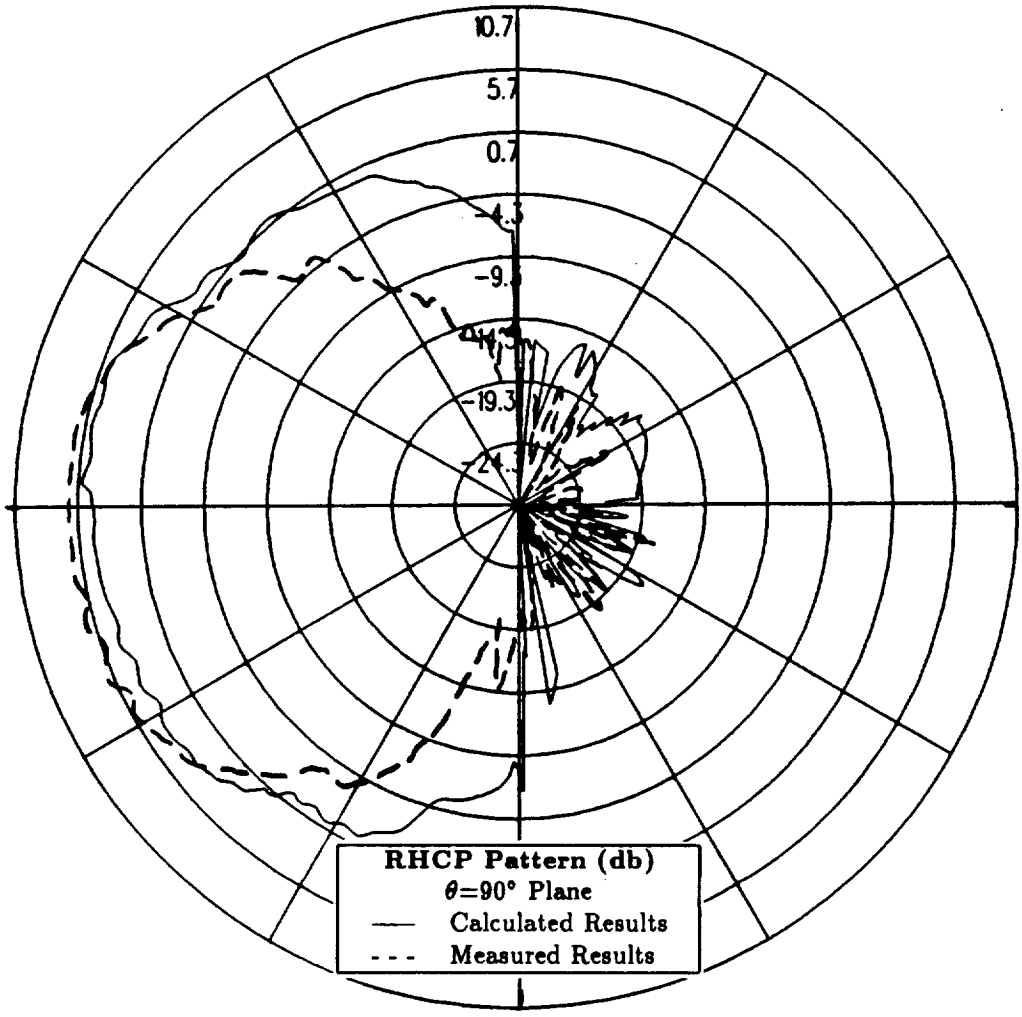

Figure 22: Azimuth plane pattern for batwing antenna on a P-3C for right hand circular polarization at 300 MHz. (Cylindrical Aircraft Model)

3.3.2 Aircraft Model with Composite Ellipsoid Fuselage

The aircraft model investigated here uses a composite ellipsoid to represent the fuselage of the P-3C aircraft. This computer model is illustrated in Figure 23, which also shows the location of the antenna on the aircraft fuselage. The calculated results at 300 MHz obtained using Version 3.1 of the NEC-BSC are compared to the measurements for the roll plane in Figure 24, for the elevation plane in Figure 25 and for the azimuth plane in Figure 26 for right hand circular polarization.

The calculated and measured roll plane results shown in Figure 24 agree to within 1–3 dB throughout the majority of the pattern. Comparing the elevation plane results in Figure 25 shows that in the region directly above the aircraft (i.e., over 30° above the horizon) the radiation patterns agree to within 1–3 dB. However, as the pattern approaches the horizon near the tail and near the nose of the aircraft, the calculated pattern reaches levels which are as much as 10–12 dB higher than the measured results. Comparing the calculated and measured azimuth plane results in Figure 26 shows that off the nose and the tail of the aircraft, the calculated levels are again as much as 10–12 dB higher than the measured levels. In the main region of the pattern, the levels for the composite ellipsoid model are 3–5 dB below Boeing's measured levels.

Comparison of the radiation patterns in this section with the patterns in Section 3.3.1 should determine which aircraft model provides a more accurate representation of the P-3C aircraft. Both models provide accurate patterns in the roll plane. In the elevation plane, both the cylindrical aircraft model and the composite ellipsoid model have calculated levels which are 10–12 dB higher than the measured levels near the tail of the aircraft. However, the composite ellipsoid model also has calculated levels which are 10–12 dB higher than the measured levels near the nose of the aircraft. In the azimuth plane, the composite ellipsoid

model has the same high levels near the nose and tail of the aircraft as well as lower levels in the main region. These lower levels observed in the main region of the azimuth pattern for the composite ellipsoid model are due to the sensitivity of the reflection point calculation in the NEC-BSC when the antenna is located near the surface of an elongated composite ellipsoid such as in this application. Because of this sensitivity in the code, any slight miscalculation in the reflection point on the ellipsoid can have a substantial effect on the radiation levels as can be seen in the main region of the azimuth plane pattern. This comparison shows that the composite ellipsoid aircraft model has the same problem as the cylindrical aircraft model with high levels on the horizon near the nose and the tail. In addition, this model has the problem in the azimuth plane described above. Therefore, the cylindrical aircraft model is a better representation of the actual P-3C aircraft than the composite ellipsoid aircraft model.

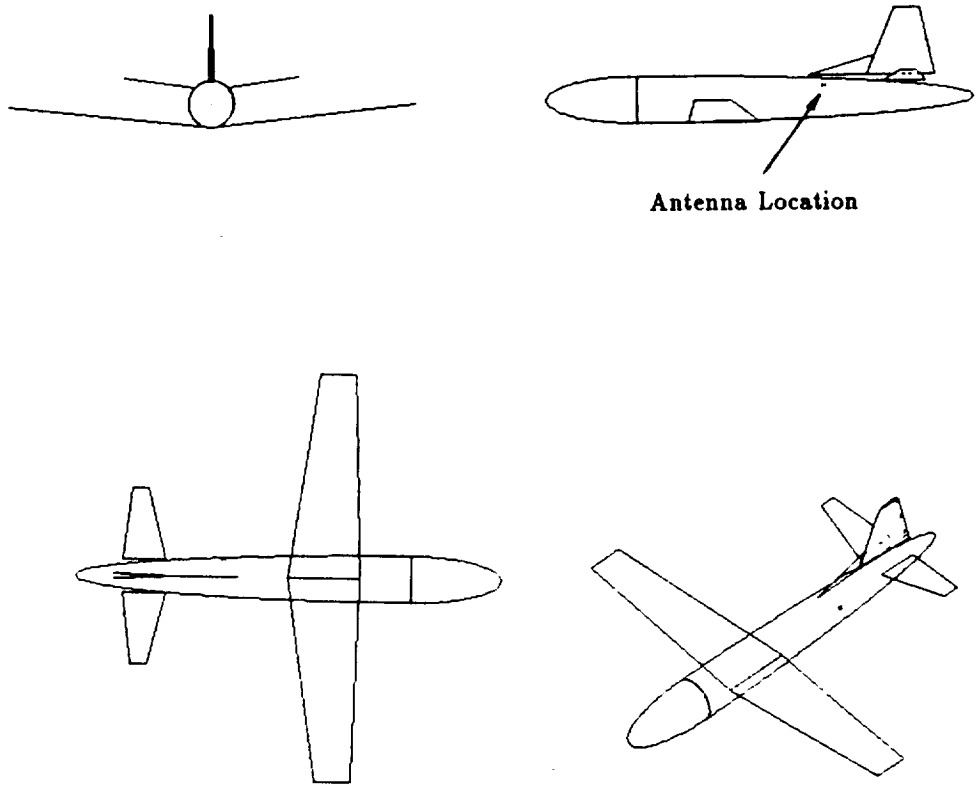

Figure 23: Geometry of the composite ellipsoid model of the P-3C aircraft used in the NEC-BSC showing the location of the antenna.

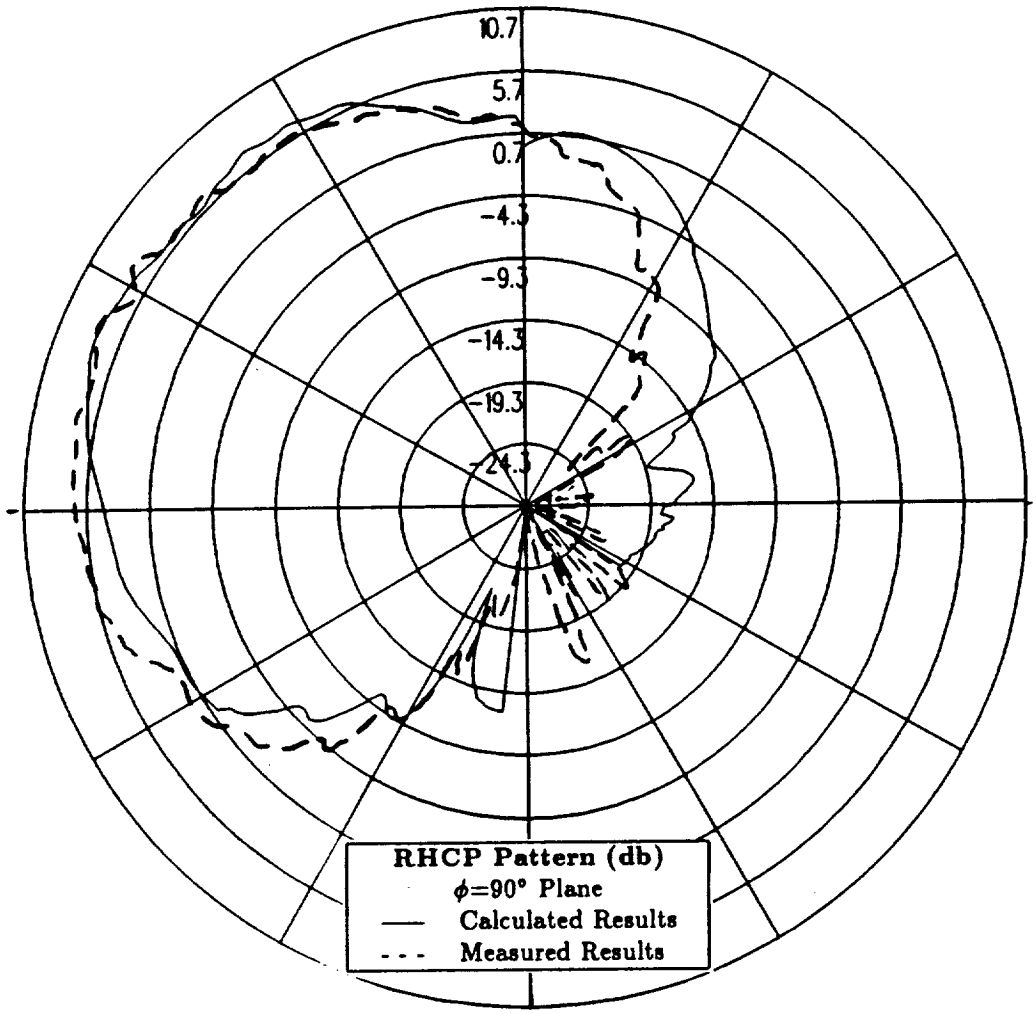

Figure 24: Roll plane pattern for batwing antenna on a P-3C for right hand circular polarization at 300 MHz. (Composite Ellipsoid Aircraft Model)

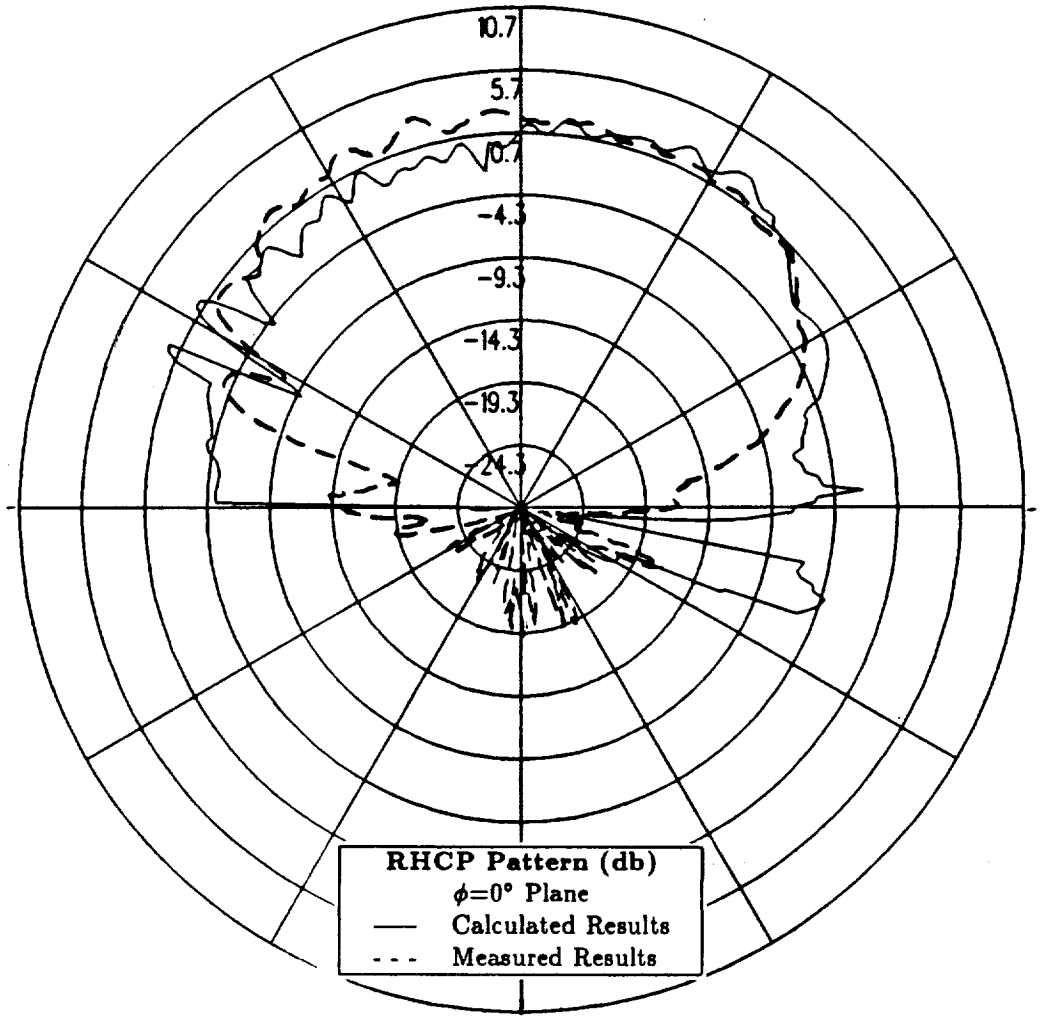

Figure 25: Elevation plane pattern for batwing antenna on a P-3C for right hand circular polarization at 300 MHz. (Composite Ellipsoid Aircraft Model)

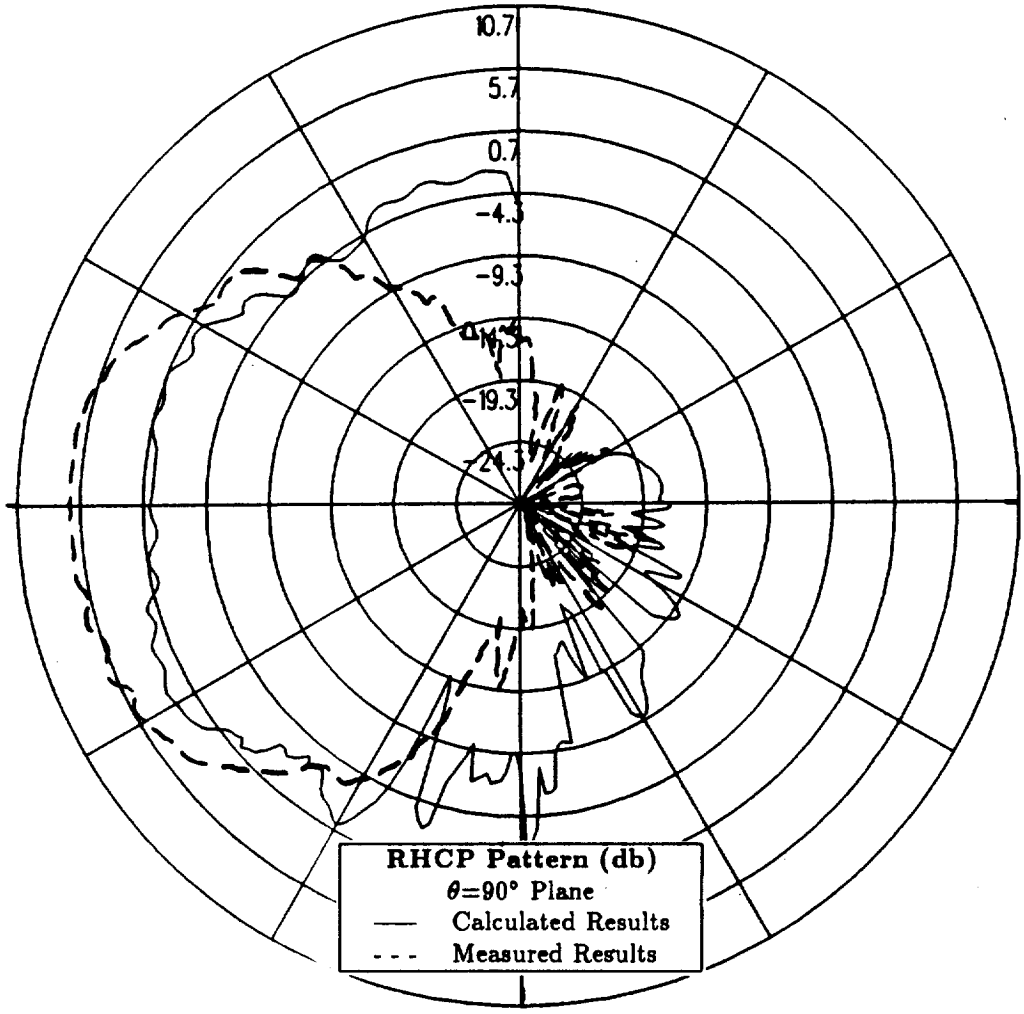

Figure 26: Azimuth plane pattern for batwing antenna on a P-3C for right hand circular polarization at 300 MHz. (Composite Ellipsoid Aircraft Model)

3.3.3 Aircraft Model with Cone Frustum Fuselage

The NEC-BSC aircraft model investigated here uses a cone frustum to represent the fuselage of the P-3C aircraft. This computer model is illustrated in Figure 27, which also shows the location of the antenna on the aircraft fuselage. Note that the cylindrical section of the fuselage is not a cylinder but rather a zero degree cone. This is relevant because different algorithms are used for a cylinder and a zero degree cone. The calculated results at 300 MHz for right hand circular polarization are compared to the measurements for the roll plane in Figure 28, for the elevation plane in Figure 29 and for the azimuth plane in Figure 30. The results obtained in this section are calculated using Version 3.1 of the NEC-BSC which includes a slight revision. This revision more accurately determines the shadowing of the cone frustum and is not included in the officially released NEC-BSC Version 3.1.

The calculated and measured roll plane results shown in Figure 28 agree to within 1–3 dB throughout the majority of the pattern, however, the calculated pattern has a slightly broader main beam than the measured pattern. Comparing the elevation plane results in Figure 29 shows that in the region directly above the aircraft (i.e., over 30° above the horizon) the radiation patterns agree to within 1–3 dB. However, as the pattern approaches the horizon near the tail and near the nose of the aircraft, the calculated pattern reaches levels which are as much as 10–15 dB higher than the measured results. Comparing the calculated and measured azimuth plane results in Figure 30 shows that the agreement is within 1–3 dB in the region 45° from the nose of the aircraft to 30° off of the tail of the aircraft. However, as the pattern approaches both the nose and the tail of the aircraft, the calculated levels increase to as much as 10–12 dB higher than the measured levels.

Comparison of the radiation patterns in this section with the patterns in Section 3.3.1 should determine which aircraft model provides a more accurate representation of the P-3C aircraft. Both models provide very similar patterns in both the azimuth plane and the elevation plane. However in the roll plane, the cone frustum model has a broader main beam than the cylindrical model. Therefore, the cone frustum aircraft model has the same problem in the azimuth plane and the elevation plane as the cylindrical aircraft model as well as the problem in the roll plane. This indicates that the cylindrical aircraft model better represents the actual P-3C aircraft than the cone frustum aircraft model.

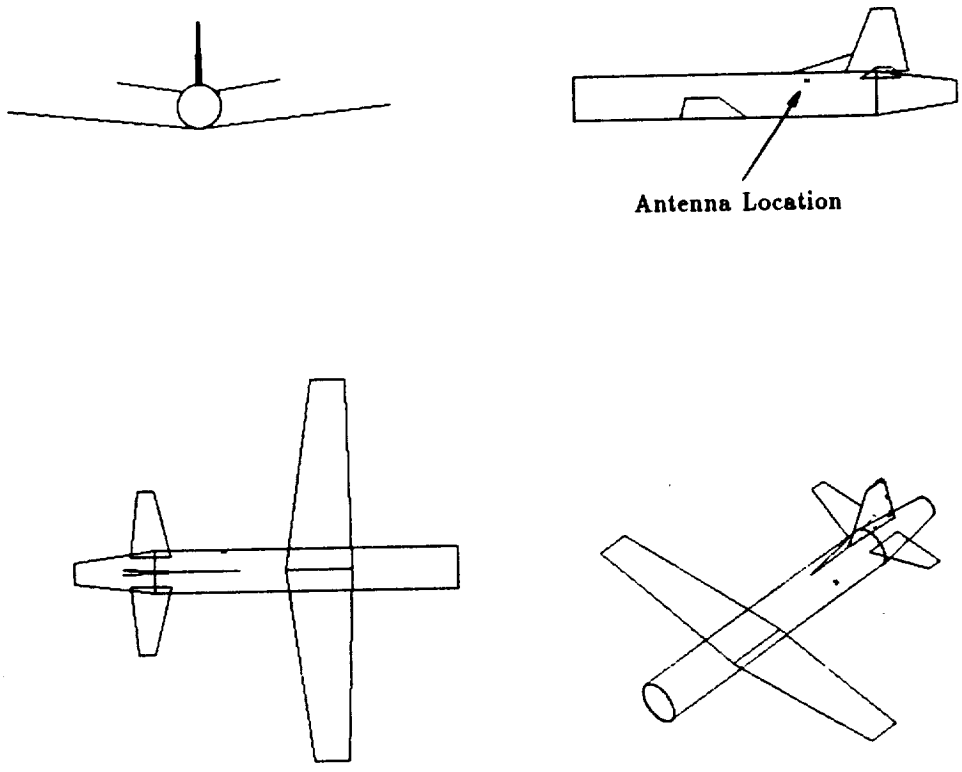

Figure 27: Geometry of the cone frustum model of the P-3C aircraft used in the NEC-BSC showing the location of the antenna.

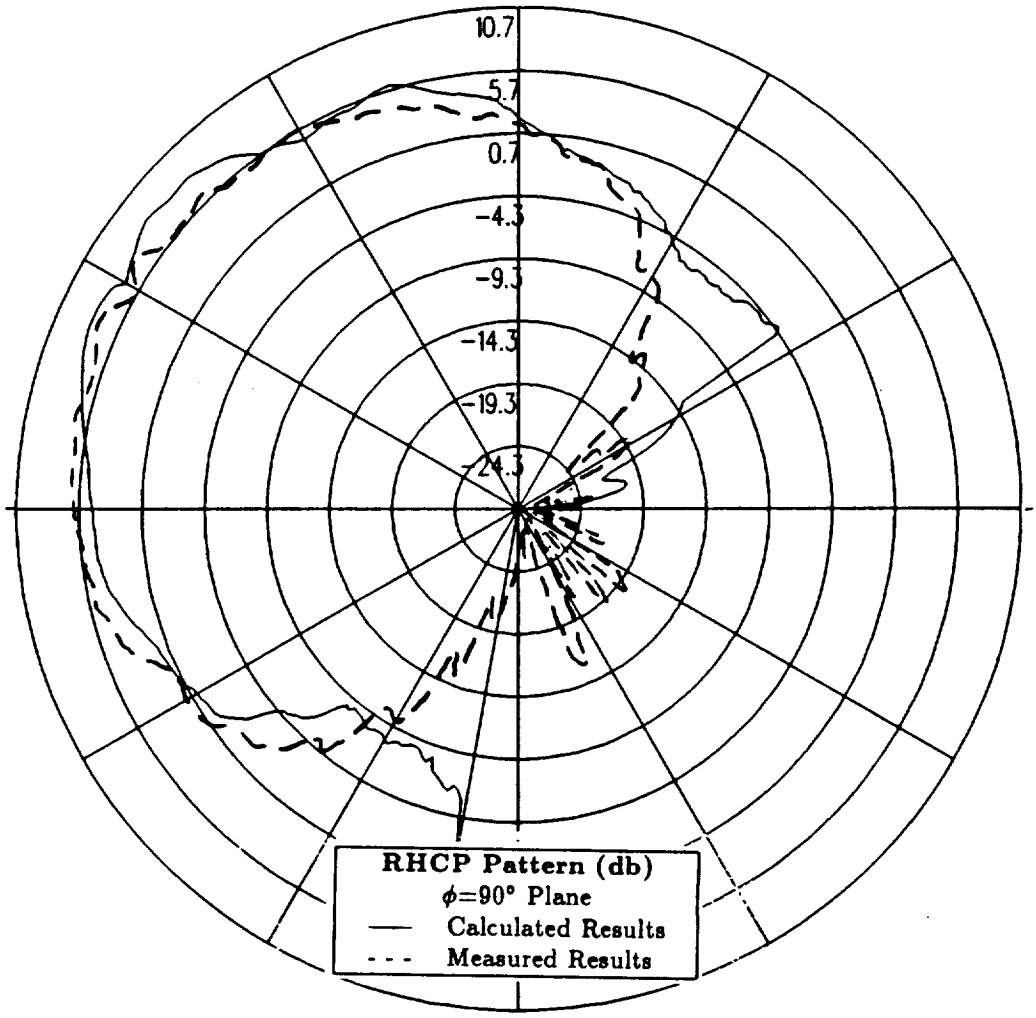

Figure 28: Roll plane pattern for batwing antenna on a P-3C for right hand circular polarization at 300 MHz. (Cone Frustum Aircraft Model)

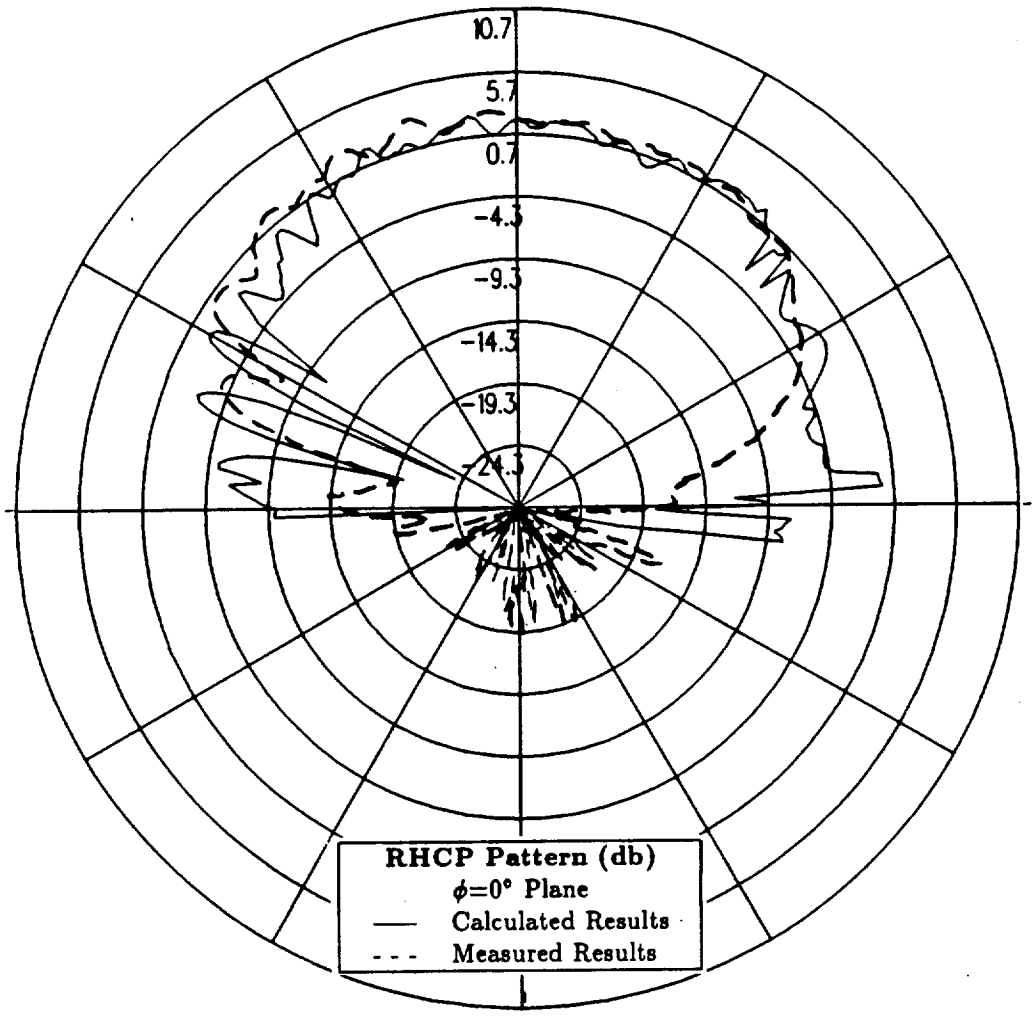

Figure 29: Elevation plane pattern for batwing antenna on a P-3C for right hand circular polarization at 300 MHz. (Cone Frustum Aircraft Model)

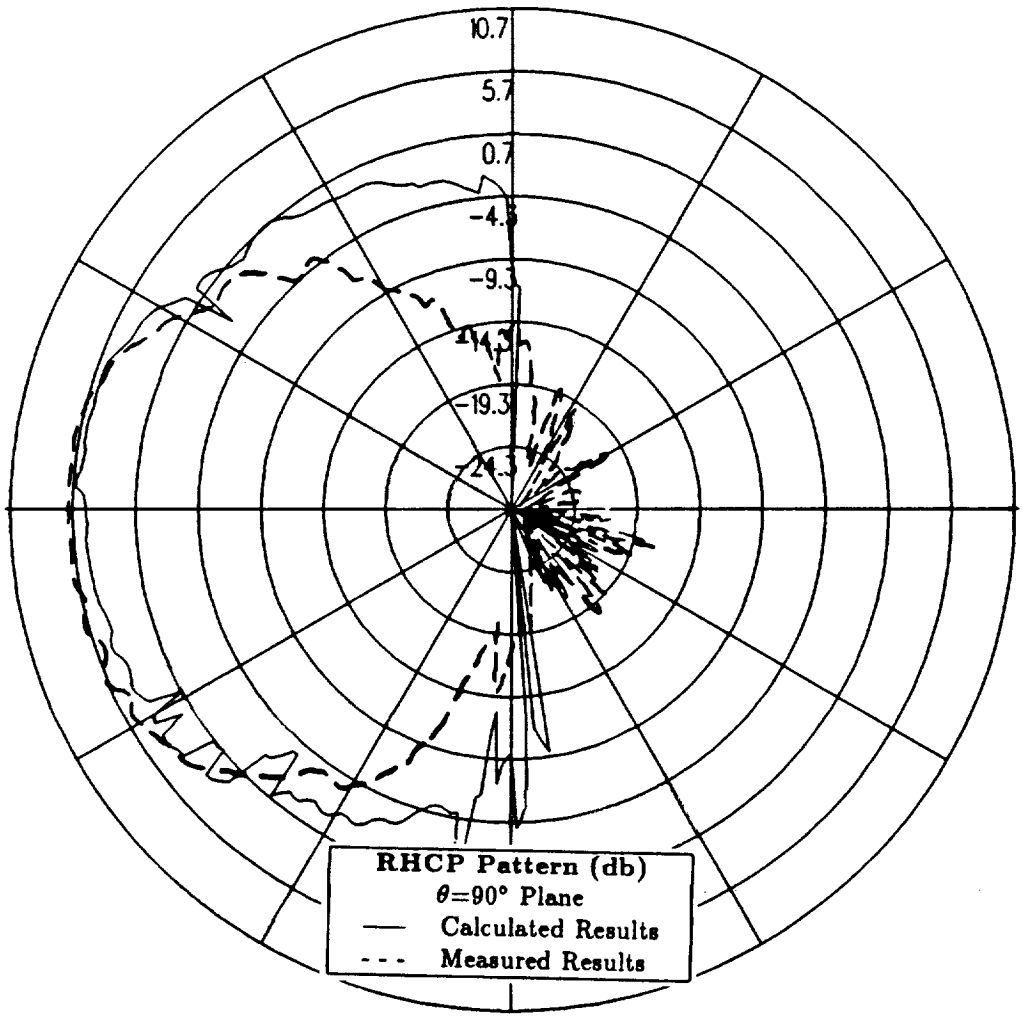

Figure 30: Azimuth plane pattern for batwing antenna on a P-3C for right hand circular polarization at 300 MHz. (Cone Frustum Aircraft Model)

3.4 Individual Fields for Cylindrical Aircraft Model

In the previous section, it is determined that the cylindrical aircraft model provided a better representation of the actual P-3C aircraft than either the composite ellipsoid model or the cone frustum model. However, this model is not entirely accurate due to the high levels on the horizon near the nose and the tail which can be seen in the elevation plane and azimuth plane in Figures 21 and 22, respectively. To gain insight into what is the cause of these high levels, the individual fields which contribute to the elevation plane are shown in Figure 31 and the fields which contribute to the azimuth plane are shown in Figure 32.

Figures 31 and 32 show that the fields which have major contributions to the radiation pattern in the regions near the nose and tail of the aircraft for both the elevation and azimuth planes are the incident field, the reflected field from the cylinder and the diffracted field from the plates. Comparing the incident field with the cylinder reflected field shows that these two terms have virtually the same radiation pattern for both the elevation plane and the azimuth plane and, therefore, constitute a matched pair. To see the relationship between this pair of terms, only these two fields are calculated for the elevation plane and the azimuth plane as shown in Figures 33 and 34, respectively. Both of these figures show that the incident field and the cylinder reflected field are in phase in the main region of the patterns, which means that there is constructive interference between the two terms. However near the nose and the tail of the aircraft, the incident field and the cylinder reflected field are out of phase which causes destructive interference between the two terms. Because the incident field and cylinder reflected field contributions near the nose and the tail of the aircraft cancel each other, the sole remaining term which could cause the high levels in these regions is the plate diffracted field. This is verified in Figures 35 and 36 where the incident field and

the cylinder reflected field can be seen with and without the plate diffracted field for both the elevation plane and the azimuth plane.

The relationship between the incident field and the cylinder reflected field which causes the destructive interference near the nose and tail of the aircraft could also be applied to the plate diffracted field if the cylinder reflected - plate diffracted field could be calculated. In this analogy, the cylinder reflected - plate diffracted field should interfere destructively with the plate diffracted field near the nose and tail of the aircraft which would cause lower radiation levels in these regions. Version 3.1 of the NEC-BSC does not contain plate - curved surface interactions. However, these plate - curved surface fields can be simulated by using an imaging technique which is described in the next section.

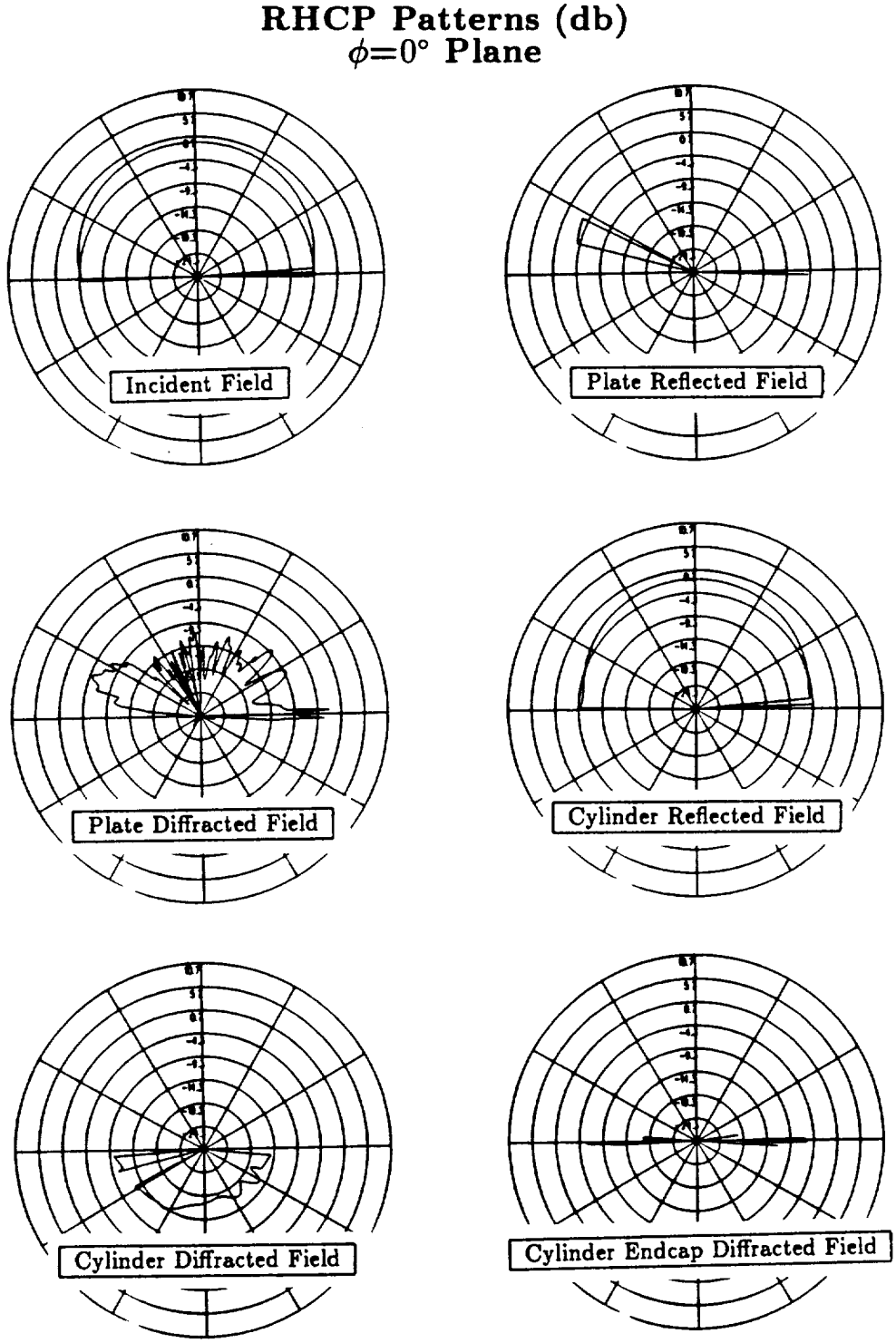

Figure 31: Individual fields which contribute to the elevation plane pattern for cylindrical aircraft model. (Right hand circular polarization at 300 MHz)

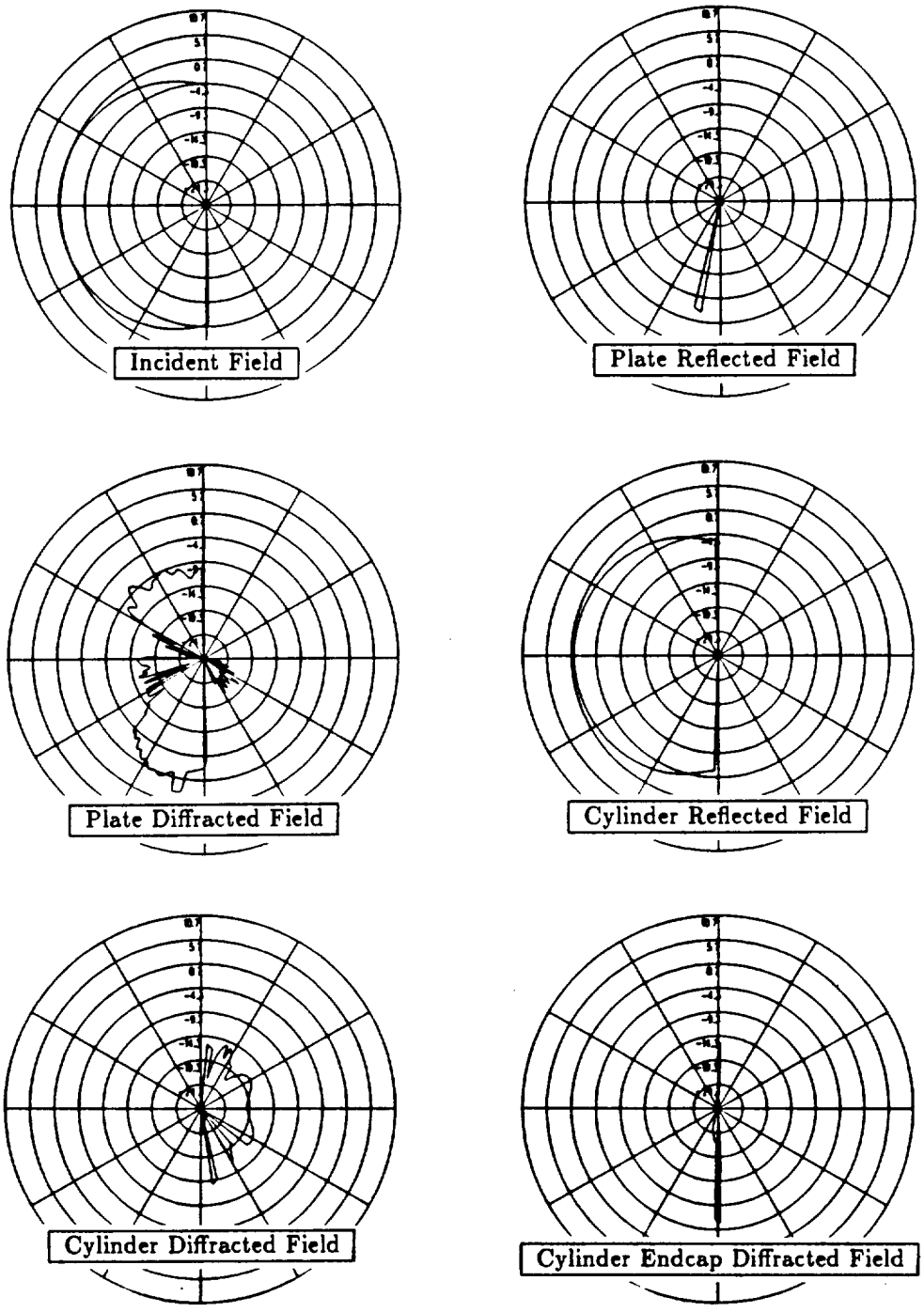

Figure 32: Individual fields which contribute to the azimuth plane pattern for cylindrical aircraft model. (Right hand circular polarization at 300 MHz)

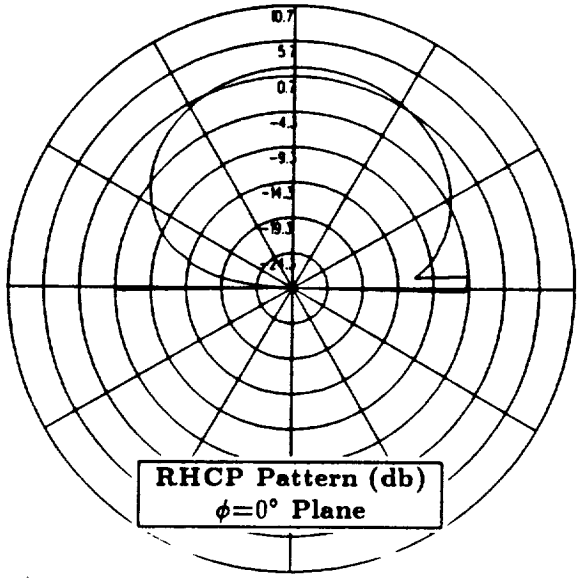

Figure 33: Incident field and cylinder reflected field in the elevation plane for cylindrical aircraft model. (Right hand circular polarization at 300 MHz)

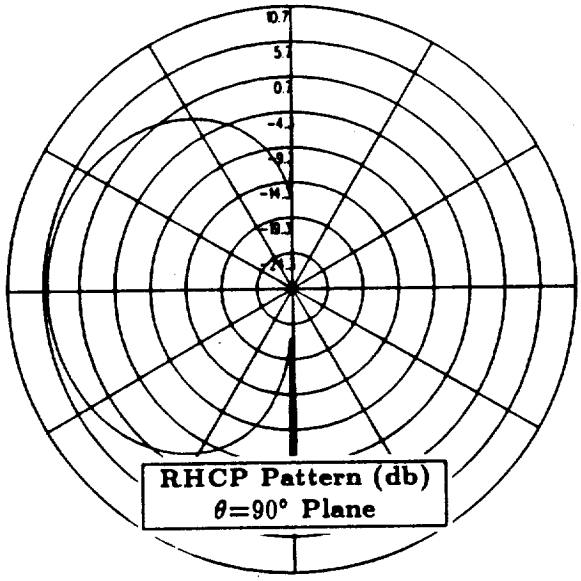

Figure 34: Incident field and cylinder reflected field in the azimuth plane for cylindrical aircraft model. (Right hand circular polarization at 300 MHz)

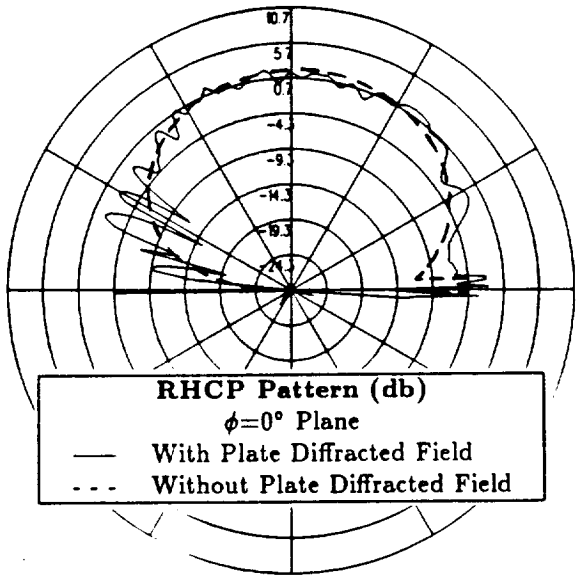

Figure 35: Incident field and cylinder reflected field with and without plate diffracted field in elevation plane. (Right hand circular polarization at 300 MHz)

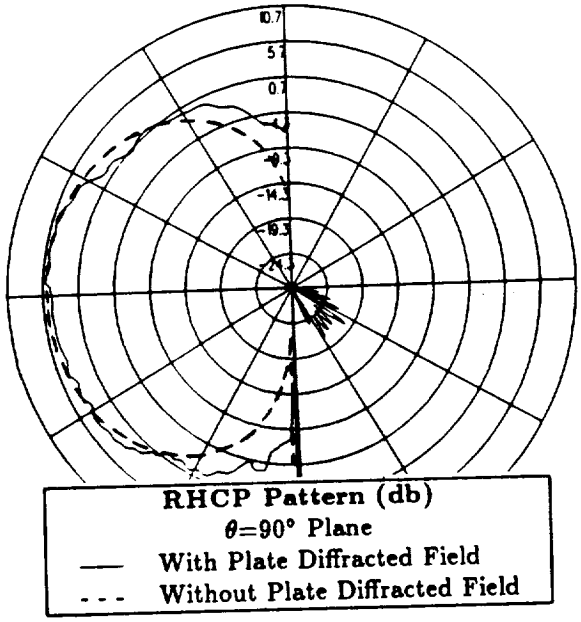

Figure 36: Incident field and cylinder reflected field with and without plate diffracted field in azimuth plane. (Right hand circular polarization at 300 MHz)

3.5 Plate - Curved Surface Fields using Imaging Technique

In this section an imaging technique is used to simulate the plate - curved surface interactions. This imaging technique will result in a simulated curved surface reflected - plate reflected field and a simulated curved surface reflected - plate diffracted field. The purpose of this imaging process is to determine if the curved surface reflected - plate diffracted field interferes destructively with the plate diffracted field near the nose and tail of the aircraft. Destructive interference between these two terms will cause lower radiation levels in these regions, which should result in better agreement between the NEC-BSC calculated patterns and the measured patterns.

In order to simulate these plate - curved surface interactions, a three step procedure is followed. Initially, the first order UTD pattern containing the present UTD terms from Version 3.1 of the NEC-BSC is calculated for the original antenna located in the presence of the complete aircraft model. Secondly, the fuselage and the original antenna are removed and an image of the original antenna with respect to the fuselage is located in the presence of the plates only. The pattern is then calculated for the fields which are determined by the plate interactions with the image source. Finally, these two patterns are added in order to create a pattern which includes these simulated plate - curved surface interactions. This imaging process is used on each of the aircraft models which are investigated in Section 3.3. The calculated results which include these simulated plate - curved surface fields are compared to the original calculated results and to the measurements for the roll plane, the elevation plane and the azimuth plane for the right hand circular polarized or co-polarized fields at 300 MHz for each of the aircraft models.

3.5.1 Aircraft Model with Cylindrical Fuselage

The NEC-BSC aircraft model investigated here uses a simple cylinder to represent the fuselage of the P-3C aircraft as illustrated in Figure 19. The calculated results which include the simulated plate - cylinder fields are compared to the original calculated results and to the measurements for the roll plane in Figure 37, for the elevation plane in Figure 38 and for the azimuth plane in Figure 39 for right hand circular polarization at 300 MHz.

Because the simulated plate - cylinder fields have only a minor effect on the roll plane pattern, both of the calculated roll plane results shown in Figure 37 agree with the measurements to within 1–2 dB throughout the majority of the pattern. The elevation plane results which include the simulated plate - cylinder fields shown in Figure 38 agree to within 1–3 dB with the measurements in the region directly above the aircraft (i.e., over 30° above the horizon) and in the region near the nose of the aircraft. However, as the pattern approaches the horizon near the tail, the calculated pattern which includes the simulated fields reaches levels which are as much as 5–8 dB higher than the measured results. The azimuth plane results which include the simulated plate - cylinder fields shown in Figure 39 agree to within 1–2 dB with the measurements in the region 45° from the nose of the aircraft to the tail of the aircraft. However, as the pattern approaches the nose of the aircraft, the calculated levels increase to as much as 5–8 dB higher than the measured levels.

Figures 38 and 39 demonstrate that the simulated plate - cylinder fields improve the agreement between the calculated and measured results in the elevation and azimuth planes. Comparing the patterns which include the simulated plate - cylinder fields to the patterns which do not show that the simulated plate - cylinder fields decrease the calculated levels by as much as 5 dB in the horizon of the

aircraft near the nose and the tail. The calculated patterns still remain higher than the measurements near the tail of the aircraft in the elevation plane and near the nose of the aircraft in the azimuth plane, however, the levels in these regions are much closer than the levels previously calculated without the simulated plate - cylinder fields.

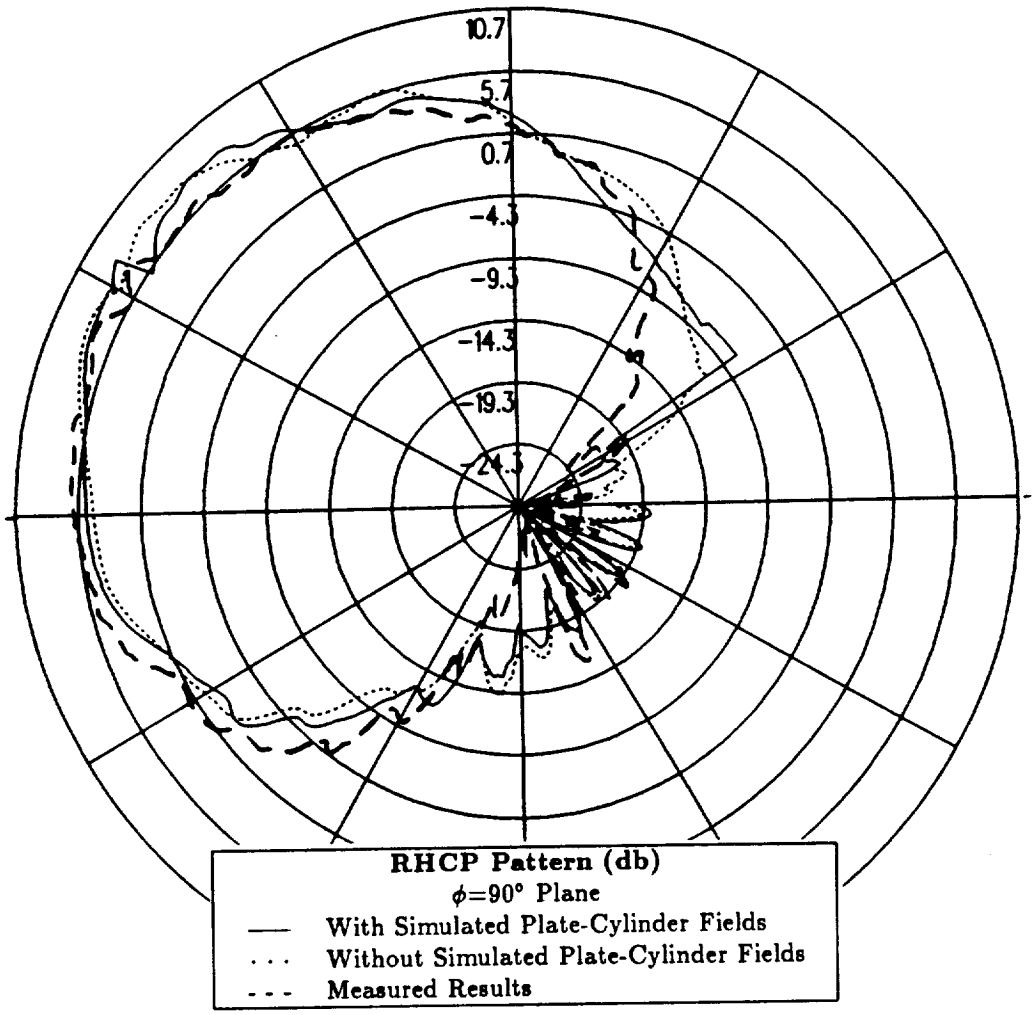

Figure 37: Roll plane pattern which includes the simulated plate - cylinder fields for right hand circular polarization at 300 MHz. (Cylindrical Aircraft Model)

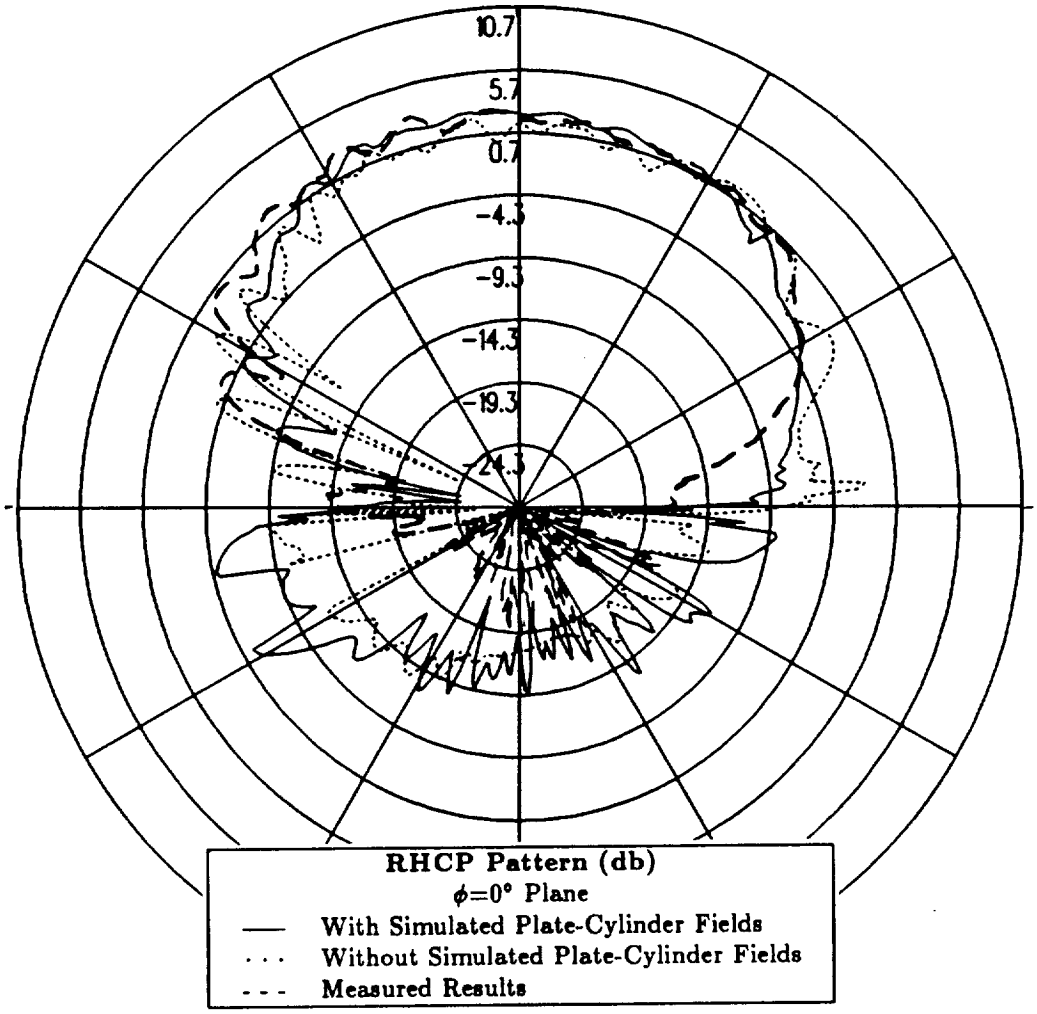

Figure 38: Elevation plane pattern which includes the simulated plate - cylinder fields for right hand circular polarization at 300 MHz. (Cylindrical Aircraft Model)

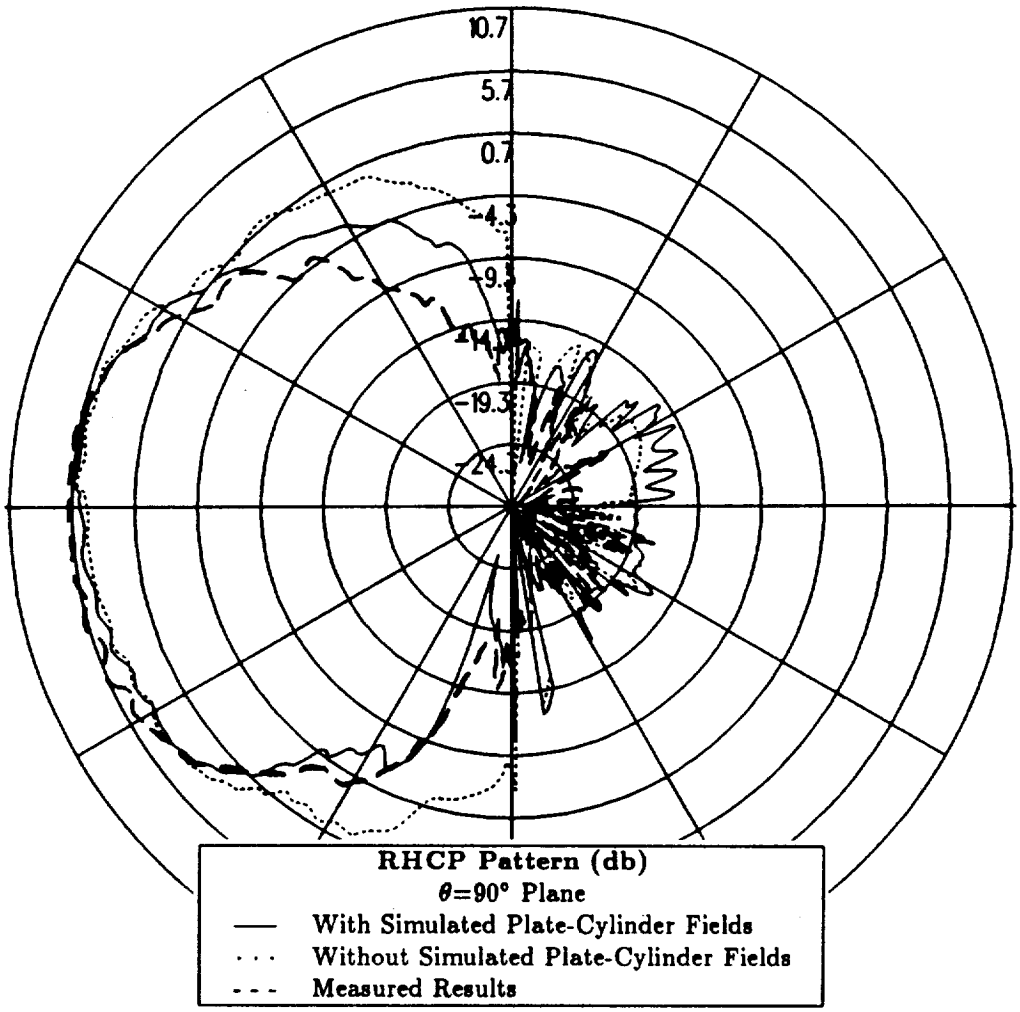

Figure 39: Azimuth plane pattern which includes the simulated plate - cylinder fields for right hand circular polarization at 300 MHz. (Cylindrical Aircraft Model)

3.5.2 Aircraft Model with Composite Ellipsoid Fuselage

The NEC-BSC aircraft model investigated here uses a composite ellipsoid to represent the fuselage of the P-3C aircraft as illustrated in Figure 23. The calculated results which include the simulated plate - ellipsoid fields are compared to the original calculated results and to the measurements for the roll plane in Figure 40, for the elevation plane in Figure 41 and for the azimuth plane in Figure 42 for right hand circular polarization at 300 MHz.

The simulated plate - ellipsoid fields have only a minor effect on the roll plane pattern, therefore, both of the calculated roll plane results shown in Figure 40 agree the measurements to within 1–3 dB throughout the majority of the pattern. Figures 41 and 42 demonstrate that the simulated plate - ellipsoid fields have only a minor effect in the elevation plane and azimuth plane as well. The patterns for the elevation and azimuth planes which include the simulated plate - ellipsoid fields shown in Figures 41 and 42, respectively, have the same problems as the patterns which do not include the simulated plate - ellipsoid fields. Therefore, the differences between the patterns calculated with the simulated plate - cylinder fields and measured patterns remain the same as the differences between the original calculated patterns and the measured patterns discussed in Section 3.3.2.

Comparing the patterns in this section which include the simulated plate - ellipsoid fields to those in the previous section for the cylindrical aircraft model which include the simulated plate - cylinder fields shows that the cylindrical aircraft model provides a much more accurate model than the composite ellipsoid model. The patterns for the cylindrical aircraft model are closer to the measurements than the patterns for the composite ellipsoid model throughout both the elevation plane and the azimuth plane. The differences between the two models are especially pronounced in the horizon of the aircraft near the nose and the tail.

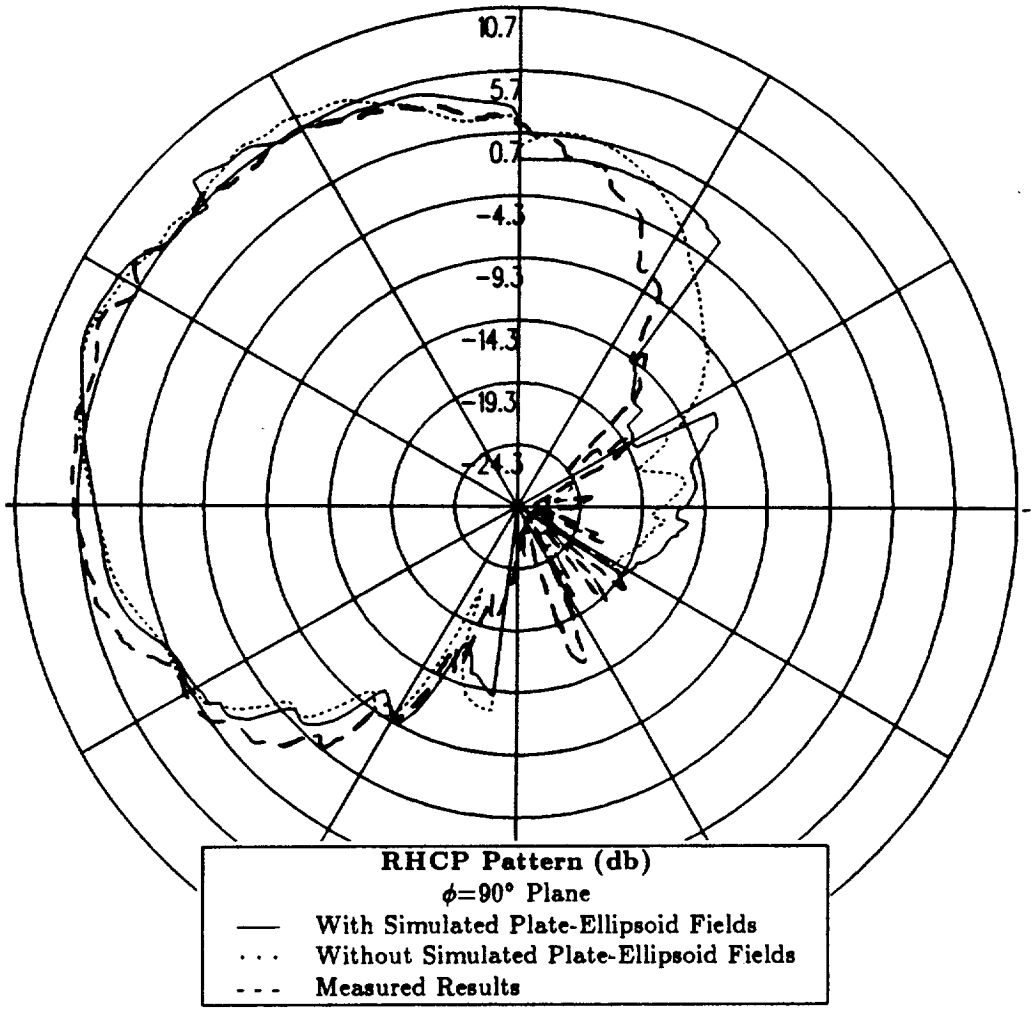

Figure 40: Roll plane pattern which includes the simulated plate - ellipsoid fields for right hand circular polarization at 300 MHz. (Composite Ellipsoid Aircraft Model)

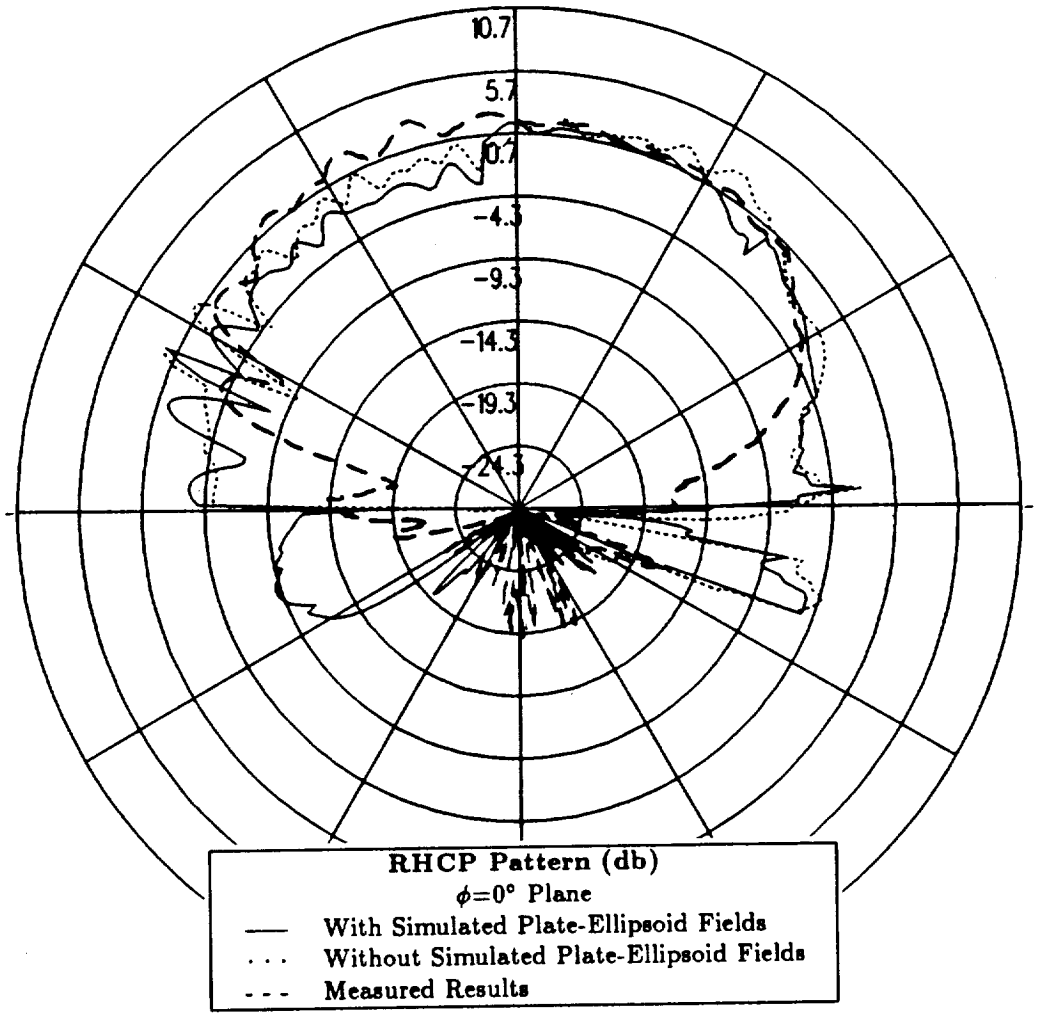

Figure 41: Elevation plane pattern which includes the simulated plate - ellipsoid fields for right hand circular polarization at 300 MHz. (Composite Ellipsoid Aircraft Model)

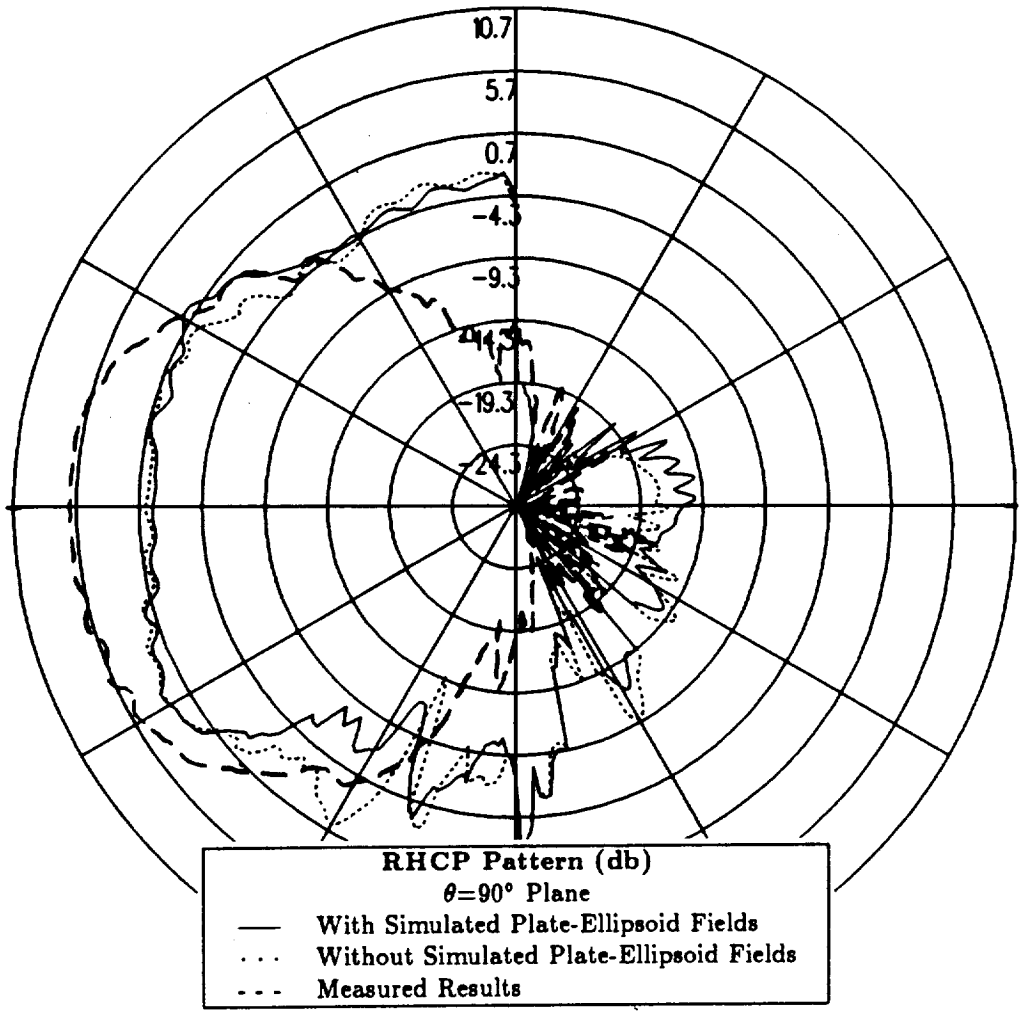

Figure 42: Azimuth plane pattern which includes the simulated plate - ellipsoid fields for right hand circular polarization at 300 MHz. (Composite Ellipsoid Aircraft Model)

3.5.3 Aircraft Model with Cone Frustum Fuselage

The NEC-BSC aircraft model investigated here uses a cone frustum to represent the fuselage of the P-3C aircraft as illustrated in Figure 27. The calculated results which include the simulated plate - cone frustum fields are compared to the original calculated results and to the measurements for the roll plane in Figure 43, for the elevation plane in Figure 44 and for the azimuth plane in Figure 45 for right hand circular polarization at 300 MHz.

The simulated plate - cone frustum fields have only a minor effect in the roll plane and the elevation plane. Therefore, the roll plane results which include the simulated plate - cone frustum fields shown in Figure 43 still have broader main beams than the measured pattern. The elevation plane results which include the simulated plate - cone frustum fields shown in Figure 44 still have calculated levels which are as much as 10–15 dB higher than the measured levels on the horizon near the nose and the tail of the aircraft. The simulated plate - cone frustum fields cause the radiation levels to be reduced near the nose and the tail of the aircraft in the azimuth plane pattern which can be seen in Figure 45. However, these calculated levels which include the plate - cone frustum fields are still up to 8 dB higher than the measured levels in the horizon of the aircraft near the nose.

Figure 45 demonstrates that the simulated plate - cone frustum fields improve the agreement between the calculated and measured results in the azimuth plane. Comparing the pattern which includes the simulated plate - cone frustum field to the pattern which does not shows that the simulated plate - cone frustum field decreases the calculated levels by as much as 5 dB in the horizon of the aircraft near the nose and the tail. The calculated pattern still remains higher than the measurements near the nose of the aircraft, however, the levels in these regions

are much closer than the levels previously calculated without the simulated plate - cone frustum fields.

Comparing the patterns in this section which include the simulated plate - cone frustum fields to those in the Section 3.5.1 for the cylindrical aircraft model which include the simulated plate - cylinder fields shows that the cylindrical aircraft model also provides a much more accurate model than the cone frustum model. The patterns for the cylindrical aircraft model are closer to the measurements than the patterns for the cone frustum model throughout all three pattern cuts taken.

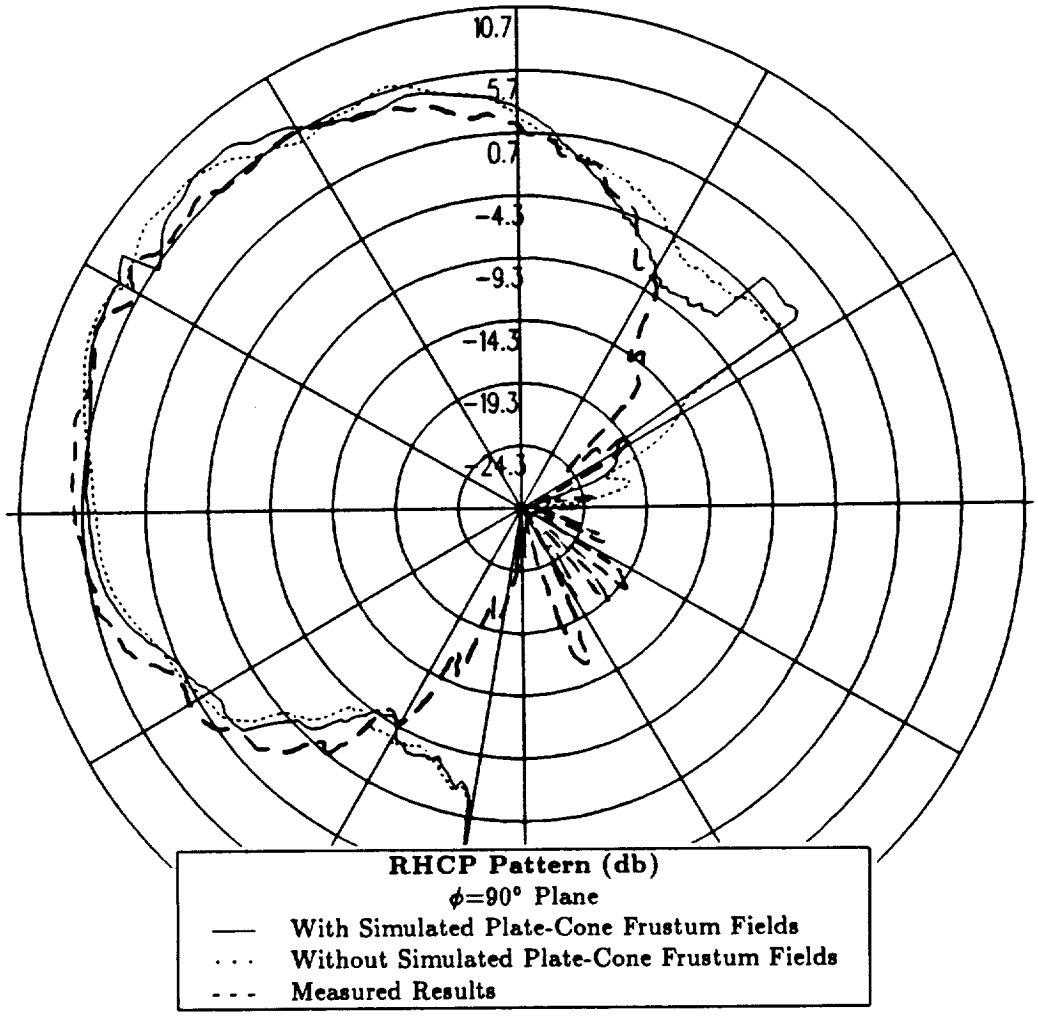

Figure 43: Roll plane pattern which includes the simulated plate - cone frustum fields for right hand circular polarization at 300 MHz. (Cone Frustum Aircraft Model)

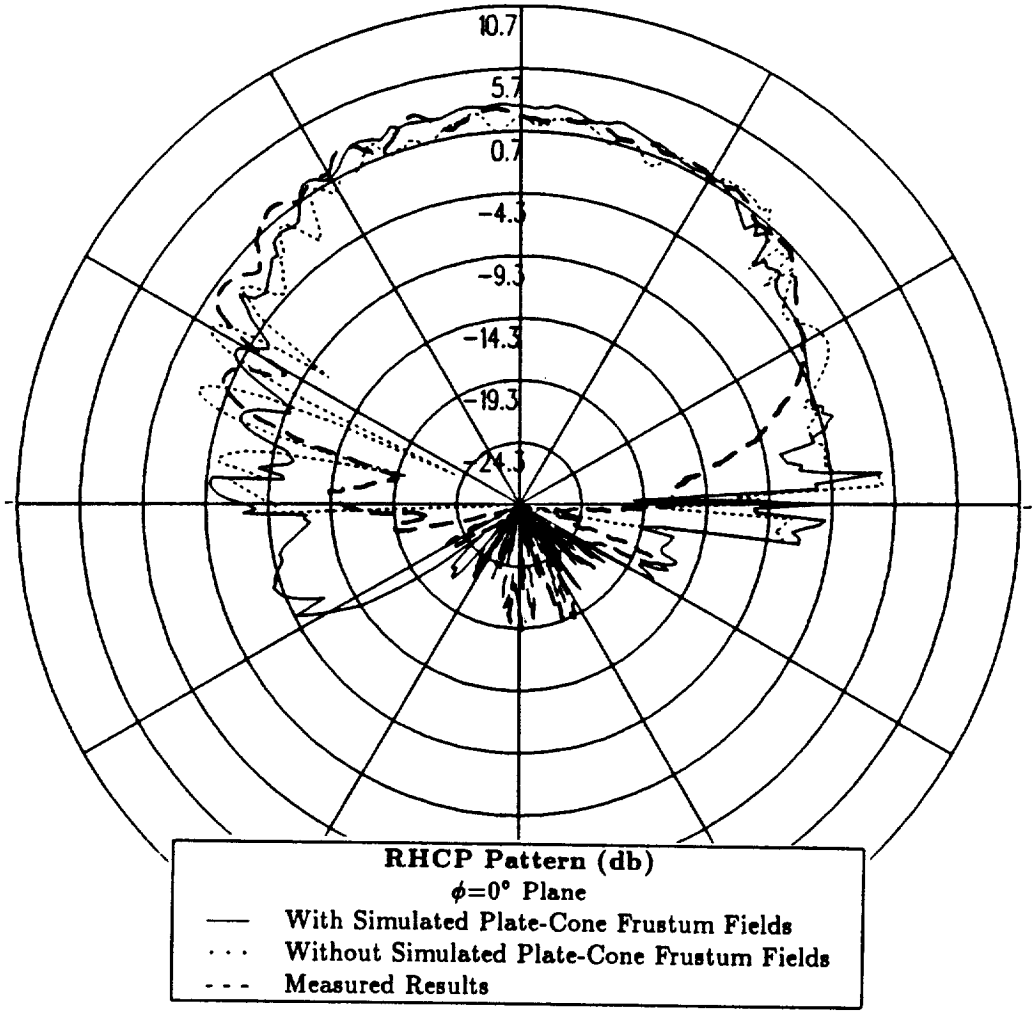

Figure 44: Elevation plane pattern which includes the simulated plate - cone frustum fields for right hand circular polarization at 300 MHz. (Cone Frustum Aircraft Model)

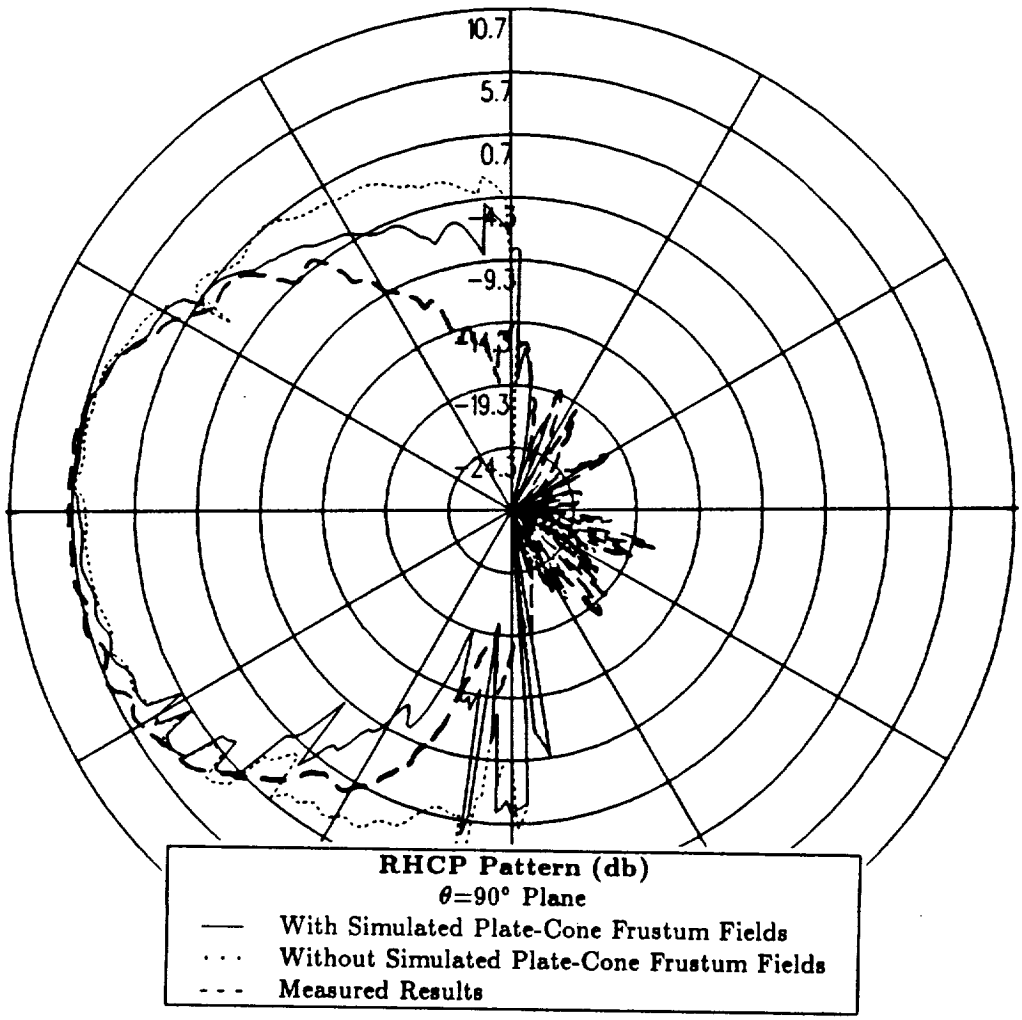

Figure 45: Azimuth plane pattern which includes the simulated plate - cone frustum fields for right hand circular polarization at 300 MHz. (Cone Frustum Aircraft Model)

3.6 Aircraft Model Conclusions

Section 3.3 shows that the radiation patterns for the three different aircraft models calculated using Version 3.1 of the NEC-BSC match the measured patterns provided by Boeing reasonably well except in the regions near the nose and the tail of the aircraft. In these regions, the fields which reflect from the fuselage and then interact with the wings and horizontal stabilizers need to be included. By including the plate - curved surface fields, the calculated radiation patterns are in better agreement with the measured patterns in these regions as seen in Section 3.5. This section demonstrates that the cylindrical aircraft model gives the best representation of the actual P-3C aircraft. This is true even though the cone frustum and composite ellipsoid models visually resemble the actual P-3C aircraft better. The reason that the cylindrical aircraft model represents the actual aircraft the best is that the most important characteristic of the aircraft is the cylindrical fuselage and the subsequent interactions between the fuselage and the wings and stabilizers. The cylindrical aircraft model most accurately models the actual fuselage and the subsequent interactions, which is why the cylindrical aircraft model is used throughout the remainder of this report except for any cases where the antenna is placed on the nose of the aircraft. In these cases, the composite ellipsoid aircraft model's elliptical nose is critical in the radiation patterns and, therefore, the composite ellipsoid model is used.

Overall, the NEC-BSC calculated radiation patterns in Section 3.5.1 show good agreement with the measured radiation patterns throughout the majority of the patterns. However, the plate - cylinder fields which are incorporated in order to improve the agreement between the calculated and measured results are only approximations and are not exact representations of the true plate - cylinder in-

teractions. Therefore, the exact plate - cylinder fields need to be permanently incorporated into the NEC-BSC. This is done in the following chapter.

Chapter 4

Improvements to the NEC-BSC

4.1 Introduction

In this chapter, the plate - cylinder interactions which are needed in Version 3.1 of the NEC-BSC will be added. The development of plate - cylinder interactions has a long history at the Ohio State University Electroscience Laboratory and this study is an extension of the work done by Marhefka and Burnside [13,14]. As noted in the previous chapter the two terms which contribute significantly to the radiation patterns for the aircraft models investigated in this study are the cylinder reflected - plate reflected field and the cylinder reflected - plate diffracted field. However, for completeness, the four primary first order plate - cylinder fields have been implemented into the NEC-BSC. These four fields are the plate reflected - cylinder reflected field, the cylinder reflected - plate reflected field, the plate diffracted - cylinder reflected field and the cylinder reflected - plate diffracted field.

Two equations are given for each of the plate - cylinder terms mentioned above. These two equations are dependent on the location of the receiver with respect to the scattering structures. First, the field is defined for the case when the receiver is in the near zone. A far zone expression for the field is then derived from the near zone expression for the case when the receiver is in the far zone. As with the

other terms in the NEC-BSC, the source must be in the near zone of the scattering structures.

The first two terms are associated with fields that are reflected from a plate as one of the interactions and are fairly straightforward since image theory can be applied. The last two terms are associated with fields that are diffracted from a plate as one of the interactions and are more complicated. These complications are due to the fact that the field diffracted by a plate can result from two mechanisms: 1) the field diffracted by the edge of the plate, and 2) the field diffracted by the corner of the plate. Therefore, both the edge diffraction and the corner diffraction must be calculated in order to determine the two terms which include diffraction from a plate as one of the interactions.

It is assumed that the fields defined in this chapter are time harmonic fields with a time dependence given by $e^{j\omega t}$, which will be suppressed throughout.

4.2 Plate Reflected - Cylinder Reflected Field

In this section the field reflected by a plate then reflected by a cylinder is discussed. First, the plate reflected - cylinder reflected field is defined for the case when the receiver is in the near zone. Then an expression for this field is derived for the case when the receiver is in the far zone by implementing far zone approximations to the near zone field. The final part of this section discusses the ray tracing techniques which are used to determine the ray path for the plate reflected - cylinder reflected field and the shadowing techniques which are used to determine if this field is present for the given source and receiver locations.

4.2.1 Plate Reflected - Cylinder Reflected Field for a Near Zone Receiver

The field reflected by a plate then reflected by a cylinder uses image theory to determine the reflection off the plate. An illustration of this plate reflected - cylinder reflected field is shown in Figure 46. First, the image location for the source is located with respect to the i^{th} plate. The field which radiates from the source then appears to be emanating from this image source location with the appropriate geometrical optics reflection coefficient factored in for the reflection from the plate. This reflected field is the incident field on the j^{th} cylinder at the corresponding reflection point Q_R and the uniform reflection coefficient is then used to determine the reflected field from the cylinder. The equation for this plate reflected - cylinder reflected term is

$$\vec{E}^{ref,ref}_{pla,cyl} = \vec{E}^{ref}_{pla}(Q_R) \cdot \bar{\bar{\mathcal{R}}} \sqrt{\frac{\rho^r_1 \rho^r_2}{(\rho^r_1 + s^r_c)(\rho^r_2 + s^r_c)}}\, e^{-jks^r_c} \,. \tag{4.1}$$

$\vec{E}^{ref}_{pla}(Q_R)$ is the field reflected by the plate which is incident on the cylinder at the reflection point Q_R and is defined by

$$\vec{E}^{ref}_{pla}(Q_R) = \vec{E}^{i}(Q_P) \cdot \bar{\bar{R}}\, \frac{e^{-jks^r_p}}{s^r_p} \tag{4.2}$$

where $\vec{E}^{i}(Q_P)$ is the field which is incident on the plate at the reflection point Q_P and is given by

$$\vec{E}^{i}(Q_P) = \vec{E}^{s}\, \frac{e^{-jks^i}}{s^i} \,. \tag{4.3}$$

Combining equations (4.1), (4.2) and (4.3) provides the near zone expression for the plate reflected - cylinder reflected field which is given by

$$\vec{E}^{ref,ref}_{pla,cyl} = \vec{E}^{s} \cdot \bar{\bar{R}} \cdot \bar{\bar{\mathcal{R}}} \sqrt{\frac{\rho^r_1 \rho^r_2}{(\rho^r_1 + s^r_c)(\rho^r_2 + s^r_c)}}\, \frac{e^{-jk(s^i + s^r_p + s^r_c)}}{s^i + s^r_p} \tag{4.4}$$

where

$\vec{E}^{s}$ = amplitude factor of source in the $\hat{d}_i$ direction

$\bar{\bar{R}}$ = geometrical optics reflection coefficient

$\bar{\bar{\mathcal{R}}}$ = uniform reflection coefficient for curved surface

ρ_1^r = principal radius of curvature of the reflected wavefront at the point of reflection Q_R on the cylinder

ρ_2^r = principal radius of curvature of the reflected wavefront at the point of reflection Q_R on the cylinder

s^i = distance from source to reflection point Q_P on the i^{th} plate

s_p^r = distance from reflection point Q_P on the i^{th} plate to reflection point Q_R on the j^{th} cylinder

s_c^r = distance from reflection point Q_R on the j^{th} cylinder to receiver

The dyadic reflection coefficients $\bar{\bar{R}}$ and $\bar{\bar{\mathcal{R}}}$ are defined in [6]. The equations defining ρ_1^r and ρ_2^r, the principal radii of curvature of the reflected wavefront, are given in [5] and the distances s^i, s_p^r and s_c^r are shown in Figure 46.

4.2.2 Plate Reflected - Cylinder Reflected Field for a Far Zone Receiver

When the receiver is in the far zone, $s_c^r \to \infty$ and the terms in equation (4.4) which contain s_c^r reduce to

$$\frac{e^{-jks_c^r}}{\sqrt{(\rho_1^r + s_c^r)(\rho_2^r + s_c^r)}} \cong e^{jk[\vec{R}(Q_R)\cdot\hat{d}]} \frac{e^{-jkr}}{r} \tag{4.5}$$

where $\vec{R}(Q_R)$ is the vector position of the reflection point Q_R on the cylinder and $\hat{d}$ is the direction vector of the field reflected from the cylinder. The term $\frac{e^{-jkr}}{r}$ will be suppressed throughout. Substituting this expression in equation (4.4) provides

the far zone expression for the plate reflected - cylinder reflected field given by

$$\vec{E}^{ref,ref}_{pla,cyl} \cong \vec{E}^{s} \cdot \bar{\bar{R}} \cdot \bar{\bar{\mathcal{R}}} \sqrt{\rho_1^r \rho_2^r} \, \frac{e^{-jk(s^i+s_p^r)}}{s^i + s_p^r} \, e^{jk[\vec{R}(Q_R)\cdot\hat{d}]} \, . \tag{4.6}$$

4.2.3 Ray Tracing and Shadowing Techniques

The ray tracing algorithm used to determine the ray path for the plate reflected - cylinder reflected field also makes use of image theory. First, the image location for the source is located with respect to the i^{th} plate. This image location is then used to find the reflection point Q_R on the curved surface of the j^{th} cylinder for the given scatter direction $\hat{d}$. When the receiver is in the near zone, an exact solution is used to determine the reflection point. When the receiver is in the far zone, the scatter direction is normally incremented by only a small amount before another field point is desired and, therefore, a time saving incremental scheme is used to find the reflection point. Both of these methods for finding the reflection point Q_R on the curved surface of the cylinder are developed in detail in [13,14].

Once the reflection point Q_R on the cylinder is determined, a check must be made to ensure that the ray path from the image source location to the reflection point Q_R passes through the i^{th} plate. If this ray does not pass through the i^{th} plate, the plate reflected - cylinder reflected field does not exist and is set to zero. If the ray does pass through the i^{th} plate, the reflection point Q_P on the plate is found. The procedure used to determine whether the ray path passes through the i^{th} plate and to find the reflection point Q_P is also described in [13,14].

The ray path for the plate reflected - cylinder reflected field is determined from the source location, the reflection point Q_P on the i^{th} plate, the reflection point Q_R on the j^{th} cylinder and the receiver location. The final step is to determine if shadowing occurs for this plate reflected - cylinder reflected ray path. If the ray path is shadowed at any point between the source and the receiver, the plate

reflected - cylinder reflected field is set to zero. The methods used to determine if a ray is shadowed or not by a plate or a cylinder are defined in [13,14]. These methods must be used three separate times for the plate reflected - cylinder reflected field: 1) to determine if there is shadowing between the source and the reflection point Q_P on the i^{th} plate, 2) to determine if there is shadowing between the reflection point Q_P on the i^{th} plate and the reflection point Q_R on the j^{th} cylinder, and 3) to determine if there is shadowing between the reflection point Q_R on the j^{th} cylinder and the receiver.

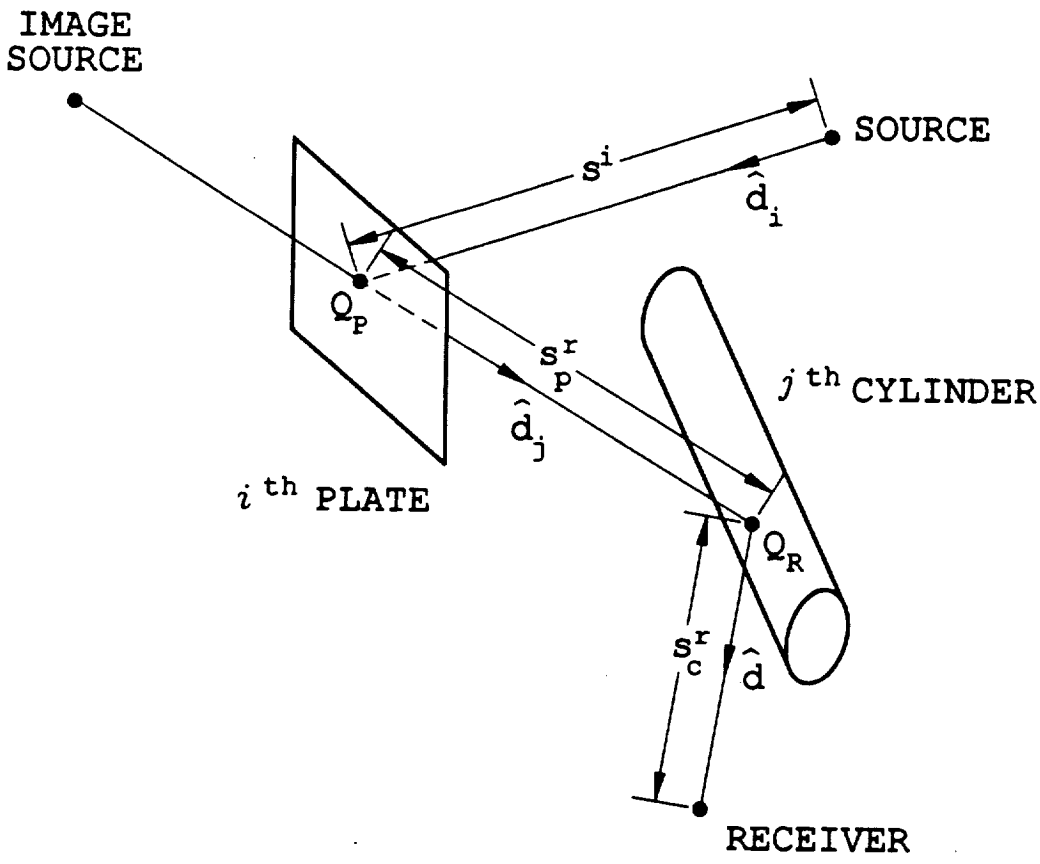

Figure 46: Illustration of plate reflected - cylinder reflected field

4.3 Cylinder Reflected - Plate Reflected Field

In this section the field reflected by a cylinder then reflected by a plate is discussed. First, the cylinder reflected - plate reflected field is defined for the case when the receiver is in the near zone. Then an expression for this field is derived for the case when the receiver is in the far zone by implementing far zone approximations to the near zone field. The final part of this section discusses the ray tracing techniques which are used to determine the ray path for the cylinder reflected - plate reflected field and the shadowing techniques which are used to determine if this field is present for the given source and receiver locations.

4.3.1 Cylinder Reflected - Plate Reflected Field for a Near Zone Receiver

The field reflected by a cylinder then reflected by a plate also uses image theory to determine the reflection off the plate. An illustration of this cylinder reflected - plate reflected field is shown in Figure 47. First, the reflection point Q_R on the j^{th} cylinder is determined for the given source location and the desired scatter direction $\hat{d}$. The incident field from the source is reflected by the cylinder at this reflection point and includes the uniform reflection coefficient. This cylinder reflected field then appears to be emanating from the image of the reflection point field caustic with the appropriate geometrical optics reflection coefficient factored in for the reflection from the plate. The equation for this cylinder reflected - plate reflected term is

$$\vec{E}^{ref,ref}_{cyl,pla} = \vec{E}^{ref}_{cyl}(Q_P) \cdot \bar{\bar{R}} \sqrt{\frac{(\rho_1^r + s_c^r)(\rho_2^r + s_c^r)}{(\rho_1^r + s_c^r + s_p^r)(\rho_2^r + s_c^r + s_p^r)}}\, e^{-jks_p^r} \qquad (4.7)$$

where the term under the square root follows from the fact that the source of the plate reflection is the image of the cylinder reflected field caustic. $\vec{E}^{ref}_{cyl}(Q_P)$ is the field reflected by the cylinder which is incident on the plate at the reflection point

Q_P and is defined by

$$\vec{E}^{ref}_{cyl}(Q_P) = \vec{E}^{i}(Q_R) \cdot \bar{\bar{\mathcal{R}}} \sqrt{\frac{\rho_1^r \rho_2^r}{(\rho_1^r + s_c^r)(\rho_2^r + s_c^r)}}\, e^{-jks_c^r} \tag{4.8}$$

where $\vec{E}^{i}(Q_R)$ is the field which is incident on the cylinder at the reflection point Q_R and is given by

$$\vec{E}^{i}(Q_R) = \vec{E}^{s}\, \frac{e^{-jks^i}}{s^i}\,. \tag{4.9}$$

Combining equations (4.7), (4.8) and (4.9) provides the near zone expression for the cylinder reflected - plate reflected field which is given by

$$\vec{E}^{ref,ref}_{cyl,pla} = \vec{E}^{s} \cdot \bar{\bar{\mathcal{R}}} \cdot \bar{\bar{R}} \sqrt{\frac{\rho_1^r \rho_2^r}{(\rho_1^r + s_c^r + s_p^r)(\rho_2^r + s_c^r + s_p^r)}}\, \frac{e^{-jk(s^i + s_c^r + s_p^r)}}{s^i} \tag{4.10}$$

where

$\vec{E}^{s}$ = amplitude factor of source in the $\hat{d}_i$ direction

$\bar{\bar{\mathcal{R}}}$ = uniform reflection coefficient for curved surface

$\bar{\bar{R}}$ = geometrical optics reflection coefficient

ρ_1^r = principal radius of curvature of the reflected wavefront at the point of reflection Q_R on the cylinder

ρ_2^r = principal radius of curvature of the reflected wavefront at the point of reflection Q_R on the cylinder

s^i = distance from source to reflection point Q_R on the j^{th} cylinder

s_c^r = distance from reflection point Q_R on the j^{th} cylinder to reflection point Q_P on the i^{th} plate

s_p^r = distance from reflection point Q_P on the i^{th} plate to receiver

The dyadic reflection coefficients $\bar{\bar{\mathcal{R}}}$ and $\bar{\bar{R}}$ are defined in [6]. The equations defining ρ_1^r and ρ_2^r, the principal radii of curvature of the reflected wavefront, are given in [5] and the distances s^i, s_c^r and s_p^r are shown in Figure 47.

4.3.2 Cylinder Reflected - Plate Reflected Field for a Far Zone Receiver

When the receiver is in the far zone, $s_p^r \rightarrow \infty$ and the terms in equation (4.10) which contain $s_c^r + s_p^r$ reduce to

$$\frac{e^{-jk(s_c^r+s_p^r)}}{\sqrt{(\rho_1^r + s_c^r + s_p^r)(\rho_2^r + s_c^r + s_p^r)}} \cong e^{jk[\vec{R}(Q_R^{im})\cdot\hat{d}]} \frac{e^{-jkr}}{r} \tag{4.11}$$

where $\vec{R}(Q_R^{im})$ is the vector position of the image of the reflection point on the cylinder and $\hat{d}$ is the direction vector of the field reflected from the plate. Suppressing $\frac{e^{-jkr}}{r}$ and substituting this expression in equation (4.10) provides the far zone expression for the cylinder reflected - plate reflected field given by

$$\vec{E}_{cyl,pla}^{ref,ref} \cong \vec{E}^s \cdot \bar{\bar{\mathcal{R}}} \cdot \bar{\bar{R}} \sqrt{\rho_1^r \rho_2^r} \frac{e^{-jks^i}}{s^i} e^{jk[\vec{R}(Q_R^{im})\cdot\hat{d}]} . \tag{4.12}$$

4.3.3 Ray Tracing and Shadowing Techniques

The ray tracing algorithm used to determine the ray path for the cylinder reflected - plate reflected field also makes use of image theory. To find the ray path for a near zone receiver, the image location for the receiver is located with respect to the i^{th} plate. Then the reflection point Q_R on the j^{th} cylinder is determined using the exact solution defined in [13,14] for the given source location and this image receiver location. When the receiver is in the far zone, the incident direction $\hat{d}_j$ to the i^{th} plate (which is also the reflection direction from the j^{th} cylinder) can be determined from the given scatter direction $\hat{d}$. The reflection point Q_R on the j^{th} cylinder can then be calculated from the source location and the cylinder reflection

direction $\hat{d}_j$ using the incremental method defined in [13,14]. An image location for the reflection point Q_R on the cylinder is then determined with respect to the i^{th} plate and defined as Q_R^{im}. This image reflection point location Q_R^{im} is then used to determine the image of the cylinder reflected field caustic which functions as the source location for the plate reflected field.

Once the image of the reflection point on the cylinder Q_R^{im} is determined, a check must be made to ensure that the ray path from this image reflection point location to the receiver passes through the i^{th} plate. If this ray does not pass through the i^{th} plate, the cylinder reflected - plate reflected field does not exist and is set to zero. If the ray does pass through the i^{th} plate, the reflection point Q_P on the plate is found using the procedure described in [13,14].

The ray path for the cylinder reflected - plate reflected field is determined from the source location, the reflection point Q_R on the j^{th} cylinder, the reflection point Q_P on the i^{th} plate and the receiver location. The final step is to determine if shadowing occurs for this cylinder reflected - plate reflected ray path. If the ray path is shadowed at any point between the source and the receiver, the cylinder reflected - plate reflected field is set to zero. The methods used to determine if a ray is shadowed or not by a plate or a cylinder are defined in [13,14]. These methods must be used three separate times for the cylinder reflected - plate reflected field: 1) to determine if there is shadowing between the source and the reflection point Q_R on the j^{th} cylinder, 2) to determine if there is shadowing between the reflection point Q_R on the j^{th} cylinder and the reflection point Q_P on the i^{th} plate, and 3) to determine if there is shadowing between the reflection point Q_P on the i^{th} plate and the receiver.

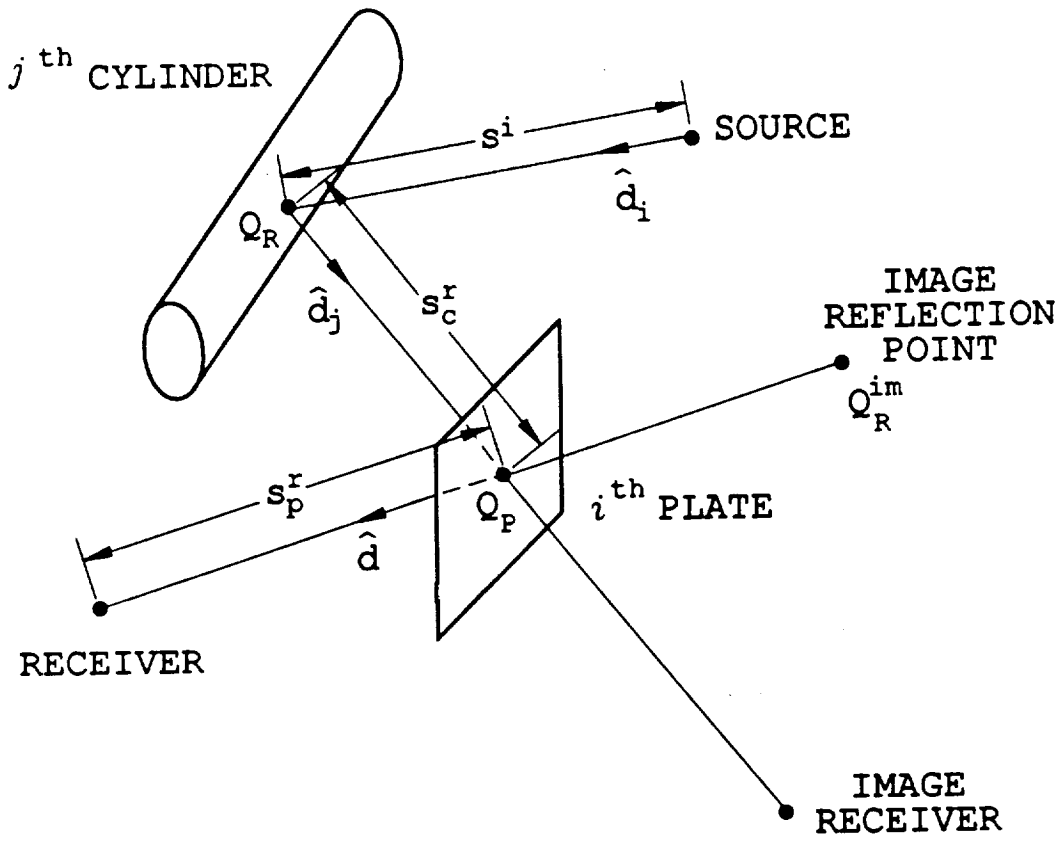

Figure 47: Illustration of cylinder reflected - plate reflected field

4.4 Plate Diffracted - Cylinder Reflected Field

In this section the field diffracted by a plate then reflected by a cylinder is discussed. As noted in Section 4.1 the field diffracted by a plate consists of both edge diffraction and corner diffraction. Because the plates used in the NEC-BSC are of finite extent, there will be two corner diffracted terms for each of the plate edges. Therefore, the total plate diffracted - cylinder reflected field will consist of an edge diffracted - cylinder reflected component and two corner diffracted - cylinder reflected components.

First, the edge diffracted - cylinder reflected component is defined for the case when the receiver is in the near zone. Then an expression for this component is derived for the case when the receiver is in the far zone by implementing far zone approximations to the near zone expression. The same procedure is used to define the near zone and far zone expressions for the corner diffracted - cylinder reflected components. Next, the ray tracing techniques which are used to determine the ray path for the plate diffracted - cylinder reflected components and the shadowing techniques which are used to determine which of these components are present for the given source and receiver locations are discussed in detail. The final part of this section defines regions in which complications arise with the plate diffracted - cylinder reflected expressions and describes the reason for these complications.

4.4.1 Edge Diffracted - Cylinder Reflected Field for a Near Zone Receiver

The field diffracted by a plate edge then reflected by a cylinder is more complicated than the plate reflected -cylinder reflected term because the incident wavefront at the reflection point on the cylinder does not appear to be emanating from a point source but rather from the edge of the plate. An illustration of this edge diffracted

- cylinder reflected field is shown in Figure 48. First, the diffraction point Q_E on the j^{th} edge of the i^{th} plate and the reflection point Q_R on the k^{th} cylinder are located for the given source and receiver locations. The field diffracted by the j^{th} edge of the i^{th} plate at Q_E is calculated using the edge diffraction coefficient. This diffracted field is incident on the k^{th} cylinder at Q_R and appears to be emanating from the plate edge. The uniform reflection coefficient is then used to determine the reflected field from the cylinder. The equation for this edge diffracted - cylinder reflected term is

$$\vec{E}^{diff,ref}_{edge,cyl} = \vec{E}^{diff}_{edge}(Q_R) \cdot \bar{\bar{\mathcal{R}}} \sqrt{\frac{\rho_1^r \rho_2^r}{(\rho_1^r + s_c^r)(\rho_2^r + s_c^r)}}\, e^{-jks_c^r} \,. \tag{4.13}$$

$\vec{E}^{diff}_{edge}(Q_R)$ is the field diffracted by the plate edge which is incident on the cylinder at the reflection point Q_R and is defined by

$$\vec{E}^{diff}_{edge}(Q_R) = \vec{E}^{i}(Q_E) \cdot \bar{\bar{D}} \sqrt{\frac{s^i}{s_e^d(s^i + s_e^d)}}\, e^{-jks_e^d} \tag{4.14}$$

where $\vec{E}^{i}(Q_E)$ is the field which is incident on the plate edge at the diffraction point Q_E and is defined by

$$\vec{E}^{i}(Q_E) = \vec{E}^{s}\, \frac{e^{-jks^i}}{s^i} \,. \tag{4.15}$$

Combining equations (4.13), (4.14) and (4.15) provides the near zone expression for the edge diffracted - cylinder reflected field which is given by

$$\vec{E}^{diff,ref}_{edge,cyl} = \vec{E}^{s} \cdot \bar{\bar{D}} \cdot \bar{\bar{\mathcal{R}}} \sqrt{\frac{\rho_1^r \rho_2^r}{(\rho_1^r + s_c^r)(\rho_2^r + s_c^r)}}\, \frac{e^{-jk(s^i + s_e^d + s_c^r)}}{\sqrt{s^i s_e^d\,(s^i + s_e^d)}} \tag{4.16}$$

where

$\vec{E}^{s}$ = amplitude factor of source in the $\hat{d}_i$ direction

$\bar{\bar{D}}$ = edge diffraction coefficient

$\bar{\bar{\mathcal{R}}}$ = uniform reflection coefficient for curved surface

ρ_1^r = principal radius of curvature of the reflected wavefront at the point of reflection Q_R on the cylinder

ρ_2^r = principal radius of curvature of the reflected wavefront at the point of reflection Q_R on the cylinder

s^i = distance from source to diffraction point Q_E on the j^{th} edge of the i^{th} plate

s_e^d = distance from diffraction point Q_E on the j^{th} edge of the i^{th} plate to reflection point Q_R on the k^{th} cylinder

s_c^r = distance from reflection point Q_R on the k^{th} cylinder to receiver

The dyadic edge diffraction coefficient $\overline{\overline{D}}$ is defined in [5] and the dyadic reflection coefficient $\overline{\overline{\mathcal{R}}}$ is defined in [6]. The distances s^i, s_e^d and s_c^r are shown in Figure 48. In [5] the equations defining ρ_1^r and ρ_2^r, the principal radii of curvature of the reflected wavefront, show that these radii are dependent on , ρ_1^i and ρ_2^i, the principal radii of curvature of the incident wavefront at the reflection point. In the previous two terms the field incident on the cylinder surface appears to be emanating from a point source, which constitutes a spherical wave incidence. Therefore, ρ_1^i and ρ_2^i are both equal to the distance from the source location to the reflection point. However, the incident field at the reflection point for this term appears to be emanating from the plate edge and the wave incident on the cylinder surface is not a spherical wave but rather resembles an astigmatic tube of rays which has two different radii of curvature. These two principal radii of curvature of the incident wavefront at the reflection point on the cylinder are defined by

$$\rho_1^i = s_e^d \tag{4.17}$$

$$\rho_2^i = s^i + s_e^d \tag{4.18}$$

where ρ_1^i is in the principal $\hat{\phi}$ direction and ρ_2^i is in the principal $\hat{\beta}_o$ direction. Equations (4.17) and (4.18) are then used to determine ρ_1^r and ρ_2^r which are used in (4.16).

The distance parameter L which is used in the edge diffraction coefficient $\overline{\overline{D}}$ is relatively simple for this edge diffracted - cylinder reflected field. The wave incident on the plate edge is a spherical wave which appears to be emanating from the source location. Since the reflection point Q_R on the cylinder surface is always in the near zone of the diffraction point Q_E, the expression for the distance parameter L remains the same whether the receiver is in the near zone or the far zone and is given by

$$L = \frac{s^i s_e^d}{s^i + s_e^d} \sin^2 \beta_o \tag{4.19}$$

where $\sin \beta_o$ is the sine of the diffracted angle β_o in the plane of the edge $\hat{e}_j$ and the incident ray $\hat{d}_i$.

4.4.2 Edge Diffracted - Cylinder Reflected Field for a Far Zone Receiver

When the receiver is in the far zone, $s_c^r \rightarrow \infty$ and the terms in equation (4.16) which contain s_c^r reduce to

$$\frac{e^{-jks_c^r}}{\sqrt{(\rho_1^r + s_c^r)(\rho_2^r + s_c^r)}} \cong e^{jk[\vec{R}(Q_R)\cdot\hat{d}]} \frac{e^{-jkr}}{r} \tag{4.20}$$

where $\vec{R}(Q_R)$ is the vector position of the reflection point Q_R on the cylinder and $\hat{d}$ is the direction vector of the field reflected from the cylinder. Suppressing $\frac{e^{-jkr}}{r}$ and substituting this expression in equation (4.16) provides the far zone expression for the edge diffracted - cylinder reflected field given by

$$\vec{E}_{edge,cyl}^{diff,ref} \cong \vec{E}^i \cdot \overline{\overline{D}} \cdot \overline{\overline{\mathcal{R}}} \sqrt{\rho_1^r \rho_2^r} \frac{e^{-jk(s^i + s_e^d)}}{\sqrt{s^i s_e^d \left(s^i + s_e^d\right)}} e^{jk[\vec{R}(Q_R)\cdot\hat{d}]} . \tag{4.21}$$

4.4.3 Corner Diffracted - Cylinder Reflected Field for a Near Zone Receiver

The field diffracted by a plate corner then reflected by a cylinder is very similar to the edge diffracted - cylinder reflected term discussed in Section 4.4.1. The primary difference between these two terms is that the incident wavefront at the reflection point on the cylinder appears to be emanating from a point source located at the corner of the plate in the corner diffracted - cylinder reflected field rather than from the edge of the plate, as in the edge diffracted - cylinder reflected field. An illustration of this corner diffracted - cylinder reflected field is shown in Figure 49. First, the reflection point Q_R on the k^{th} cylinder is located for the given receiver location when the j^{th} corner of the i^{th} plate is used as the source location. The field diffracted by the j^{th} corner of the i^{th} plate at Q_C is calculated using the corner diffraction coefficient. This diffracted field is incident on the k^{th} cylinder at Q_R and appears to be emanating from the corner of the plate. The uniform reflection coefficient is then used to determine the reflected field from the cylinder. The equation for this corner diffracted - cylinder reflected term is

$$\vec{E}^{diff,ref}_{corn,cyl} = \vec{E}^{diff}_{corn}(Q_R) \cdot \bar{\bar{\mathcal{R}}} \sqrt{\frac{\rho^r_1 \rho^r_2}{(\rho^r_1 + s^r_c)(\rho^r_2 + s^r_c)}}\, e^{-jks^r_c} \,. \tag{4.22}$$

$\vec{E}^{diff}_{corn}(Q_R)$ is the field diffracted by the plate corner which is incident on the cylinder at the reflection point Q_R and is defined by

$$\vec{E}^{diff}_{corn}(Q_R) = \vec{E}^{i}(Q_C) \cdot \bar{\bar{D}}_c \frac{e^{-jks^d_c}}{s^d_c} \,. \tag{4.23}$$

where $\vec{E}^{i}(Q_C)$ is the field which is incident on the plate corner and is defined by

$$\vec{E}^{i}(Q_C) = \vec{E}^{s} \frac{e^{-jks^i}}{s^i} \,. \tag{4.24}$$

Combining equations (4.22), (4.23) and (4.24) provides the near zone expression for the corner diffracted - cylinder reflected field which is given by

$$\vec{E}^{diff,ref}_{corn,cyl} = \vec{E}^{s} \cdot \bar{\bar{D}}_c \cdot \bar{\bar{\mathcal{R}}} \sqrt{\frac{\rho_1^r \rho_2^r}{(\rho_1^r + s_c^r)(\rho_2^r + s_c^r)}} \frac{e^{-jk(s^i + s_c^d + s_c^r)}}{s^i s_c^d} \tag{4.25}$$

where

$\vec{E}^s$ = amplitude factor of source in the $\hat{d}_i$ direction

$\bar{\bar{D}}_c$ = corner diffraction coefficient

$\bar{\bar{\mathcal{R}}}$ = uniform reflection coefficient for curved surface

ρ_1^r = principal radius of curvature of the reflected wavefront at the point of reflection Q_R on the cylinder

ρ_2^r = principal radius of curvature of the reflected wavefront at the point of reflection Q_R on the cylinder

s^i = distance from source to the j^{th} corner of the i^{th} plate

s_c^d = distance from the j^{th} corner of the i^{th} plate to reflection point Q_R on the k^{th} cylinder

s_c^r = distance from reflection point Q_R on the k^{th} cylinder to receiver

The dyadic corner diffraction coefficient $\bar{\bar{D}}_c$ is defined in [15] and the dyadic reflection coefficient $\bar{\bar{\mathcal{R}}}$ is defined in [6]. The equations defining ρ_1^r and ρ_2^r, the principal radii of curvature of the reflected wavefront, are given in [5]. For this term ρ_1^i and ρ_2^i, which are needed to determine ρ_1^r and ρ_2^r, are both equal to s_c^d because the field incident on the cylinder surface appears to be emanating from the corner of the plate.

The distances s^i, s_c^d and s_c^r are shown in Figure 49. It should be noted that the distances s^i, s_c^d and s_c^r which are used in this section are not equal to the

distances s^i, s_e^d and s_c^r which are used for the edge diffracted - cylinder reflected field in Section 4.4.1. These distances are not the same because the diffraction and reflection points are different for the edge diffracted and the corner diffracted fields. Likewise, the direction vectors $\hat{d}_i$, $\hat{d}_j$ and $\hat{d}$ are different for this corner diffracted - cylinder reflected field than they are for the edge diffracted - cylinder reflected field defined in Section 4.4.1.

The distance parameter L_c which is used in the corner diffraction coefficient $\bar{\bar{D}}_c$ is also relatively simple for this corner diffracted - cylinder reflected field. The wave incident on the corner of the plate is a spherical wave which appears to be emanating from the source location. Since the reflection point Q_R on the cylinder surface is always in the near zone of the corner, the expression for the distance parameter L_c remains the same whether the receiver is in the near zone or the far zone and is given by

$$L_c = \frac{s^i s_c^d}{s^i + s_c^d} \,. \tag{4.26}$$

4.4.4 Corner Diffracted - Cylinder Reflected Field for a Far Zone Receiver

When the receiver is in the far zone, $s_c^r \to \infty$ and the terms in equation (4.25) which contain s_c^r reduce to

$$\frac{e^{-jks_c^r}}{\sqrt{(\rho_1^r + s_c^r)(\rho_2^r + s_c^r)}} \cong e^{jk[\vec{R}(Q_R)\cdot\hat{d}]} \frac{e^{-jkr}}{r} \tag{4.27}$$

where $\vec{R}(Q_R)$ is the vector position of the reflection point Q_R on the cylinder and $\hat{d}$ is the direction vector of the field reflected from the cylinder. Suppressing $\frac{e^{-jkr}}{r}$ and substituting this expression in equation (4.25) provides the far zone expression for the corner diffracted - cylinder reflected field given by

$$\vec{E}_{corn,cyl}^{diff,ref} \cong \vec{E}^i \cdot \bar{\bar{D}}_c \cdot \bar{\bar{\mathcal{R}}} \sqrt{\rho_1^r \rho_2^r} \, \frac{e^{-jk(s^i + s_c^d)}}{s^i s_c^d} \, e^{jk[\vec{R}(Q_R)\cdot\hat{d}]} \,. \tag{4.28}$$

C-2

4.4.5 Ray Tracing and Shadowing Techniques for Edge Diffracted - Cylinder Reflected Field

The ray tracing algorithm used to determine the ray path for the edge diffracted - cylinder reflected field uses an iterative process to find the appropriate diffraction point and reflection point. To begin this iterative process, the midway point on the j^{th} edge of the i^{th} plate is chosen as the starting diffraction point. This diffraction point is then used as a source location in order to find a reflection point on the k^{th} cylinder for the given scatter direction $\hat{d}$. The method used to find this reflection point uses an exact solution when the receiver is in the near zone and an incremental solution when the receiver is in the far zone as discussed in Section 4.2.3. This reflection point is then used as a receiver location in order to find a new diffraction point on the j^{th} edge of the i^{th} plate for the given source location. Because the reflection point on the cylinder is always in the near zone of the plate edge, the method used to find this new diffraction point uses an exact solution derived for a near zone receiver which is defined in [13,14].

Once this diffraction point and reflection point are found, a check is made to determine if the ray path defined by these points satisfies both the law of diffraction at the plate edge and the law of reflection at the cylinder surface. If the ray path does not satisfy both the law of diffraction and the law of reflection, then the above process is repeated. The previous diffraction point is used as a source location in order to find a new reflection point on the cylinder. This new reflection point is then used as a receiver location in order to find a new diffraction point for the given source location. The new ray path defined by these new diffraction and reflection points is then checked to determine if both the law of diffraction and the law of reflection are satisfied. This process is repeated until the ray path is found which satisfies both the law of diffraction and the law of reflection. Then the diffraction

point Q_E and the reflection point Q_R are valid and the ray tracing for this edge diffracted - cylinder reflected field is complete.

The routine which determines the diffraction point Q_E described above assumes that the plate edge is infinite. Therefore, once the diffraction point is found, it must be determined whether the point Q_E is on the finite edge of the i^{th} plate. If the diffraction point is on the finite edge, then the edge diffracted - cylinder reflected field is calculated. If the diffraction point is not on the finite edge, then the edge diffracted - cylinder reflected field does not exist and is set to zero.

The ray path for the edge diffracted - cylinder reflected field is determined from the source location, the diffraction point Q_E on the j^{th} edge of the i^{th} plate, the reflection point Q_R on the k^{th} cylinder and the receiver location. The final step is to determine if shadowing occurs for this edge diffracted - cylinder reflected ray path. If the ray path is shadowed at any point between the source and the receiver, the edge diffracted - cylinder reflected field is set to zero. The methods used to determine if a ray is shadowed or not by a plate or a cylinder are defined in [13,14] and must be used three separate times for the edge diffracted - cylinder reflected field: 1) to determine if there is shadowing between the source and the diffraction point Q_E on the j^{th} edge of the i^{th} plate, 2) to determine if there is shadowing between the diffraction point Q_E on the j^{th} edge of the i^{th} plate and the reflection point Q_R on the k^{th} cylinder, and 3) to determine if there is shadowing between the reflection point Q_R on the k^{th} cylinder and the receiver.

4.4.6 Ray Tracing and Shadowing Techniques for Corner Diffracted - Cylinder Reflected Field

The ray tracing algorithm used to determine the ray path for the corner diffracted - cylinder reflected field is relatively simple. The j^{th} corner of the i^{th} plate is used as a source location in order to find a reflection point on the k^{th} cylinder for the

given scatter direction $\hat{d}$. The method used to find this reflection point uses an exact solution when the receiver is in the near zone and an incremental solution when the receiver is in the far zone as discussed in Section 4.2.3. The j^{th} corner of the i^{th} plate and the reflection point Q_R, along with the given source and receiver locations, define the ray path for this corner diffracted - cylinder reflected field. The same procedure is then followed for the $j + 1^{th}$ corner of the i^{th} plate to determine the ray path for the corner diffracted - cylinder reflected field from this corner.

The final step is to determine if shadowing occurs for the corner diffracted - cylinder reflected ray path. If the ray path is shadowed at any point between the source and the receiver, the corner diffracted - cylinder reflected field is set to zero. The methods used to determine if a ray is shadowed or not by a plate or a cylinder are defined in [13,14] and must be used three separate times for the corner diffracted - cylinder reflected field: 1) to determine if there is shadowing between the source and the the j^{th} corner of the i^{th} plate, 2) to determine if there is shadowing between the j^{th} corner of the i^{th} plate and the reflection point Q_R on the k^{th} cylinder, and 3) to determine if there is shadowing between the reflection point Q_R on the k^{th} cylinder and the receiver. The same procedure is then followed for the $j+1^{th}$ corner of the i^{th} plate to determine if shadowing occurs for the corner diffracted - cylinder reflected field from this corner.

4.4.7 Regions where Plate Diffracted - Cylinder Reflected Field is Not Valid

Equations (4.16) and (4.21) are valid for the edge diffracted - cylinder reflected field for a receiver in the near zone and the far zone, respectively, except when the edge diffracted ray is in the transition region of the j^{th} edge of the i^{th} plate. Likewise, equations (4.25) and (4.28) are valid for the corner diffracted - cylinder reflected

fields except when the corner diffracted ray is in the transition region of the j^{th} corner of the i^{th} plate. The problems arise because UTD assumes that the incident wavefront on the surface of the cylinder is in the form of a ray optical field. In the transition region of the plate edge and the plate corner, the true representation of the diffracted fields is much more complicated and is not a true ray optical field. Therefore, the incident field at the reflection point Q_R on the k^{th} cylinder is not ray optical and equations (4.16), (4.21), (4.25) and (4.28) are not completely valid. However, it can be assumed that the fields in the transition region will give a reasonable engineering representation for the field in any event. In practice these approximations appear to give useable answers to this complicated problem, since the regions in which they are not valid are rather small in extent.

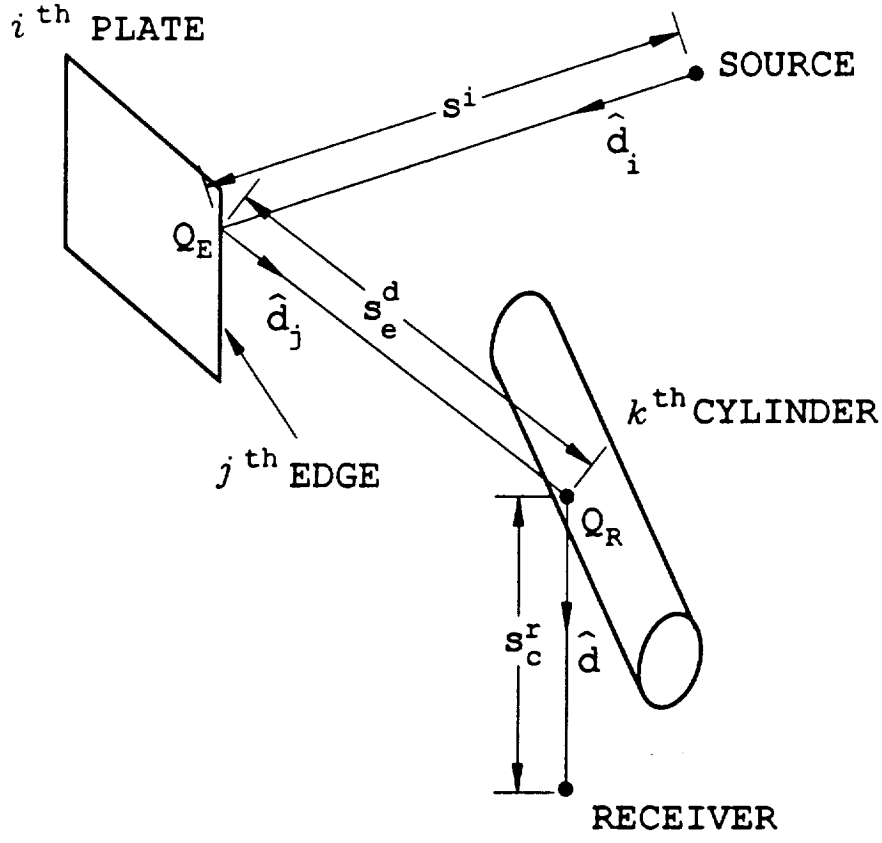

Figure 48: Illustration of edge diffracted - cylinder reflected field

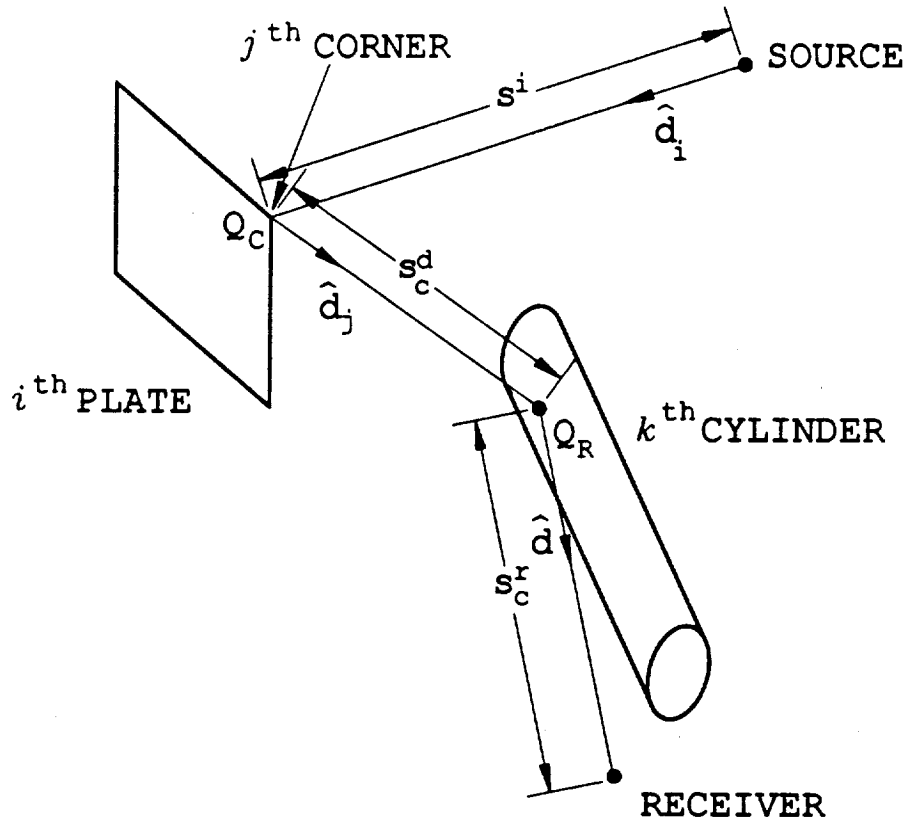

Figure 49: Illustration of corner diffracted - cylinder reflected field

4.5 Cylinder Reflected - Plate Diffracted Field

In this section the field reflected by a cylinder then diffracted by a plate is discussed. As noted in Section 4.1 the field diffracted by a plate consists of both edge diffraction and corner diffraction. Because the plates used in the NEC-BSC code are of finite extent, there will be two corner diffracted terms for each of the plate edges. Therefore, the total cylinder reflected - plate diffracted field will consist of a cylinder reflected - edge diffracted component and two cylinder reflected - corner diffracted components.

First, the cylinder reflected - edge diffracted component is defined for the case when the receiver is in the near zone. Then an expression for this component is derived for the case when the receiver is in the far zone by implementing far zone approximations to the near zone expression. The same procedure is used to define the near zone and far zone expressions for the cylinder reflected - corner diffracted components. Next, the ray tracing techniques which are used to determine the ray path for these cylinder reflected - plate diffracted components and the shadowing techniques which are used to determine which of these components are present for the given source and receiver locations are discussed in detail. The final part of this section defines regions in which complications arise with the cylinder reflected - plate diffracted expressions and describes the reason for these complications.

4.5.1 Cylinder Reflected - Edge Diffracted Field for a Near Zone Receiver

The field reflected by a cylinder then diffracted by a plate edge is also complicated because the incident wavefront at the diffraction point on the plate edge does not appear to be emanating from a point source but rather from the caustic distance of the reflected field from the cylinder. An illustration of this cylinder reflected -

edge diffracted field is shown in Figure 50. First, the reflection point Q_R on the k^{th} cylinder and the diffraction point Q_E on the j^{th} edge of the i^{th} plate are located for the given source and receiver locations. The field reflected by the k^{th} cylinder at Q_R is calculated using the uniform reflection coefficient. This reflected field is incident on the j^{th} edge of the i^{th} plate at Q_E and appears to be emanating from the reflected field caustic of the cylinder. The edge diffraction coefficient is then used to determine the diffracted field from the plate edge. The equation for this cylinder reflected - edge diffracted term is

$$\vec{E}^{ref,diff}_{cyl,edge} = \vec{E}^{ref}_{cyl}(Q_E) \cdot \bar{\bar{D}} \sqrt{\frac{\rho^i_e}{s^d_e\,(\rho^i_e + s^d_e)}}\, e^{-jks^d_e} \tag{4.29}$$

where ρ^i_e is the reflected field caustic. $\vec{E}^{ref}_{cyl}(Q_E)$ is the field reflected by the cylinder which is incident on the plate edge at the diffraction point Q_E and is defined by

$$\vec{E}^{ref}_{cyl}(Q_E) = \vec{E}^{i}(Q_R) \cdot \bar{\bar{\mathcal{R}}} \sqrt{\frac{\rho^r_1 \rho^r_2}{(\rho^r_1 + s^r_c)(\rho^r_2 + s^r_c)}}\, e^{-jks^r_c} \tag{4.30}$$

where $\vec{E}^i(Q_R)$ is the field which is incident on the cylinder surface at the reflection point Q_R and is defined by

$$\vec{E}^i(Q_R) = \vec{E}^s\, \frac{e^{-jks^i}}{s^i}\,. \tag{4.31}$$

Combining equations (4.29), (4.30) and (4.31) provides the near zone expression for the cylinder reflected - edge diffracted field which is given by

$$\vec{E}^{ref,diff}_{cyl,edge} = \vec{E}^s \cdot \bar{\bar{\mathcal{R}}} \cdot \bar{\bar{D}} \sqrt{\frac{\rho^r_1 \rho^r_2}{(\rho^r_1 + s^r_c)(\rho^r_2 + s^r_c)}} \sqrt{\frac{\rho^i_e}{s^d_e\,(\rho^i_e + s^d_e)}}\, \frac{e^{-jk(s^i + s^r_c + s^d_e)}}{s^i} \tag{4.32}$$

where

$\vec{E}^s$ = amplitude factor of source in the $\hat{d}_i$ direction

$\bar{\bar{\mathcal{R}}}$ = uniform reflection coefficient for curved surface

$\bar{\bar{D}}$ = edge diffraction coefficient

ρ_1^r = principal radius of curvature of the reflected wavefront at the point of reflection Q_R on the cylinder

ρ_2^r = principal radius of curvature of the reflected wavefront at the point of reflection Q_R on the cylinder

ρ_e^i = radius of curvature of the incident wavefront at the point of diffraction Q_E in the plane of the edge $\hat{e}_j$ and the incident ray $\hat{d}_j$

s^i = distance from source to reflection point Q_R on the k^{th} cylinder

s_c^r = distance from reflection point Q_R on the k^{th} cylinder to diffraction point Q_E on j^{th} edge of the i^{th} plate

s_e^d = distance from diffraction point Q_E on the j^{th} edge of the i^{th} plate to receiver

The dyadic reflection coefficient $\bar{\bar{\mathcal{R}}}$ is defined in [6] and the dyadic edge diffraction coefficient $\bar{\bar{D}}$ is defined in [5]. The distances s^i, s_c^r and s_e^d are shown in Figure 50. The equations defining ρ_1^r and ρ_2^r, the principal radii of curvature of the reflected wavefront, are given in [5]. For this term ρ_1^i and ρ_2^i, which are needed to determine ρ_1^r and ρ_2^r, are both equal to s^i because the field incident on the cylinder surface appears to be emanating from a point source. The reflected field caustic ρ_e^i is the radius of curvature of the incident wavefront at the point of diffraction Q_E in the plane of the edge $\hat{e}_j$ and the incident ray $\hat{d}_j$ and is defined by

$$\rho_e^i = \frac{(\rho_1^r + s_c^r)(\rho_2^r + s_c^r)}{(\rho_2^r + s_c^r)\cos^2\alpha + (\rho_1^r + s_c^r)\cos^2\beta} \tag{4.33}$$

where $\cos\alpha$ and $\cos\beta$ are defined by

$$\cos\alpha = \frac{\hat{X}_1^r \cdot \hat{e}_j}{\sin\beta_o} \tag{4.34}$$

$$\cos\beta = \frac{\hat{X}_2^r \cdot \hat{e}_j}{\sin\beta_o} \,. \tag{4.35}$$

$\hat{X}_1^r$ and $\hat{X}_2^r$ are the principal directions of the reflected wavefronts defined in [5] and $\sin\beta_o$ is the sine of the diffracted angle β_o in the plane of the edge $\hat{e}_j$ and the incident ray $\hat{d}_j$.

The distance parameter L which is used in the edge diffraction coefficient $\overline{\overline{D}}$ is more complicated for this cylinder reflected - edge diffracted field. The distance parameter is more complicated because the wave incident on the plate edge is not a spherical wave which emanates from a point source but rather resembles an astigmatic tube of rays which has two different radii of curvature. These radii of curvature are dependent on the reflected field caustic distances of the cylinder. The expression for the distance parameter L when the receiver is in the near zone is

$$L = \frac{s_e^d\,(\rho_e^i + s_e^d)(\rho_1^r + s_c^r)(\rho_2^r + s_c^r)}{\rho_e^i\,(\rho_1^r + s_c^r + s_e^d)(\rho_2^r + s_c^r + s_e^d)}\,\sin^2\beta_o \tag{4.36}$$

where again $\sin\beta_o$ is the sine of the diffracted angle β_o in the plane of the edge $\hat{e}_j$ and the incident ray $\hat{d}_j$.

4.5.2 Cylinder Reflected - Edge Diffracted Field for a Far Zone Receiver

When the receiver is in the far zone, $s_e^d \to \infty$ and the terms in equation (4.32) which contain s_e^d reduce to

$$\frac{e^{-jks_e^d}}{\sqrt{s_e^d\,(\rho_e^i + s_e^d)}} \cong e^{jk[\vec{R}(Q_E)\cdot\hat{d}]}\,\frac{e^{-jkr}}{r} \,. \tag{4.37}$$

where $\vec{R}(Q_E)$ is the vector position of the diffraction point Q_E on the plate edge and $\hat{d}$ is the direction vector of the field reflected from the cylinder. Suppressing $\frac{e^{-jkr}}{r}$ and substituting this expression in equation (4.32) provides the far zone expression

for the cylinder reflected - edge diffracted field given by

$$\vec{E}^{ref,diff}_{cyl,edge} \cong \vec{E}^{s} \cdot \bar{\bar{R}} \cdot \bar{\bar{D}} \sqrt{\frac{\rho_1^r \rho_2^r}{(\rho_1^r + s_c^r)(\rho_2^r + s_c^r)}} \sqrt{\rho_e^i} \, \frac{e^{-jk(s^i + s_c^r)}}{s^i} \, e^{jk[\vec{R}(Q_B)\cdot\hat{d}]} \, . \qquad (4.38)$$

When the receiver is in the far zone, the distance parameter L in equation (4.36) reduces to

$$L = \frac{(\rho_1^r + s_c^r)(\rho_2^r + s_c^r)}{\rho_e^i} \sin^2 \beta_o \, . \qquad (4.39)$$

4.5.3 Cylinder Reflected - Corner Diffracted Field for a Near Zone Receiver

The field reflected by a cylinder then diffracted by a plate corner is very similar to the cylinder reflected - edge diffracted term discussed in Section 4.5.1. The primary difference between these two terms is that the field at the receiver appears to be emanating from a point source located at the corner of the plate in the cylinder reflected - corner diffracted field rather than from the edge of the plate, as in the cylinder reflected - edge diffracted field. An illustration of this corner diffracted - cylinder reflected field is shown in Figure 51. First, the reflection point Q_R on the k^{th} cylinder is located for the given source location when the j^{th} corner of the i^{th} plate is used as the receiver location. The field reflected by the k^{th} cylinder at Q_R is calculated using the uniform reflection coefficient. This reflected field is incident on the j^{th} corner of the i^{th} plate at Q_C and appears to be emanating from the reflected field caustic of the cylinder. The corner diffraction coefficient is then used to determine the diffracted field from the corner of the plate. The equation for this cylinder reflected - corner diffracted term is

$$\vec{E}^{ref,diff}_{cyl,corn} = \vec{E}^{ref}_{cyl}(Q_C) \cdot \bar{\bar{D}}_c \, \frac{e^{-jks_c^d}}{s_c^d} \, . \qquad (4.40)$$

$\vec{E}^{ref}_{cyl}(Q_C)$ is the field reflected by the cylinder which is incident on the corner of the plate and is defined by

$$\vec{E}^{ref}_{cyl}(Q_C) = \vec{E}^{i}(Q_R) \cdot \bar{\bar{\mathcal{R}}} \sqrt{\frac{\rho^r_1 \rho^r_2}{(\rho^r_1 + s^r_c)(\rho^r_2 + s^r_c)}}\, e^{-jks^r_c} \tag{4.41}$$

where $\vec{E}^{i}(Q_R)$ is the field which is incident on the cylinder surface at the reflection point Q_R and is defined by

$$\vec{E}^{i}(Q_R) = \vec{E}^{s}\, \frac{e^{-jks^i}}{s^i}\,. \tag{4.42}$$

Combining equations (4.40), (4.41) and (4.42) provides the near zone expression for the cylinder reflected - corner diffracted field which is given by

$$\vec{E}^{ref,diff}_{cyl,corn} = \vec{E}^{s} \cdot \bar{\bar{\mathcal{R}}} \cdot \bar{\bar{D}}_c \sqrt{\frac{\rho^r_1 \rho^r_2}{(\rho^r_1 + s^r_c)(\rho^r_2 + s^r_c)}}\, \frac{e^{-jk(s^i + s^r_c + s^d_c)}}{s^i s^d_c} \tag{4.43}$$

where

$\vec{E}^{s}$ = amplitude factor of source in the $\hat{d}_i$ direction

$\bar{\bar{\mathcal{R}}}$ = uniform reflection coefficient for curved surface

$\bar{\bar{D}}_c$ = corner diffraction coefficient

ρ^r_1 = principal radius of curvature of the reflected wavefront at the point of reflection Q_R on the cylinder

ρ^r_2 = principal radius of curvature of the reflected wavefront at the point of reflection Q_R on the cylinder

s^i = distance from source to reflection point Q_R on the k^{th} cylinder

s^r_c = distance from reflection point Q_R on the k^{th} cylinder to the j^{th} corner of the i^{th} plate

s^d_c = distance from the j^{th} corner of the i^{th} plate to receiver

The dyadic reflection coefficient $\bar{\bar{\mathcal{R}}}$ is defined in [6] and the dyadic corner diffraction coefficient $\bar{\bar{D}}_c$ is defined in [15]. The equations defining ρ_1^r and ρ_2^r, the principal radii of curvature of the reflected wavefront, are given in [5]. For this term ρ_1^i and ρ_2^i, which are needed to determine ρ_1^r and ρ_2^r, are both equal to s^i because the field incident on the cylinder surface appears to be emanating from a source location.

The distances s^i, s_c^r and s_c^d are shown in Figure 51. It should be noted that the distances s^i, s_c^r and s_c^d which are used in this section are not equal to the distances s^i, s_c^r and s_e^d which are used for the cylinder reflected - edge diffracted field in Section 4.5.1. These distances are not the same because the reflection and diffraction points are different for the edge diffracted and the corner diffracted fields. Likewise, the direction vectors $\hat{d}_i$, $\hat{d}_j$ and $\hat{d}$ are different for this cylinder reflected - corner diffracted field than they are for the cylinder reflected - edge diffracted field defined in Section 4.5.1.

The distance parameter L_c which is used in the corner diffraction coefficient $\bar{\bar{D}}_c$ is more complicated for this cylinder reflected - corner diffracted field. The distance parameter is more complicated because the wave incident on the corner of the plate is not a spherical wave which emanates from a point source but rather resembles an astigmatic tube of rays which has two different radii of curvature. These radii of curvature are dependent on the reflected field caustic distances of the cylinder. The expression for the distance parameter L_c when the receiver is in the near zone is

$$L_c = \frac{\rho_e^i \, s_c^d}{\rho_e^i + s_c^d} \tag{4.44}$$

where ρ_e^i is the reflected field caustic defined in equation (4.33).

4.5.4 Cylinder Reflected - Corner Diffracted Field for a Far Zone Receiver

When the receiver is in the far zone, $s_c^d \rightarrow \infty$ and the terms in equation (4.43) which contain s_c^d reduce to

$$\frac{e^{-jks_c^d}}{s_c^d} \cong e^{jk[\vec{R}(Q_C)\cdot\hat{d}]} \frac{e^{-jkr}}{r} \tag{4.45}$$

where $\vec{R}(Q_C)$ is the vector position of the j^{th} corner of the i^{th} plate and $\hat{d}$ is the direction vector of the field diffracted by the plate corner. Suppressing $\frac{e^{-jkr}}{r}$ and substituting this expression in equation (4.43) provides the far zone expression for the cylinder reflected - corner diffracted field given by

$$\vec{E}_{cyl,corn}^{ref,diff} \cong \vec{E}^s \cdot \bar{\bar{\mathcal{R}}} \cdot \bar{\bar{D}}_c \sqrt{\frac{\rho_1^r \rho_2^r}{(\rho_1^r + s_c^r)(\rho_2^r + s_c^r)}} \frac{e^{-jk(s^i + s_c^r)}}{s^i} e^{jk[\vec{R}(Q_C)\cdot\hat{d}]} . \tag{4.46}$$

When the receiver is in the far zone, the distance parameter L_c in equation (4.44) reduces to

$$L_c = \rho_e^i \tag{4.47}$$

where again ρ_e^i is the reflected field caustic.

4.5.5 Ray Tracing and Shadowing Techniques for Cylinder Reflected - Edge Diffracted Field

The ray tracing algorithm used to determine the ray path for the cylinder reflected - edge diffracted field uses an iterative process to find the appropriate reflection point and diffraction point. To begin this iterative process, the j^{th} corner on the i^{th} plate is chosen as the starting diffraction point. This diffraction point is then used as a receiver location in order to find a reflection point on the k^{th} cylinder for the given incident direction $\hat{d}_i$. The method used to find this reflection point uses the exact solution defined in [13,14] because the diffraction point on the plate edge is always in the near zone of the cylinder. This reflection point is then used

as a source location in order to find a new diffraction point on the j^{th} edge of the i^{th} plate for the given receiver location. Whether the receiver is in the near zone or the far zone, this new diffraction point can be found using an exact solution. The equations which define the exact solutions derived for both a near zone and far zone receiver are given in [13,14]. Finally, this new diffraction point is used as a source location in order to find a new reflection point on the cylinder.

Once this reflection point and diffraction point are found, a check is made to determine if the ray path defined by these points satisfies both the law of reflection at the cylinder surface and the law of diffraction at the plate edge. If the ray path does not satisfy both the law of reflection and the law of diffraction, then the above process is repeated. The previous reflection point is used as a source location in order to find a new diffraction point on the plate edge. This new diffraction point is then used as a receiver location in order to find a new reflection point for the given source location. The new ray path defined by these new reflection and diffraction points is then checked to determine if both the law of reflection and the law of diffraction are satisfied. This process is repeated until the ray path is found which satisfies both the law of reflection and the law of diffraction. Then the reflection point Q_R and the diffraction point Q_E are valid and the ray tracing for this cylinder reflected - edge diffracted field is complete.

The routine which determines the diffraction point Q_E described above assumes that the plate edge is infinite. Therefore, once the diffraction point is found, it must be determined whether the point Q_E is on the finite edge of the i^{th} plate. If the diffraction point is on the finite edge, then the cylinder reflected - edge diffracted field is calculated. If the diffraction point is not on the finite edge, then the cylinder reflected - edge diffracted field does not exist and is set to zero. The corner diffracted fields are calculated whether the edge diffracted field exists or not.

The ray path for the cylinder reflected - edge diffracted field is determined from the source location, the reflection point Q_R on the k^{th} cylinder, the diffraction point Q_E on the j^{th} edge of the i^{th} plate and the receiver location. The final step is to determine if shadowing occurs for this cylinder reflected - edge diffracted ray path. If the ray path is shadowed at any point between the source and the receiver, the cylinder reflected - edge diffracted field is set to zero. The methods used to determine if a ray is shadowed or not by a plate or a cylinder are defined in [13,14] and must be used three separate times for the cylinder reflected - edge diffracted field: 1) to determine if there is shadowing between the source and reflection point Q_R on the k^{th} cylinder, 2) to determine if there is shadowing between the reflection point Q_R on the k^{th} cylinder and the diffraction point Q_E on the j^{th} edge of the i^{th} plate, and 3) to determine if there is shadowing between the diffraction point Q_E on the j^{th} edge of the i^{th} plate and the receiver.

4.5.6 Ray Tracing and Shadowing Techniques for Cylinder Reflected - Corner Diffracted Field

The ray tracing algorithm used to determine the ray path for the cylinder reflected - corner diffracted field is relatively simple. The j^{th} corner of the i^{th} plate is used as a receiver location in order to find a reflection point on the k^{th} cylinder for the given source location. The method used to find this reflection point uses the exact solution defined in [13,14] because the corner of the plate is always in the near zone of the cylinder. The reflection point Q_R and the j^{th} corner of the i^{th} plate, along with the given source and receiver locations, define the ray path for this cylinder reflected - corner diffracted field. The same procedure is then followed for the $j+1^{th}$ corner of the i^{th} plate to determine the ray path for the cylinder reflected - corner diffracted field from this corner.

The final step is to determine if shadowing occurs for the cylinder reflected - corner diffracted ray path. If the ray path is shadowed at any point between the source and the receiver, the cylinder reflected - corner diffracted field is set to zero. The methods used to determine if a ray is shadowed or not by a plate or a cylinder are defined in [13,14] and must be used three separate times for the cylinder reflected - corner diffracted field: 1) to determine if there is shadowing between the source and reflection point Q_R on the k^{th} cylinder, 2) to determine if there is shadowing between the reflection point Q_R on the k^{th} cylinder and the j^{th} corner of the i^{th} plate, and 3) to determine if there is shadowing between the j^{th} corner of the i^{th} plate and the receiver. The same procedure is then followed for the $j+1^{th}$ corner of the i^{th} plate to determine if shadowing occurs for the cylinder reflected - corner diffracted field from this corner.

4.5.7 Regions where Cylinder Reflected - Plate Diffracted Field is Not Valid

Equations (4.32) and (4.38) are valid for the cylinder reflected - edge diffracted field and equations (4.43) and (4.46) are valid for the cylinder reflected - corner diffracted fields for a receiver in the near zone and the far zone, respectively, except when the cylinder reflected ray is in the transition region of the k^{th} cylinder. The problem arises because UTD assumes that the incident wavefront at the diffraction point is in the form of a ray optical field. In the transition region of the cylinder, the true representation of the reflected field is much more complicated and is not a true ray optical field. Therefore, the incident field at the diffraction point on the i^{th} plate is not ray optical and equations (4.32), (4.38), (4.43) and (4.46) are not completely valid. However, it can again be assumed that the fields in the transition region will give a reasonable engineering representation for the field in any event. In practice these approximations appear to give useable answers to this

complicated problem, since the regions in which they are not valid are rather small in extent.

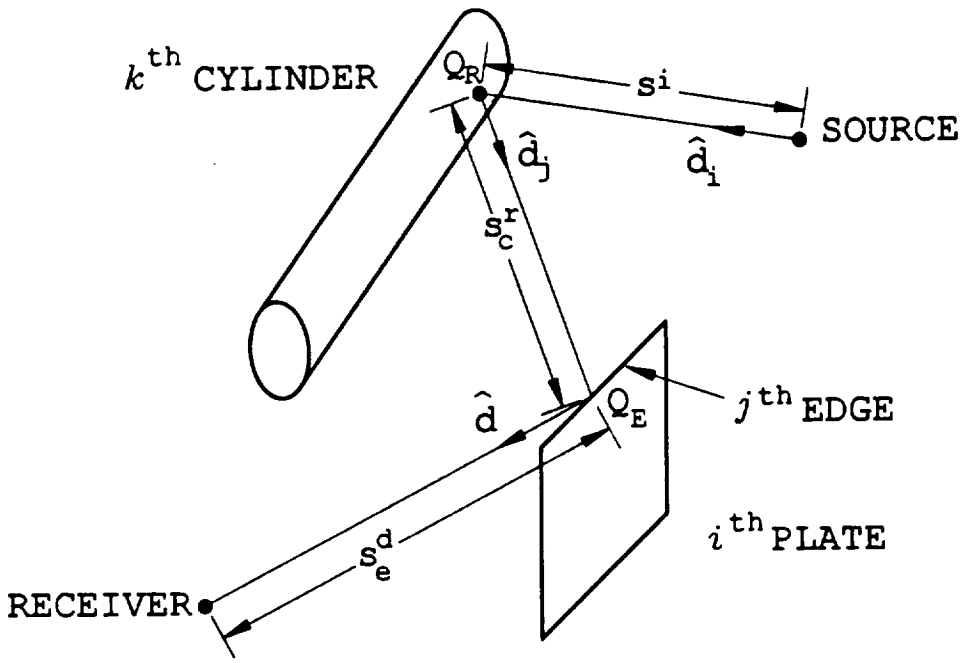

Figure 50: Illustration of cylinder reflected - edge diffracted field

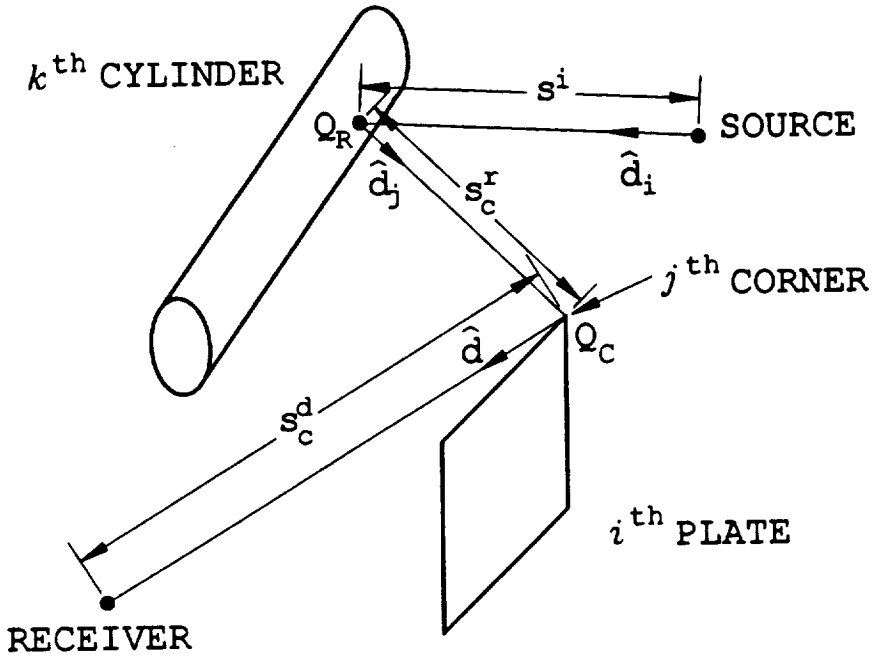

Figure 51: Illustration of cylinder reflected - corner diffracted field

Chapter 5

Aircraft Model Validation

5.1 Introduction

In this chapter the improved NEC-BSC, which includes the plate - cylinder interactions defined in the previous chapter, is used to validate the cylindrical aircraft model investigated in Chapter 3. The validation process includes a sensitivity study to ensure that the aircraft model contains the basic structural features essential to the radiation patterns and an antenna location study to ensure that the aircraft model is valid for different antenna locations. The NEC-BSC calculated patterns in this chapter are compared to measurements conducted by Boeing on a 1/17 scale model of the P-3C aircraft [11] and by Lockheed on a 1/10 scale model of the P-3C aircraft [16]. These patterns are compared for both right hand and left hand circular polarizations in the roll plane, the elevation plane, the azimuth plane and conical cuts from 10° to 30° above the horizon for the various studies performed in this chapter unless noted otherwise.

Section 5.2 compares the improved NEC-BSC calculated patterns for the cylindrical aircraft model with the primary antenna location to the measured patterns provided by Boeing and to the NEC-BSC Version 3.1 calculated patterns. In Section 5.3 a sensitivity study is done on the cylindrical aircraft model to ensure that the basic structural features of the aircraft which are essential to the radiation patterns are included. Sections 5.4 and 5.5 compare the NEC-BSC calculated patterns

for the cylindrical aircraft model to the measured results provided by Lockheed and Boeing, respectively, for two different antenna locations. Section 5.6 summarizes the work done in this chapter and comments on the NEC-BSC model representation of the P-3C aircraft.

5.2 Comparison of Improved NEC-BSC Results with Boeing Results for Primary Antenna Location

In this section, the results computed with the improved NEC-BSC for the antenna location studied in Chapter 3 are compared to the measured results provided by Boeing and to the original Version 3.1 NEC-BSC calculated patterns from Section 3.3.1. The cylindrical aircraft model illustrated in Figure 19 is used in the NEC-BSC. The results at 300 MHz for the right hand circular polarized or co-polarized fields are compared for the roll plane in Figure 52, for the elevation plane in Figure 53, for the azimuth plane in Figure 54 and for the conical planes 10°, 20° and 30° above the horizon in Figures 55, 56 and 57, respectively. For completeness, the left hand circular polarized or cross-polarized results are also included. These cross-polarized results are shown for the roll plane in Figure 58, for the elevation plane in Figure 59, for the azimuth plane in Figure 60 and for the conical planes 10°, 20° and 30° above the horizon in Figures 61, 62 and 63, respectively.

The roll plane results for the co-polarized field shown in Figure 52 indicate that the results calculated using the improved version of the NEC-BSC agree with the measured results to within 1–2 dB throughout the pattern. Comparing the co-polarized elevation plane results in Figure 53 shows that the improved NEC-BSC results and the measured results agree to within 1–3 dB throughout the complete pattern except in the region on the horizon near the tail of the aircraft where the

calculated levels increase to as much as 8 dB higher than the measured levels. Comparing the co-polarized results for the azimuth plane in Figure 54 shows that the agreement between the improved NEC-BSC results and the measured results is within 1–2 dB throughout the complete pattern except in the 45° region directly off the nose of the aircraft where the calculated levels increase to as much as 5–8 dB higher than the measured levels. Comparing the co-polarized results for the conical planes in Figures 55, 56 and 57 shows that the agreement between the improved NEC-BSC results and the measured results is within 1–2 dB throughout the majority of the pattern for all three conic cuts taken. Therefore, the higher levels which are seen in the horizon near the nose and the tail of the aircraft disappear as the pattern cut is taken slightly above the horizon.

Comparing the co-polarized results obtained using the improved NEC-BSC with the results obtained using Version 3.1 of the NEC-BSC shows that the plate - cylinder interactions which are implemented in the NEC-BSC improve the agreement between the calculated and measured patterns. The improvement is most noticeable in the horizon of the aircraft in the regions off the nose and the tail where the calculated radiation levels are reduced to levels which are much closer to the measured levels. Although the calculated levels are still 5–8 dB higher than the measured levels in a few small regions, these improved calculated patterns very closely model the measured patterns on the whole.

Comparing the co-polarized results in this section with the results obtained using the simulated plate - cylinder fields in Section 3.5.1 shows that the simulated plate - cylinder fields give an accurate representation of the actual plate - cylinder fields defined in Chapter 4. Because the simulated plate - cylinder terms accurately represent the actual plate - cylinder terms, the analogy can be made that the simulated plate - ellipsoid and plate - cone frustum fields which are implemented in Sections 3.5.2 and 3.5.3, respectively, are accurate representations of the actual

plate - ellipsoid and plate - cone frustum fields which have not been implemented in the NEC-BSC at this time. The radiation patterns in Section 3.5 show that the cylindrical aircraft model is more accurate than the composite ellipsoid model and the cone frustum model when the imaging technique is used. Therefore, the conclusion can be made that the cylindrical aircraft model is more accurate when using the improved NEC-BSC than the composite ellipsoid model and the cone frustum model would be even if the plate - ellipsoid and plate - cone frustum fields are implemented in the code.

The cross-polarized results are shown in Figures 58 through 63. These figures show that the agreement between the calculated and measured results for the cross-polarized fields is not as good as the agreement found for the co-polarized fields. This difference between the calculated and measured results partly occurs because the cross-polarized radiation levels are lower than the co-polarized radiation levels. Therefore, higher order terms which do not have a noticeable effect on the co-polarized field can have a significant effect on the cross-polarized field. Because these higher order terms are not practical to implement in the NEC-BSC at this time, the calculated cross-polarized results are not as accurate as the co-polarized results. Another reason for the difference between the calculated and measured cross-polarized results could be due to the inaccuracy of the Boeing cross-polarized measurements. The cross-polarized results provided by Lockheed for a similar antenna location are given in Section 5.4 and are in better agreement with the calculated results, therefore, the accuracy of the Boeing cross-polarized measurements must be questioned. However, the primary emphasis of this report is on the co-polarized results so the accuracy of the cross-polarized results is not critical. These cross-polarized results are included only to provide additional information.

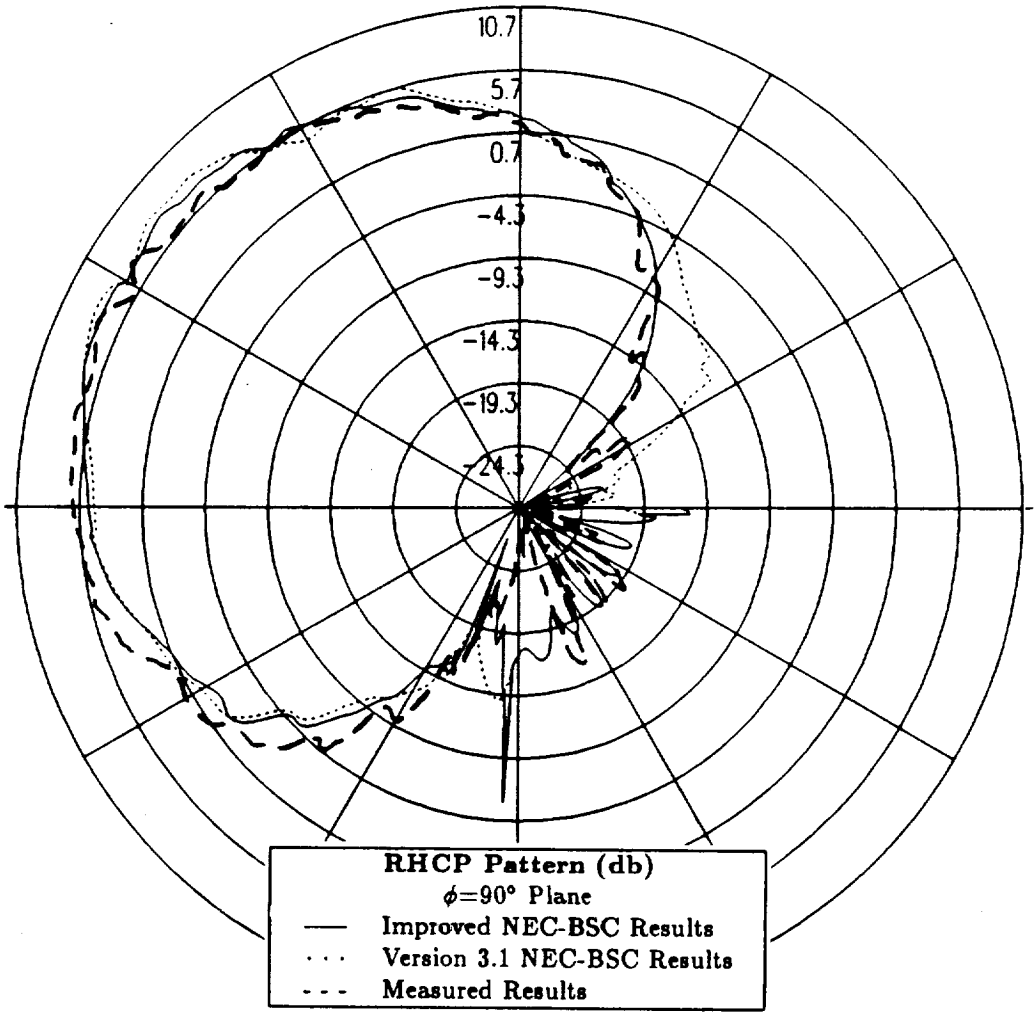

Figure 52: Roll plane pattern for primary antenna location in Boeing report for right hand circular polarization at 300 MHz.

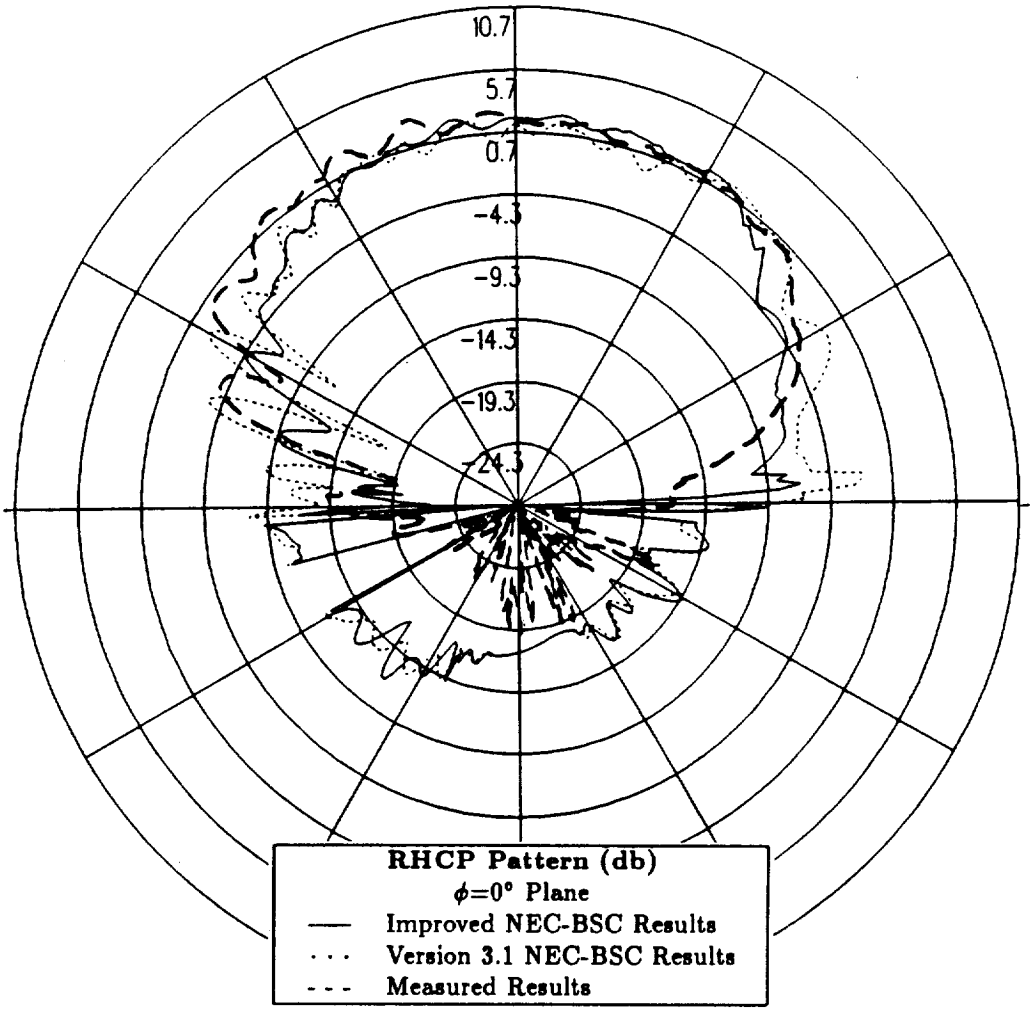

Figure 53: Elevation plane pattern for primary antenna location in Boeing report for right hand circular polarization at 300 MHz.

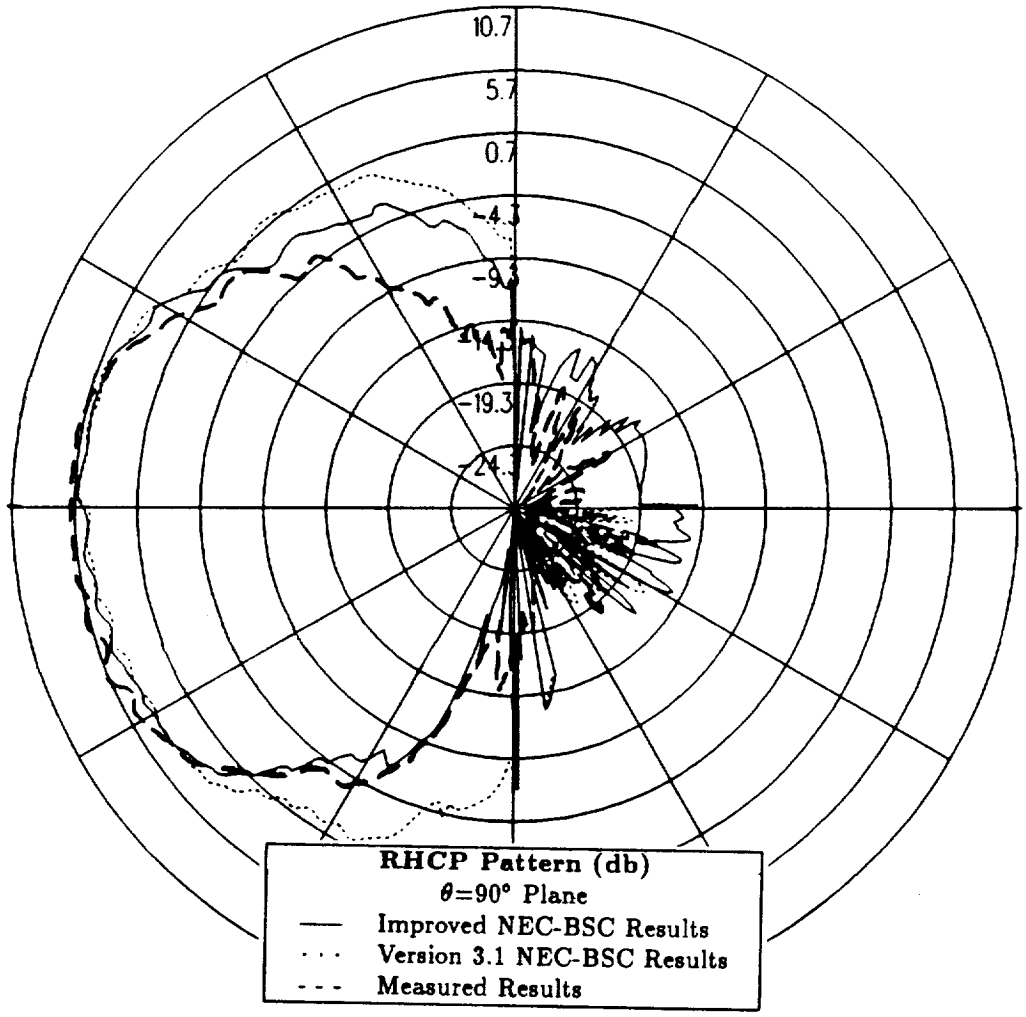

Figure 54: Azimuth plane pattern for primary antenna location in Boeing report for right hand circular polarization at 300 MHz.

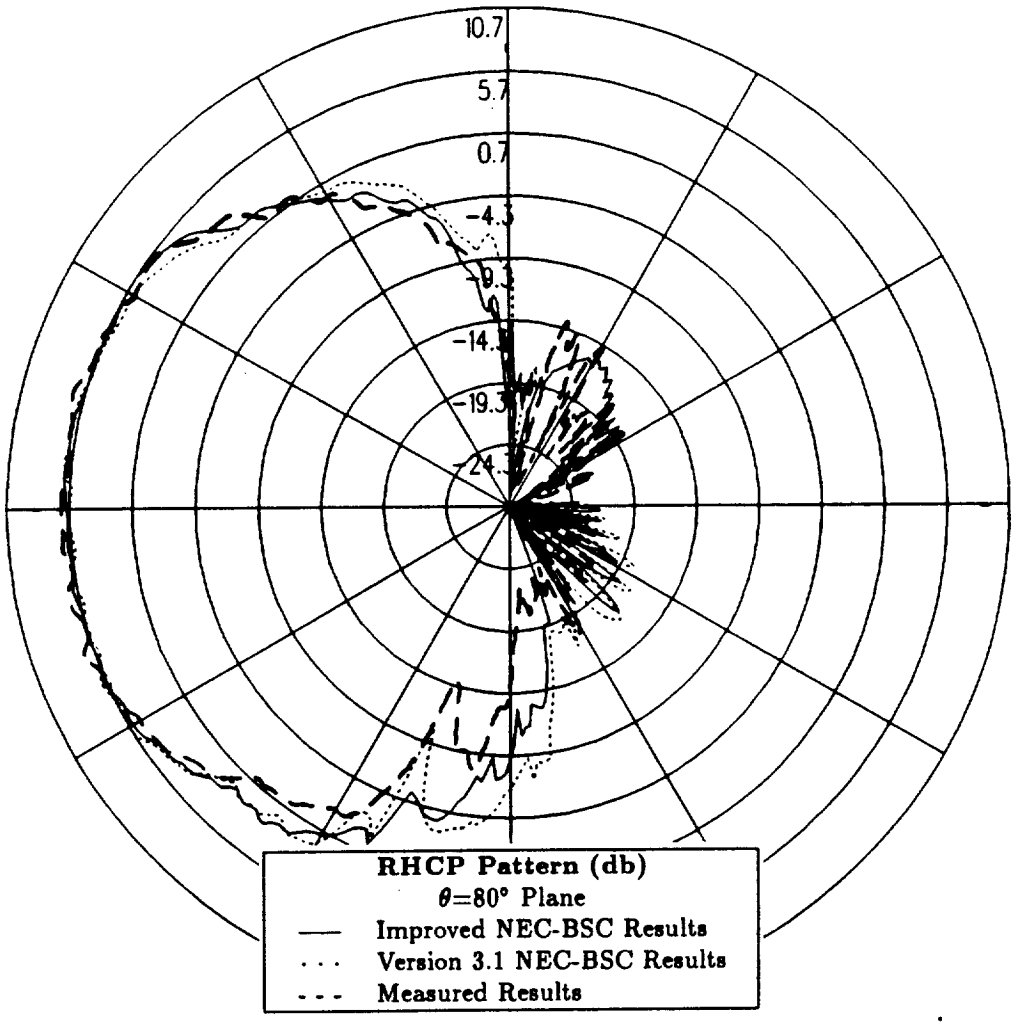

Figure 55: Conical plane pattern 10° above the horizon for primary antenna location in Boeing report for right hand circular polarization at 300 MHz.

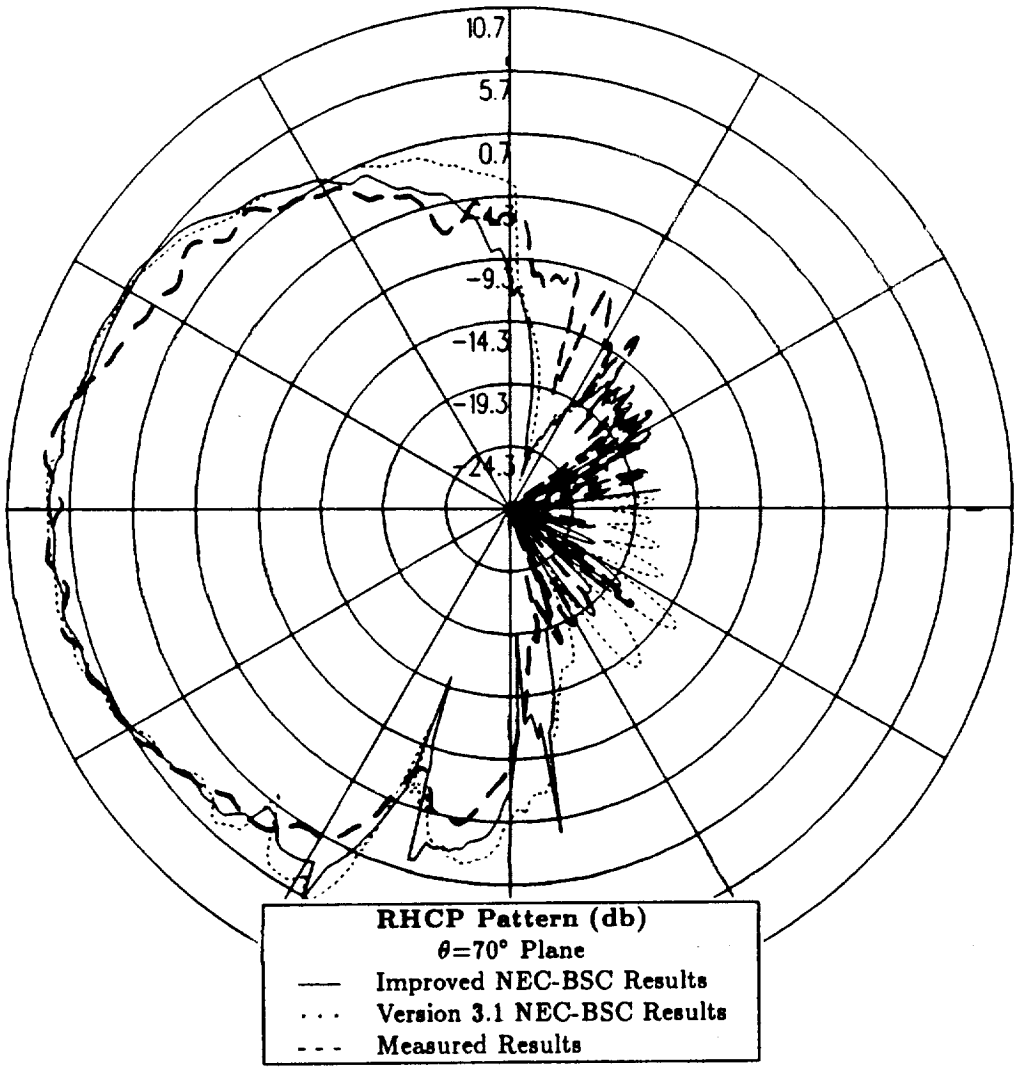

Figure 56: Conical plane pattern 20° above the horizon for primary antenna location in Boeing report for right hand circular polarization at 300 MHz.

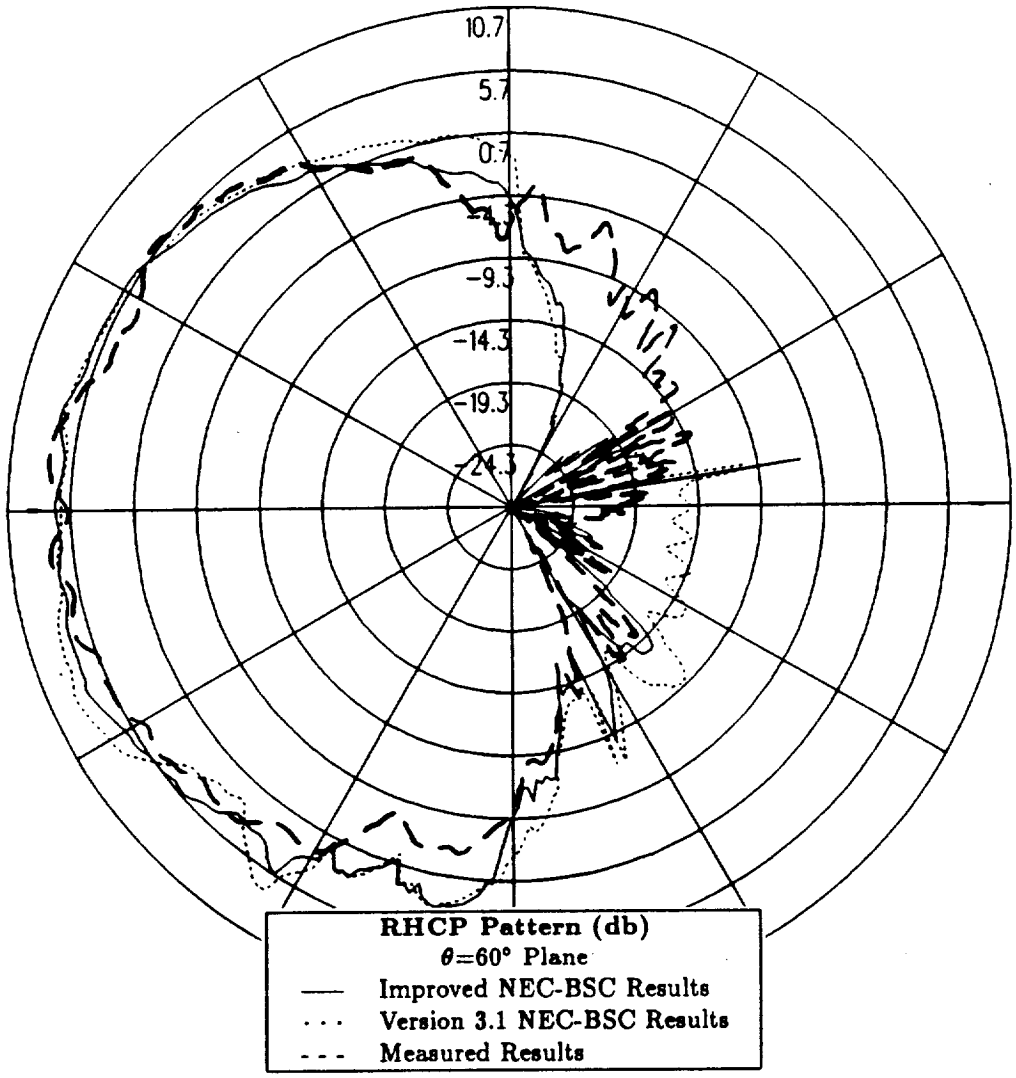

Figure 57: Conical plane pattern 30° above the horizon for primary antenna location in Boeing report for right hand circular polarization at 300 MHz.

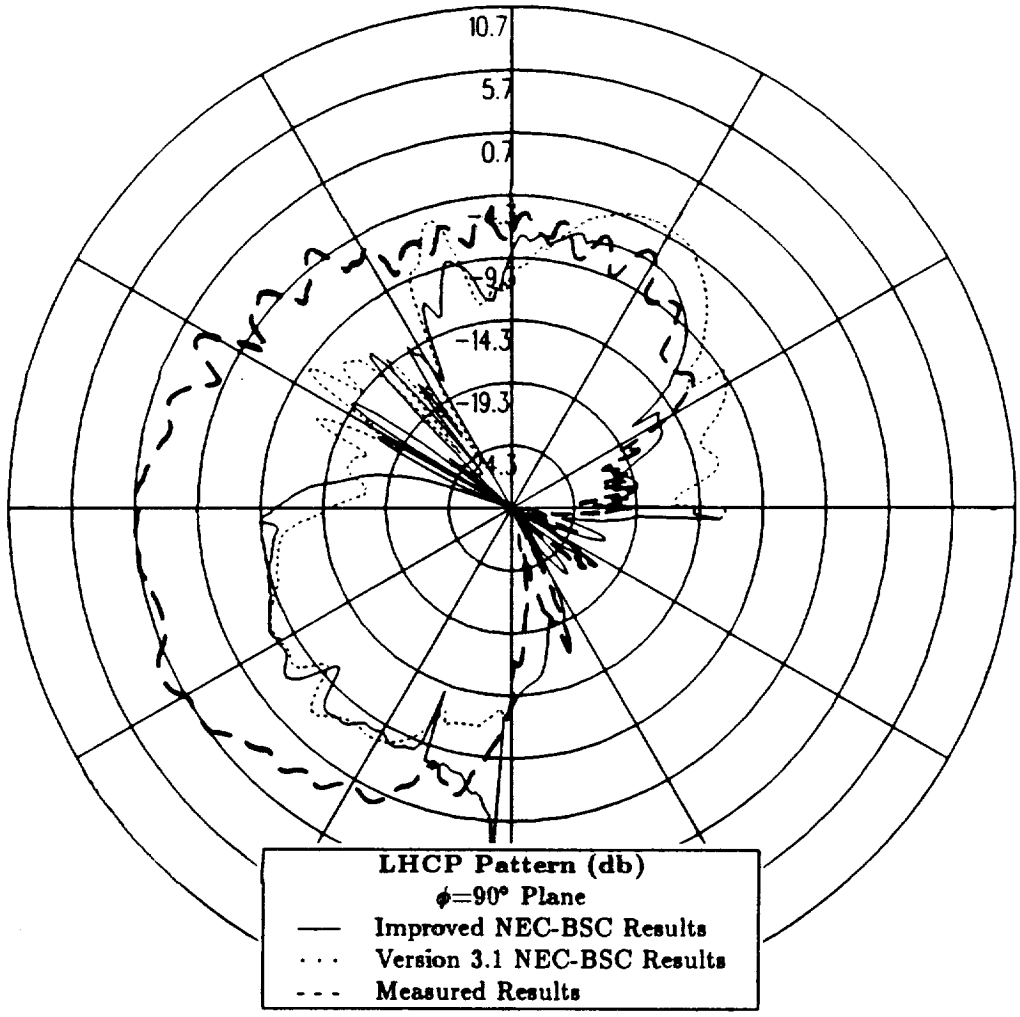

Figure 58: Roll plane pattern for primary antenna location in Boeing report for left hand circular polarization at 300 MHz.

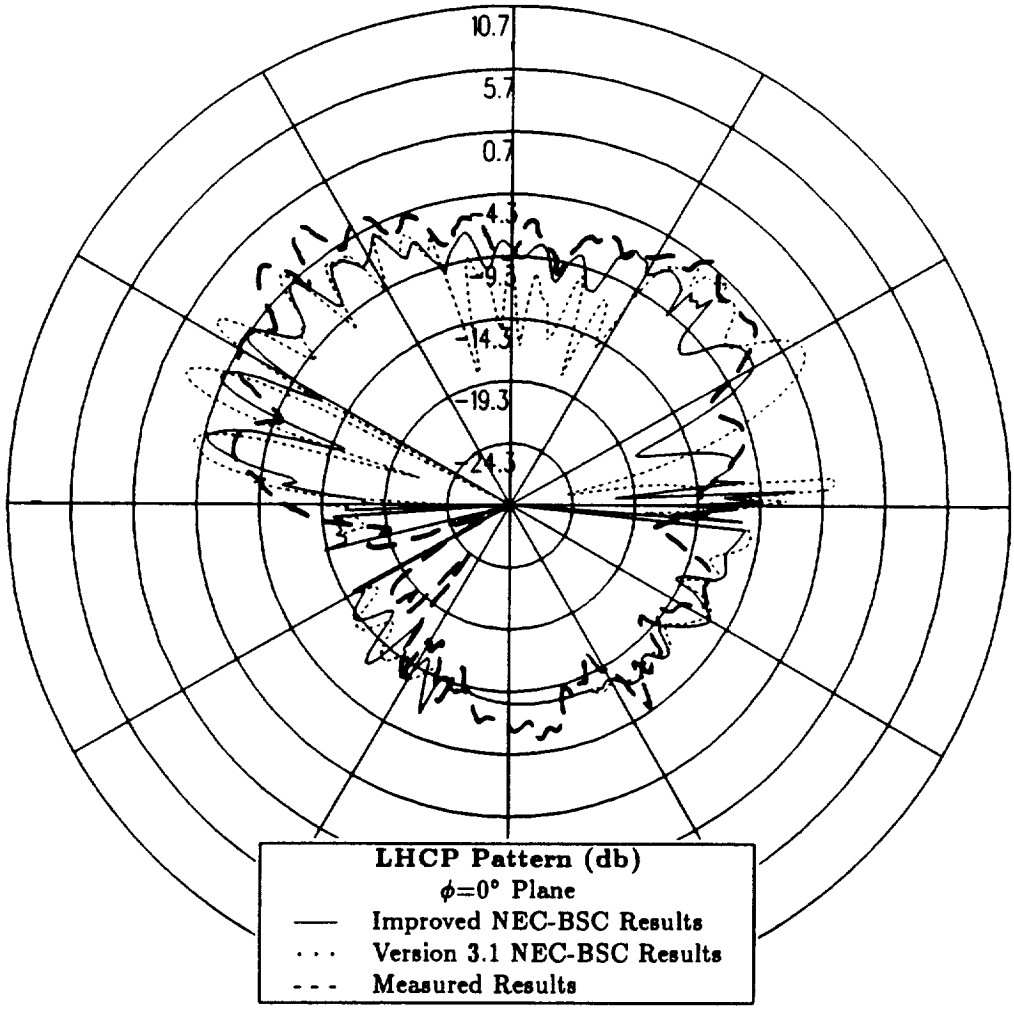

Figure 59: Elevation plane pattern for primary antenna location in Boeing report for left hand circular polarization at 300 MHz.

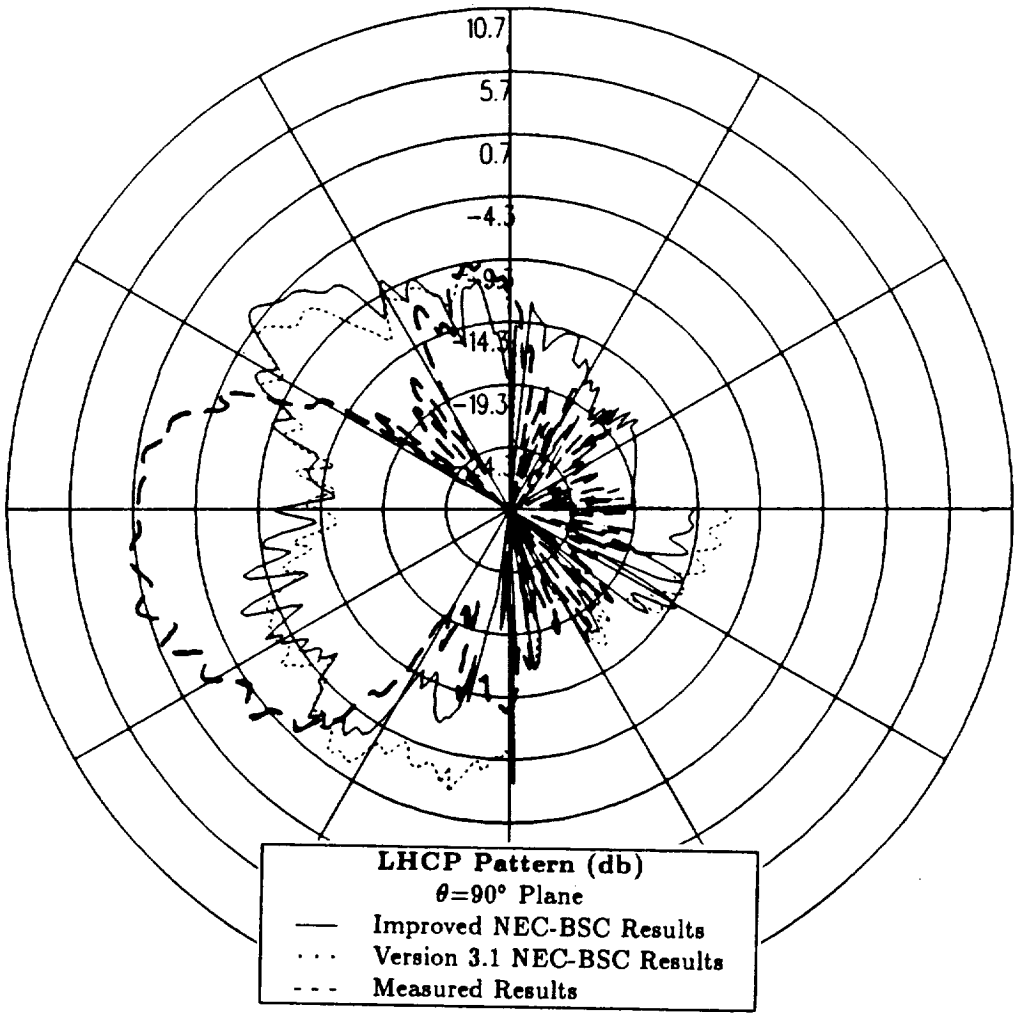

Figure 60: Azimuth plane pattern for primary antenna location in Boeing report for left hand circular polarization at 300 MHz.

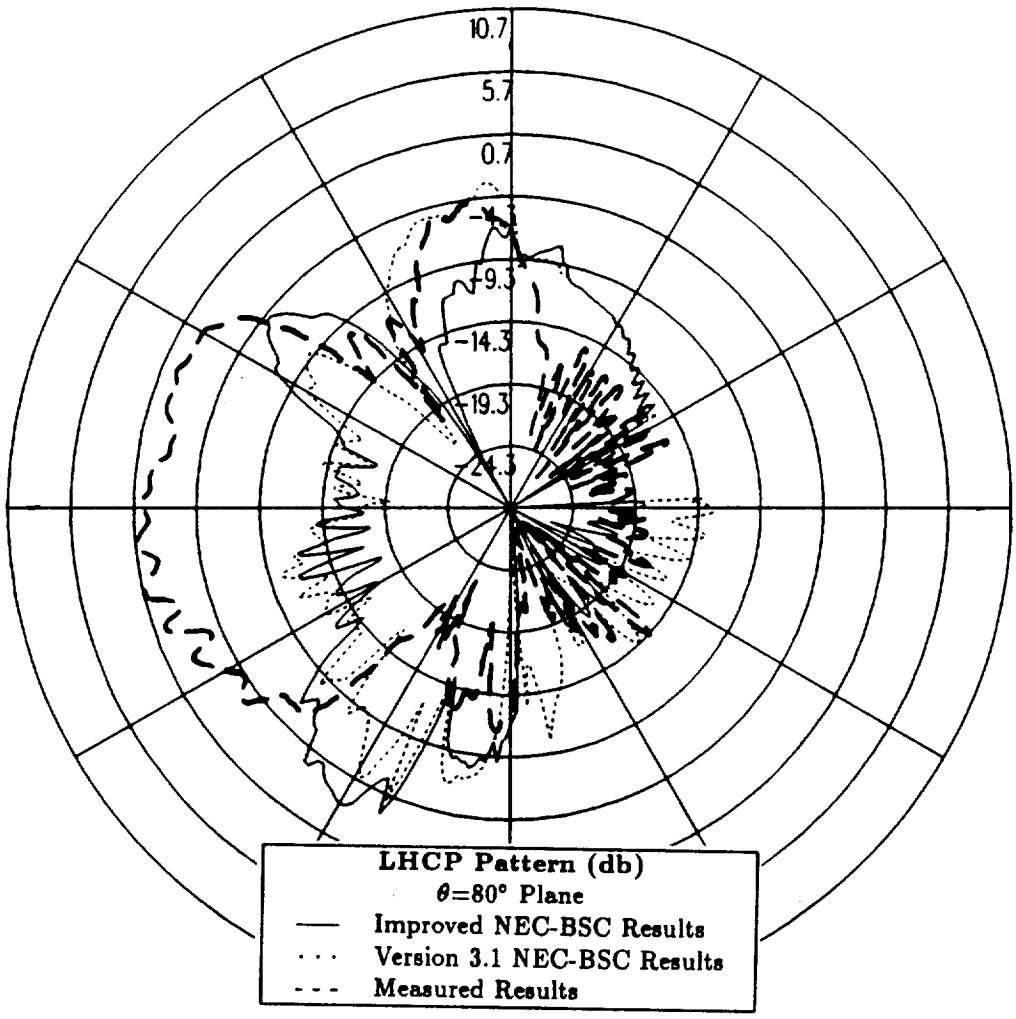

Figure 61: Conical plane pattern 10° above the horizon for primary antenna location in Boeing report for left hand circular polarization at 300 MHz.

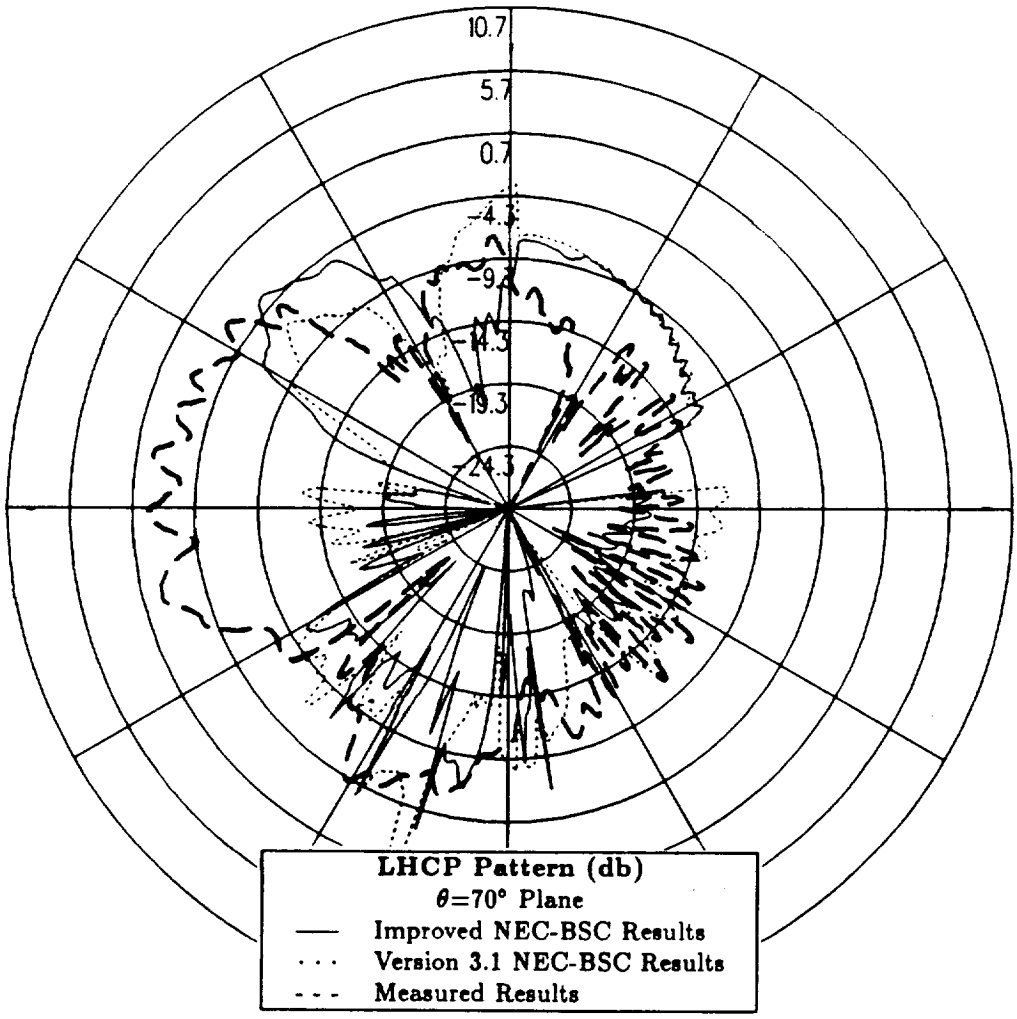

Figure 62: Conical plane pattern 20° above the horizon for primary antenna location in Boeing report for left hand circular polarization at 300 MHz.

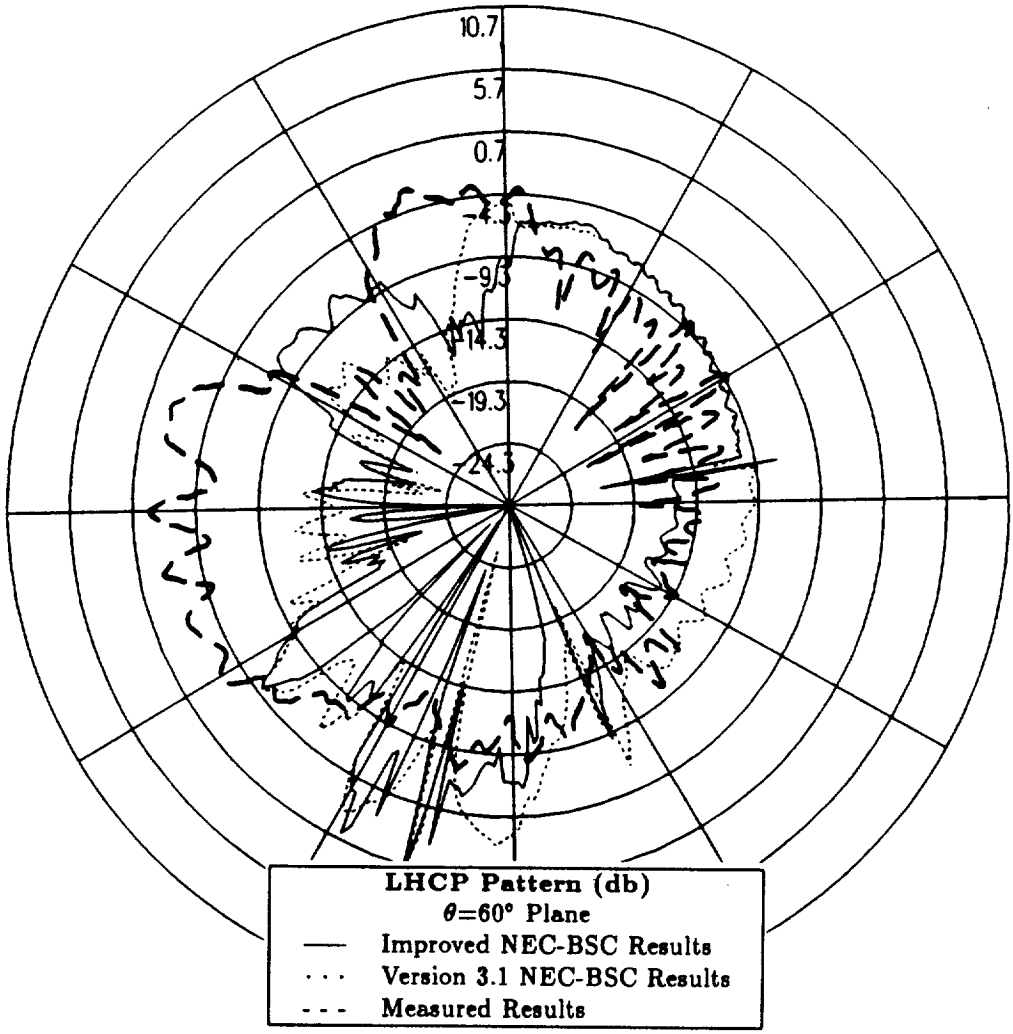

Figure 63: Conical plane pattern 30° above the horizon for primary antenna location in Boeing report for left hand circular polarization at 300 MHz.

5.3 Sensitivity Study for Cylindrical Aircraft Model using Improved NEC-BSC

In this section a sensitivity study is done on the cylindrical aircraft model to ensure that the basic structural features of the aircraft which are essential to the radiation patterns are included. The previous section illustrated that the radiation patterns calculated using the improved NEC-BSC with the cylindrical aircraft model provide excellent agreement with the scale model measurements of the actual P-3 aircraft throughout the majority of the patterns investigated. The sole exception is in the horizon of the aircraft near the nose and the tail where the calculated levels are higher than the measured levels. Therefore, this sensitivity study investigates additional structural features of the aircraft which may improve the agreement between the calculated and measured results in these areas of the radiation patterns.

Experience with the modeling capabilities of the NEC-BSC has shown that the model only needs to match the real scattering object near the antenna and in the general proximity of the pattern cut desired. For the cylindrical aircraft model and the antenna location illustrated in Figure 19, the most important structural feature which affects the radiation pattern in the horizon of the aircraft is the aircraft wing. Three separate tests are run to investigate a more accurate way to model the aircraft wing. First, models for the aircraft engines and propeller blades are added to the previous aircraft model to observe the effect on the radiation patterns. The second test involves tilting the front edge of the wings up in order to more closely model the actual wing surface and observe its effect on the radiation patterns. Finally, the double diffracted fields which result from the edges of the wing are added to the radiation pattern to see its effect.

5.3.1 Cylindrical Aircraft Model with Detailed Engine Models

The original cylindrical aircraft model investigated in Chapter 3 does not include structures which represent the engines or the propeller blades on the actual P-3C aircraft. In this section models for both engines and the propeller blades are included on the side of the aircraft which contains the antenna. The improved NEC-BSC is then used to see the effect which the engine models have on the radiation patterns especially in the horizon of the aircraft in the regions near the nose and the tail. If the agreement between the calculated and measured results is improved, then the engine models are essential to the radiation patterns and must be included in the aircraft model.

The cylindrical aircraft model which includes the detailed engine models used in the NEC-BSC for this sensitivity study is illustrated in Figure 64. The results at 300 MHz for the right hand circular polarized or co-polarized fields are compared for the roll plane in Figure 65, for the elevation plane in Figure 66, for the azimuth plane in Figure 67 and for the conical planes 10°, 20° and 30° above the horizon in Figures 68, 69 and 70, respectively. Because the co-polarized results are of primary importance in this report, the left hand circular polarized or cross-polarized results are not included in this sensitivity study.

The roll plane results shown in Figure 65 indicate that the calculated pattern for the detailed model of the aircraft compares very well to both the calculated pattern for the simple aircraft model and the measured pattern. Therefore, the engine models have very little effect in this pattern cut. Comparing the elevation plane results in Figure 66 indicates that the calculated pattern for the detailed model of the aircraft compares very well to the calculated pattern for the simple aircraft model. Therefore, the calculated results and the measured results agree to within 1–3 dB throughout the complete pattern except in the region on the

horizon near the tail of the aircraft where the calculated levels increase to as much as 8 dB higher than the measured levels.

Comparing the azimuth plane results in Figure 67 shows that the engine models affect the results in this pattern cut especially near the nose and the tail of the aircraft. The calculated pattern for the detailed aircraft model contains spikes in these areas which are caused by the presence of the engines. These spikes are present because the engines cannot be accurately modeled using the simple building blocks in the NEC-BSC. The most accurate method of interpreting the pattern in the areas where the spikes are present is to take the average in these areas. If this is done, the calculated pattern for the detailed aircraft model compares very well to the calculated pattern for the simple aircraft model except in the region near the nose where the levels for the detailed model may be 1–2 dB lower than the levels for the simple model. Comparing the results for the conical planes in Figures 68, 69 and 70 shows that the calculated pattern for the detailed aircraft model agrees to within 1–3 dB to both the calculated pattern for the simple aircraft model and the measured pattern. Therefore, the spikes which are present in the horizon of the aircraft due to the presence of the engines begin to disappear as the pattern cut is taken slightly above the horizon.

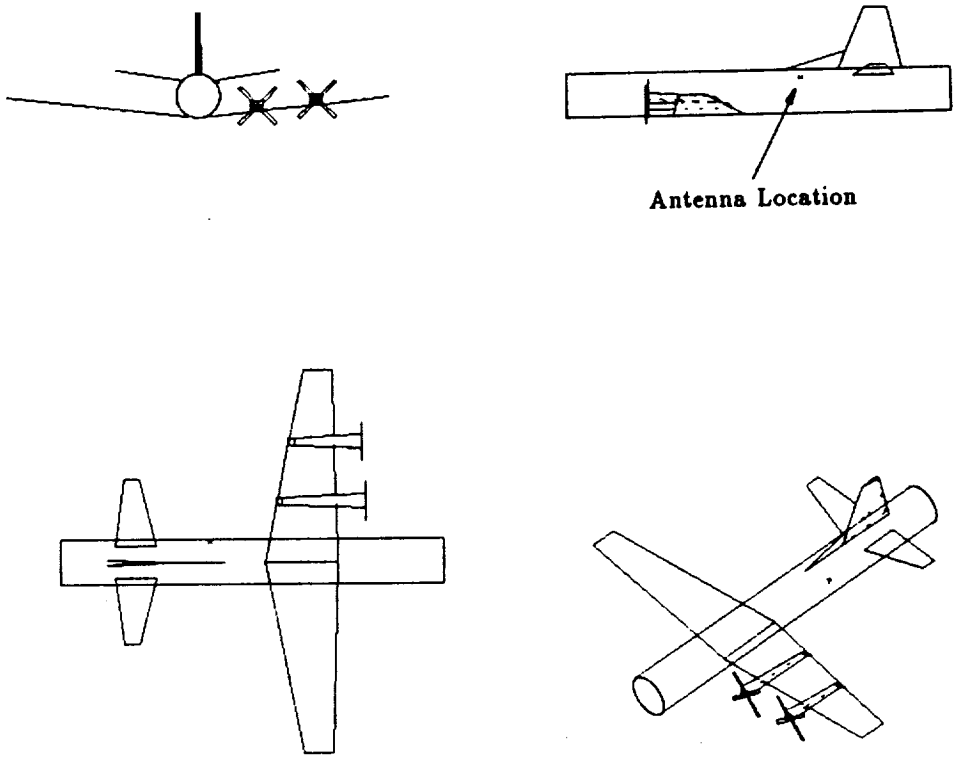

Figure 64: Geometry of the cylindrical model of the P-3C aircraft which includes the detailed engine models used in the NEC-BSC showing the primary Boeing antenna location.

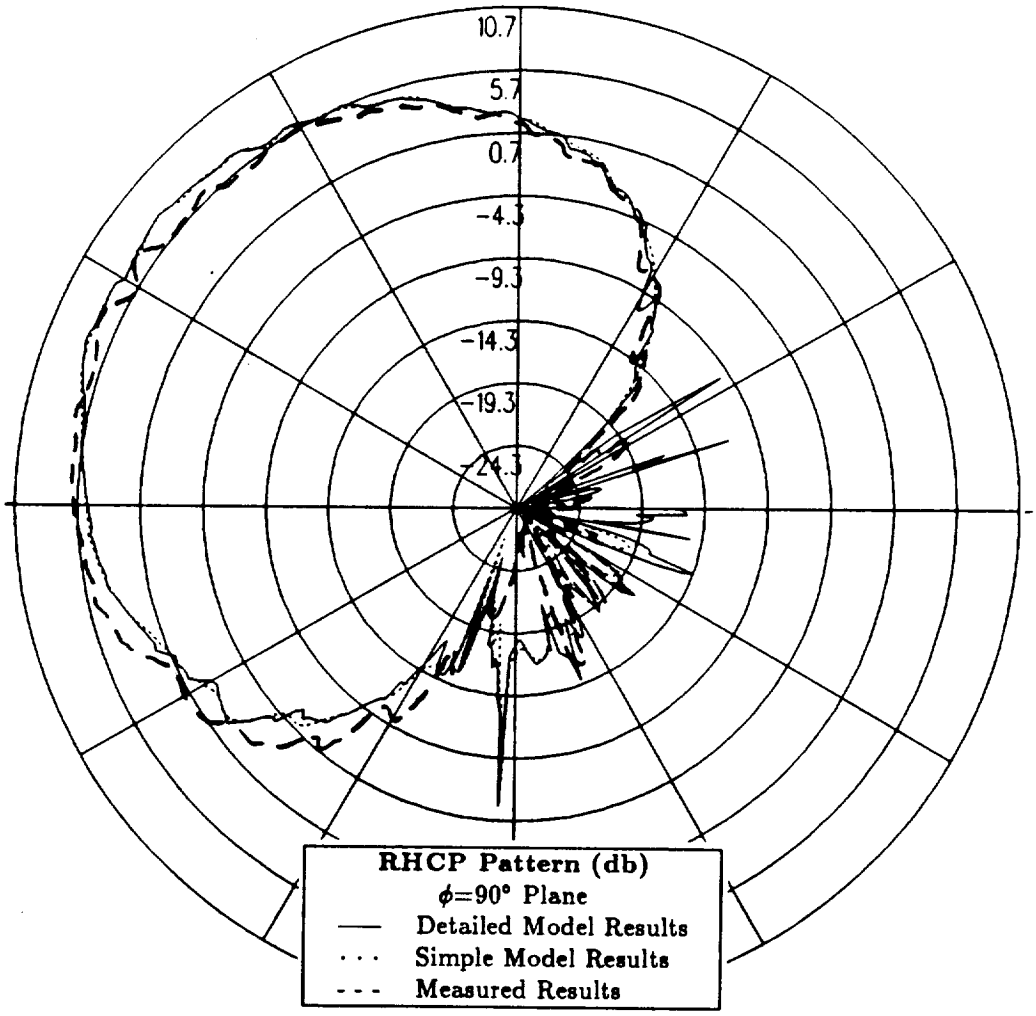

Figure 65: Roll plane pattern using aircraft model which includes detailed engine models for primary antenna location in Boeing report for right hand circular polarization at 300 MHz.

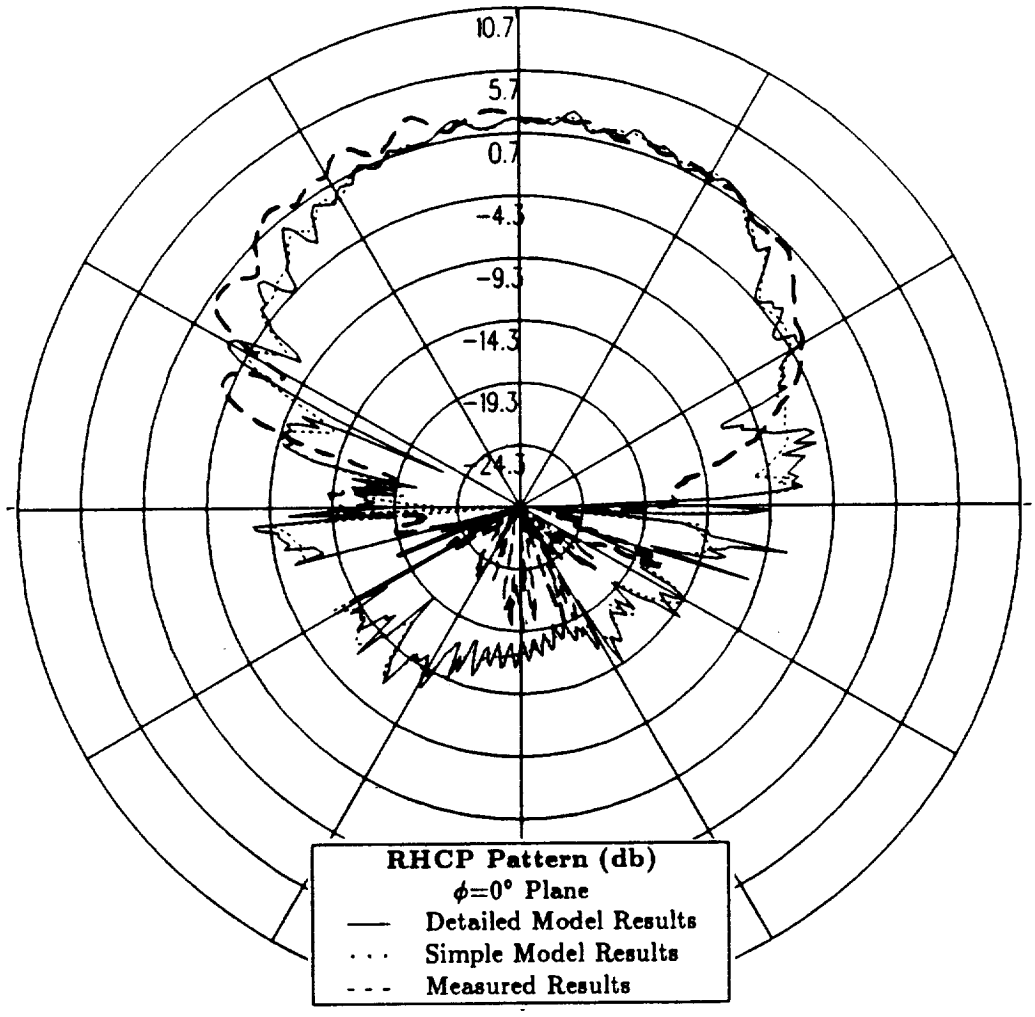

Figure 66: Elevation plane pattern using aircraft model which includes detailed engine models for primary antenna location in Boeing report for right hand circular polarization at 300 MHz.

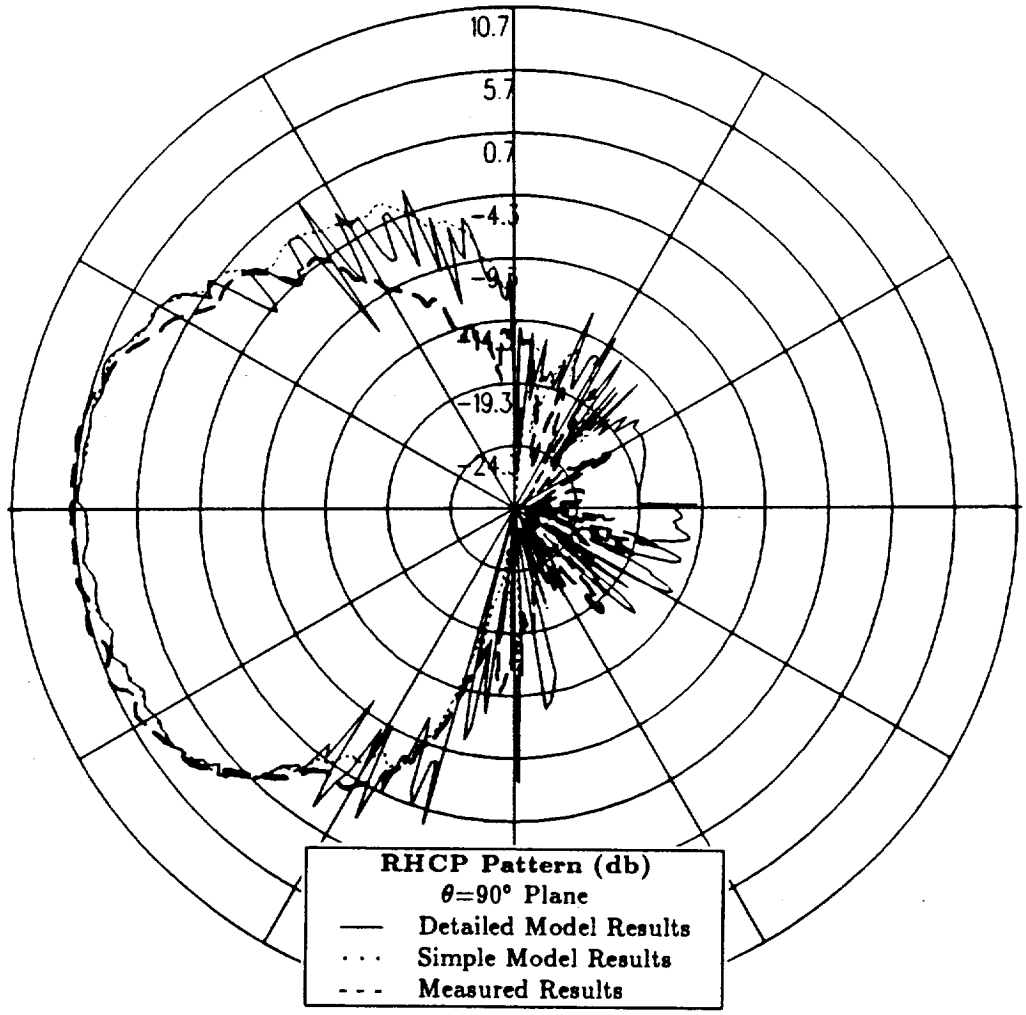

Figure 67: Azimuth plane pattern using aircraft model which includes detailed engine models for primary antenna location in Boeing report for right hand circular polarization at 300 MHz.

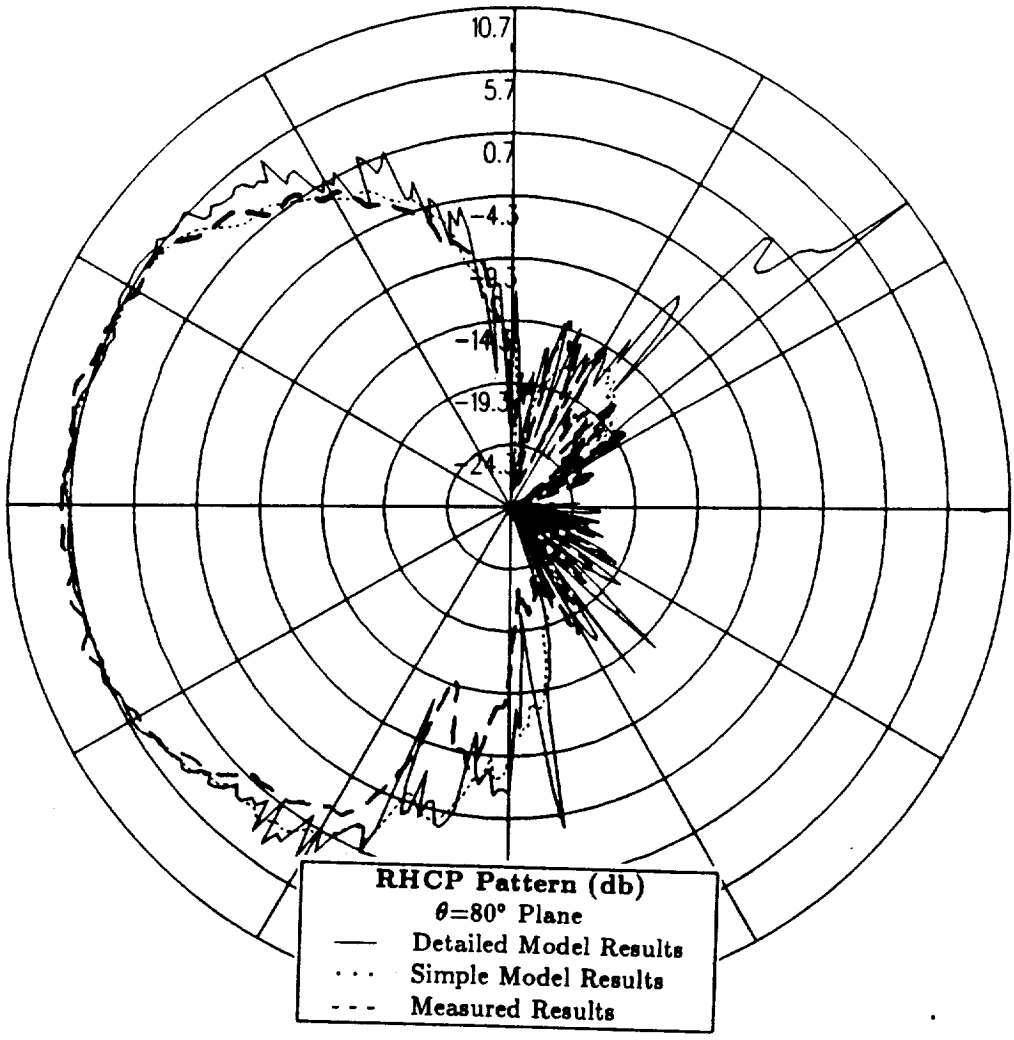

Figure 68: Conical plane pattern 10° above the horizon using aircraft model which includes detailed engine models for primary antenna location in Boeing report for right hand circular polarization at 300 MHz.

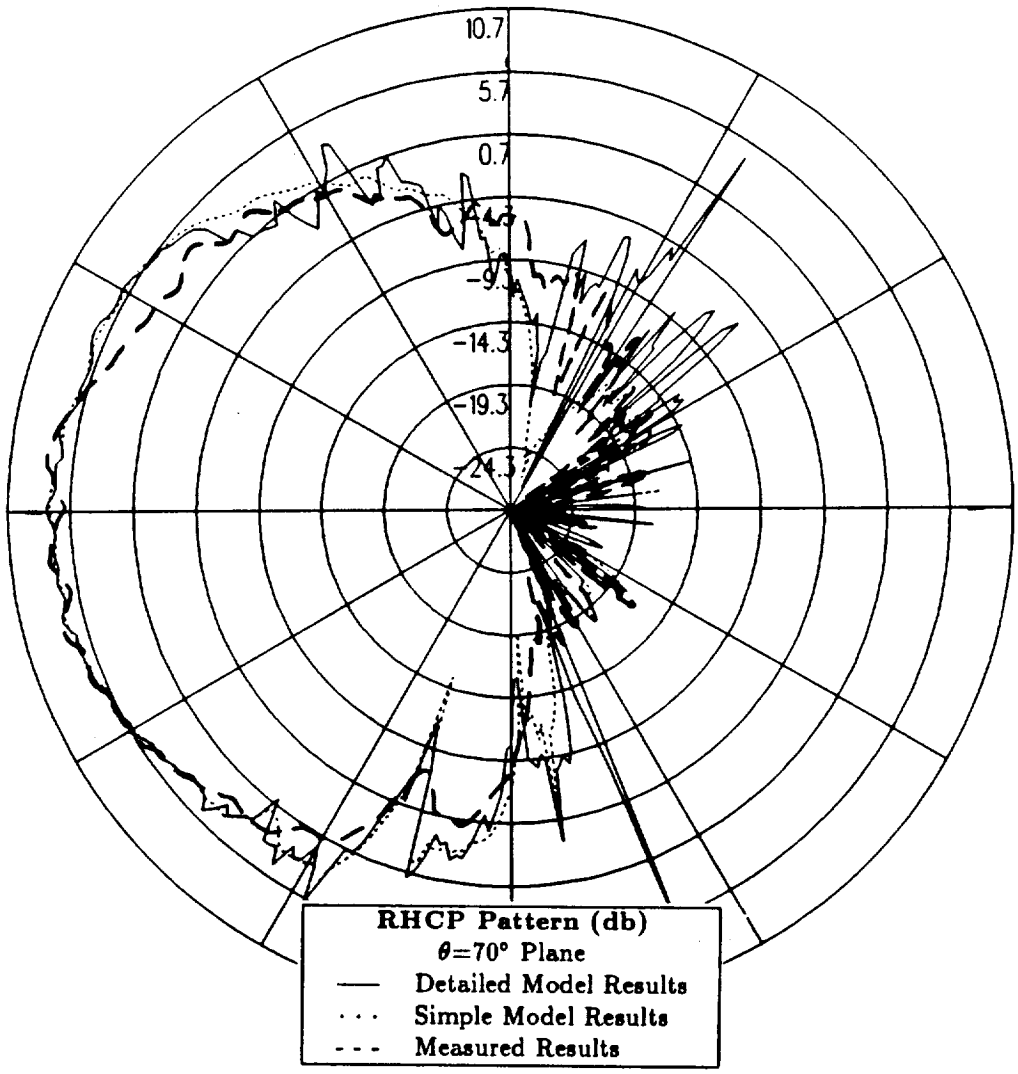

Figure 69: Conical plane pattern 20° above the horizon using aircraft model which includes detailed engine models for primary antenna location in Boeing report for right hand circular polarization at 300 MHz.

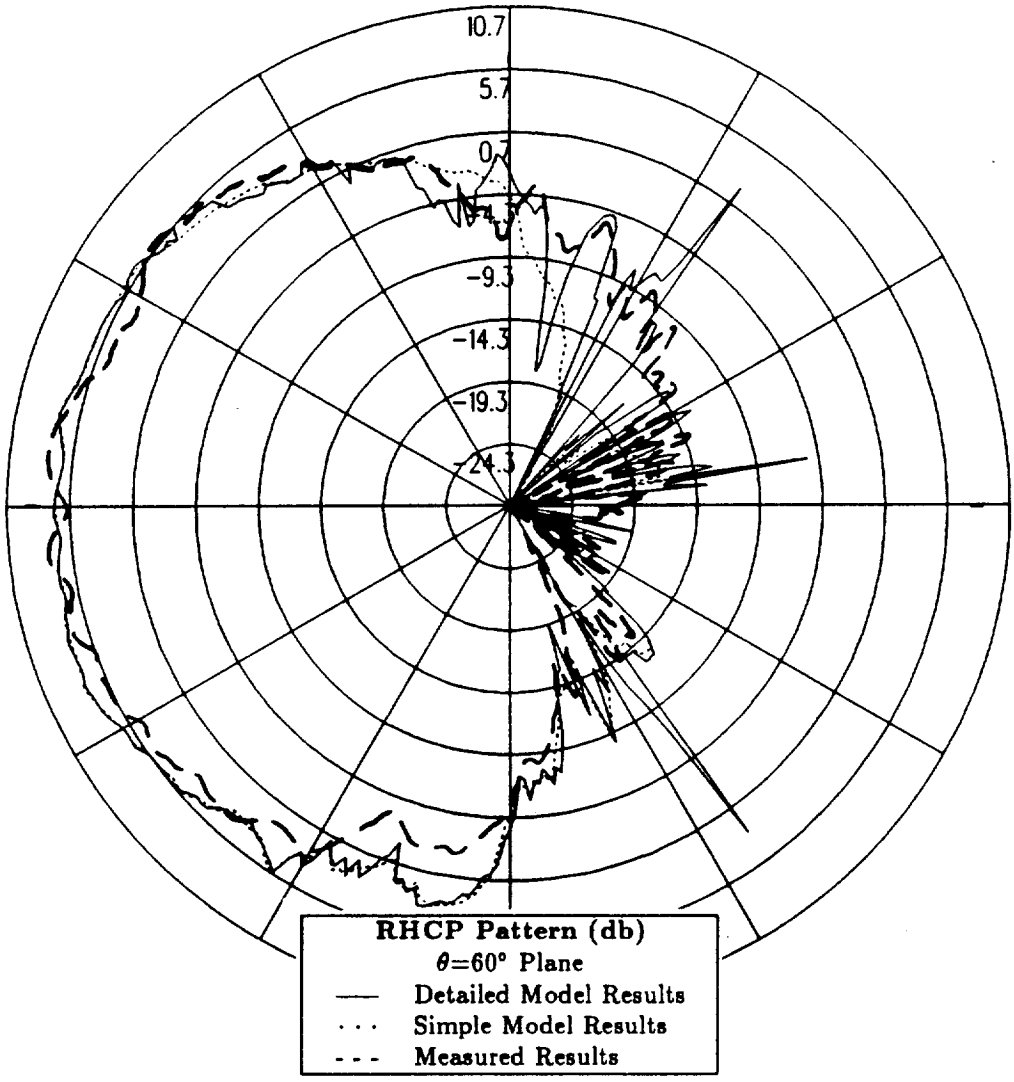

Figure 70: Conical plane pattern 30° above the horizon using aircraft model which includes detailed engine models for primary antenna location in Boeing report for right hand circular polarization at 300 MHz.

5.3.2 Cylindrical Aircraft Model with Tilted Wings

The wing surfaces on the actual P-3C aircraft are not flat as depicted in the original cylindrical aircraft model investigated in Chapter 3 but rather are convex surfaces. In this section the front edge of the wings are tilted up 5° in order to more accurately model the convex surface of the wings. The improved NEC-BSC is then used to see the effect which the tilted wings have on the radiation patterns especially in the horizon of the aircraft in the regions near the nose and the tail. If the agreement between the calculated and measured results is improved, then the tilted wings are essential to the radiation patterns and must be incorporated in the aircraft model.

The cylindrical aircraft model which includes the tilted wings used in the NEC-BSC for this sensitivity study is illustrated in Figure 71. The results at 300 MHz for the right hand circular polarized or co-polarized fields are compared for the roll plane in Figure 72, for the elevation plane in Figure 73, for the azimuth plane in Figure 74 and for the conical planes 10°, 20° and 30° above the horizon in Figures 75, 76 and 77, respectively. Because the co-polarized results are of primary importance in this report, the left hand circular polarized or cross-polarized results are not included in this sensitivity study.

The roll plane results shown in Figure 72 indicate that the calculated pattern for the aircraft model with tilted wings compares very well to both the calculated pattern for the original aircraft model with flat wings and the measured pattern. Comparing the elevation plane results in Figure 73 indicates that the calculated pattern for the aircraft model with the tilted wings compares very well to the calculated pattern for the aircraft model with flat wings. Therefore, the tilt of the wings has very little effect in either of these pattern cuts. Comparing the azimuth plane results in Figure 74 shows that the tilt of the wings does have a

small effect on the results in this pattern cut in the 45° region directly off the nose of the aircraft where the calculated levels are reduced by approximately 1 dB. Comparing the results for the conical planes in Figures 75, 76 and 77 shows that the calculated pattern for the aircraft model with tilted wings compares very well to both the calculated pattern for the aircraft model with flat wings and the measured pattern. Therefore, the slightly lower levels which are present in the horizon of the aircraft due to the tilt of the wings disappear as the pattern cut is taken slightly above the horizon.

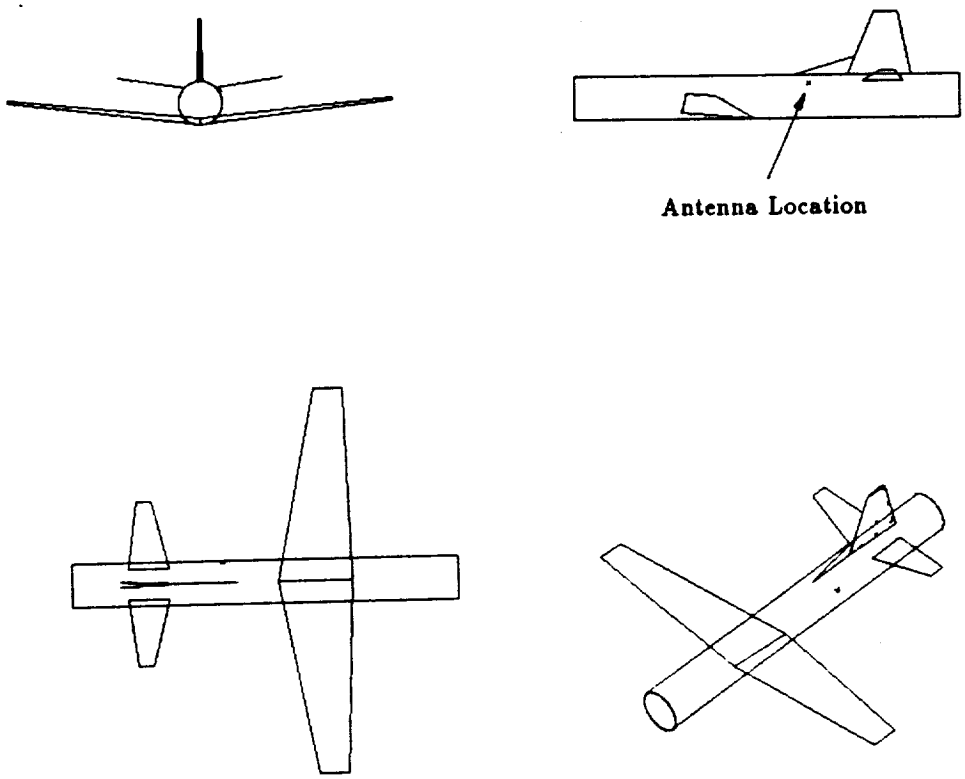

Figure 71: Geometry of the cylindrical model of the P-3C aircraft with tilted wings used in the NEC-BSC showing the primary Boeing antenna location.

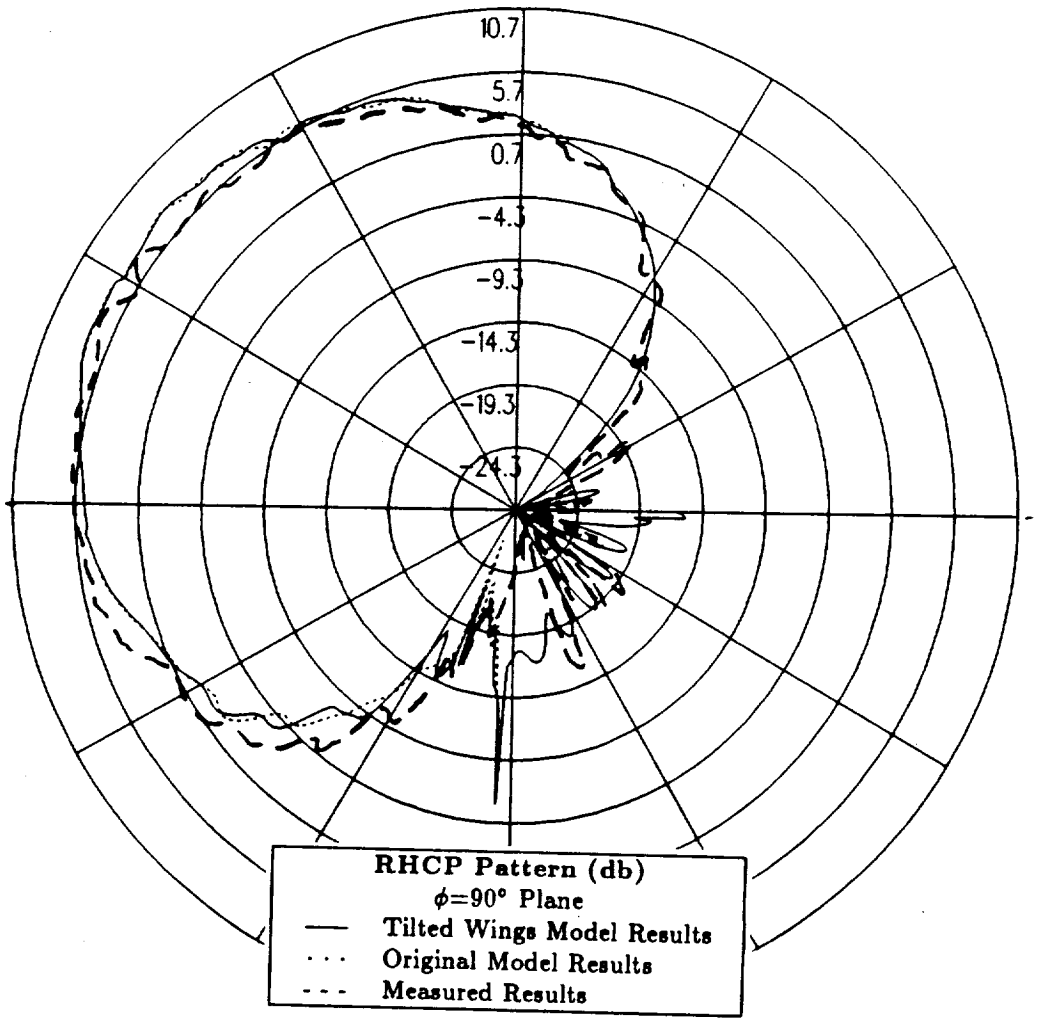

Figure 72: Roll plane pattern using aircraft model with tilted wings for primary antenna location in Boeing report for right hand circular polarization at 300 MHz.

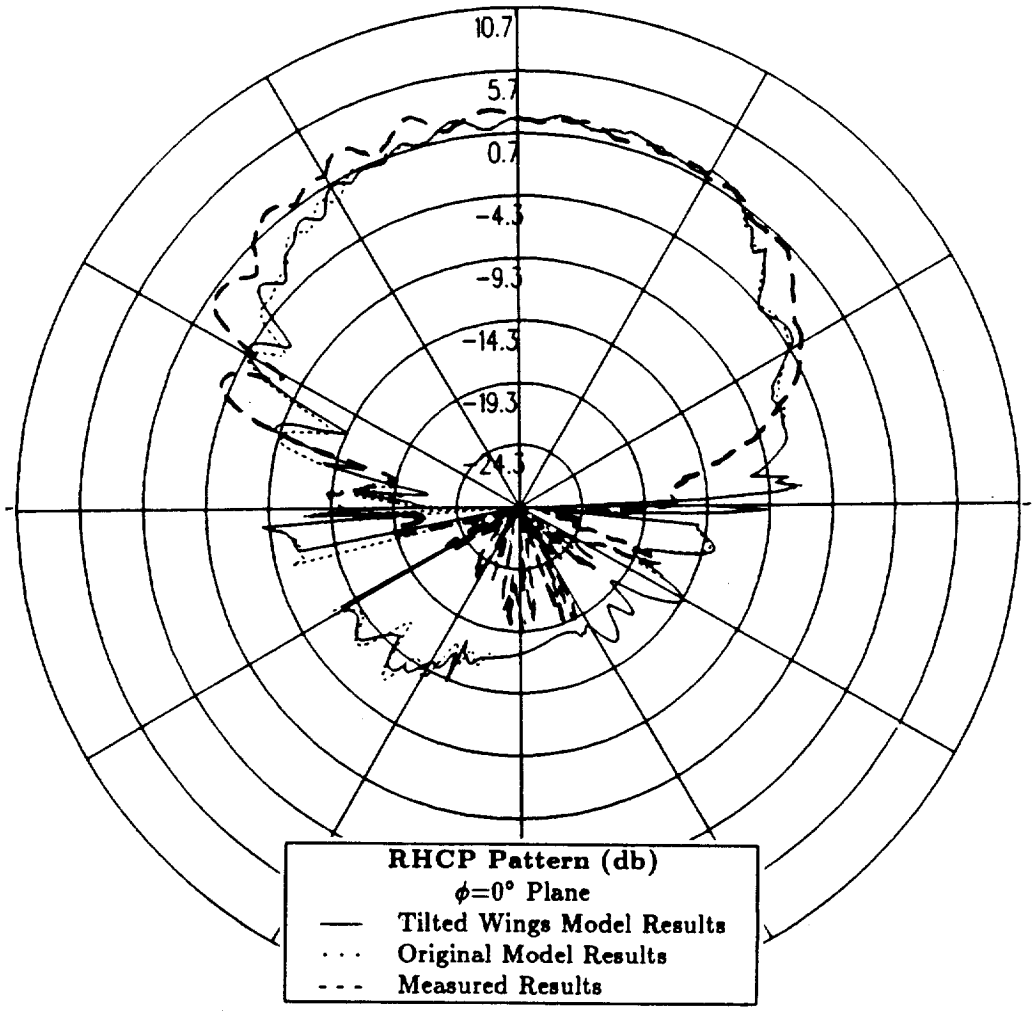

Figure 73: Elevation plane pattern using aircraft model with tilted wings for primary antenna location in Boeing report for right hand circular polarization at 300 MHz.

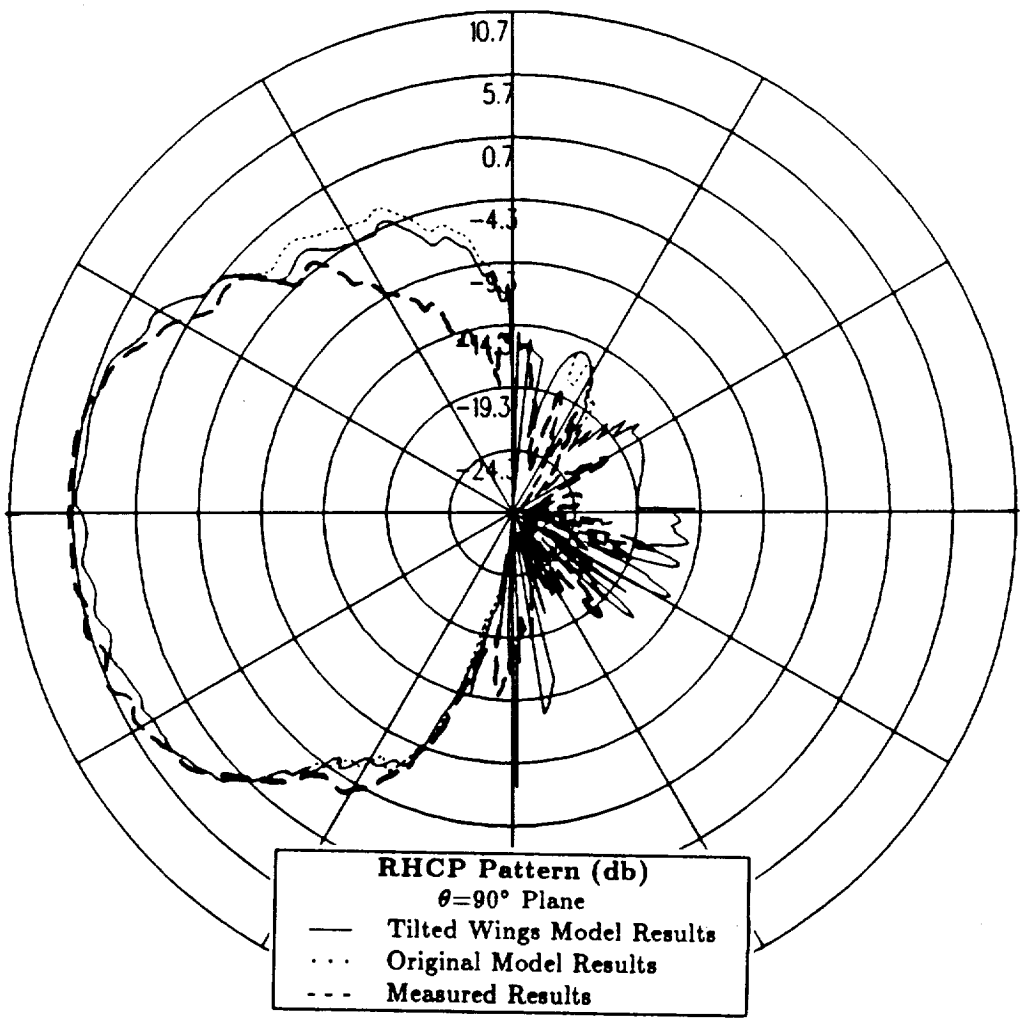

Figure 74: Azimuth plane pattern using aircraft model with tilted wings for primary antenna location in Boeing report for right hand circular polarization at 300 MHz.

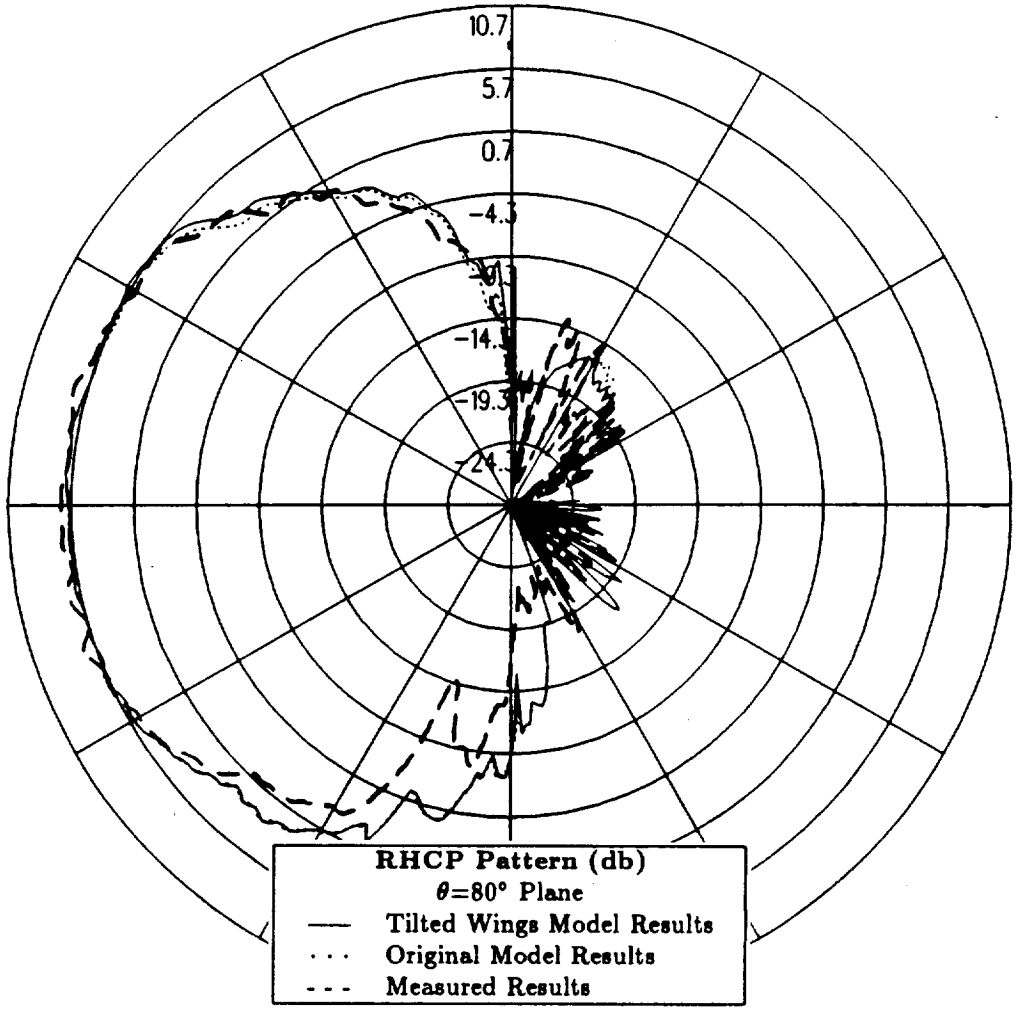

Figure 75: Conical plane pattern 10° above the horizon using aircraft model with tilted wings for primary antenna location in Boeing report for right hand circular polarization at 300 MHz.

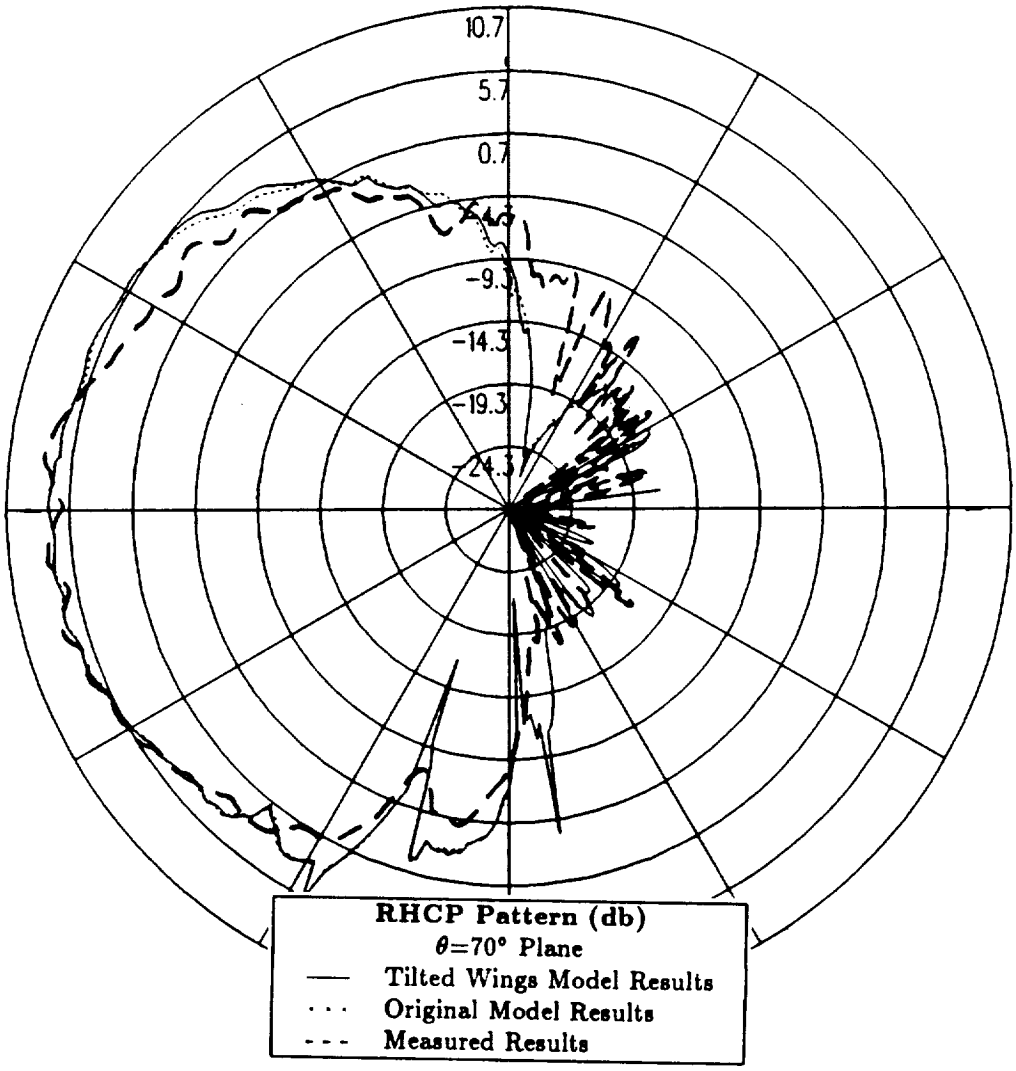

Figure 76: Conical plane pattern 20° above the horizon using aircraft model with tilted wings for primary antenna location in Boeing report for right hand circular polarization at 300 MHz.

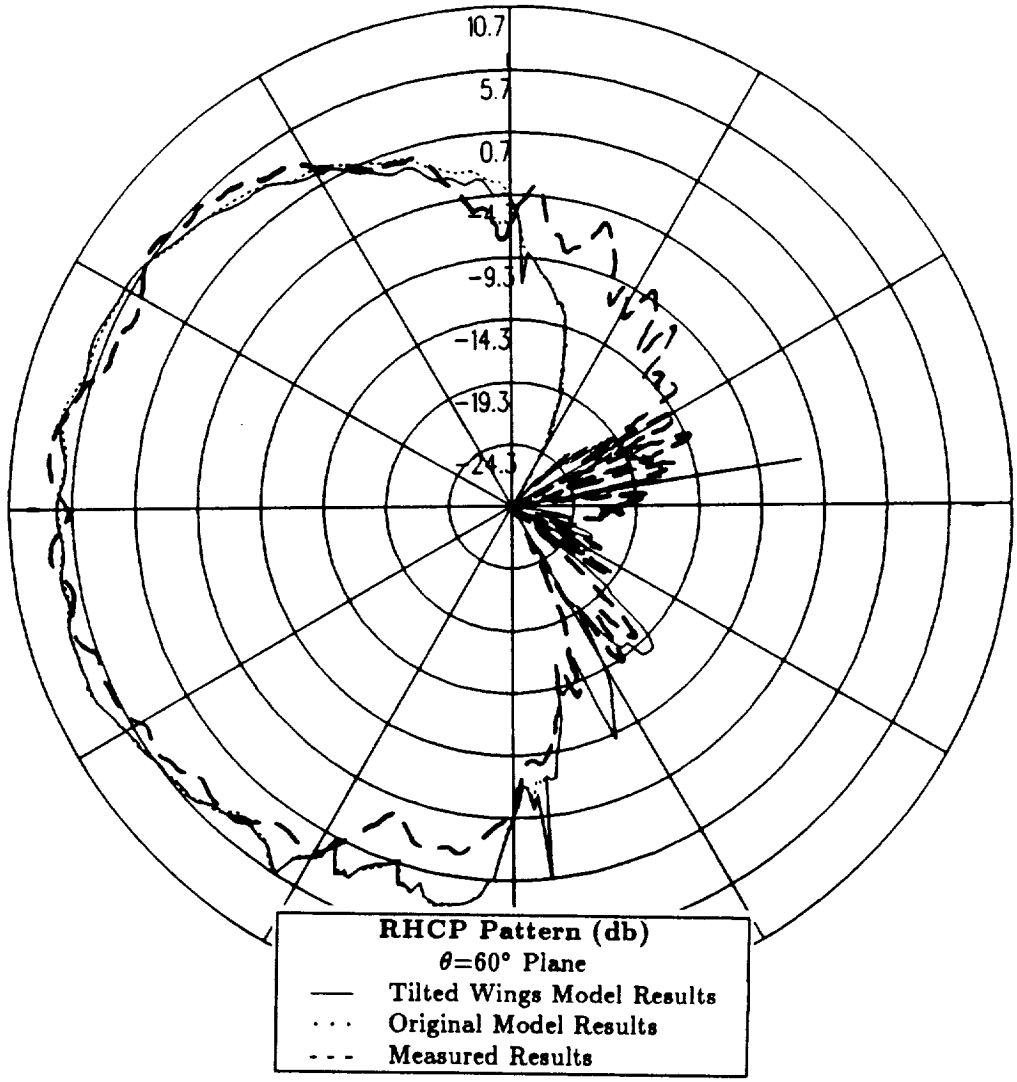

Figure 77: Conical plane pattern 30° above the horizon using aircraft model with tilted wings for primary antenna location in Boeing report for right hand circular polarization at 300 MHz.

5.3.3 Cylindrical Aircraft Model which Includes Double Diffracted Fields for the Wing

The improved NEC-BSC does not calculate double diffracted fields. However, the double diffracted fields which emanate from the wings and the cylinder reflected - double diffracted fields which are reflected by the fuselage and then emanate from the wings could contribute significantly especially in the horizon of the aircraft in the regions near the nose and the tail. In this section these double diffracted fields have been added to see the effect on the radiation patterns. Because the cylinder reflected - double diffracted fields cannot be calculated, the imaging technique described in Section 3.5 is used to simulate the cylinder reflected - double diffracted fields.

The cylindrical aircraft model used in the NEC-BSC for this sensitivity study is illustrated in Figure 19. The results at 300 MHz for the right hand circular polarized or co-polarized fields are compared for the roll plane in Figure 78, for the elevation plane in Figure 79, for the azimuth plane in Figure 80 and for the conical planes 10°, 20° and 30° above the horizon in Figures 81, 82 and 83, respectively. Again the co-polarized results are of primary importance in this report so the left hand circular polarized or cross-polarized results are not included in this sensitivity study.

The roll plane results shown in Figure 78 indicate that the calculated pattern which includes the double diffracted fields compares very well to both the previous calculated pattern and the measured pattern. Comparing the elevation plane results in Figure 79 indicates that the calculated pattern which includes the double diffracted fields compares very well to the previous calculated pattern. Therefore, the double diffracted fields have very little effect in either of these pattern cuts. Comparing the azimuth plane results in Figure 80 shows that the double diffracted fields have a small effect on the results in this pattern cut at 45° directly off the

nose of the aircraft where the calculated level is reduced by approximately 1 dB. Comparing the results for the conical planes in Figures 81, 82 and 83 shows that the calculated pattern which includes the double diffracted fields compares very well to both the previous calculated pattern and the measured pattern. Therefore, the slightly lower levels which are present in the horizon of the aircraft due to the double diffracted fields disappear as the pattern cut is taken slightly above the horizon.

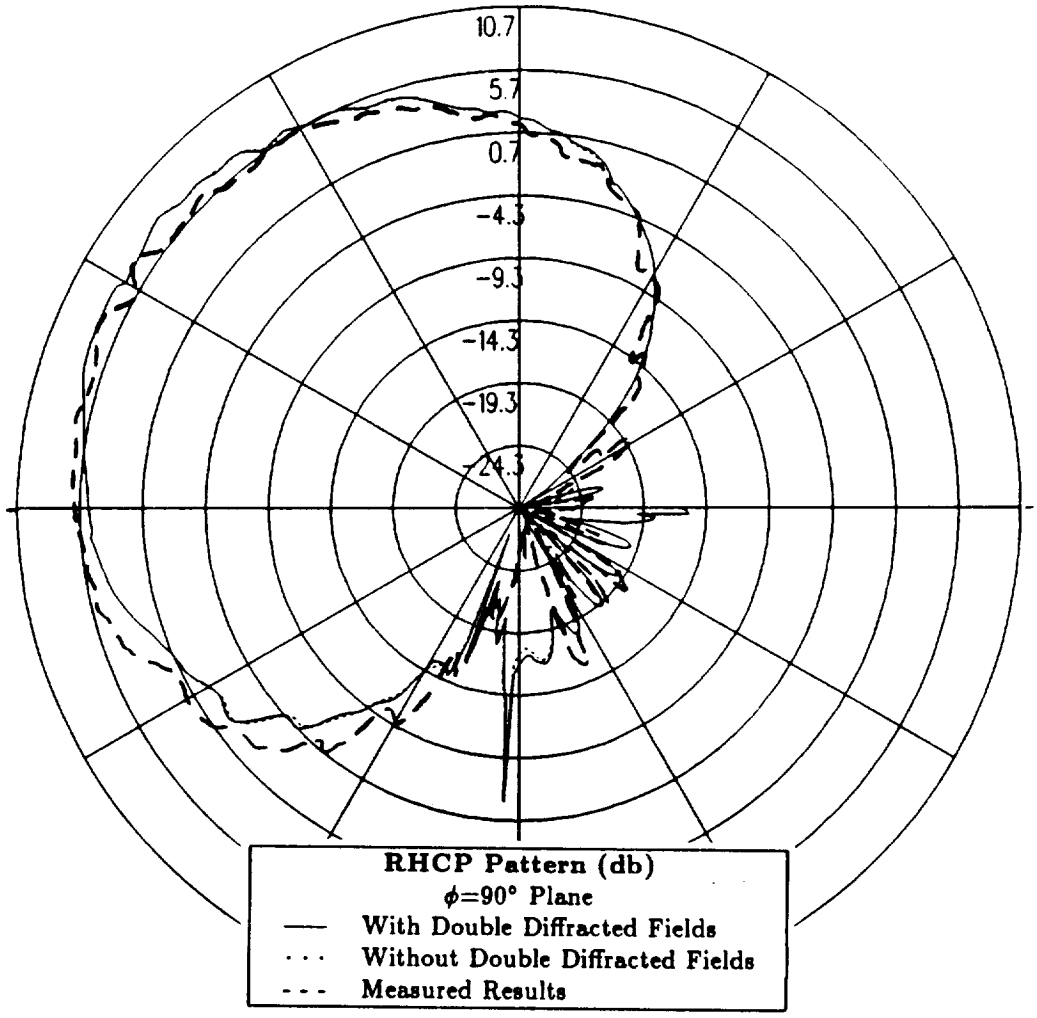

Figure 78: Roll plane pattern which includes double diffracted fields for primary antenna location in Boeing report for right hand circular polarization at 300 MHz.

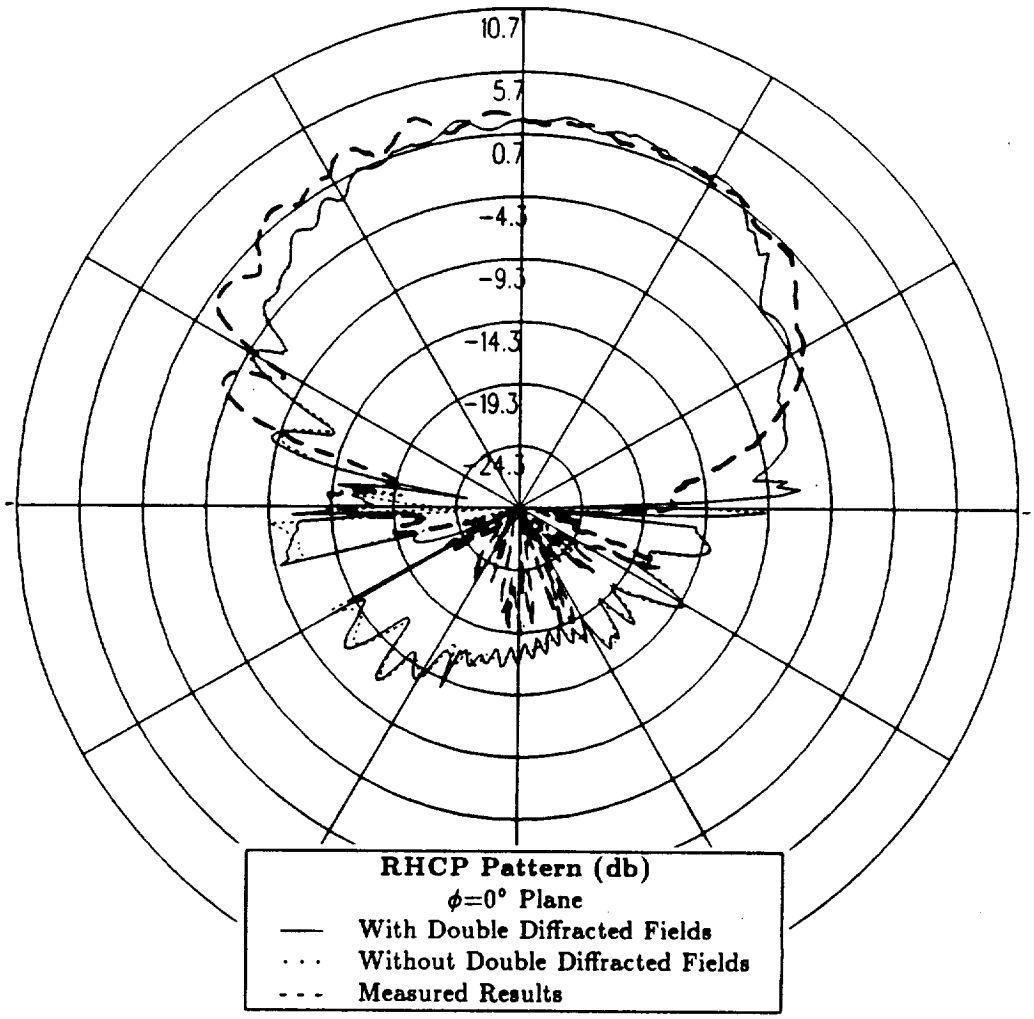

Figure 79: Elevation plane pattern which includes double diffracted fields for primary antenna location in Boeing report for right hand circular polarization at 300 MHz.

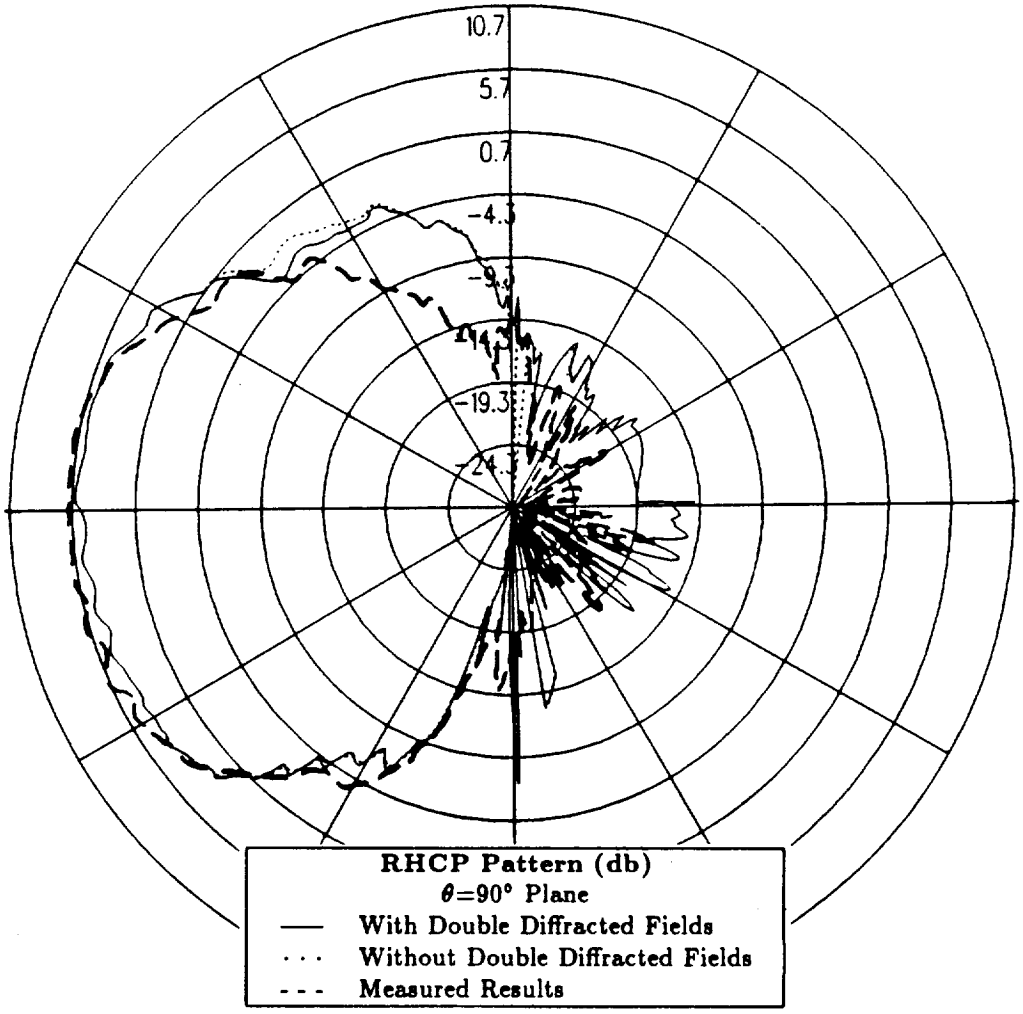

Figure 80: Azimuth plane pattern which includes double diffracted fields for primary antenna location in Boeing report for right hand circular polarization at 300 MHz.

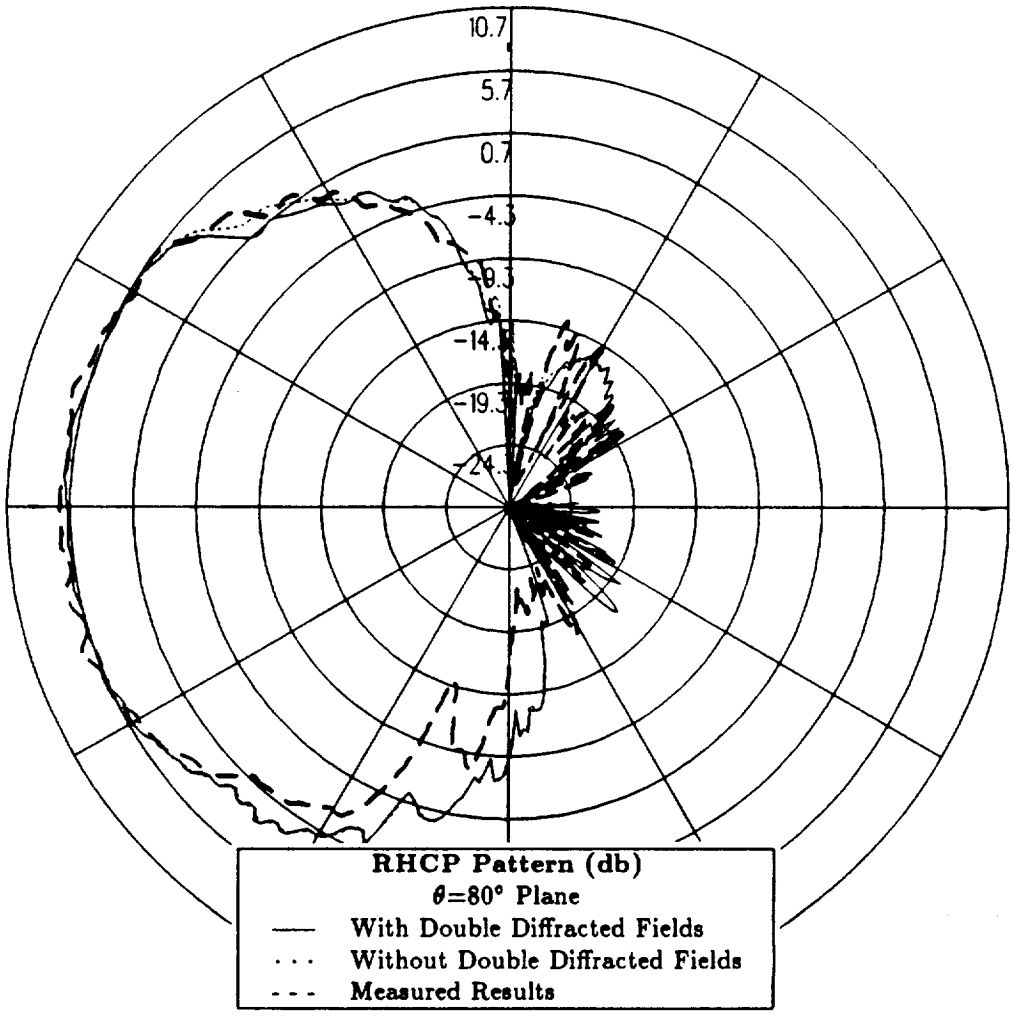

Figure 81: Conical plane pattern 10° above the horizon which includes double diffracted fields for primary antenna location in Boeing report for right hand circular polarization at 300 MHz.

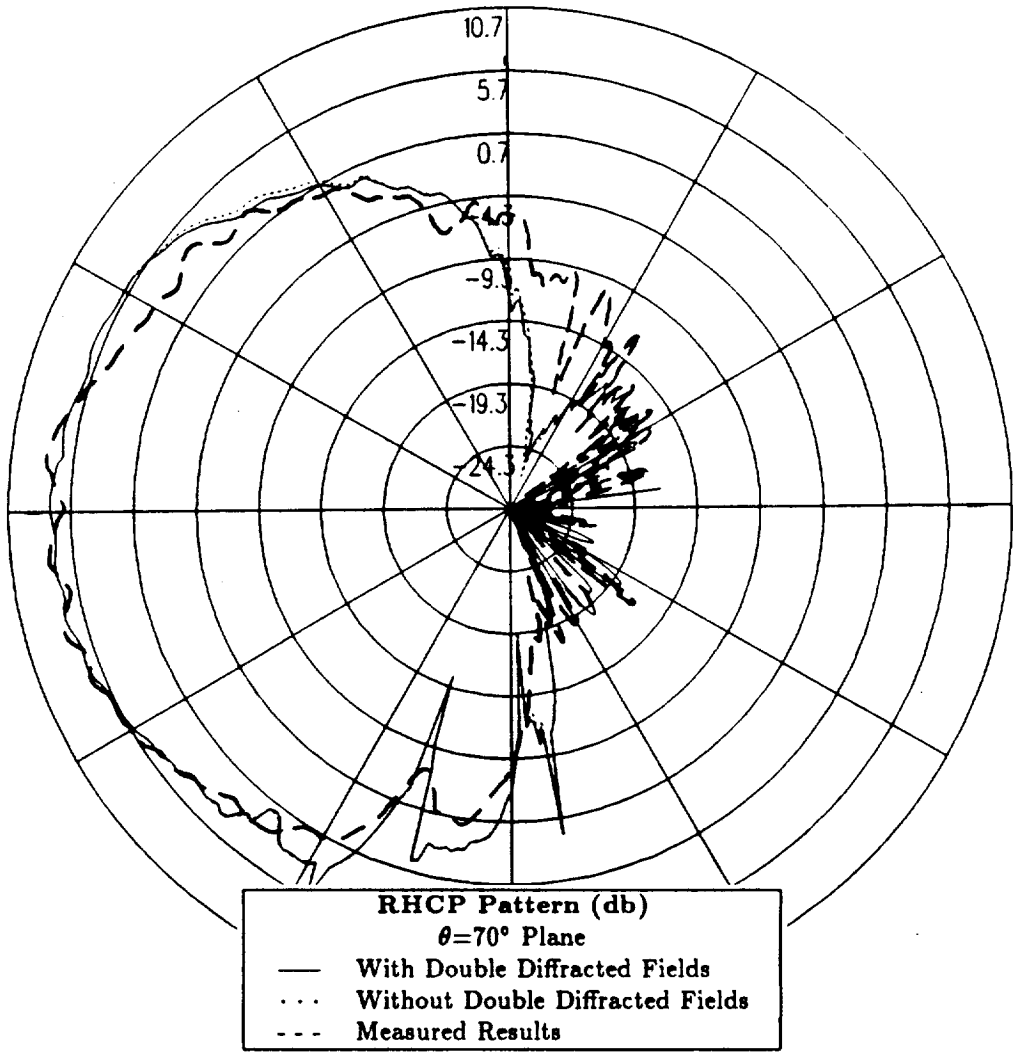

Figure 82: Conical plane pattern 20° above the horizon which includes double diffracted fields for primary antenna location in Boeing report for right hand circular polarization at 300 MHz.

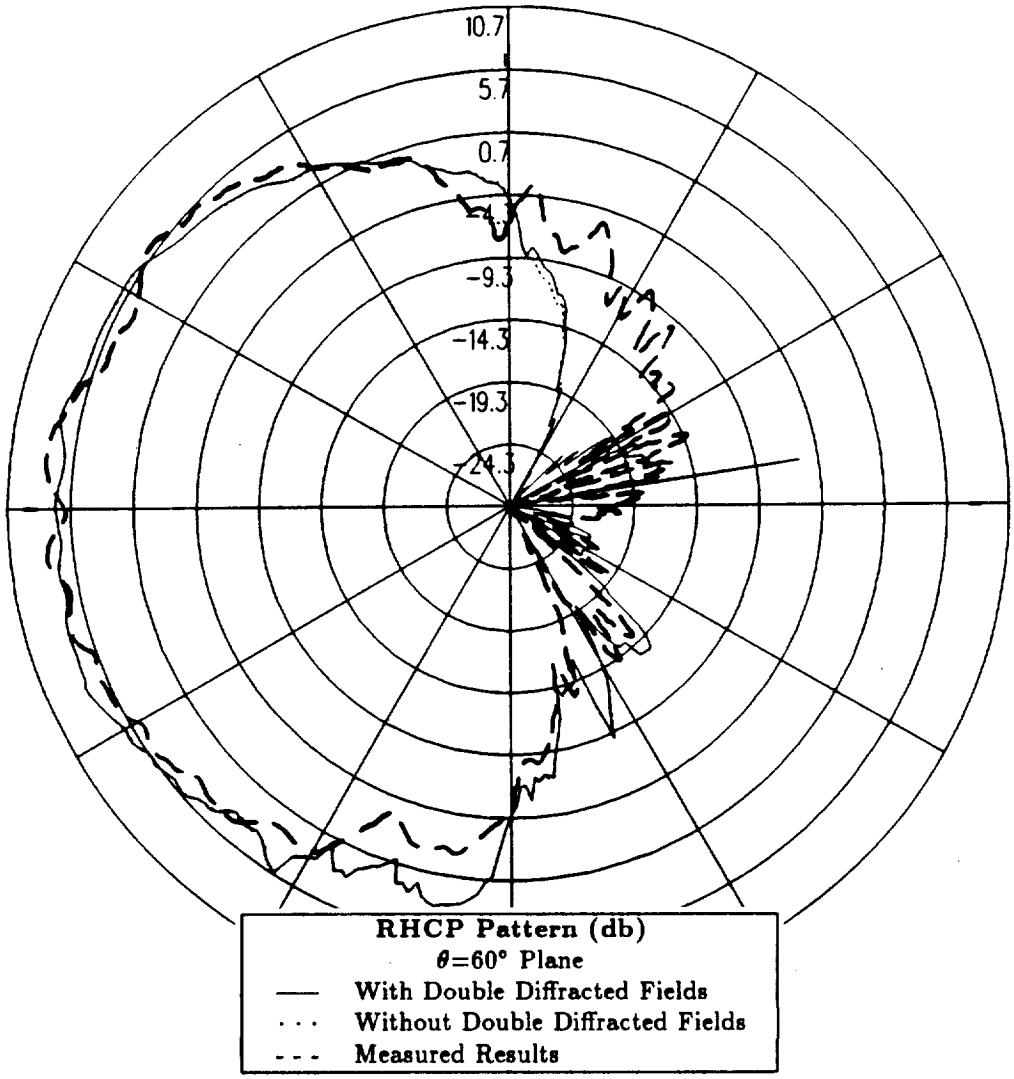

Figure 83: Conical plane pattern 30° above the horizon which includes double diffracted fields for primary antenna location in Boeing report for right hand circular polarization at 300 MHz.

5.4 Comparison of Improved NEC-BSC Results with Lockheed Results for Alternative Antenna Location

In this section, the results computed with the improved NEC-BSC are compared to the measured results for the antenna location defined in the Lockheed report as Top FS 806 BL 38.7L . This designation means that the antenna is located on the port side of the fuselage between the wing and the horizontal stabilizer 38.7° down from the top center-line. The cylindrical aircraft model used in the NEC-BSC is illustrated in Figure 84, which also shows the location of the antenna on the aircraft fuselage. The calculated results at 300 MHz for the right hand circular polarized or co-polarized fields are compared with measurements for the roll plane in Figure 85, for the elevation plane in Figure 86, for the azimuth plane in Figure 87 and for the conical planes 10°, 20° and 30° above the horizon in Figures 88, 89 and 90, respectively. For completeness, the left hand circular polarized or cross-polarized results are also included. These cross-polarized results are shown for the roll plane in Figure 91, for the elevation plane in Figure 92, for the azimuth plane in Figure 93 and for the conical planes 10°, 20° and 30° above the horizon in Figures 94, 95 and 96, respectively.

The calculated and measured roll plane results for the co-polarized field shown in Figure 85 agree to within 1–2 dB throughout the majority of the pattern. Comparing the co-polarized elevation plane results in Figure 86 shows that the calculated results and the measured results agree to within 1–2 dB throughout the complete pattern except in the region on the horizon near the nose and the tail of the aircraft where the calculated levels increase to as much as 5 dB higher than the measured levels. Comparing the co-polarized results for the azimuth plane in Figure 87 shows that the NEC-BSC calculated results are higher than the measured

results especially near the nose and the tail of the aircraft where the calculated levels increase to as much as 5–8 dB higher than the measured levels. Comparing the co-polarized results for the conical planes in Figures 88, 89 and 90 shows that the agreement between the calculated results and the measured results is within 1–3 dB throughout the majority of the pattern for all three conic cuts taken. Therefore, the higher levels which are seen in the horizon near the nose and the tail of the aircraft disappear as the pattern cut is taken slightly above the horizon.

The cross-polarized results are shown in Figures 91 through 96. Again the agreement between the calculated and measured results for the cross-polarized fields is not as good as the agreement found for the co-polarized fields. However, the agreement between the measured results and the Lockheed results in this section for the cross-polarized component is better than the agreement between the measured results and the Boeing results shown in Sections 5.2 and 5.5.

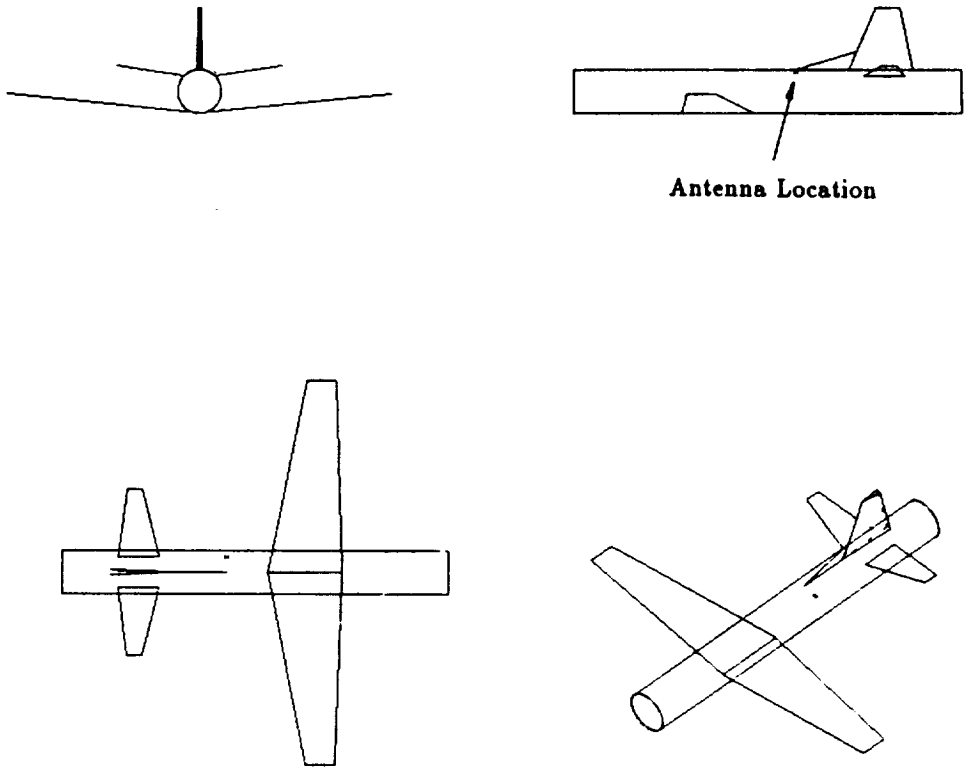

Figure 84: Geometry of the cylindrical model of the P-3C aircraft used in the NEC-BSC showing the Lockheed antenna location.

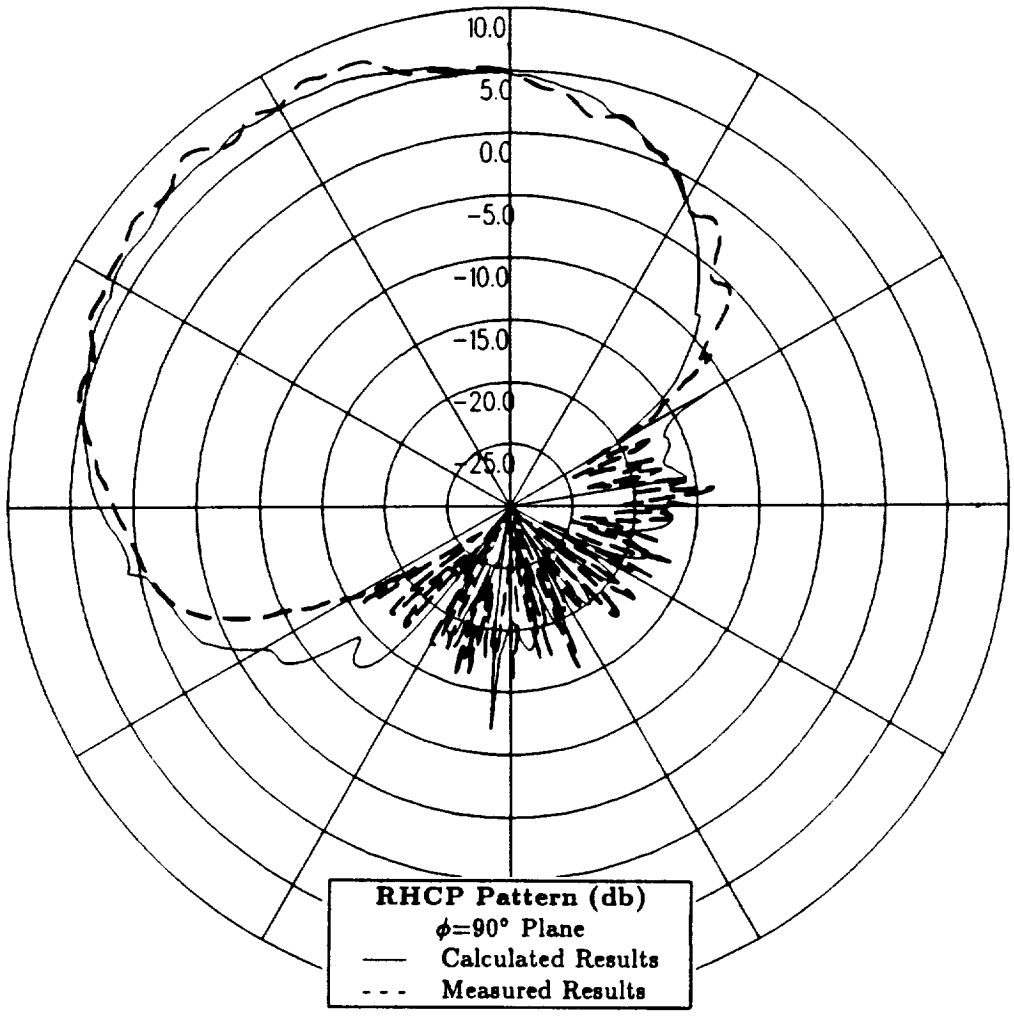

Figure 85: Roll plane pattern for antenna location in Lockheed report for right hand circular polarization at 300 MHz.

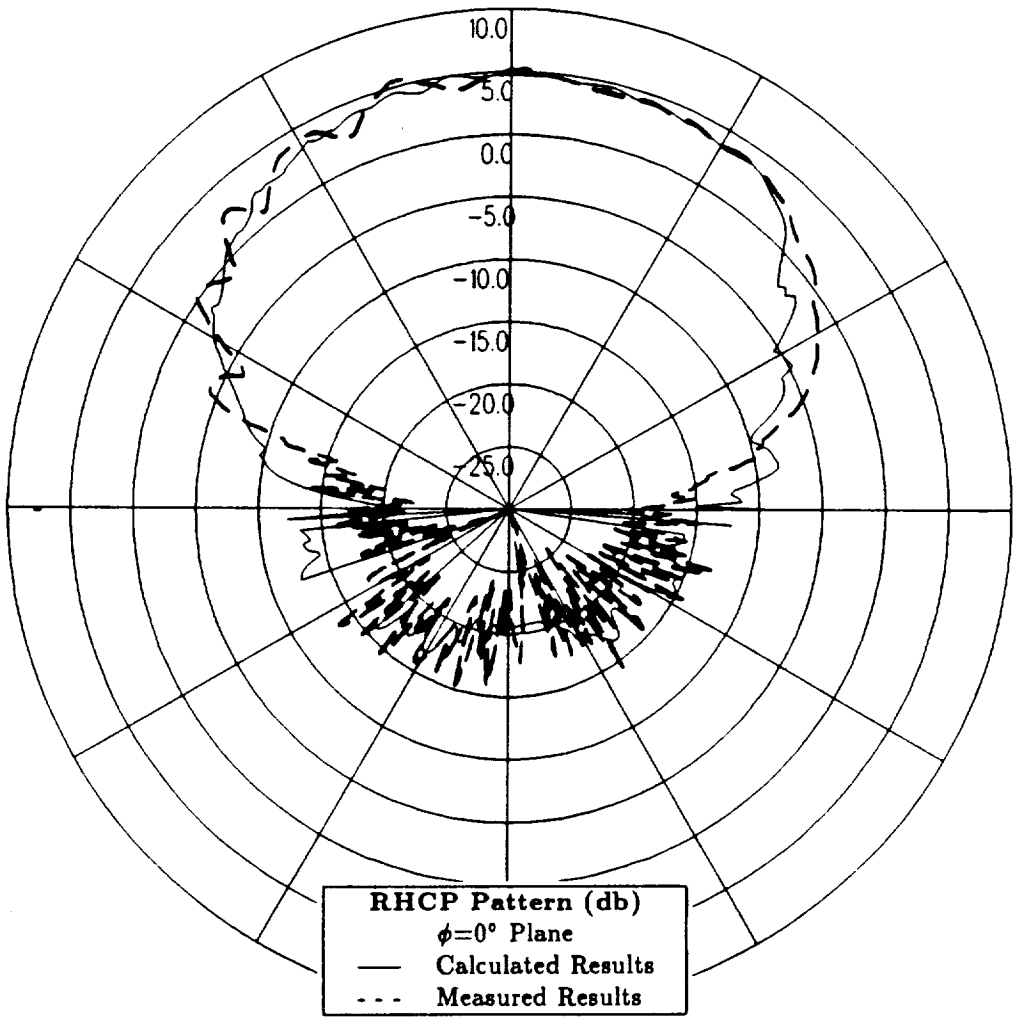

Figure 86: Elevation plane pattern for antenna location in Lockheed report for right hand circular polarization at 300 MHz.

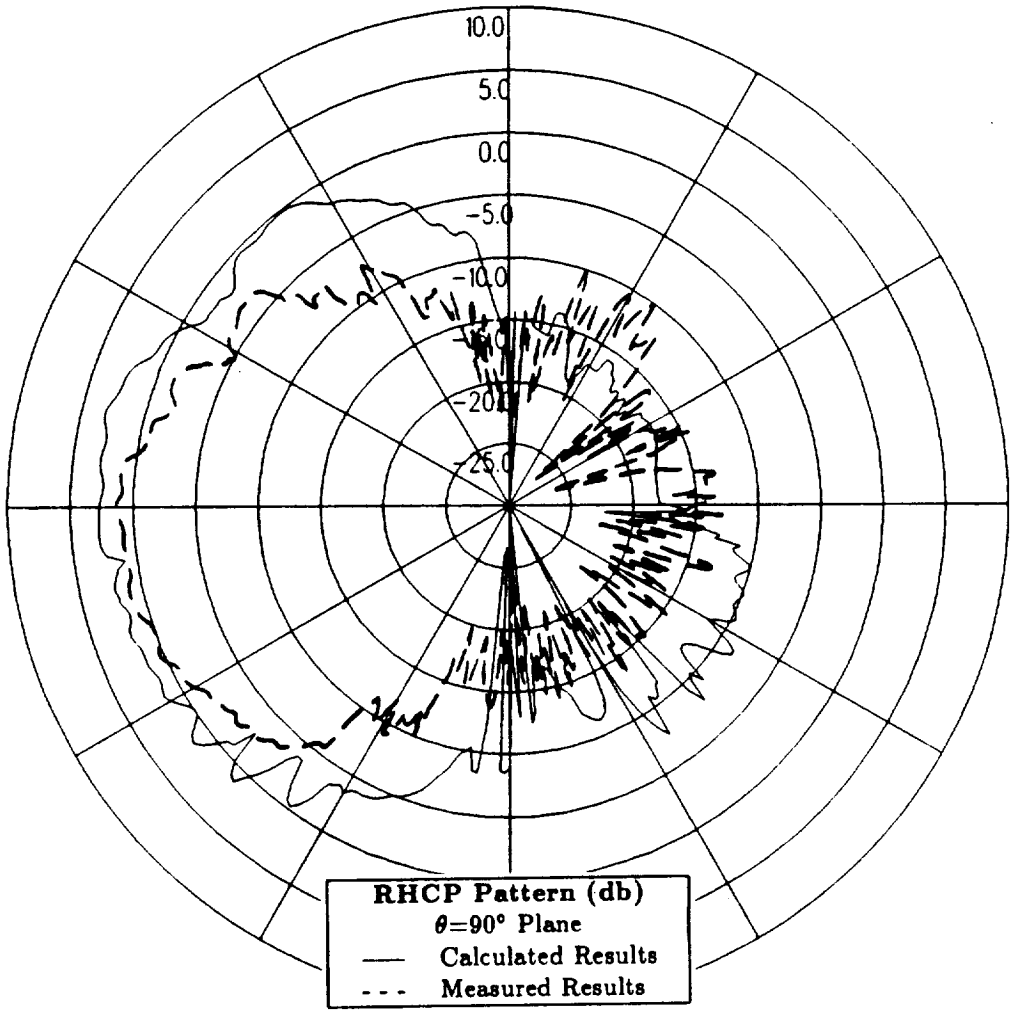

Figure 87: Azimuth plane pattern for antenna location in Lockheed report for right hand circular polarization at 300 MHz.

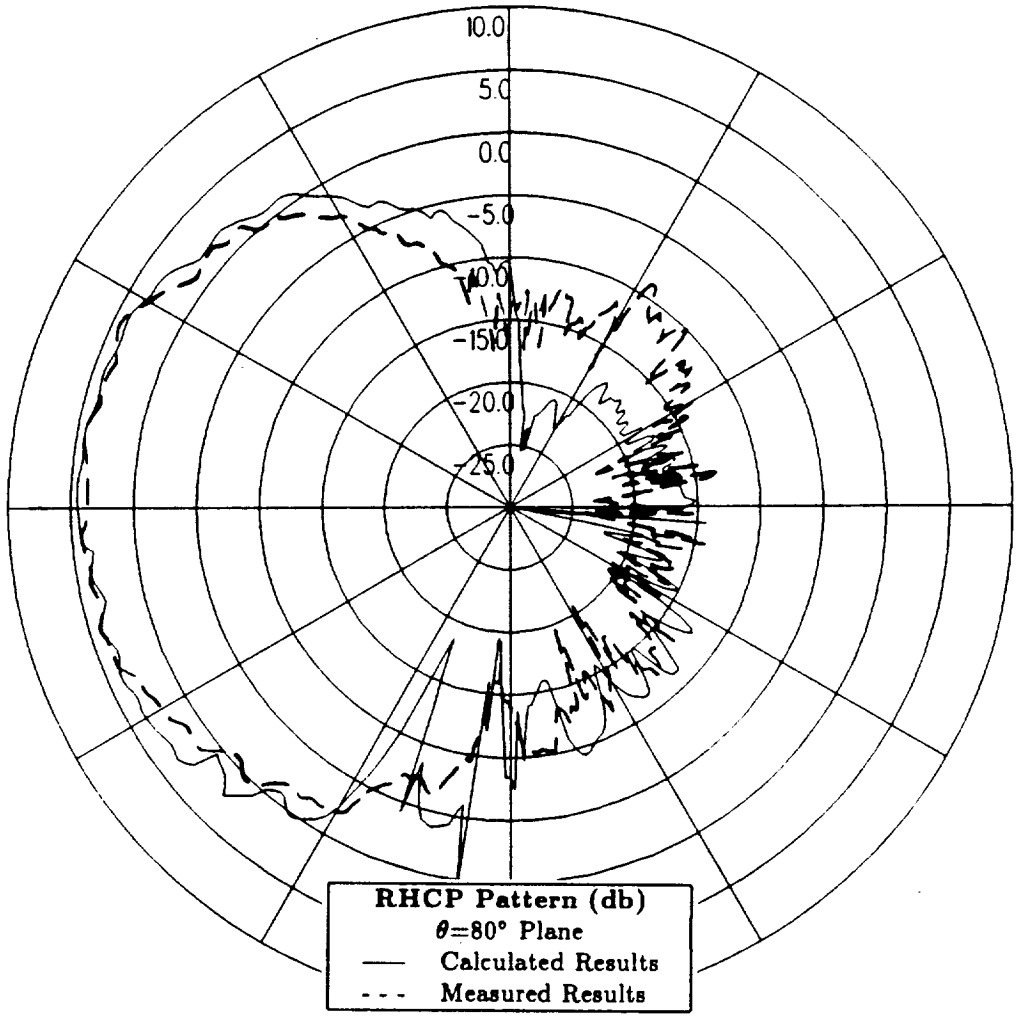

Figure 88: Conical plane pattern 10° above the horizon for antenna location in Lockheed report for right hand circular polarization at 300 MHz.

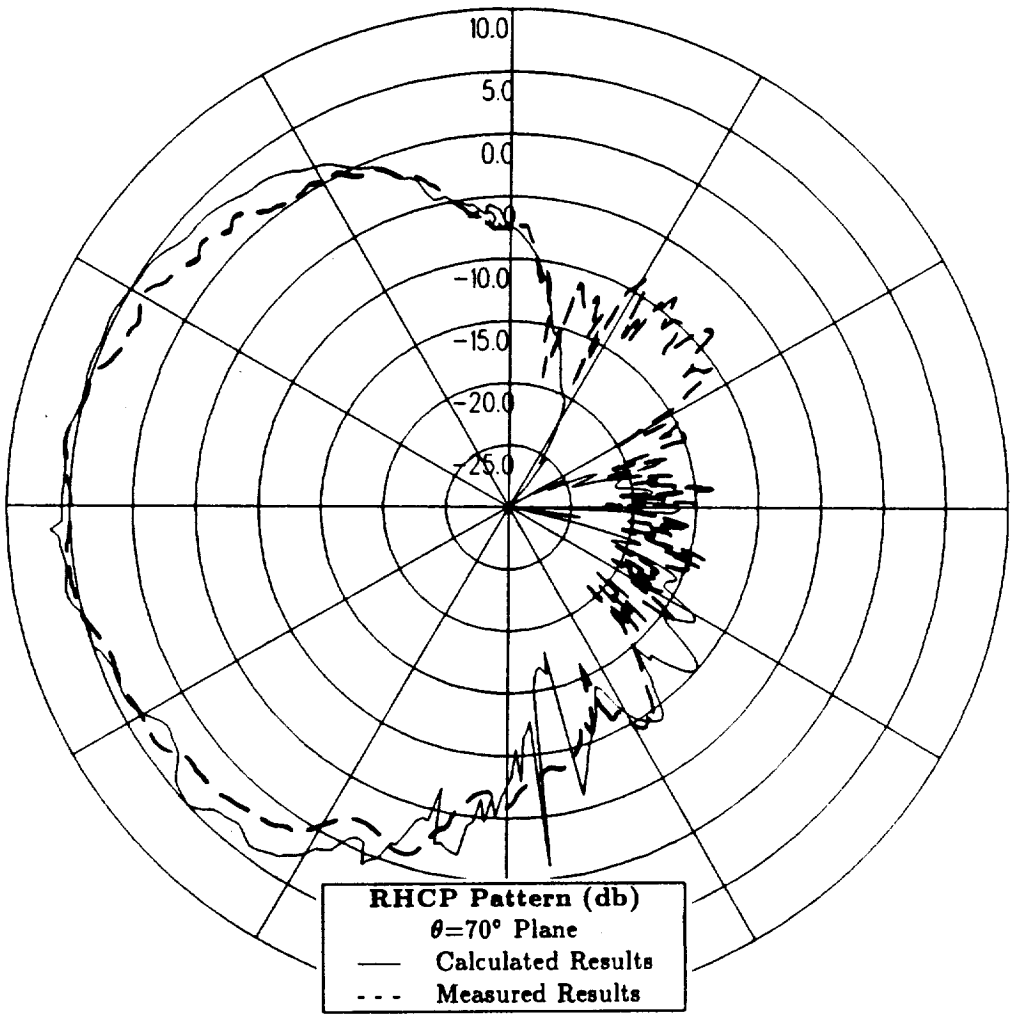

Figure 89: Conical plane pattern 20° above the horizon for antenna location in Lockheed report for right hand circular polarization at 300 MHz.

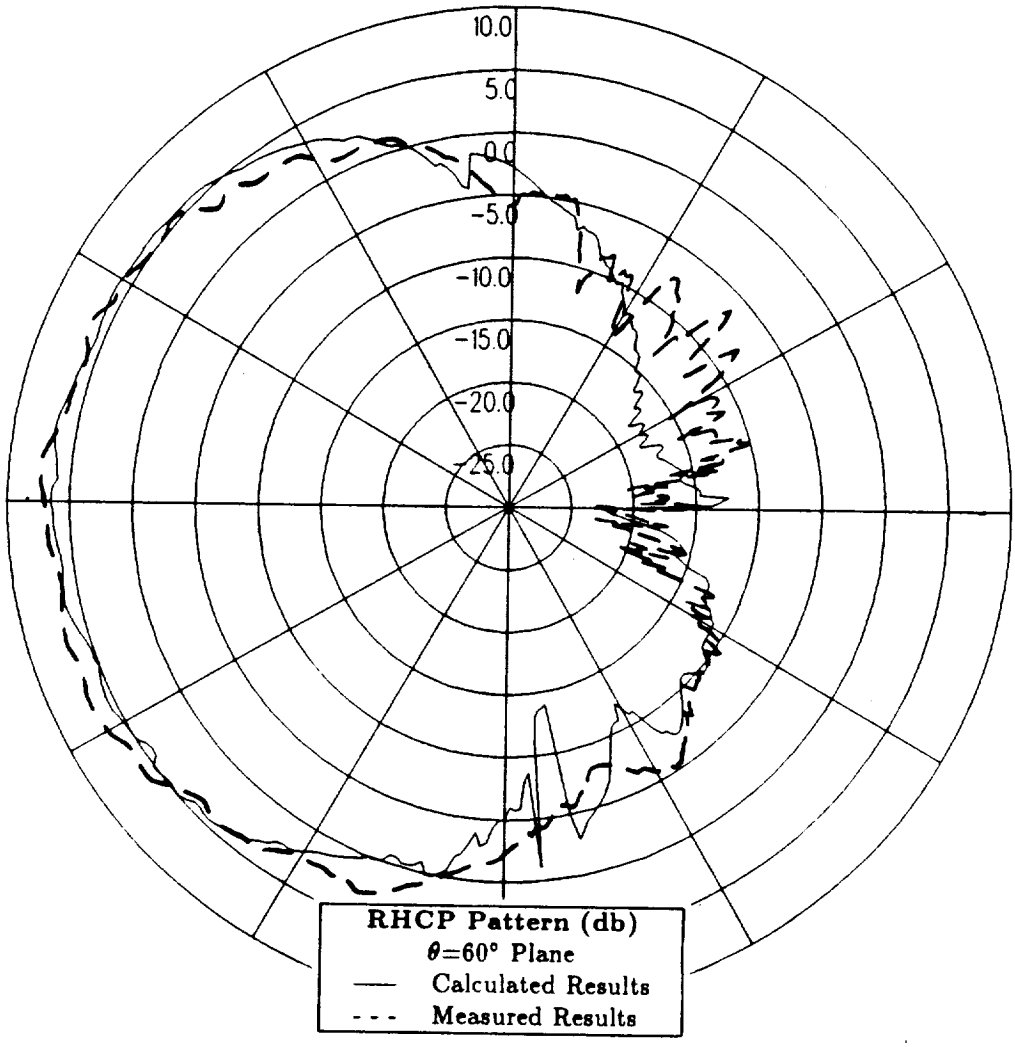

Figure 90: Conical plane pattern 30° above the horizon for antenna location in Lockheed report for right hand circular polarization at 300 MHz.

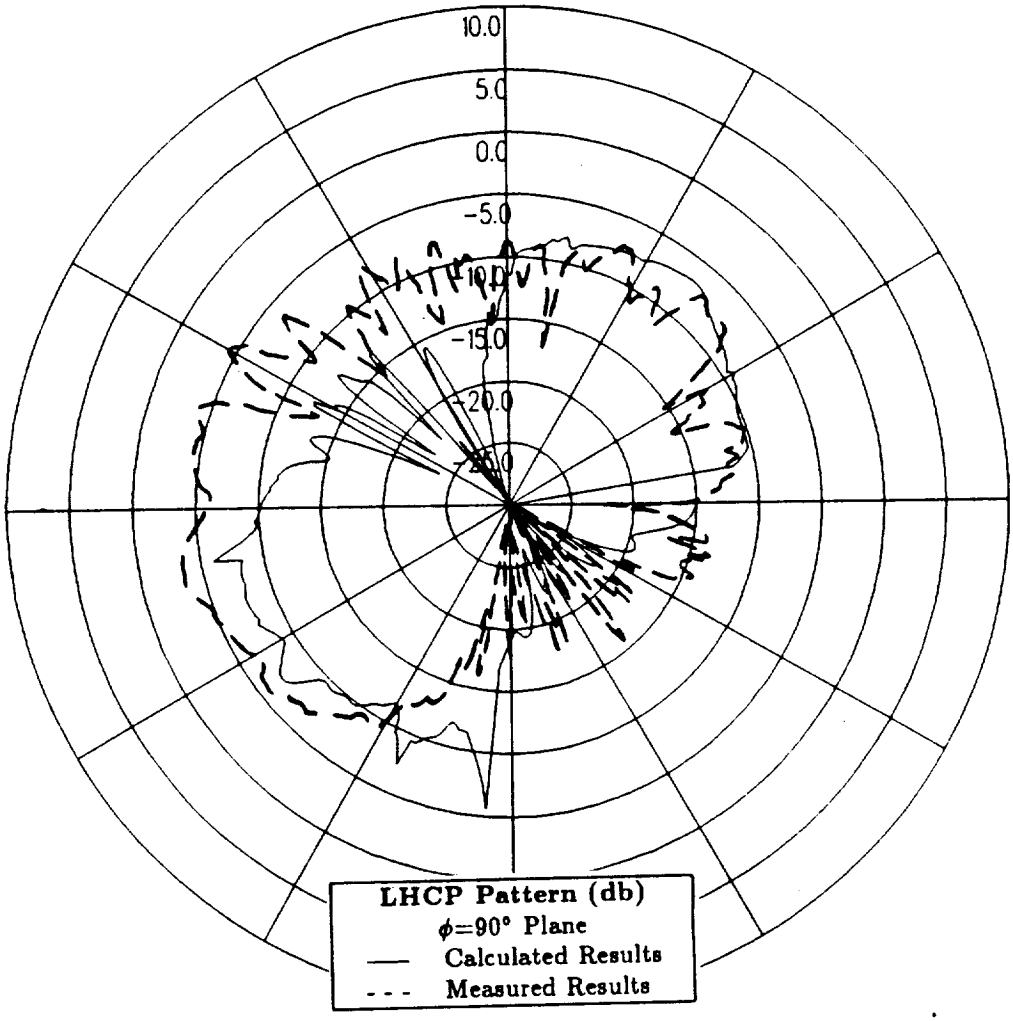

Figure 91: Roll plane pattern for antenna location in Lockheed report for left hand circular polarization at 300 MHz.

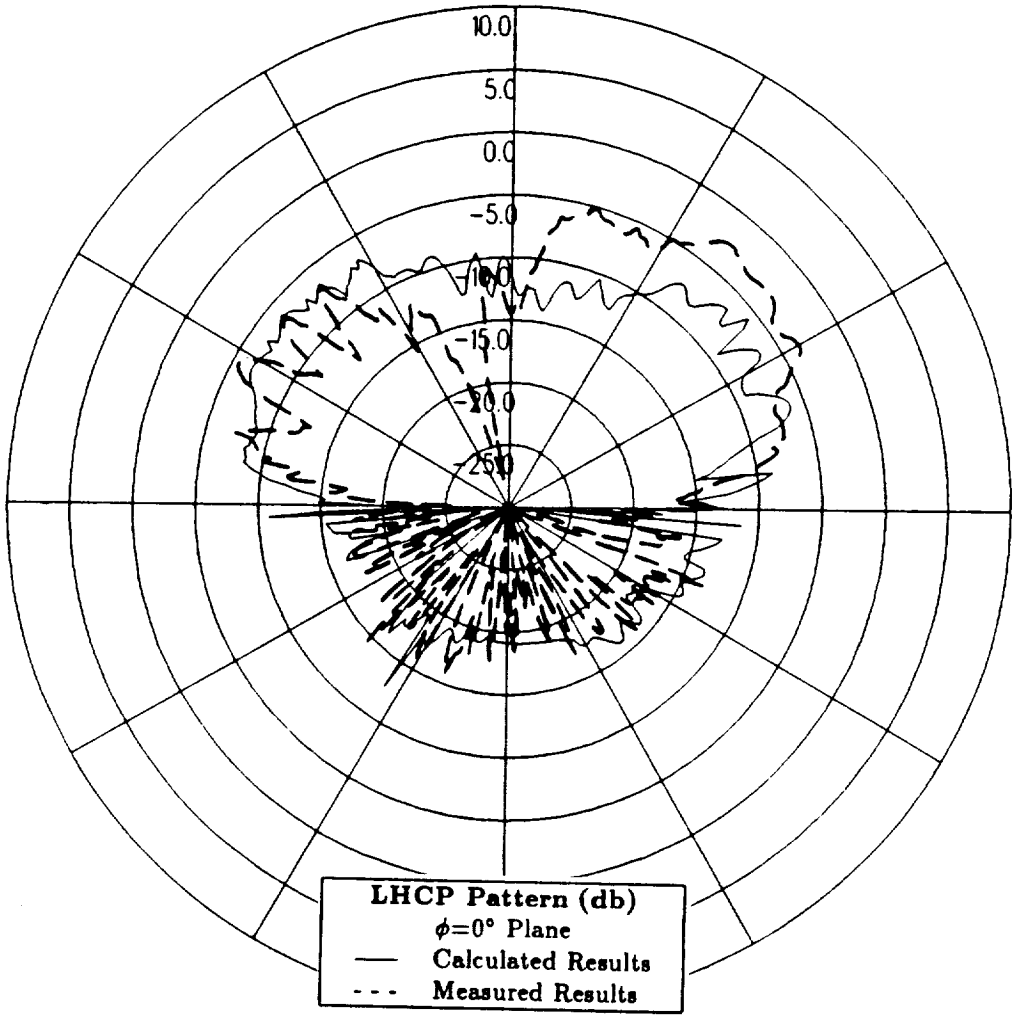

Figure 92: Elevation plane pattern for antenna location in Lockheed report for left hand circular polarization at 300 MHz.

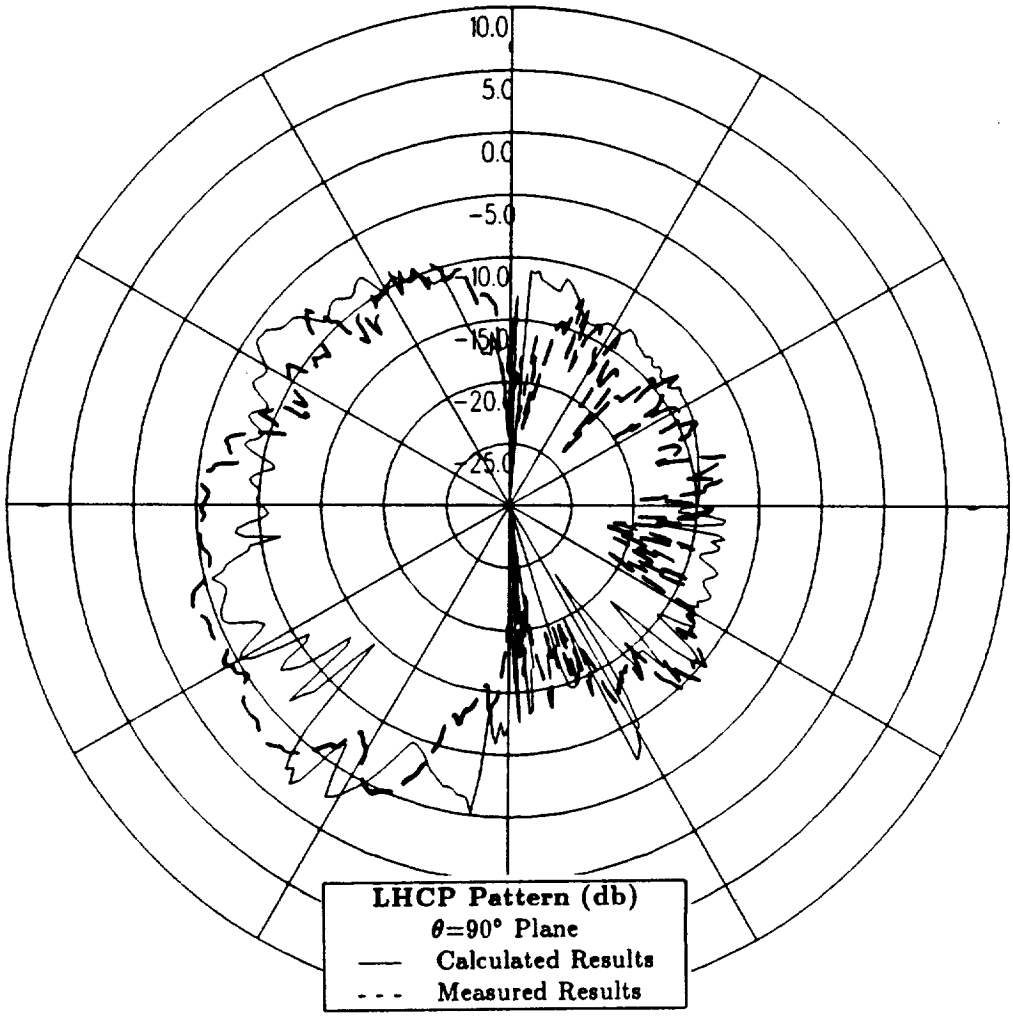

Figure 93: Azimuth plane pattern for antenna location in Lockheed report for left hand circular polarization at 300 MHz.

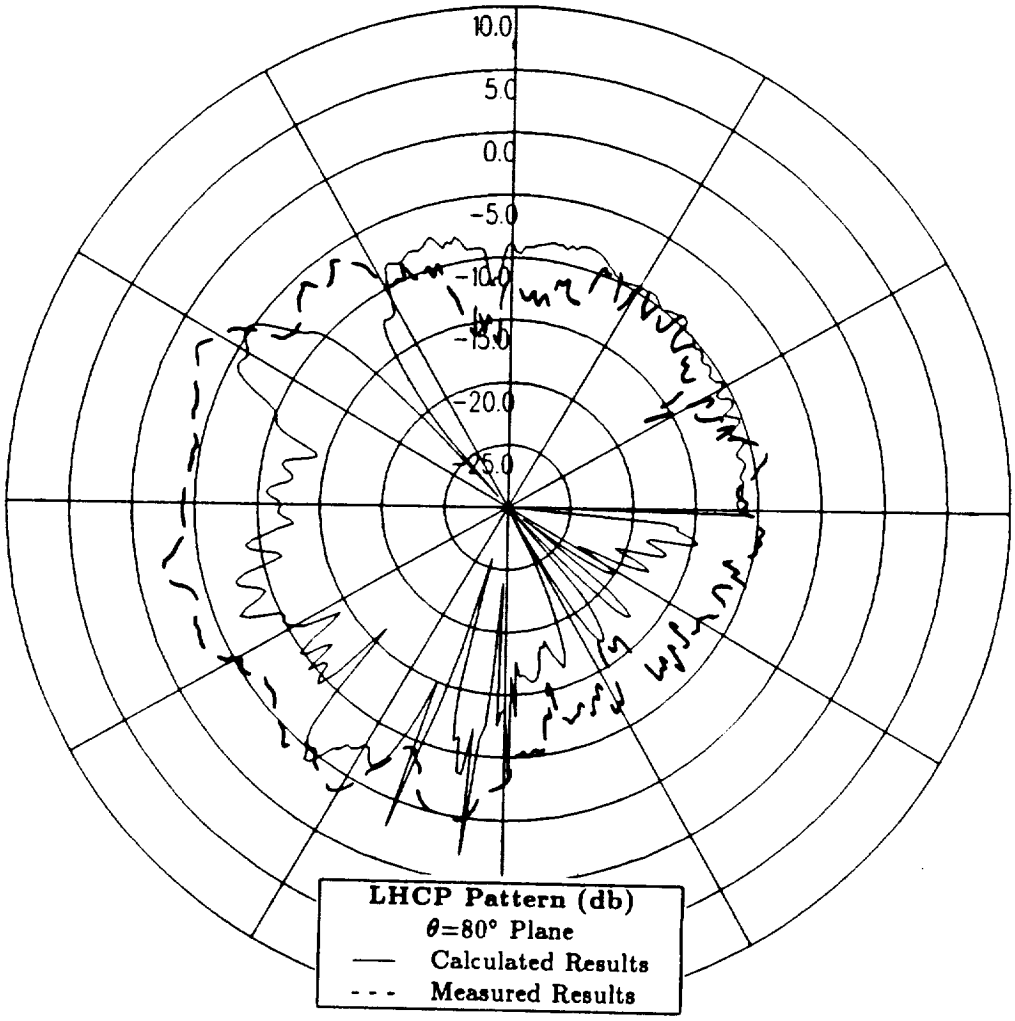

Figure 94: Conical plane pattern 10° above the horizon for antenna location in Lockheed report for left hand circular polarization at 300 MHz.

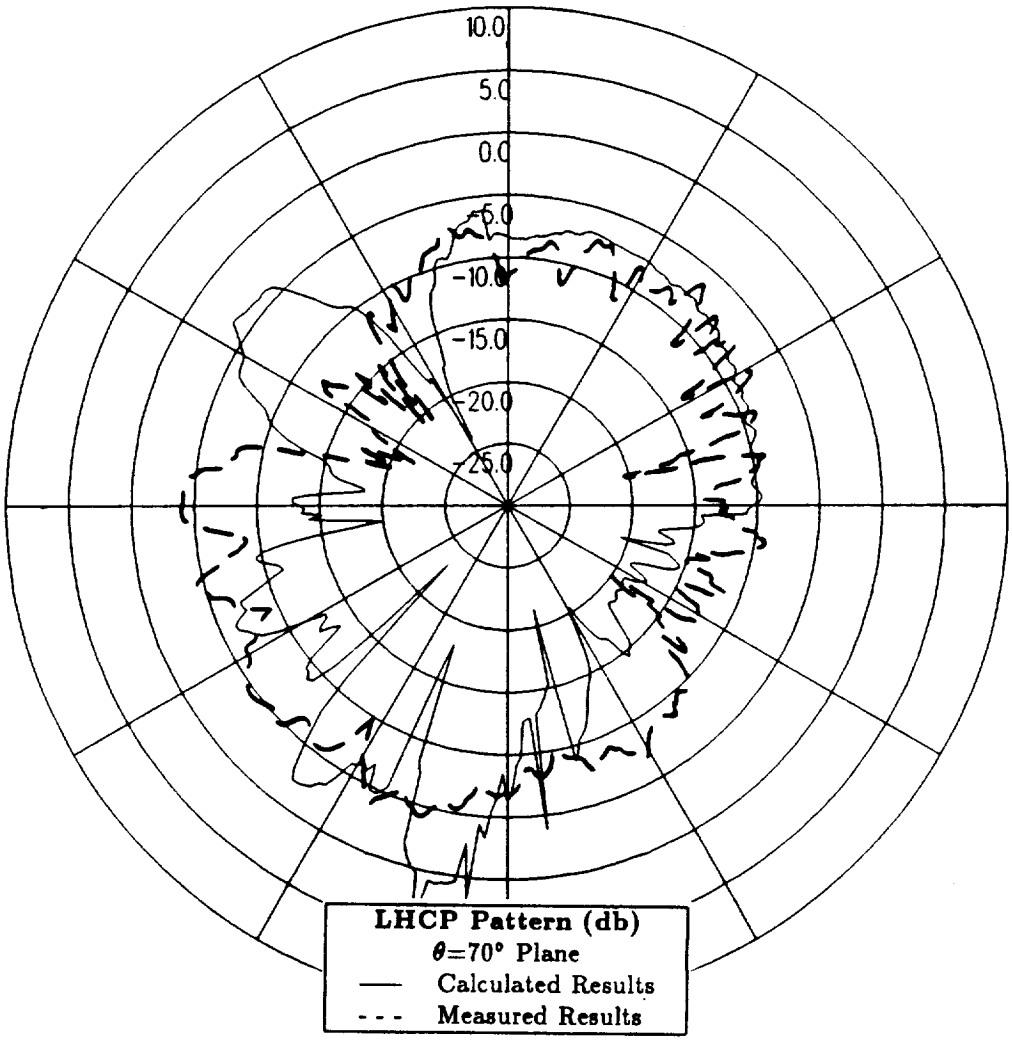

Figure 95: Conical plane pattern 20° above the horizon for antenna location in Lockheed report for left hand circular polarization at 300 MHz.

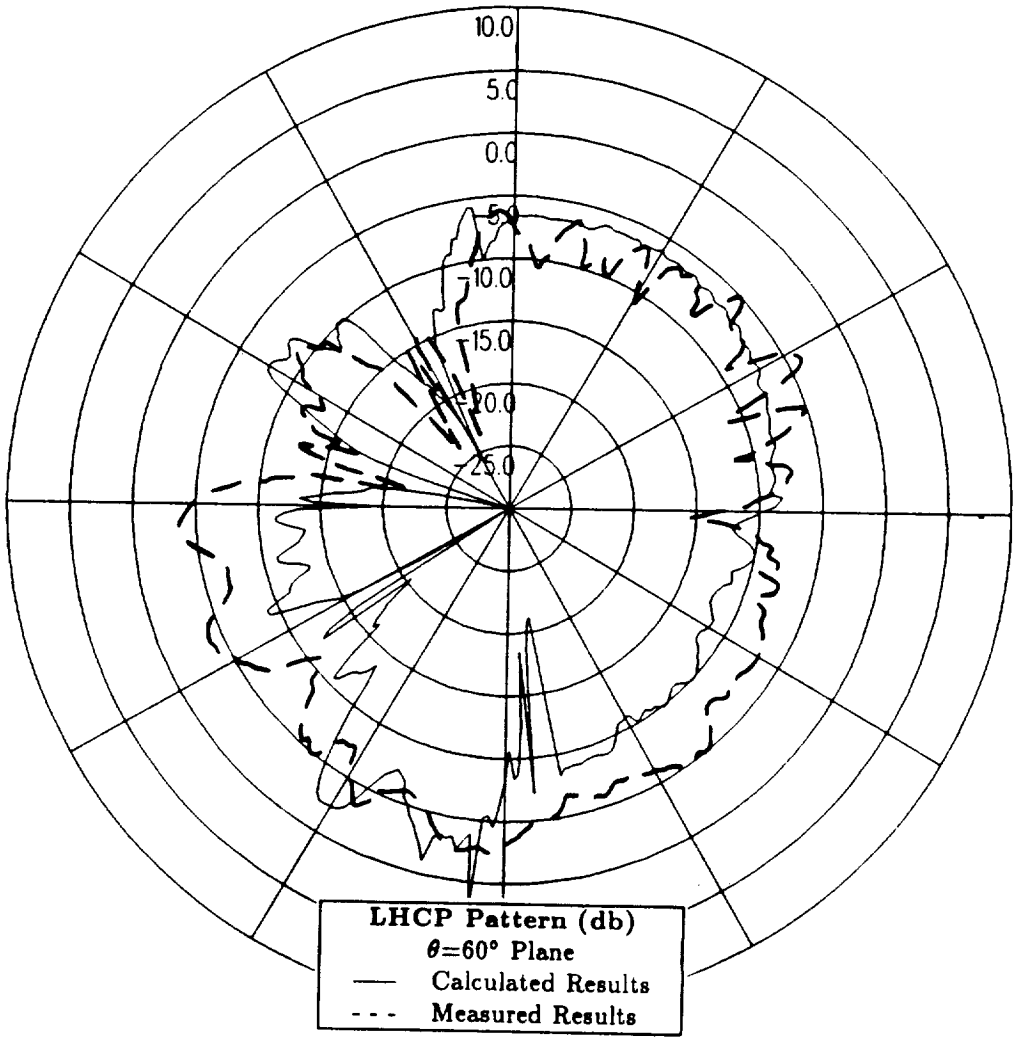

Figure 96: Conical plane pattern 30° above the horizon for antenna location in Lockheed report for left hand circular polarization at 300 MHz.

5.5 Comparison of Improved NEC-BSC Results with Boeing Results for Alternative Antenna Location

In this section, the results computed with the improved NEC-BSC are compared to the measured results for the antenna location defined in the Boeing report as Station 297 LBL 55.7 . This designation means that the antenna is located on the port side of the fuselage near the nose 55.7° down from the top center-line. The cylindrical aircraft model used in the NEC-BSC is illustrated in Figure 97, which also shows the location of the antenna on the aircraft fuselage. The calculated results at 300 MHz for the right hand circular polarized or co-polarized fields are compared with measurements for the roll plane in Figure 98, for the elevation plane in Figure 99 for the azimuth plane in Figure 100 and for the conical planes 10°, 20° and 30° above the horizon in Figures 101, 102 and 103, respectively. For completeness, the left hand circular polarized or cross-polarized results are also included. These cross-polarized results are shown for the roll plane in Figure 104, for the elevation plane in Figure 105, for the azimuth plane in Figure 106 and for the conical planes 10°, 20° and 30° above the horizon in Figures 107, 108 and 109, respectively.

The calculated and measured roll plane results for the co-polarized field shown in Figure 98 agree to within 1–2 dB throughout the complete pattern. Comparing the co-polarized elevation plane results in Figure 99 shows that the calculated results and the measured results agree to within 1–3 dB throughout the complete pattern except in the region on the horizon near the tail of the aircraft where the calculated levels increase to as much as 5 dB higher than the measured levels. Comparing the co-polarized results for the azimuth plane in Figure 100 shows that the agreement between the calculated and measured levels is within 1–2 dB

throughout this pattern cut. Comparing the co-polarized results for the conical planes in Figures 101, 102 and 103 shows that the agreement between the calculated results and the measured results is within 1–2 dB throughout the majority of the pattern for all three conic taken. Therefore, the higher levels which are seen in the horizon near the tail of the aircraft in the elevation plane disappear as the pattern cut is taken slightly above the horizon.

The cross-polarized results are shown in Figures 104 through 109. Again the agreement between the calculated and measured results for the cross-polarized fields is not as good as the agreement found for the co-polarized fields due to the reasons given in Section 5.2. These cross-polarized results are included only to provide additional information.

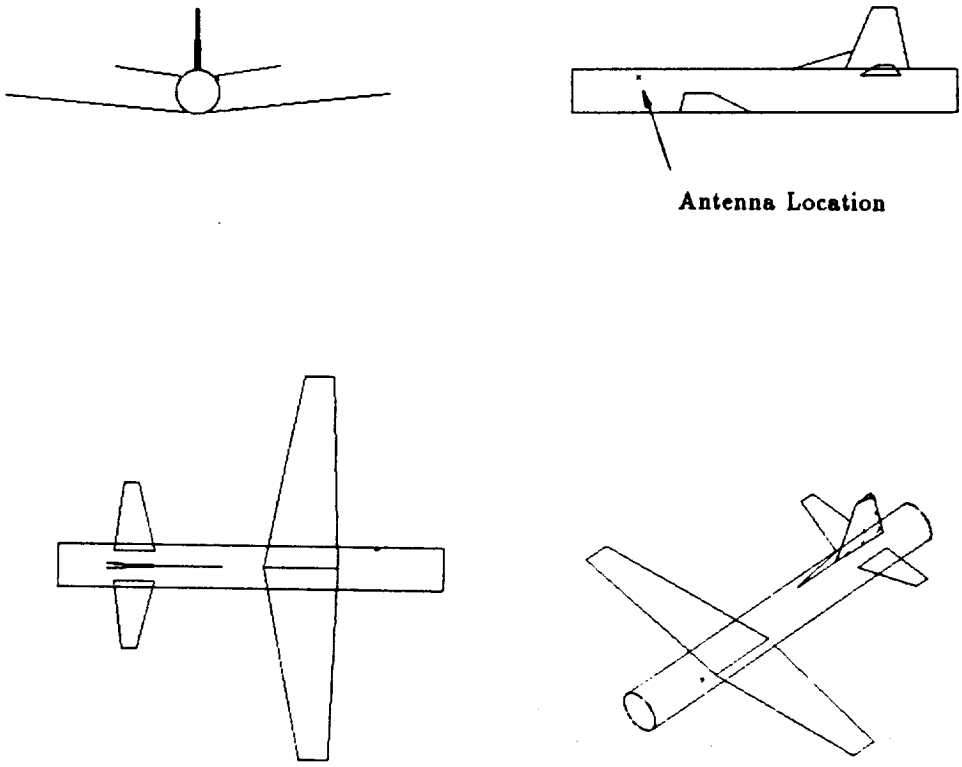

Figure 97: Geometry of the cylindrical model of the P-3C aircraft used in the NEC-BSC showing the alternative Boeing antenna location.

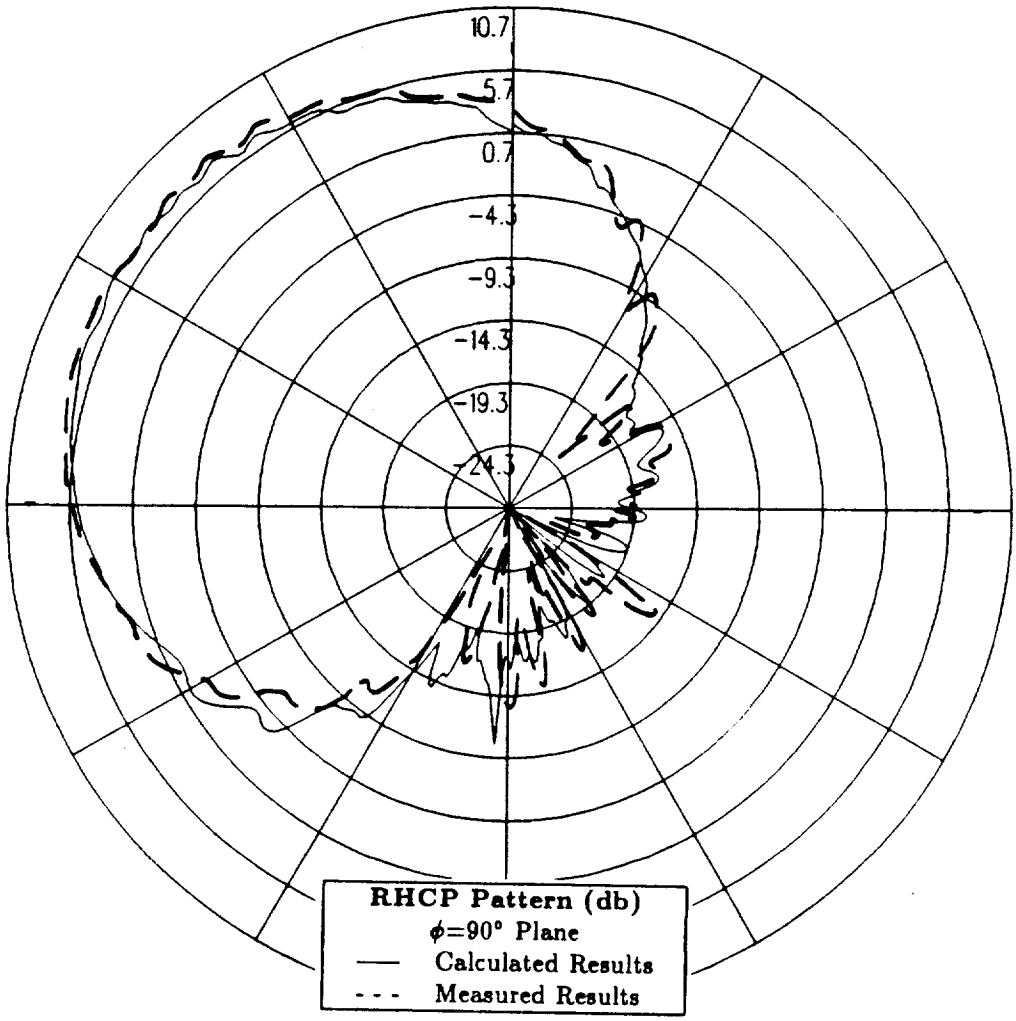

Figure 98: Roll plane pattern for altenative antenna location in Boeing report for right hand circular polarization at 300 MHz.

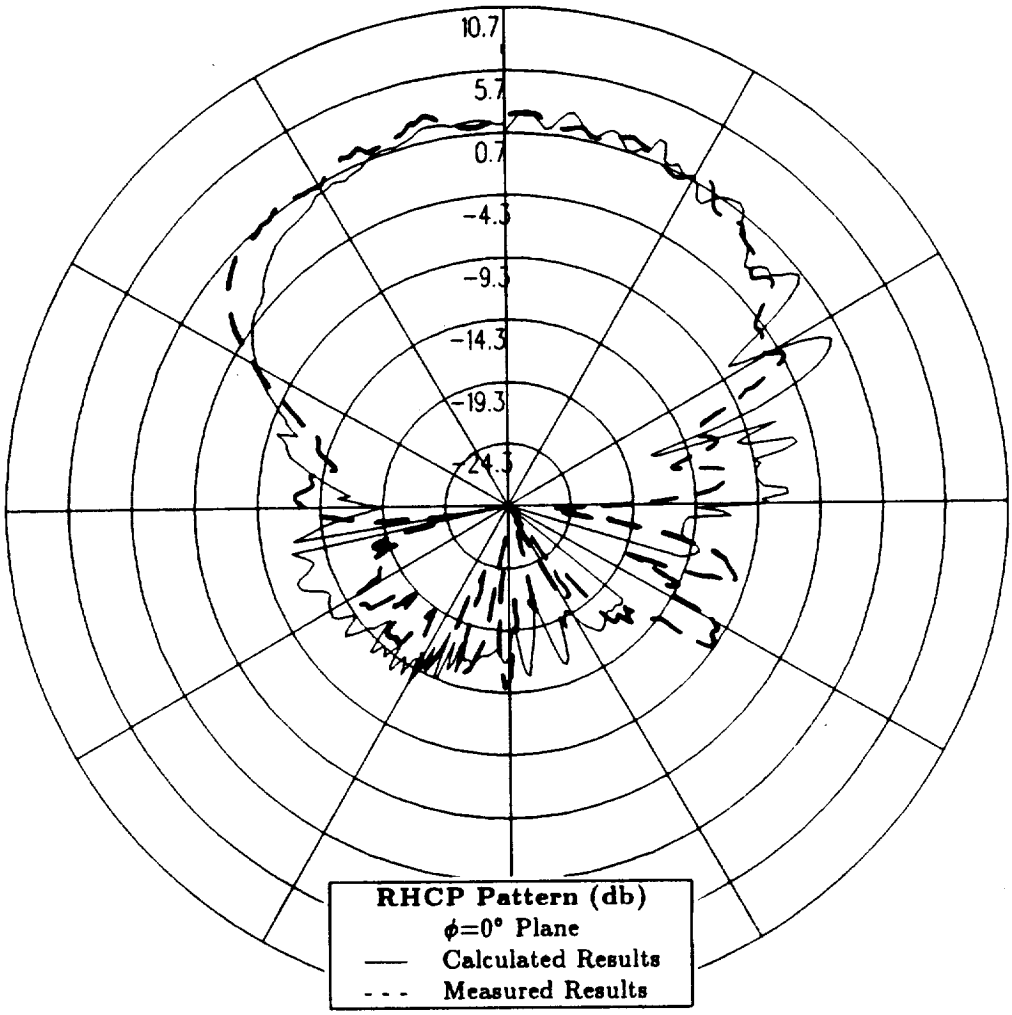

Figure 99: Elevation plane pattern for alternative antenna location in Boeing report for right hand circular polarization at 300 MHz.

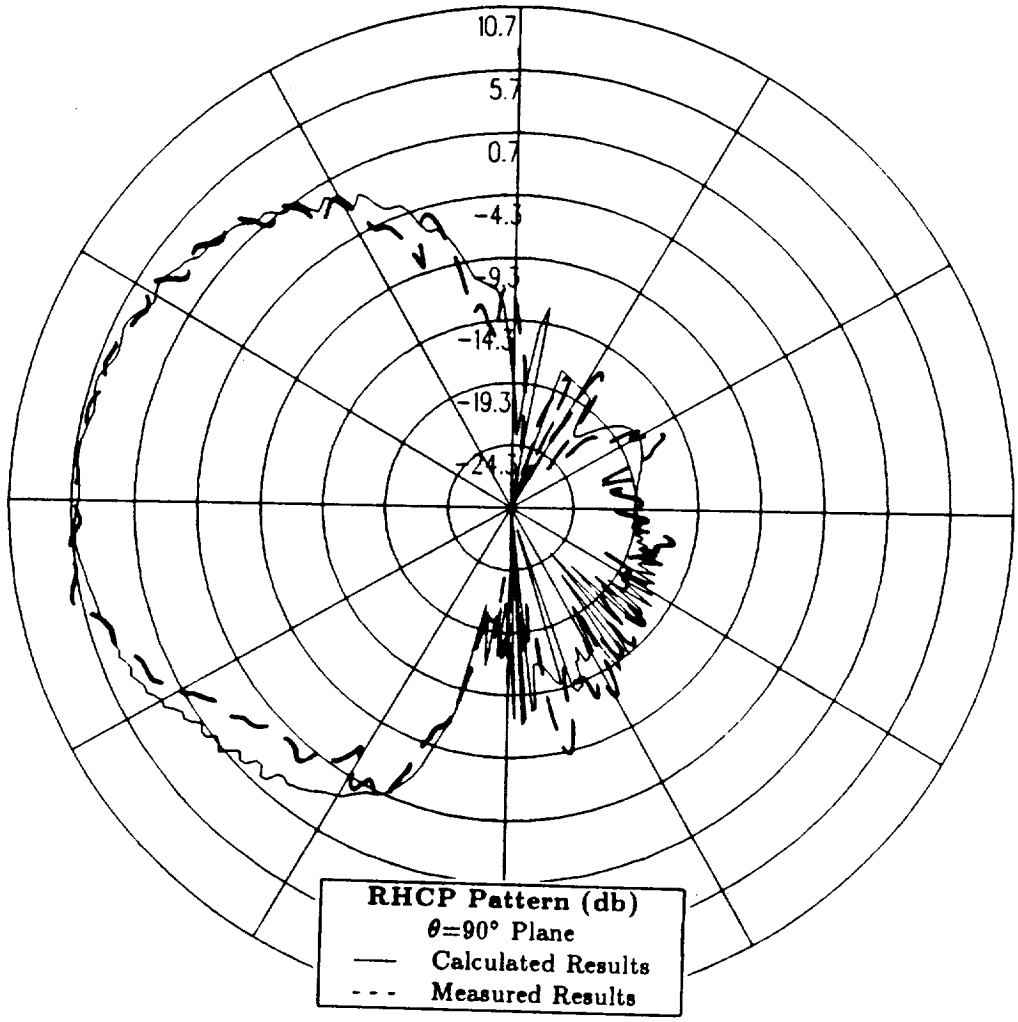

Figure 100: Azimuth plane pattern for alternative antenna location in Boeing report for right hand circular polarization at 300 MHz.

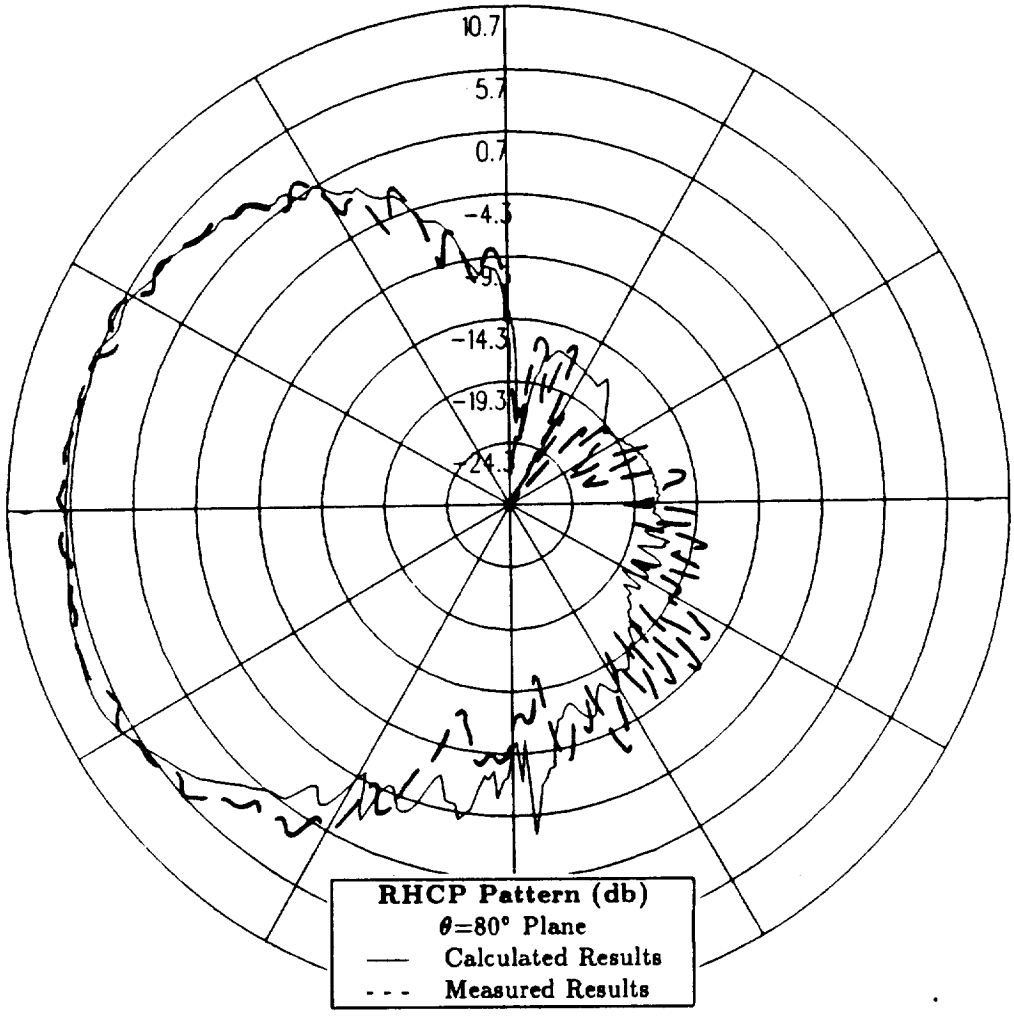

Figure 101: Conical plane pattern 10° above the horizon for alternative antenna location in Boeing report for right hand circular polarization at 300 MHz.

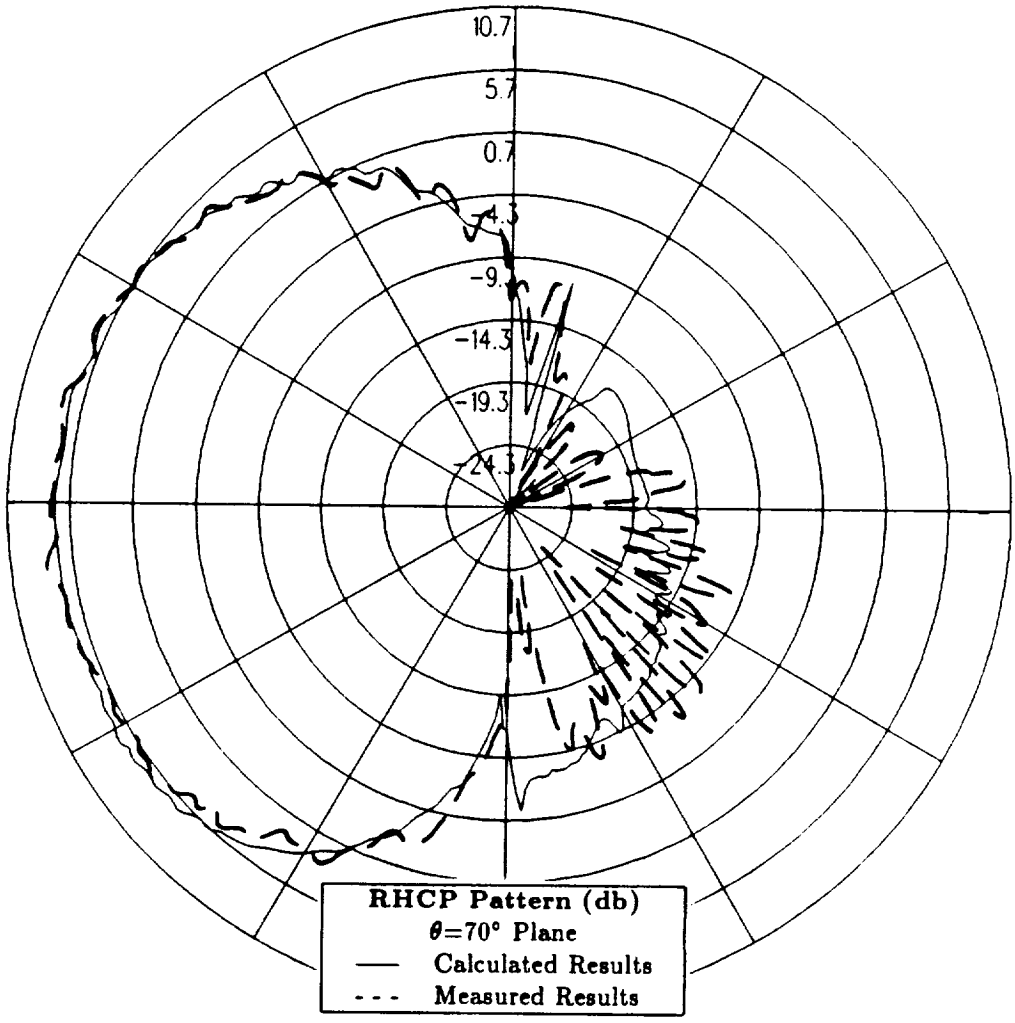

Figure 102: Conical plane pattern 20° above the horizon for alternative antenna location in Boeing report for right hand circular polarization at 300 MHz.

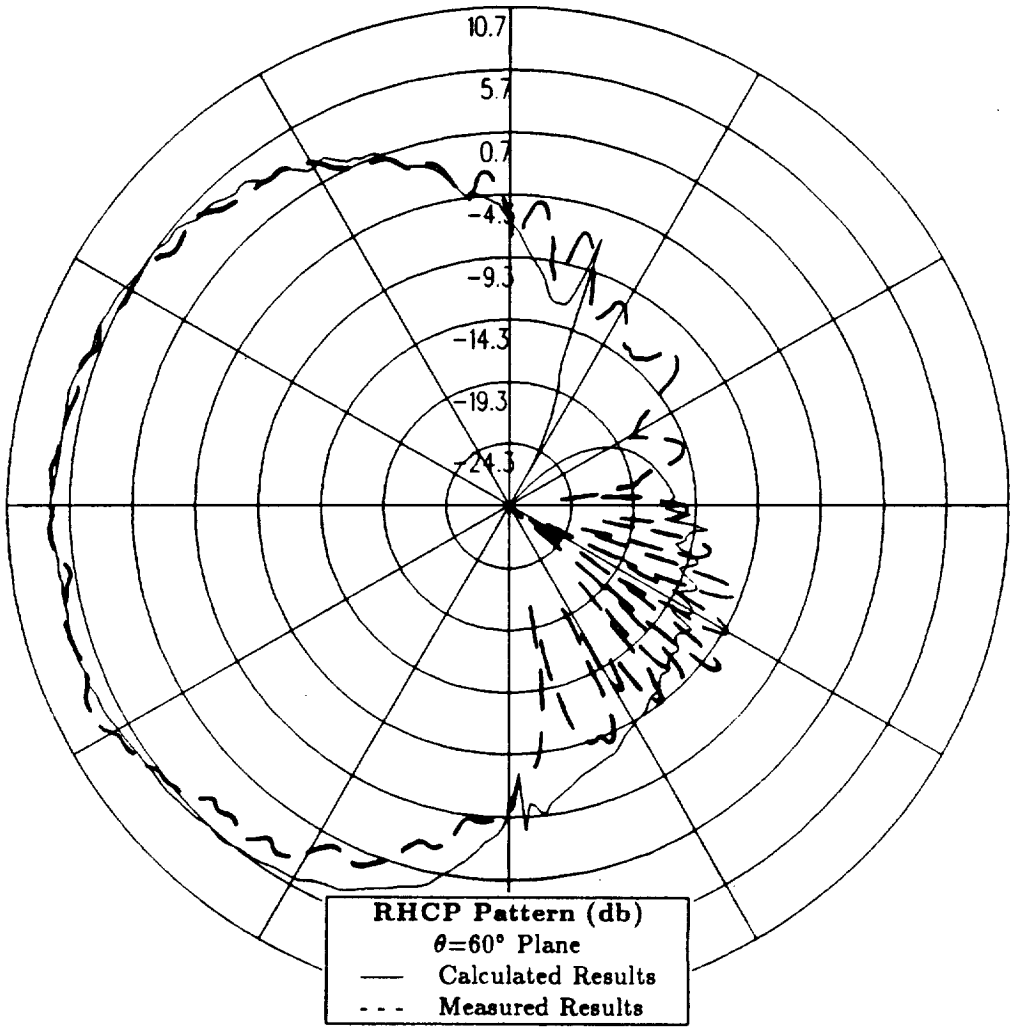

Figure 103: Conical plane pattern 30° above the horizon for alternative antenna location in Boeing report for right hand circular polarization at 300 MHz.

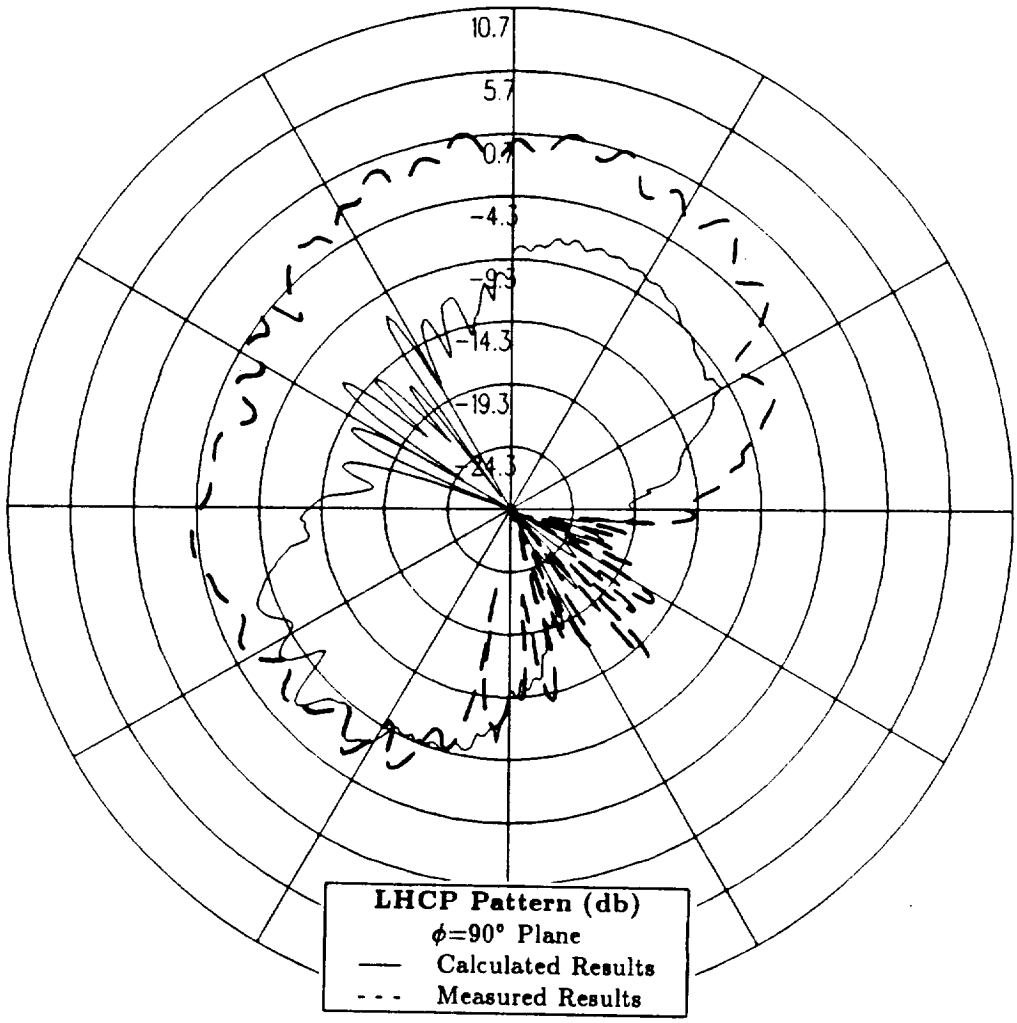

Figure 104: Roll plane pattern for alternative antenna location in Boeing report for left hand circular polarization at 300 MHz.

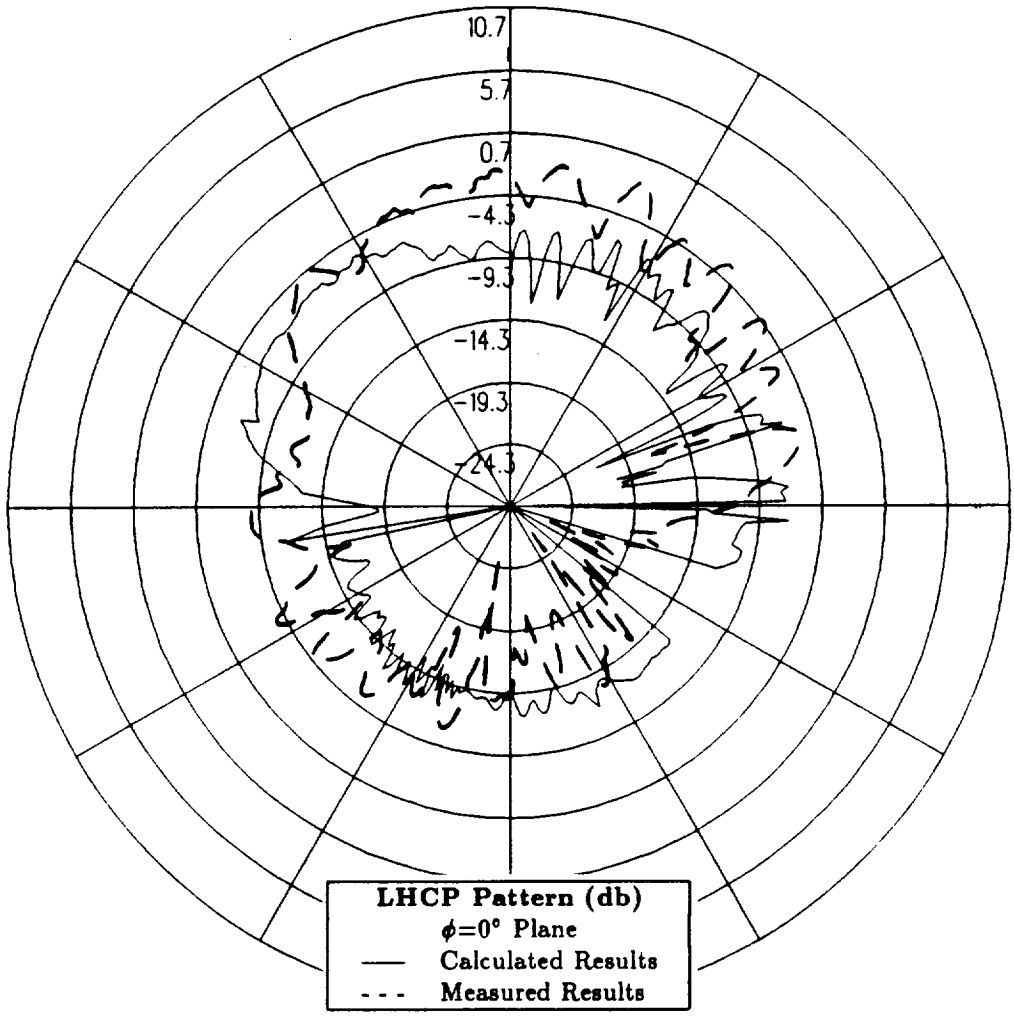

Figure 105: Elevation plane pattern for alternative antenna location in Boeing report for left hand circular polarization at 300 MHz.

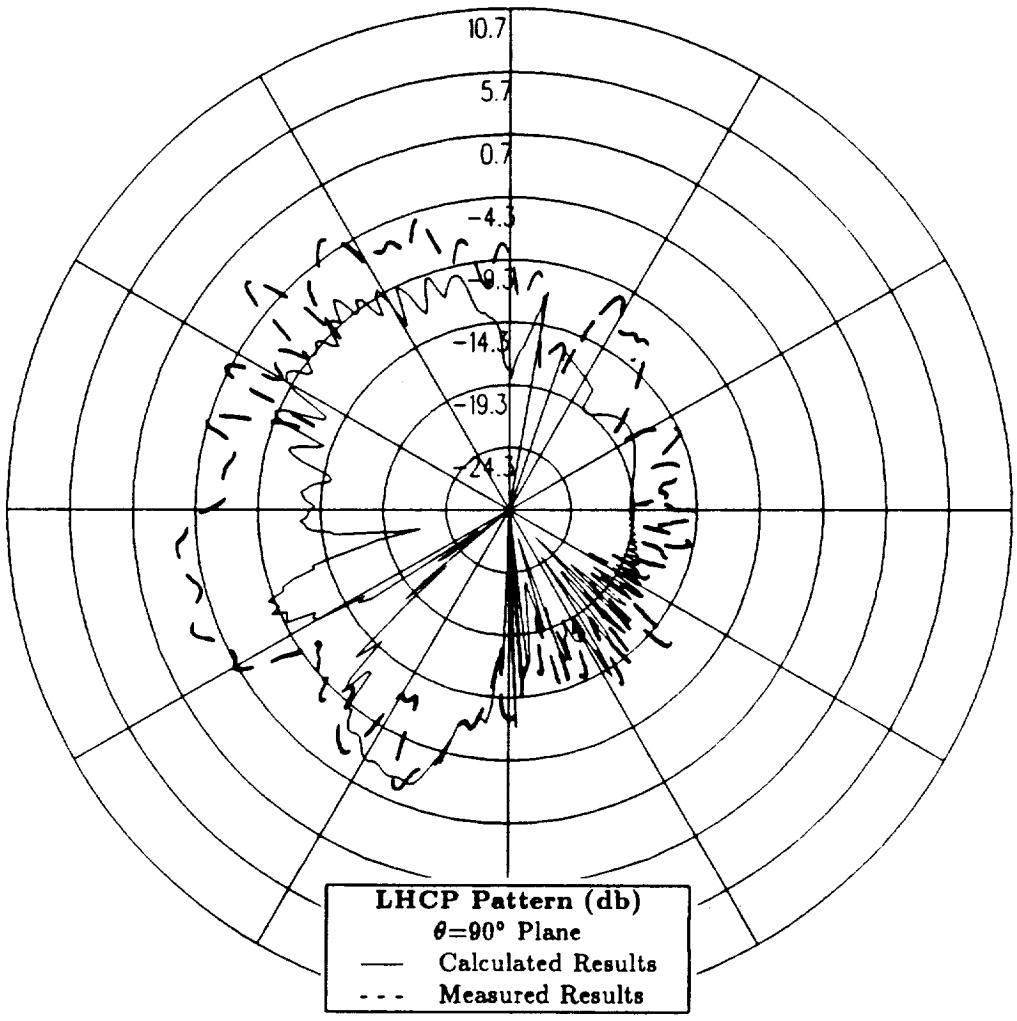

Figure 106: Azimuth plane pattern for alternative antenna location in Boeing report for left hand circular polarization at 300 MHz.

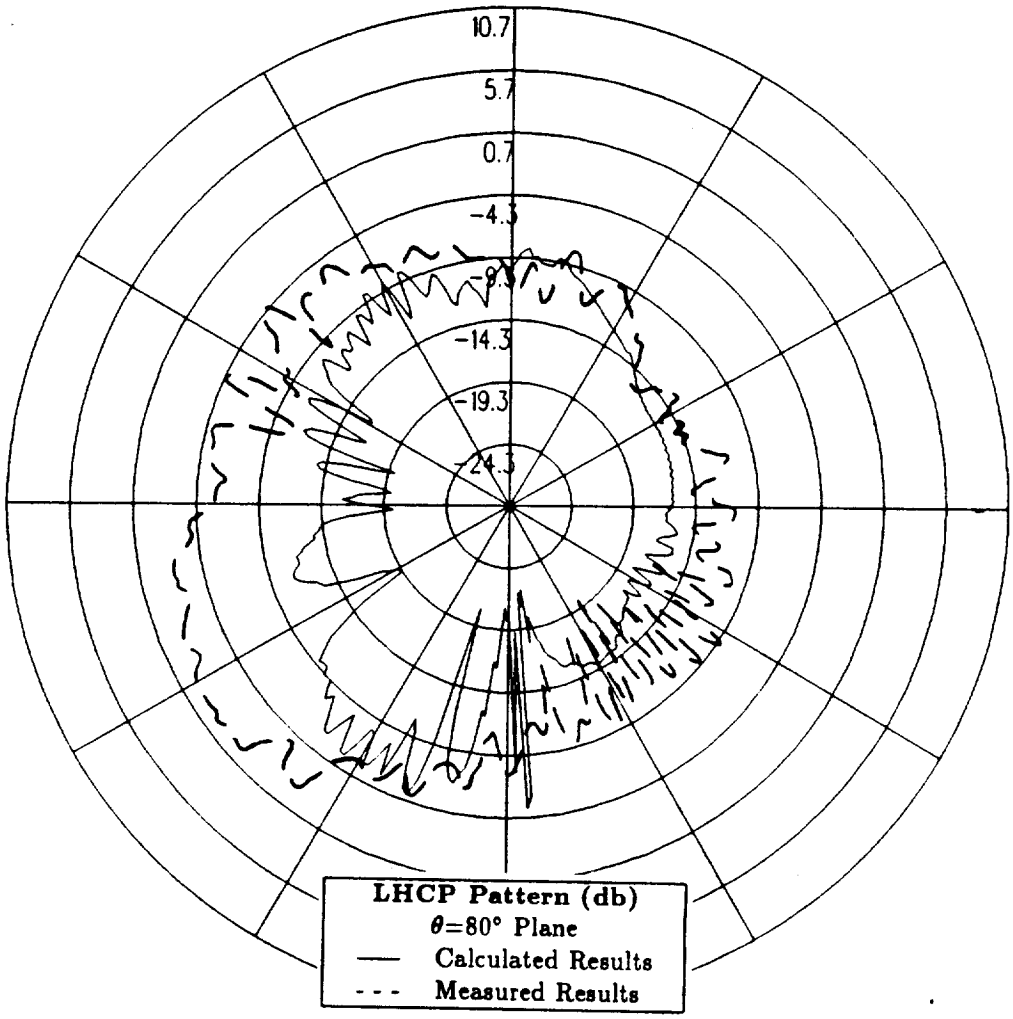

Figure 107: Conical plane pattern 10° above the horizon for alternative antenna location in Boeing report for left hand circular polarization at 300 MHz.

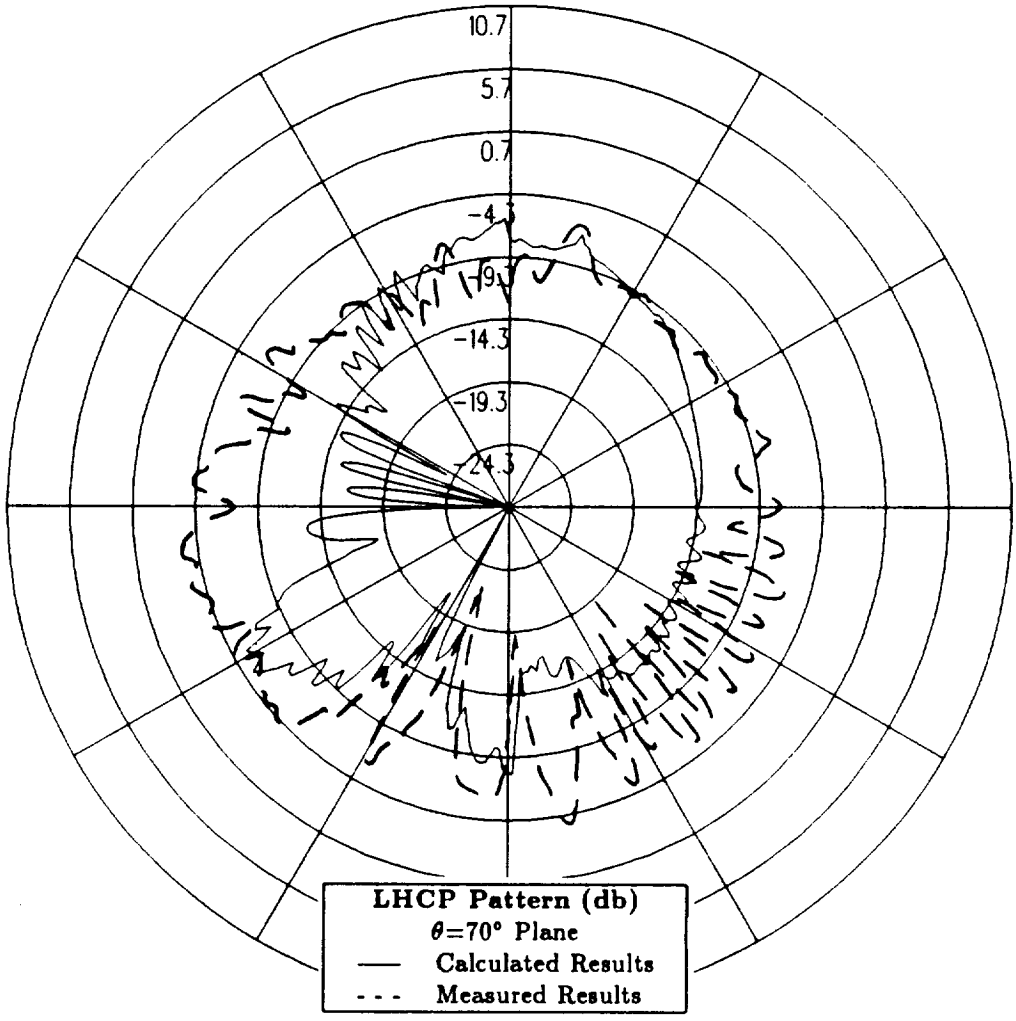

Figure 108: Conical plane pattern 20° above the horizon for alternative antenna location in Boeing report for left hand circular polarization at 300 MHz.

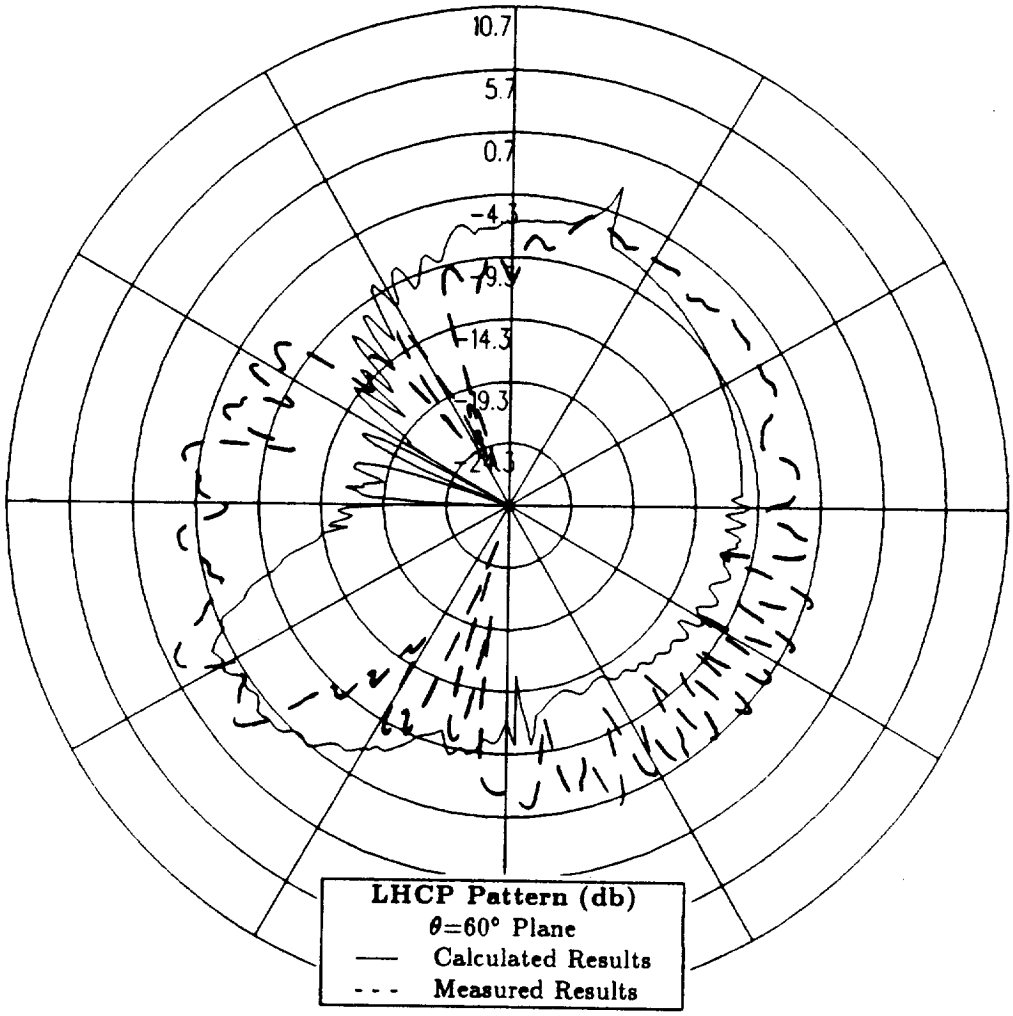

Figure 109: Conical plane pattern 30° above the horizon for alternative antenna location in Boeing report for left hand circular polarization at 300 MHz.

5.6 Aircraft Model Conclusions

In Section 5.2, it has been shown that the radiation patterns calculated using the improved NEC-BSC, which includes the plate - cylinder interactions, provide better agreement with the measured patterns than the Version 3.1 calculated radiation patterns. The improvement is most noticeable in the horizon of the aircraft in the regions near the nose and the tail where the calculated radiation levels are reduced to levels which are much closer to the measured levels. Although the calculated levels are still up to 5 dB higher than the measured levels in a few small regions, these improved calculated patterns very closely model the measured patterns on the whole. Therefore, the cylindrical aircraft model which is used in this section provides an accurate representation of the actual P-3C aircraft when using the improved NEC-BSC.

The sensitivity study presented in Section 5.3 confirms the accuracy of the simple cylindrical aircraft model. The more detailed aircraft model which includes engine and propeller blade models causes spikes to appear in the radiation pattern in the horizon of the aircraft near the nose and the tail. By averaging the radiation levels in the region near the nose, the calculated levels for the detailed model are 1–2 dB less than the calculated levels for the simple model. However, the CPU time required to run the detailed aircraft model is over four times the CPU time required to run the simple aircraft model. Although the detailed model contains slightly improved levels in the horizon of the aircraft near the nose, the presence of the spikes and the greatly increased CPU time does not justify using the detailed model. The final two tests which are investigated to see the effect on the radiation patterns in the horizon of the aircraft near the nose involve tilting the aircraft wings and adding double diffraction terms to the pattern. Both of these tests cause the calculated levels to decrease by approximately 1 dB in the

horizon of the aircraft near the nose when compared to the original cylindrical aircraft model patterns. However, the slightly lower levels in this region disappear as the pattern cut is taken above the horizon. Because the radiation levels for these two tests investigated in the sensitivity study are only slightly lower than the level for the original cylindrical model and these lower levels disappear as the pattern cut is taken above the horizon, the features considered in the sensitivity study do not significantly improve the agreement between the calculated and measured patterns. Therefore, the simple cylindrical aircraft model which has been investigated initially remains the best representation of the actual P-3C aircraft.

Sections 5.4 and 5.5 provide additional evidence as to the validity of the cylindrical aircraft model. These sections compare the NEC-BSC calculated patterns for the cylindrical aircraft model to the measured results provided by Lockheed and Boeing, respectively, for two different antenna locations. Both of these tests confirm that the cylindrical aircraft model provides an accurate representation of the actual aircraft model. The Lockheed test investigated in Section 5.4, in which the antenna location is similar to the location studied for the primary Boeing location, still contains the problem with high calculated levels in the horizon of the aircraft near the nose and the tail. However, the calculated patterns agree with the measurements as the pattern cuts are taken above the horizon. The additional Boeing test investigated in Section 5.5, in which the antenna location is on the fuselage of the aircraft near the nose, provides excellent agreement between the calculated levels and the measured levels throughout all of the pattern cuts taken.

The disagreement which remains between the calculated results and the measured results in the region about the nose near the horizon of the aircraft is likely due to the modeling capability of the NEC-BSC. The engines of the P-3C aircraft have a substantial influence on the radiation patterns in this area. Therefore, the absence of the aircraft engines is probably the cause of the disagreements between

the calculated and measured results in the azimuth plane for the simple cylindrical aircraft model. Section 5.3.1 shows that the presence of the engine models improves the agreement between the calculated pattern and the measured pattern in this region. However, the spikes which are present in the azimuth pattern illustrate that the simple building blocks used to model the engines do not provide an accurate representation of the actual aircraft engines. If more complex shapes could be implemented in the code which would allow the user to more closely model the actual shape of the engines, the ability of the NEC-BSC to more accurately predict the radiation patterns, especially in this specific region, would be improved.

Another possible explanation for the differences between the calculated results and the measured results in this region is that the measurements provided by Boeing and Lockheed along the axis of the aircraft fuselage are not as accurate as the measured results for the remainder of the patterns. It is possible that the the scale model antenna and the scale model aircraft do not provide an accurate representation of the actual configuration along the axis of the aircraft. This also could explain the differences between the calculated and measured levels which are found in this region.

Chapter 6

Conclusions

The purpose of this study is to use Version 3.1 of the NEC-BSC to perform a UHF SATCOM antenna siting study on an aircraft. In this report, the case investigated involves a circular polarized crossed dipole antenna located on the fuselage of a P-3C aircraft. However, this procedure can be performed for any type of antenna located on any type of aircraft as long as the antenna is not surface mounted. The NEC-BSC is not able to accurately represent an antenna which is mounted directly to the surface of the aircraft.

There are two major steps that are needed to validate the accuracy of the NEC-BSC in evaluating the performance of a SATCOM antenna on an aircraft. In the first step, the antenna model which is used in the NEC-BSC must be validated. In this particular study, a circular polarized antenna composed of crossed dipoles has been used to represent the Dorne & Margolin DM 1501341 Batwing SATCOM antenna. In order to validate this antenna model, the NEC-BSC calculated patterns for the antenna have been compared to measured patterns provided by the manufacturer and measured patterns provided by Naval Air Test Center. Also, these NEC-BSC calculated antenna patterns have been compared to results calculated using a moment method solution and an exact eigenvalue solution. In each of these comparisons, the NEC-BSC calculated antenna patterns have been in

good agreement with the corresponding measured patterns or calculated patterns found using other methods. Therefore, there is a high level of confidence in the antenna model which has been used throughout this report.

The second step is to validate the aircraft model which is used in the NEC-BSC. The validity of the aircraft model is determined by comparing the NEC-BSC calculated patterns to measurements conducted by Boeing on a 1/17 scale model of the P-3C aircraft [11]. The study performed in Section 3.3 indicates that the radiation patterns calculated using the various aircraft models do not accurately match the the measured radiation patterns near the nose and the tail of the aircraft when Version 3.1 of the NEC-BSC is used. After further investigation, the reason that the calculated radiation patterns do not closely agree with the measured patterns is discovered to be due to the absence of curved surface reflected - plate diffracted fields in Version 3.1 of the NEC-BSC. Simulation of these curved surface reflected - plate diffracted fields is then included and it is determined that the aircraft model which uses a simple cylinder to represent the fuselage of the aircraft provides the most accurate representation of the actual P-3C aircraft.

After the four primary first order plate - cylinder fields are added to Version 3.1 of the NEC-BSC, the cylindrical aircraft model is validated using the improved code. The validation process includes a sensitivity study to ensure that the aircraft model contains the basic structural features essential to the radiation patterns and an antenna location study to ensure that the aircraft model is valid for different antenna locations. The validity of the cylindrical aircraft model can be determined by comparing the NEC-BSC calculated patterns to measurements conducted by Boeing on a 1/17 scale model of the P-3C aircraft [11] and by Lockheed on a 1/10 scale model of the P-3C aircraft [16]. The sensitivity study performed in Section 5.3 demonstrates that the simple cylindrical aircraft model contains the basic structural features which are essential to the radiation patterns. The location

study performed in Sections 5.4 and 5.5 demonstrates that the simple cylindrical aircraft model is also valid for alternative antenna locations.

This study demonstrates that the improved NEC-BSC can be used to accurately assess the radiation patterns for the circular polarized crossed dipole antenna located on a P-3C aircraft. In Chapter 5, the validity of the simple cylindrical aircraft model to represent the actual P-3C aircraft is confirmed. Overall, the NEC-BSC calculated patterns show good agreement with the measured results for the various antenna locations throughout the majority of the areas of interest. The sole exception is in small regions about the nose and tail near the horizon of the aircraft where the NEC-BSC calculated patterns are slightly higher than the measured patterns. Therefore, there is a high level of confidence in the accuracy of the NEC-BSC calculated radiation patterns in all areas except this small region. A study can now be done to investigate other potential locations for this circular polarized crossed dipole antenna on a P-3C. A high level of confidence can then be placed in the accuracy of these NEC-BSC calculated radiation patterns for all areas except these small regions about the nose and tail near the horizon of the aircraft.

This study emphasizes the ability of the NEC-BSC to complement other design techniques such as scale model measurements. The code is a fast and cost effective means to anticipate problems at the early design stages and to optimize parameters such as reasonable siting locations. A limited set of measurements then can be more cost effectively utilized to confirm the prospective locations.

Bibliography

[1] R. J. Marhefka and J. W. Silvestro, "Near Zone - Basic Scattering Code, User's Manual with Space Station Applications," Technical Report 718422-13, The Ohio State University ElectroScience Laboratory, Department of Electrical Engineering, March 1988. Prepared under Grant No. NSG 1613 for National Aeronautics and Space Administration.

[2] R. J. Marhefka, D. Bensman, and D. DeCarlo, "A SATCOM Antenna Siting Study on an Aircraft Using the NEC-BSC V3.1," in *6th Annual Review, Applied Computational Electromagnetics Society*, Naval Postgraduate School, Monterey, California, March 1990.

[3] D. Bensman and R. J. Marhefka, "SATCOM Antenna Siting Study on a P-3C Using the NEC-BSC V3.1," Technical Report 721711-2, The Ohio State University ElectroScience Laboratory, Department of Electrical Engineering, April 1990. Prepared under Grant No. NAG2-542 for Naval Air Test Center and National Aeornautics and Space Administration.

[4] W. D. Burnside and R. J. Marhefka, "Antennas On Aircraft, Ships, or Any Large, Complex Environment," in *Antenna Handbook: Theory, Applications, and Design*, (Y. T. Lo and S. W. Lee, eds.), Ch. 20, New York: Van Nostrand Reinhold Co. Inc., 1988.

[5] R. G. Kouyoumjian and P. H. Pathak, "A Uniform Geometrical Theory of Diffraction for an Edge in a Perfectly-Conducting Surface," *Proc. IEEE*, Vol. 62, pp. 1448-1461, November 1974.

[6] P. H. Pathak, W. D. Burnside, and R. J. Marhefka, " A Uniform GTD Analysis of the Diffraction of Electromagnetic Waves by a Smooth Convex Surface," *IEEE Trans. on Antennas and Propagation*, Vol. AP-28, pp. 631-642, September 1980.

[7] P. H. Pathak, "Techniques for High-Frequency Problems," in *Antenna Handbook: Theory, Applications, and Design*, (Y. T. Lo and S. W. Lee, eds.), Ch. 4, New York: Van Nostrand Reinhold Co. Inc., 1988.

[8] J. D. Kraus, *Antennas*, 2nd ed., pp. 70-81. McGraw-Hill Book Co., 1988.

[9] E. H. Newman, "A User's Manual for the Electromagnetic Surface Patch Code: ESP Version IV," Technical Report 716199-11, The Ohio State University ElectroScience Laboratory, Department of Electrical Engineering, August 1988. Prepared under Grant No. NSG 1498 for National Aeronautics and Space Administration.

[10] R. F. Harrington, *Time-Harmonic Electromagnetic Fields*, pp. 232-238. McGraw-Hill Book Co., 1961.

[11] S. Hunter, "P-3 Update IV Antenna Test Report," Document No. D385-66744-1, Boeing, Airborne Antenna System Group, May 1988. Prepared under Contract No. N00019-87-C-0269 for Naval Air Test Center.

[12] *Jane's All the World's Aircraft*, (J. W. R. Taylor, ed.), pp. 356-357. McGraw-Hill Book Co., 1973.

[13] R. J. Marhefka, "Analysis of Aircraft Wing-Mounted Antenna Patterns," Technical Report 2902-25, The Ohio State University ElectroScience Laboratory, Department of Electrical Engineering, June 1976. Prepared under Grant No. NGL 36-008-0138 for National Aeornautics and Space Administration.

[14] Short course notes on "The Modern Geometrical Theory of Diffraction," Vols. 1,2 and 3, The Ohio State University ElectroScience Laboratrory, Department of Electrical Engineering, 1982.

[15] F. A. Sikta, W. D. Burnside, T. Chu and L. Peters,Jr., " First- Order Equivalent Current and Corner Diffraction Scattering from Flat Plate Structures," *IEEE Trans. on Antennas and Propagation*, Vol. AP-31, pp. 584-589, July 1983.

[16] Laboratory Report No. LR 30132, Lockheed, Avionics Systems Laboratory. Prepared under authority of Engineering Test Request 7731-10-554, Work Order 31-7211-1110.